

On Inverse Form Finding for Anisotropic Materials in the Logarithmic Strain Space

Inverse Formfindung für anisotrope Materialien im logarithmischen Verzerrungsraum

Der Technischen Fakultät der
Universität Erlangen-Nürnberg

zur Erlangung des Grades

DOKTOR-INGENIEUR

vorgelegt von

Sandrine Germain

Erlangen — 2013

Als Dissertation genehmigt von der
Technischen Fakultät der
Universität Erlangen-Nürnberg

Tag der Einreichung: 05.11.2012
Tag der Promotion: 23.04.2013
Dekanin: Prof. Dr.-Ing. habil. M. Merklein
Berichterstatter: Prof. Dr.-Ing. habil. P. Steinmann
Prof. Dr.-Ing. Dr.-Ing. E.h. A.E. Tekkaya

Schriftenreihe Technische Mechanik
Band 8 - 2013

Sandrine Germain

**On Inverse Form Finding for Anisotropic
Materials in the Logarithmic Strain Space**

Herausgeber: Prof. Dr.-Ing. habil. Paul Steinmann
Prof. Dr.-Ing. habil. Kai Willner

Erlangen 2013

Impressum

Prof. Dr.-Ing. habil. Paul Steinmann
Prof. Dr.-Ing. habil. Kai Willner
Lehrstuhl für Technische Mechanik
Universität Erlangen-Nürnberg
Egerlandstraße 5
91058 Erlangen
Tel: +49 (0)9131 85 28502
Fax: +49 (0)9131 85 28503

ISSN 2190-023X

© Sandrine Germain
Alle Rechte, insbesondere das
der Übersetzung in fremde
Sprachen, vorbehalten. Ohne
Genehmigung des Autors ist
es nicht gestattet, dieses Heft
ganz oder teilweise auf
photomechanischem,
elektronischem oder sonstigem
Wege zu vervielfältigen.

Vorwort

Die vorliegende Arbeit entstand während meiner Tätigkeit als wissenschaftliche Mitarbeiterin am Lehrstuhl für Technische Mechanik (LTM) der Universität Erlangen-Nürnberg (Januar 2009 - April 2013). Sie basiert auf Ergebnissen, die im Rahmen des DFG SFB/Transregio 73: „*Umformtechnische Herstellung von komplexen Funktionsbauteilen mit Nebenformelementen aus Feinblechen - Blechmassivumformung -*“ im Teilprojekt C3: „*Parameter- und Formoptimierung in der finiten Elastoplastizität*“ erarbeitet wurden.

Besonders herzlich möchte ich mich bei Herrn Prof. Dr.-Ing. habil. Paul Steinmann bedanken. Er hat diese Arbeit angeregt und hat mir viel Freiheit gegeben, eigene Ideen umzusetzen. Weiterhin möchte ich mich bei Herrn Prof. Dr.-Ing. habil. Kai Willner für die Zusammenarbeit im TR73/C3 bedanken. Bei Herrn Prof. Dr.-Ing. Dr.-Ing. E.h. A. Erman Tekkaya bedanke ich mich für das Interesse an meiner Arbeit und die Übernahme der Rolle als Zweitgutachter.

Ich bedanke mich desweiteren bei Herrn Dr.-Ing. Michael Scherer für die zahlreichen und hilfreichen Diskussionen zu Beginn meiner Dissertation und bei Herrn Dr.-Ing. Ali Javili und Herrn Dr.-Ing. Henrik Keller für das kritische Korrekturlesen dieser Dissertation. Allen Mitarbeitern des LTM und Mitgliedern des TR73 danke ich für die angenehme Arbeitsatmosphäre und die gute Zusammenarbeit, insbesondere meinem Bürokollegen Stefan Schmaltz.

Je remercie en particulier mes parents pour leur aide, confiance et soutien durant toutes ces années. Ils m'ont permis d'entreprendre et de réaliser mes études dans les meilleures conditions possibles. Meinem Freund Philip danke ich ganz besonders für seine Hilfe, seine Unterstützung und seine Aufmunterung während der Höhen und Tiefen dieser vier Jahre.

Nürnberg, Juni 2013

Sandrine Germain

*Il est bien des choses qui ne paraissent impossibles
que tant qu'on ne les a pas tentées*

André Gide

Abstract

A challenge in the design of functional parts is the determination of the initial, undeformed shape such that under a given load a part will obtain the desired deformed shape. This is an inverse form finding problem and it is posed as follows: the deformed shape, the mechanical loading, and the boundary conditions are given, whereas the inverse deformation map that determines the material configuration, i.e., the undeformed shape, is sought. Inverse form finding methods are useful tools in conceiving designs in less time and at lower cost than with experiments or direct computational design.

In the present work two inverse form finding methods are presented for the optimal determination of the initial shape of formed functional components, considering anisotropic hyperelastic and elastoplastic behaviours. The material is modelled by a macroscopic phenomenological approach in the logarithmic strain space for large strains based on the small strains theory. This model uses the laws of thermodynamics to describe the macroscopic behaviour of the material. The anisotropy in the material is formulated through the eight crystal systems according to the spectral decomposition of the fourth-order elasticity tensor using the Kelvin modes. A Cauchy formulation of the boundary value problem, called inverse mechanical problem, allows to determine the undeformed configuration of a functional component. All quantities are parametrised in the spatial coordinates. This formulation is suitable when dealing with hyperelastic materials. For elastoplastic behaviour, the provided deformed configuration, load, and boundary conditions are no longer sufficient to compute the wanted undeformed configuration. The set of internal variables corresponding to the deformed configuration is equally required in this case. Usually the set of internal variables at the deformed state is unknown before the computation of the undeformed configuration in elastoplasticity. Therefore a gradient-based shape optimisation is used in this work according to an inverse problem via successive iterations of a direct mechanical problem. The objective function of the inverse form finding problem is defined by a least squares minimisation of the difference between the target and the current deformed configuration of the workpiece. The design variables are defined by the discretised nodes of the functional component with the finite element method (node-based shape optimisation). This choice leads, however, to mesh distortions in the undeformed shape, which are avoided by using a recursive algorithm. Between two iterative steps of the algorithm the current optimised undeformed configuration is used in the computation of the next value of the objective function. The total applied force is then split over all entities.

In the computation of both inverse form finding methods, deformed workpieces with different geometries, material parameters and crystal systems were used. The inverse mechanical problem and the shape optimisation formulation in hyperelasticity gave identical results with respect to the geometry of the obtained undeformed shape. Nevertheless the computational costs of the inverse mechanical formulation were about 2000 times lower. For elastoplastic behaviours the shape optimisation formulation has to be computed with the recursive algorithm in order to avoid mesh distortions. All the results were validated by the comparison between the given deformed configuration of the workpiece and the directly computed deformed configuration of the workpiece. A difference of about 10^{-6} to 10^{-24} mm was achieved with both inverse form finding methods.

Keywords: Inverse form finding, Shape optimisation, Anisotropy, Elastoplasticity, Logarithmic strain

Zusammenfassung

Eine Herausforderung bei der Herstellung und dem Entwurf von Bauteilen ist die Bestimmung des initialen, undeformierten Zustands des Bauteiles, so dass es unter Anwendung einer bekannten Kraft die gewünschte deformierte Form erreicht. Dieses Problem wird im Bereich der Materialwissenschaften als inverse Formfindung bezeichnet. Inverse Formfindungsmethoden sind nützliche Instrumente, um gewünschte Bauteildesigns in kürzerer Zeit und zu geringeren Kosten zu entwerfen und herzustellen, als dies mit experimentellen Methoden oder durch direkte mechanische Berechnung möglich wäre. Das inverse Formfindungsproblem ist wie folgt definiert: die deformierte Form des Bauteils, die mechanischen Kräfte und die Randbedingungen sind gegeben, die undeformierte Form des Bauteils stellt die gesuchte Größe dar.

In dieser Arbeit werden zwei Methoden zur inversen Formfindung für anisotrope hyperelastische und elastoplastische Probleme vorgestellt und erweitert. Der Werkstoff wird zunächst mit dem logarithmischen Verzerrungsmaß makroskopisch und phänomenologisch für große Deformationen modelliert, basierend auf der Theorie der kleinen Deformationen. Dieses Modell nutzt die thermodynamischen Sätze, um das makroskopische Verhalten der Materialien zu beschreiben. Die Anisotropie des Materials wird durch die acht Kristallsysteme entsprechend der spektralen Dekomposition des vierstufigen Elastizitäts-Tensors mit Kelvin Moden beschrieben. Cauchy's Ansatz der Randwertprobleme, ein sogenanntes inverses mechanisches Problem, erlaubt es, die undeformierte Form des Bauteils zu berechnen. Dabei sind alle Größen in räumlichen Koordinaten parametrisiert. Dieser Ansatz ist für hyperelastisches Verhalten von Materialien geeignet nicht aber für elastoplastisches. Für elastoplastische Materialien müssten auch die internen Materialvariablen der deformierten Konfiguration bekannt sein. Da dies bei der inversen Berechnung nicht der Fall ist, wird in dieser Arbeit eine gradienten-basierte Formoptimierungsmethode zur Berechnung des undeformierten Materialzustands benutzt, die ein inverses Problem durch sukzessive Iterationen eines direkten Problems berechnet. Die Zielfunktion des inversen Formfindungsproblems ist dabei als Fehlerquadratminimierung zwischen der bekannten und der zu berechnenden deformierten Konfiguration des Bauteils definiert. Als Designvariablen werden die Diskretisierungsknoten des Bauteils mit der finiten Elemente Methode definiert. Diese Formoptimierungsmethode kann allerdings zu Netzverzerrungen in der undeformierten Form des Bauteils führen, welche durch die Anwendung eines rekursiven Algorithmus vermieden werden können. Dabei wird bei jeder Verknüpfung die aktuell optimierte Form zur Berechnung des darauffolgenden Funktionswertes verwendet und die applizierte Gesamtkraft auf alle Instanzen aufgeteilt.

Für die Berechnung der undeformierten Form wurden deformierte Bauteile verschiedener Größen mit unterschiedlichen Materialparametern und Symmetrieklassen simuliert. Bei der Berechnung für hyperelastische Materialien liefern die Formoptimierung und die inverse mechanische Formulierung gleiche Ergebnisse hinsichtlich der durch die inverse Formfindung gefundenen undeformierten Konfiguration. Letztere Methode benötigt eine um den Faktor 2000 geringeren rechnerischen Zeitaufwand. Für die Berechnung des elastoplastischen Materialsverhaltens ist die oben beschriebene Formoptimierungsmethode unter Anwendung des rekursiven Ansatzes erforderlich. Die Ergebnisse werden durch Vergleiche mit der direkt berechneten, deformierten Form evaluiert. Für die Formoptimierung und die inverse mechanische Formulierung wurden dabei Abweichungen zwischen 10^{-6} und 10^{-24} mm festgestellt.

Résumé

Un challenge dans la conception de pièces mécaniques fonctionnelles est la détermination de la forme initiale ou non déformée telle que sous l'effet d'une force donnée cette pièce mécanique ait la forme déformée souhaitée. C'est un problème inverse appelé "recherche de forme par méthode inverse". La recherche de forme par méthode inverse est un outil essentiel qui permet de concevoir le design de pièces mécaniques en un moindre temps et à des coûts moins élevés que ceux nécessaires lors de la conception par la réalisation d'essais mécaniques ou par simulation informatique directe. Le problème de recherche de forme par méthode inverse est posé comme suit: la géométrie de la pièce mécanique déformée, la force mécanique appliquée ainsi que les conditions limites sont données tandis que la géométrie de la pièce non déformée est recherchée.

Dans cette thèse deux méthodes de recherche de forme par méthode inverse sont présentées et développées pour des comportements anisotropiques hyperélastiques et élastoplastiques. Le matériau est tout d'abord modélisé par une approche macroscopique et phénoménologique pour des grandes déformations basée sur une mesure logarithmique et sur la théorie des petites déformations. Le modèle utilise les lois de la thermodynamique pour décrire le comportement macroscopique du matériau hyperélastique ou élastoplastique. L'anisotropie présente dans le matériau est formulée à travers les huit systèmes cristallins selon la décomposition spectrale du tenseur élastique du quatrième ordre en utilisant les modes de Kelvin. La formulation de Cauchy du problème aux limites appelé problème mécanique inverse permet de trouver la pièce mécanique non déformée en paramétrisant toutes les données en coordonnées spatiales. Cette formulation est pertinente pour des matériaux hyperélastiques. Pour un comportement élastoplastique, en revanche, pourvoir la géométrie de la pièce mécanique déformée, la force appliquée ainsi que les conditions limites ne suffit plus. Le vecteur des variables internes de la pièce déformée doit aussi être fourni. Puisque ce vecteur n'est en pratique initialement pas connu, l'optimisation de forme basée sur la méthode des gradients est utilisée dans cette thèse afin de trouver la géométrie initiale de la pièce mécanique non déformée par des successions itératives du problème mécanique direct. La fonction objectif est définie par la méthode des moindres carrés entre la géométrie de la pièce déformée donnée et la géométrie de la pièce déformée calculée. Les noeuds provenant de la discrétisation de la pièce mécanique non déformée par la méthode des éléments finis sont choisis comme variables de conception (optimisation de forme basée sur les noeuds). Une distorsion du maillage de la pièce non déformée peut apparaître lorsque la force appliquée est trop importante. Ce problème peut être résolu en utilisant un algorithme récursif. A chaque itération, la pièce non déformée optimisée actuelle est utilisée dans l'évaluation suivante de la fonction objectif où la force totale appliquée est découpée suivant ces entités.

Lors de l'application des deux méthodes de recherche de forme par méthode inverse, différentes géométries, différents paramètres matériau ainsi que différentes symétries cristallines furent utilisées. L'optimisation de forme ainsi que la formulation du problème mécanique inverse pour un comportement hyperélastique donnèrent la même géométrie de pièce non déformée. La dernière méthode eut néanmoins besoin de 2000 fois moins de temps de calcul. Pour un comportement élastoplastique l'optimisation de forme augmentée de l'algorithme récursif est indispensable afin de déterminer la géométrie de la pièce non déformée. Tous les résultats obtenus furent validés en comparant la géométrie de la pièce mécanique déformée, qui fut donnée, avec la géométrie de la pièce déformée calculée avec la formulation directe du problème mécanique. Pour chacune des deux méthodes un écart de 10^{-6} à 10^{-24} mm fut obtenu.

Contents

Chapter 1 Introduction	1
1.1 Motivation	1
1.2 Outline of the present work	4
Chapter 2 Basics of continuum mechanics	7
2.1 Kinematics of geometrically nonlinear continuum mechanics	7
2.2 Balance principles in mechanics	9
2.2.1 Mass balance	9
2.2.2 Momentum balance	10
2.2.3 Balance of mechanical energy	13
2.2.4 Entropy balance	15
Chapter 3 The macroscopic constitutive model in logarithmic strain space	17
3.1 The additive Lagrangian formulation in elastoplasticity	18
3.2 Energy storage and elastic stress response	19
3.3 The anisotropic yield criterion and the yield surface	20
3.4 Anisotropic plastic flow rule and the hardening law	22
3.5 The return mapping algorithm	22
3.5.1 The incremental plastic multiplier	25
3.5.2 Elastoplastic tangent modulus	28
Chapter 4 Spectral decomposition and the Kelvin modes	31
4.1 Spectral decomposition	31
4.2 Typical Kelvin modes	33
4.3 The Kelvin mode formulation for isotropic material	37
4.4 The Kelvin mode formulation for anisotropic materials	38
4.4.1 The cubic crystal system	38
4.4.2 The orthorhombic (orthotropic) crystal system	39
4.4.3 The trigonal crystal system	41
4.4.4 Monoclinic crystal system	42
4.4.5 The triclinic crystal system	44
4.4.6 The tetragonal crystal system	45
4.4.7 The hexagonal crystal system (transverse isotropy)	48
4.4.8 A numerical example	52
Chapter 5 Determining the deformed shape from equilibrium	55
5.1 The direct mechanical problem	55
5.2 Finite element analysis	56
5.2.1 Discretisation	58

5.2.2	The Newton–Raphson method	59
5.2.3	Linearisation of the weak form	60
5.3	Numerical examples	63
5.3.1	Isotropic hyperelastic material	63
5.3.2	Anisotropic hyperelastic material	63
5.3.3	Isotropic elastoplastic material	65
5.3.4	Anisotropic elastoplastic material	67
Chapter 6	Determining the undeformed shape from equilibrium	73
6.1	The inverse mechanical problem	74
6.2	Finite element analysis	75
6.2.1	Discretisation	75
6.2.2	The Newton–Raphson method	76
6.2.3	Linearisation of the weak form	77
6.3	Numerical examples	80
6.3.1	Isotropic hyperelastic material	80
6.3.2	Anisotropic hyperelastic material	83
6.3.3	Isotropic elastoplastic material	90
6.4	Discussion	93
6.4.1	Example 1	96
6.4.2	Example 2	97
Chapter 7	Determining the undeformed shape from shape optimisation	99
7.1	Definition of the optimisation problem	99
7.2	The Limited Memory Broyden–Fletcher–Goldfarb–Shanno method	100
7.3	Sensitivity analysis	101
7.3.1	Numerical gradient	102
7.3.2	Analytical gradient	103
7.4	A recursive algorithm for avoiding mesh distortion	104
7.5	Numerical examples	106
7.5.1	Isotropic hyperelastic material	107
7.5.2	Anisotropic hyperelastic material	111
7.5.3	Isotropic elastoplastic material	112
7.5.4	Anisotropic elastoplastic material	114
7.6	Discussion	117
Chapter 8	Conclusion and outlook	119
Appendices		121
List of Symbols		125
List of Figures		129
List of Tables		135

Bibliography	137
Index	143

CHAPTER 1

Introduction

1.1 Motivation

The objective of the present work is the development of continuum-mechanical and computational methods for the optimal determination of the initial shape of formed functional components. Anisotropic hyperelastic and elastoplastic behaviours should be considered. A challenge in the design of functional parts is the determination of the initial, undeformed shape such that under a given load a part will obtain the desired deformed shape. This is an inverse form finding problem and it is posed as follows: the deformed shape, the mechanical loading, and the boundary conditions are given, whereas the inverse deformation map that determines the material configuration, i.e., the undeformed shape, is sought. This problem is the inverse of the standard direct kinematic analysis, in which the undeformed shape is known and the deformed one, unknown. Inverse form finding methods are useful tools. Designs can then be conceived in less time and at lower cost than with experiments or direct computational design.



Figure 1.1: Undeformed (left) circular and deformed (right) aluminium plates.

A practical use of inverse form finding can be illustrated by an example from the trans-regional project TR73¹. A circular plate² made of aluminium is deformed by incremental forces acting on the border of the plate. The undeformed configuration of the plate is illustrated in Figure 1.1 on the left, whereas the obtained deformed configuration is illustrated on the right. The three holes in the middle of the plate allow the plate to rotate, so that the workpiece moves and not the tool. The objective of the manufacturing process is a circular gear wheel,

¹Deutsche Forschungsgemeinschaft, Sonderforschungsbereich Transregio 73 (www.tr-73.de)

²The plates were provided by TR73/TPA4, IUL/TU Dortmund

which was obviously not achieved correctly. The question which arises is then: How should the undeformed plate be initially manufactured so that at the end of the incremental forming process the deformed plate is circular and not rectangular as illustrated in Figure 1.1 on the right. This question can be fully answered by using inverse form finding methods.

The present work has two major parts: an inverse mechanical approach and a shape optimisation approach for the aforementioned problem. Both methods will be briefly compared.

Govindjee et al. proposed in [1, 2] a numerical procedure for the determination of the undeformed shape of a continuous body, which is based on the work done by Shield in [3]. Their work is limited to isotropic compressible neo-Hookean materials and incompressible materials. One outcome of their work is the recognition that the weak form of the inverse motion problem based on the Cauchy stress is more efficient and straightforward than the weak form based on the Eshelby stress (energy momentum tensor). The governing equation underlying the numerical analysis of the inverse form finding problem is therefore the common weak form of the balance of momentum formulated in terms of the Cauchy stress tensor. However, the unconventional issue is that all quantities are parametrised in the spatial coordinates. Temperature changes in the undeformed and deformed configuration have been taken in consideration by Govindjee et al. in [4] for orthotropic nonlinear elasticity and axisymmetry using a St. Venant type material. An application of their method has been developed by Koishi et al. in [5] for the purpose of tire design. Yamada proposed in [6] another approach as in [1] based on an arbitrary Lagrangian–Eulerian kinematic description. The arbitrary Lagrangian–Eulerian description is approximated by a finite element discretisation. Later on, Fachinotti et al. extended in [7, 8] the method proposed in [1] for the case of anisotropic hyperelasticity for a St. Venant type material, i.e., a material characterised by a quadratic free energy density in terms of the Green–Lagrange strain. Albanesi et al. extended in [9, 10] this work to the inverse analysis of large displacement beams in the elastic range. Lu et al. proposed in [11] a computational method of inverse elastostatics for anisotropic hyperelastic solids in the context of fibrous hyperelastic solids and provide explicit stress function for soft tissue models. Zhou et al. presented in [12] an inverse method for thin wall structures modelled as geometrically exact stress resultant shells.

These methods for the determination of the undeformed shape have not considered anisotropic hyperelastic and elastoplastic material behaviour with a formulation in the logarithmic strain space. In a first step, the method originally proposed by Govindjee et al. in [1] is therefore extended for this purpose, following Germain et al. in [13, 14, 15]. The governing equation for the resulting finite element analysis is the weak form of the balance of momentum formulated in terms of the deformed configuration using the Cauchy stress tensor, here called the inverse mechanical formulation. All quantities are parametrised in the spatial coordinates. The material is modelled by a macroscopic phenomenological approach following the standard literature on material modelling, see for example de Souza Neto et al. [16], Holzapfel [17], Ogden [18], or Bonet et al. [19]. A logarithmic strain space formulation with a structure adopted from the geometrically linear theory is used, and follows closely the methods developed by Miehe et al. in [20, 21] and by Apel in [22]. The anisotropy in the material is formulated through the eight crystal systems by means of the spectral decomposition of the fourth-order elasticity tensor using the Kelvin modes, as in Mehrabadi et al. [23], Sutcliffe [24], Cowin et al. [25, 26], Chadwick and al. [27], and Mahnken [28]. An additive Lagrangian formulation is adopted. The formulation of the yield criterion and the yield surface is given after presenting the description of the energy storage and the elastic response. The plastic flow rule and hardening law are defined for anisotropic elastoplasticity. The elastoplastic constitutive initial value problem is solved by a

return mapping algorithm (or plastic corrector step) following the one presented in Simo and al. [29] for J2 plasticity and in de Souza Neto et al. [16], extended here to the case of anisotropic elastoplastic materials in the logarithmic strain space. It was found that the inverse mechanical formulation is appropriate when dealing with hyperelastic materials, illustrated by three numerical examples. For elastoplastic behaviour, the provided deformed configuration, load, and boundary conditions are, however, no longer sufficient for obtaining the sought undeformed configuration, according to Germain et al. [15]. However it is demonstrated in this work, by considering an uniaxial tension experiment in 1D, that if the set of internal variables corresponding to the deformed configuration is previously given, the wanted undeformed configuration can be obtained for elastoplastic materials. Two numerical examples, for isotropic elastoplasticity, are presented. However, the inverse mechanical formulation remains inadequate for elastoplastic behaviour.

To overcome this problem, shape optimisation methods can be used, since the set of internal variables at the deformed state is usually unknown before the computation of the undeformed configuration in elastoplasticity.

Shape optimisation is a large topic. Indeed, the volume, the stiffness, the thickness, etc., of the considered shape can be optimised³, see for example Haftka et al. [39], Samareh [40], Schwarz [41], Bletzinger et al. [42, 43, 44], Fourment et al. [45, 46], Badrinarayanan et al. [47], Srikanth et al. [48], and Chenot et al. [49]. Shape optimisation of elastoplastic structures can be found in Schwarz [41], Maute et al. [50], and Schwarz et al. [51]. In the present work, gradient-based shape optimisation (Luenberger [52], Nocedal et al. [53], Schmidt [54]) is used in the sense of an inverse problem via successive iterations of a direct mechanical problem as described in Sousa et al. [55], Ponthot et al. [56], and Germain et al. [57], in order to reach the wanted undeformed shape. The objective function is defined by a least squares minimisation of the difference between the target and the current deformed configuration of the workpiece. In order to minimise the objective function and subsequently use gradient-based shape optimisation, the optimisation algorithm requires the gradient of the objective function with respect to the design variables, i.e., a sensitivity analysis. In shape optimisation, the design variables can be defined, for example, by Bézier surfaces or B-splines (Samareh [40], Yao [58]), which describe the boundary of the shape, or as in this work, by the nodes obtained with the finite element method, i.e., node-based shape optimisation. Sensitivity analysis is also a topic widely discussed, and can be divided into two major branches: continuous and discrete. Variational, or continuous, sensitivity analysis provides the computation of the gradient of the continuum problem with respect to the design variables, and the discretisation comes afterwards, see for example Schwarz [41], Srikanth et al. [48], Ganapathysubramanian et al. [59], Archarjee et al. [60], Barthold [61] and Schwarz et al. [62]. On the contrary, in a discrete sensitivity analysis, the discretisation of the mechanical problem is carried out first. The gradient with respect to the design variables is then calculated from the discretised problem, see for example Schwarz [41]. In the present work, the discrete formulation is used because all the equations obtained in the formulation of the inverse mechanical formulation previously described can be reused. Furthermore the gradient of the objective function can be computed either numerically or analytically. A simple finite difference will provide the numerical gradient. The programming of this gradient is straightforward but the computational costs are high. Moreover when the spacing is not properly chosen, this leads to relevant errors (Haftka et al. [63], Burg [64]). Analytical gradients are therefore more appropriate, but challenging to

³Parameter identification can also be formulated as an optimisation problem, see for example Kleuter et al. [30] and Mahnken et al. [31, 32, 33, 34, 35, 36, 37, 38].

find. Burg summarised in [64] the costs and benefits of these different methods for obtaining the gradient. In this work, a sensitivity analysis is performed by providing the analytical gradient of the objective function with respect to the material coordinates of the finite element mesh, where the crucial step is the mechanical equilibrium equation as described in Scherer et al. [65, 66]. Using a node-based shape optimisation leads, however, to mesh distortions in the undeformed shape. Scherer et al. proposed a new regularisation technique, which consists of adding an artificial inequality constraint to the optimisation problem, a fictitious total strain energy that measures the shape change of the design with respect to the reference design. In the present work, the mesh distortions are avoided by using a recursive algorithm as presented by Germain et al. in [67, 68]. Between two iterative steps of the algorithm, the current optimised undeformed configuration is used in the computation of the next value of the objective function. The total applied force is then split between all entities. Several examples in this work illustrate the shape optimisation formulation for isotropic and anisotropic hyperelastic and elastoplastic materials when the recursive algorithm is applied.

Finally a comparison between the inverse mechanical problem and the shape optimisation formulation is presented. For hyperelasticity, both methods give identical results in consideration of the geometry of the obtained undeformed shape as in Germain et al. [69, 70]. Nevertheless the inverse mechanical formulation has computational costs about 2000 times lower, for the same example. For elastoplastic behaviour, the shape optimisation formulation has to be computed with the recursive algorithm in order to avoid mesh distortions. All the results are validated through a comparison between the given deformed configuration of the workpiece and the direct computed deformed configuration of the workpiece. A difference of about 10^{-6} to 10^{-24} mm is achieved with both inverse form finding methods.

1.2 Outline of the present work

The present work has seven chapters and two appendices. The following is a short outline of the contents of the chapters and appendices:

Chapter 2 This chapter deals with the basics of continuum mechanics, where besides a review of the most important laws in continuum mechanics, it also introduces the notation used in the later chapters.

Chapter 3 This chapter presents a macroscopic phenomenological model in the logarithmic strain space with a structure adopted from the geometrically linear theory for both isotropic and anisotropic elastoplastic behaviour. This model is later used in Chapter 5, Chapter 6, and Chapter 7.

Chapter 4 In this chapter the spectral decomposition of the fourth-order elasticity tensor is presented for the eight crystal systems as a function of the typical Kelvin modes. It is later used in the numerical examples presented in Chapter 5, Chapter 6, and Chapter 7.

Chapter 5 For the model introduced, this chapter describes the determination of the deformed shape of a functional component from the equilibrium equation using the finite element method, i.e., the direct mechanical problem. Several numerical examples illustrate the development presented in this chapter for isotropic and anisotropic hyperelastic and elastoplastic

materials.

Chapter 6 This chapter deals with the determination of the undeformed shape of a functional component from the equilibrium equation using the finite element method, when the deformed configuration of the shape, the mechanical loading, and the boundary conditions are given, i.e., the inverse mechanical problem. The uniqueness of the solution is discussed for elastoplastic behaviour. Several numerical examples illustrate the development presented in this chapter for isotropic and anisotropic hyperelastic and elastoplastic materials.

Chapter 7 This chapter deals with the determination of the undeformed shape of a functional component using shape optimisation methods in the sense of an inverse problem via successive iterations of the direct mechanical formulation. Several numerical examples illustrate the development presented in this chapter for isotropic and anisotropic hyperelastic and elastoplastic materials. A comparison between both inverse form finding methods is presented as well.

Chapter 8 This chapter summarises and gives some brief perspectives of the presented research.

Appendix A-B The appendix consists of two parts. Appendix A contains the proof of the decomposition of the fourth-order tangent operator in the material configuration. In Appendix B, the proof of the decomposition of the fourth-order tangent operator in the spatial configuration is given.

CHAPTER 2

Basics of continuum mechanics

Within this chapter, the basics of continuum mechanics is provided. Besides the review of the most important laws of continuum mechanics, the aim is also to introduce the notation used in the forthcoming chapters.

This chapter is structured as follows: The kinematics of geometrically nonlinear continuum mechanics are first presented. The mass balance, the momentum balance, the balance of energy, and the entropy balance are given in the material and spatial configurations resuming and following the work done by Holzapfel in [17] chapter 4. The basics of continuum mechanics might also be found in de Souza Neto et al. [16], Ogden [18], Bonet et al. [19], Gonzales et al. [71] and Wriggers [72]. Parts of this chapter have been published by Germain et al. in [13, 14, 15, 57, 68].

2.1 Kinematics of geometrically nonlinear continuum mechanics

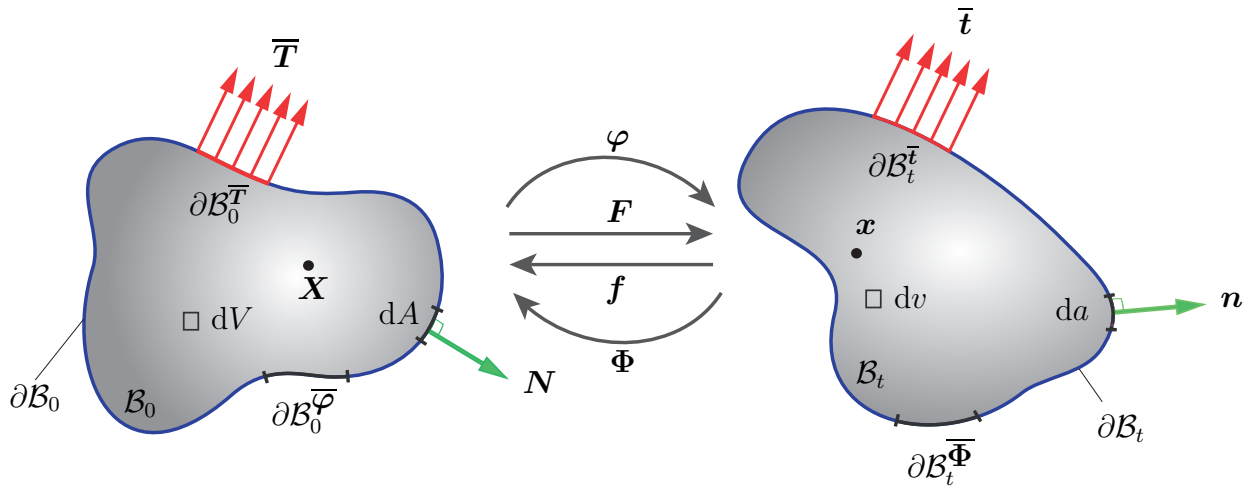


Figure 2.1: Material (right) and spatial (left) configurations.

Let $\mathcal{B}_0 \subset \mathbb{R}^3$ denote the material or undeformed configuration of a continuum body parametrised by the material coordinates \mathbf{X} with respect to the Cartesian basis \mathbf{E}_I at time $t = 0$. $\mathcal{B}_t \subset \mathbb{R}^3$ is the corresponding spatial or deformed configuration parametrised by the spatial coordinates \mathbf{x} with respect to the Cartesian basis \mathbf{e}_i at time t , as depicted in Figure 2.1. Subsequently, the

bases \mathbf{E}_I and \mathbf{e}_i are taken to be coincident with $I, i = 1, 2, 3$. The boundary of \mathcal{B}_0 is assumed to be decomposed into disjoint parts, so that

$$\partial\mathcal{B}_0 = \partial\mathcal{B}_0^{\bar{T}} \cup \partial\mathcal{B}_0^{\bar{\Phi}} \quad \text{with} \quad \partial\mathcal{B}_0^{\bar{T}} \cap \partial\mathcal{B}_0^{\bar{\Phi}} = \emptyset, \quad (2.1)$$

where $\partial\mathcal{B}_0^{\bar{T}}$ is the Neumann type boundary condition and $\partial\mathcal{B}_0^{\bar{\Phi}}$ is the Dirichlet type boundary condition. The boundary of \mathcal{B}_t is likewise assumed to be decomposed into disjoint parts, so that

$$\partial\mathcal{B}_t = \partial\mathcal{B}_t^{\bar{T}} \cup \partial\mathcal{B}_t^{\bar{\Phi}} \quad \text{with} \quad \partial\mathcal{B}_t^{\bar{T}} \cap \partial\mathcal{B}_t^{\bar{\Phi}} = \emptyset, \quad (2.2)$$

where $\partial\mathcal{B}_t^{\bar{T}}$ is the Neumann type boundary condition and $\partial\mathcal{B}_t^{\bar{\Phi}}$ is the Dirichlet type boundary condition. The direct nonlinear deformation map

$$\mathbf{x} = \boldsymbol{\varphi}(\mathbf{X}) : \mathcal{B}_0 \longrightarrow \mathcal{B}_t \quad (2.3)$$

gives the position of each spatial point $\mathbf{x} \in \mathcal{B}_t$ as a function of its material counterpart $\mathbf{X} \in \mathcal{B}_0$. The corresponding linear tangent map or, rather, the direct deformation gradient tensor, is defined by

$$\mathbf{F} = \text{Grad}\boldsymbol{\varphi}, \quad (2.4)$$

where $\text{Grad}(\cdot)$ denotes the gradient operator with respect to the material coordinates \mathbf{X} . In index notation, the direct deformation gradient tensor is

$$\mathbf{F} = \sum_{i,j=1}^3 F_{ij} \mathbf{e}_i \otimes \mathbf{e}_j \quad \text{with} \quad F_{ij} = \frac{\partial x_i}{\partial X_j}. \quad (2.5)$$

The Jacobian determinant of Equation 2.4, which describes the local change of the volume due to the deformation, is required to be positive

$$J = \det \mathbf{F} > 0. \quad (2.6)$$

The volume element dv in the spatial configuration is related to the volume element dV in the material configuration by the Jacobian determinant J

$$dv = J dV. \quad (2.7)$$

The surface area element da in the spatial configuration is related to the surface area element dA in the material configuration and the cofactor of \mathbf{F} by Nanson's formula

$$d\mathbf{n} = \text{COF}(\mathbf{F}) \cdot dA \mathbf{N} = J \mathbf{F}^{-T} \cdot \mathbf{N} dA, \quad (2.8)$$

where the unit vectors \mathbf{n} and \mathbf{N} are the outward normals to da and dA , respectively. The inverse nonlinear deformation map

$$\mathbf{X} = \boldsymbol{\Phi}(\mathbf{x}) : \mathcal{B}_t \longrightarrow \mathcal{B}_0 \quad (2.9)$$

gives the position of each material point $\mathbf{X} \in \mathcal{B}_0$ as a function of its spatial counterpart $\mathbf{x} \in \mathcal{B}_t$. The corresponding linear tangent map or, rather, the inverse deformation gradient tensor, is given by

$$\mathbf{f} = \text{grad}\boldsymbol{\Phi}, \quad (2.10)$$

where $\text{grad}(\cdot)$ denotes the gradient operator with respect to the spatial coordinates \boldsymbol{x} . In index notation, the inverse deformation gradient tensor is

$$\boldsymbol{f} = \sum_{i,j=1}^3 f_{ij} \boldsymbol{e}_i \otimes \boldsymbol{e}_j \quad \text{with} \quad f_{ij} = \frac{\partial X_i}{\partial x_j}. \quad (2.11)$$

The Jacobian determinant of the inverse deformation gradient is likewise required to be positive

$$j = \det \boldsymbol{f} > 0. \quad (2.12)$$

The volume element dV in the material configuration is related to the volume element dv in the spatial configuration by the Jacobian determinant j

$$dV = j dv. \quad (2.13)$$

The surface area element dA in the material configuration is likewise related to the surface area element da in the spatial configuration by the Jacobian determinant j and the transpose of the inverse of the deformation gradient \boldsymbol{f}

$$\boldsymbol{N} dA = j \boldsymbol{f}^{-T} \cdot \boldsymbol{n} da. \quad (2.14)$$

From the above definitions it follows that the inverse deformation map is a nonlinear map which is inverse to the direct nonlinear deformation map

$$\boldsymbol{\Phi} = \boldsymbol{\varphi}^{-1}. \quad (2.15)$$

Thus the inverse and direct deformation gradients, together with their Jacobian determinants, are simply related through an algebraic inversion

$$\boldsymbol{f} = \boldsymbol{F}^{-1} \quad \text{and} \quad j = J^{-1}. \quad (2.16)$$

2.2 Balance principles in mechanics

The objective of this section is to derive in both the material and spatial configurations, balance laws, namely, mass balance, momentum balance, the balance of mechanical energy, and entropy balance.

2.2.1 Mass balance

The conservation of mass postulates that mass cannot be produced or destroyed (in non-relativistic physics), i.e., there are no mass sources or mass losses. The mass of a body is thus conserved during the motion and remains the mass in the material configuration, so that

$$m = m(\mathcal{B}_0) = m(\mathcal{B}_t) > 0. \quad (2.17)$$

As a function of the reference mass density ρ_0 and the spatial mass density ρ , the mass m might be rewritten as

$$m = \int_{\mathcal{B}_0} \rho_0(\boldsymbol{X}) dV = \int_{\mathcal{B}_t} \rho(\boldsymbol{x}, t) dv = \text{const} > 0 \quad \forall t, \quad (2.18)$$

which implies the material time derivative or the rate form

$$\dot{m} = \frac{D}{Dt} m(\mathcal{B}_0) = \frac{D}{Dt} m(\mathcal{B}_t) = \frac{D}{Dt} \int_{\mathcal{B}_t} \rho(\mathbf{x}, t) dv = 0. \quad (2.19)$$

Remark:

- ρ_0 is time-independent.
- If the mass density does not depend on $\mathbf{X} \in \mathcal{B}_0$, the material configuration is said to be homogeneous.

2.2.2 Momentum balance

Newton's second law of motion in Newton [73] at page 19 states that “*The alteration of motion is ever proportional to the motive force impress'd; and is made in the direction of the right line in which that force is impress'd*”, i.e., the acceleration of an object is dependent upon the net force acting upon the object and the mass of the object, i.e.,

$$\mathfrak{F}(t) = m\mathbf{a}, \quad (2.20)$$

where $\mathfrak{F}(t)$ is the net force at time t , \mathbf{a} is the acceleration field in the spatial configuration, and m is the mass of the object. The acceleration field written as a function of the material time derivative of the velocity field of the object in the spatial configuration is

$$\mathbf{a} = \dot{\mathbf{v}} = \frac{D\mathbf{v}}{Dt} = \frac{D}{Dt} \frac{\partial \varphi(\mathbf{X}, t)}{\partial t}. \quad (2.21)$$

Thus Equation 2.20 becomes

$$\mathfrak{F}(t) = m \frac{D\mathbf{v}}{Dt}. \quad (2.22)$$

Since the mass m is constant (Eq. 2.18), m can be introduced in the derivative as

$$\mathfrak{F}(t) = \frac{D(m\mathbf{v})}{Dt}. \quad (2.23)$$

Introducing the mass balance into Equation 2.23, Newton's second law of motion written as a function of the mass balance in the spatial configuration is obtained

$$\mathfrak{F}(t) = \frac{D}{Dt} \int_{\mathcal{B}_t} \rho(\mathbf{x}, t) \mathbf{v} dv. \quad (2.24)$$

Furthermore the velocity \mathbf{V} in the material configuration is equal to the velocity \mathbf{v} in the spatial configuration. Indeed,

$$\mathbf{V}(\mathbf{X}, t) = \mathbf{V}(\Phi(\mathbf{x}, t), t) = \mathbf{V}(\varphi^{-1}(\mathbf{x}, t), t) = \mathbf{v}(\mathbf{x}, t). \quad (2.25)$$

Thus Newton's second law of motion in the material configuration is

$$\mathfrak{F}(t) = \frac{D}{Dt} \int_{\mathcal{B}_0} \rho_0(\mathbf{X}) \mathbf{V} dV. \quad (2.26)$$

Thereby the balance of linear momentum is postulated as

$$\mathfrak{F}(t) = \frac{D}{Dt} \int_{\mathcal{B}_t} \rho(\mathbf{x}, t) \mathbf{v} \, dv = \frac{D}{Dt} \int_{\mathcal{B}_0} \rho_0(\mathbf{X}) \mathbf{V} \, dV \quad (2.27)$$

in the spatial and material configurations, respectively. According to Reynold's transport theorem, the balance of linear momentum might be rewritten as

$$\mathfrak{F}(t) = \int_{\mathcal{B}_t} \rho(\mathbf{x}, t) \frac{D\mathbf{v}}{Dt} \, dv = \int_{\mathcal{B}_0} \rho_0(\mathbf{X}) \frac{D\mathbf{V}}{Dt} \, dV \quad (2.28)$$

or

$$\mathfrak{F}(t) = \int_{\mathcal{B}_t} \rho(\mathbf{x}, t) \dot{\mathbf{v}} \, dv = \int_{\mathcal{B}_0} \rho_0(\mathbf{X}) \dot{\mathbf{V}} \, dV. \quad (2.29)$$

From the momentum balance, the equations of motion in the material and spatial configurations follow. The resultant force $\mathfrak{F}(t)$ in the spatial configuration is also the addition of Cauchy's traction vector $\bar{\mathbf{t}}$ and the body force \mathbf{b} as in [17]

$$\mathfrak{F}(t) = \int_{\partial\mathcal{B}_t^{\bar{\mathbf{t}}}} \bar{\mathbf{t}} \, da + \int_{\mathcal{B}_t} \mathbf{b} \, dv. \quad (2.30)$$

Thus with Equation 2.29, the following expression is obtained

$$\int_{\partial\mathcal{B}_t^{\bar{\mathbf{t}}}} \bar{\mathbf{t}} \, da + \int_{\mathcal{B}_t} \mathbf{b} \, dv = \int_{\mathcal{B}_t} \rho(\mathbf{x}, t) \dot{\mathbf{v}} \, dv. \quad (2.31)$$

Cauchy's stress theorem states that

$$\bar{\mathbf{t}}(\mathbf{x}, t, \mathbf{n}) = \boldsymbol{\sigma}(\mathbf{x}, t) \cdot \mathbf{n}, \quad (2.32)$$

where $\boldsymbol{\sigma}$ is the symmetric Cauchy stress tensor. For the sake of readability, the dependency on \mathbf{x} and t are subsequently omitted. Introducing Equation 2.32 in Equation 2.31, it follows that

$$\int_{\mathcal{B}_t} \rho \dot{\mathbf{v}} \, dv = \int_{\partial\mathcal{B}_t^{\bar{\mathbf{t}}}} \boldsymbol{\sigma} \cdot \mathbf{n} \, da + \int_{\mathcal{B}_t} \mathbf{b} \, dv. \quad (2.33)$$

Using the divergence theorem, which relates the volume integral of the divergence in \mathcal{B}_t to the surface integral of an associated field over the bounding surface $\partial\mathcal{B}_t^{\bar{\mathbf{t}}}$ by

$$\int_{\partial\mathcal{B}_t^{\bar{\mathbf{t}}}} \boldsymbol{\sigma} \cdot \mathbf{n} \, da = \int_{\mathcal{B}_t} \operatorname{div} \boldsymbol{\sigma} \, dv, \quad (2.34)$$

in Equation 2.33 the following expression

$$\int_{\mathcal{B}_t} \rho \dot{\mathbf{v}} \, dv = \int_{\mathcal{B}_t} \operatorname{div} \boldsymbol{\sigma} \, dv + \int_{\mathcal{B}_t} \mathbf{b} \, dv \quad (2.35)$$

is obtained, where $\operatorname{div}(\cdot)$ denotes the spatial divergence operator with respect to the spatial coordinates \mathbf{x} . Thus Cauchy's first equation of motion in the spatial configuration is given by

$$\int_{\mathcal{B}_t} [\operatorname{div} \boldsymbol{\sigma} + \mathbf{b} - \rho \dot{\mathbf{v}}] \, dv = \mathbf{0}. \quad (2.36)$$

This equation holds for any volume v , thus, Cauchy's first equation of motion in local form postulates

$$\operatorname{div}\boldsymbol{\sigma} + \mathbf{b} - \rho\dot{\mathbf{v}} = \mathbf{0} \quad \forall \mathbf{x} \in v \quad \text{and} \quad \forall t. \quad (2.37)$$

In the index notation, Cauchy's first equation of motion in the spatial configuration is

$$\frac{\partial \sigma_{ij}}{\partial x_j} + b_i - \rho\dot{v}_i = 0 \quad (2.38)$$

with $i, j = 1, 2, 3$. If no body forces are taken into account and if the acceleration is assumed to be zero for all $\mathbf{x} \in \mathcal{B}_t$, Equation 2.37 becomes

$$\operatorname{div}\boldsymbol{\sigma} = \mathbf{0} \quad (2.39)$$

and is referred to as Cauchy's equation of equilibrium in elastostatics. The same argument yields the equation of motion in the material configuration. For every surface element in Figure 2.1 Cauchy's traction vector and the first Piola–Kirchhoff traction vector are related by

$$\bar{\mathbf{t}}(\mathbf{x}, t, \mathbf{n}) \, da = \bar{\mathbf{T}}(\mathbf{X}, t, \mathbf{N}) \, dA. \quad (2.40)$$

Furthermore Cauchy's stress theorem also postulates that

$$\bar{\mathbf{T}}(\mathbf{X}, t, \mathbf{N}) = \mathbf{P}(\mathbf{X}, t) \cdot \mathbf{N}, \quad (2.41)$$

where \mathbf{P} is the first Piola–Kirchhoff stress tensor. Associating the balance of linear momentum with the first Piola–Kirchhoff traction vector $\bar{\mathbf{T}}$ and the body force \mathbf{B} in the material configuration, it follows that

$$\int_{\partial\mathcal{B}_0^{\bar{\mathbf{T}}}} \bar{\mathbf{T}} \, dA + \int_{\mathcal{B}_0} \mathbf{B} \, dV = \int_{\mathcal{B}_0} \rho_0(\mathbf{X}) \dot{\mathbf{V}} \, dV. \quad (2.42)$$

From now on, the dependence on \mathbf{X} and t will be omitted for the sake of legibility. With Cauchy's stress theorem (Eq. 2.41), Equation 2.42 becomes

$$\int_{\partial\mathcal{B}_0^{\bar{\mathbf{T}}}} \mathbf{P} \cdot \mathbf{N} \, dA + \int_{\mathcal{B}_0} \mathbf{B} \, dV = \int_{\mathcal{B}_0} \rho_0 \dot{\mathbf{V}} \, dV. \quad (2.43)$$

Using the divergence theorem, which relates the volume integral of the divergence in \mathcal{B}_0 to the surface integral of an associated field over the bounding surface $\partial\mathcal{B}_0^{\bar{\mathbf{T}}}$ by

$$\int_{\partial\mathcal{B}_0^{\bar{\mathbf{T}}}} \mathbf{P} \cdot \mathbf{N} \, dA = \int_{\mathcal{B}_0} \operatorname{Div} \mathbf{P} \, dV, \quad (2.44)$$

in Equation 2.43 the following equation

$$\int_{\mathcal{B}_0} \rho_0 \dot{\mathbf{V}} \, dV = \int_{\mathcal{B}_0} \operatorname{Div} \mathbf{P} \, dV + \int_{\mathcal{B}_0} \mathbf{B} \, dV \quad (2.45)$$

is obtained, where $\operatorname{Div}(\cdot)$ denotes the material divergence operator with respect to the material coordinates \mathbf{X} . Thus Cauchy's first equation of motion in the material configuration becomes

$$\int_{\mathcal{B}_0} [\operatorname{Div} \mathbf{P} + \mathbf{B} - \rho_0 \dot{\mathbf{V}}] \, dV = \mathbf{0}. \quad (2.46)$$

This equation holds for any volume V , thus, Cauchy's first equation of motion in local form postulates

$$\operatorname{Div} \boldsymbol{P} + \boldsymbol{B} - \rho_0 \dot{\boldsymbol{V}} = \mathbf{0} \quad \forall \boldsymbol{X} \in V \quad \text{and} \quad \forall t. \quad (2.47)$$

In index notation, Cauchy's first equation of motion in the material configuration is

$$\frac{\partial P_{ij}}{\partial X_j} + B_i - \rho_0 \dot{V}_i = 0 \quad (2.48)$$

with $i, j = 1, 2, 3$. If no body forces are taken into account and if the acceleration is assumed to be zero for all $\boldsymbol{X} \in \mathcal{B}_0$, the previous equation simplifies to

$$\operatorname{Div} \boldsymbol{P} = \mathbf{0}. \quad (2.49)$$

Remark: Cauchy's first equation of motion in the material and spatial configurations are also related through the Piola transform as explained in Hughes et al. [74] and Steinmann et al. [75].

2.2.3 Balance of mechanical energy

In this section only mechanical energy is considered, i.e., thermal, electric, magnetic, etc., energies are neglected. The balance of mechanical energy in the spatial configuration is defined as a function of the external mechanical power $\mathcal{P}_{\text{ext}}(t)$, the stress power $\mathcal{P}_{\text{int}}(t)$ and the rate of kinetic energy $\mathcal{K}(t)$ by

$$\frac{D}{Dt} \mathcal{K}(t) + \mathcal{P}_{\text{int}}(t) - \mathcal{P}_{\text{ext}}(t) = \mathbf{0}. \quad (2.50)$$

The external mechanical power is

$$\mathcal{P}_{\text{ext}}(t) = \int_{\partial \mathcal{B}_t^{\bar{\boldsymbol{t}}}} \bar{\boldsymbol{t}} \cdot \boldsymbol{v} \, da + \int_{\mathcal{B}_t} \boldsymbol{b} \cdot \boldsymbol{v} \, dv. \quad (2.51)$$

The stress power is

$$\mathcal{P}_{\text{int}}(t) = \int_{\mathcal{B}_t} \boldsymbol{\sigma} : \boldsymbol{d} \, dv, \quad (2.52)$$

where

$$\boldsymbol{d} = \frac{1}{2}(\operatorname{grad} \boldsymbol{v} + \operatorname{grad}^T \boldsymbol{v}). \quad (2.53)$$

The kinetic energy is defined by

$$\mathcal{K}(t) = \int_{\mathcal{B}_t} \frac{1}{2} \rho \boldsymbol{v} \cdot \boldsymbol{v} \, da. \quad (2.54)$$

The balance of mechanical energy in the material configuration is based on the fact that

$$\int_{\partial \mathcal{B}_t^{\bar{\boldsymbol{t}}}} \bar{\boldsymbol{t}} \cdot \boldsymbol{v} \, da = \int_{\partial \mathcal{B}_0^{\bar{\boldsymbol{T}}}} \bar{\boldsymbol{T}} \cdot \boldsymbol{V} \, dA \quad (2.55)$$

and

$$\int_{\mathcal{B}_t} \boldsymbol{b} \cdot \boldsymbol{v} \, dv = \int_{\mathcal{B}_0} \boldsymbol{B} \cdot \boldsymbol{V} \, dV. \quad (2.56)$$

Thus the external mechanical power becomes

$$\mathcal{P}_{\text{ext}}(t) = \int_{\partial\mathcal{B}_0^T} \bar{\mathbf{T}} \cdot \mathbf{V} \, dA + \int_{\mathcal{B}_0} \mathbf{B} \cdot \mathbf{V} \, dV. \quad (2.57)$$

By using the properties of symmetric and skew tensors, the spatial velocity gradient $\text{grad}\mathbf{v}$ can be decomposed into \mathbf{d} from Equation 2.53 and

$$\mathbf{w} = \frac{1}{2}(\text{grad}\mathbf{v} - \text{grad}^T \mathbf{v}), \quad (2.58)$$

so that

$$\text{grad}\mathbf{v} = \mathbf{d} + \mathbf{w} = \dot{\mathbf{F}} \cdot \mathbf{F}^{-1}, \quad (2.59)$$

where $\dot{\mathbf{F}}$ is the rate of the deformation gradient \mathbf{F} . By carrying out a double contraction between $\boldsymbol{\sigma}$ and $\text{grad}\mathbf{v}$, it follows that

$$\boldsymbol{\sigma} : \text{grad}\mathbf{v} = \boldsymbol{\sigma} : \mathbf{d} + \boldsymbol{\sigma} : \mathbf{w} = \boldsymbol{\sigma} : \dot{\mathbf{F}} \cdot \mathbf{F}^{-1}. \quad (2.60)$$

The second term vanishes due to the symmetry of the Cauchy stress tensor, thus

$$\boldsymbol{\sigma} : \mathbf{d} = \boldsymbol{\sigma} : \dot{\mathbf{F}} \cdot \mathbf{F}^{-1}. \quad (2.61)$$

Incorporating Equation 2.61 into Equation 2.52 and using the Piola transform $\mathbf{P} = J\boldsymbol{\sigma}\mathbf{F}^{-T}$, the stress power is transformed into

$$\mathcal{P}_{\text{int}}(t) = \int_{\mathcal{B}_0} \mathbf{P} : \dot{\mathbf{F}} \, dV. \quad (2.62)$$

According to Equation 2.25, the kinetic energy amounts to

$$\mathcal{K}(t) = \int_{\mathcal{B}_0} \frac{1}{2} \rho_0 \mathbf{V} \cdot \mathbf{V} \, dA. \quad (2.63)$$

Since the system will be supposed to be quasi-static, the derivative of the kinetic energy will vanish. Hence, Equation 2.50 becomes

$$\mathcal{P}_{\text{int}}(t) - \mathcal{P}_{\text{ext}}(t) = \mathbf{0}, \quad (2.64)$$

or, in the spatial configuration,

$$\int_{\mathcal{B}_t} \boldsymbol{\sigma} : \mathbf{d} \, dv - \int_{\partial\mathcal{B}_t^T} \bar{\mathbf{T}} \cdot \mathbf{v} \, da - \int_{\mathcal{B}_t} \mathbf{b} \cdot \mathbf{v} \, dv = \mathbf{0} \quad (2.65)$$

or, in the material configuration,

$$\int_{\mathcal{B}_0} \mathbf{P} : \dot{\mathbf{F}} \, dV - \int_{\partial\mathcal{B}_0^T} \bar{\mathbf{T}} \cdot \mathbf{V} \, dA - \int_{\mathcal{B}_0} \mathbf{B} \cdot \mathbf{V} \, dV = \mathbf{0}. \quad (2.66)$$

2.2.4 Entropy balance

The first law of thermodynamics postulates the conservation of energy and is mathematically expressed in the material configuration by

$$\dot{e} = \mathcal{P}_{\text{int}}(t) + R - \text{Div}\mathbf{Q} = \mathbf{P} : \dot{\mathbf{F}} + R - \text{Div}\mathbf{Q}, \quad (2.67)$$

where \mathbf{Q} is the vector field corresponding to the heat flux, \dot{e} is the rate of specific internal energy, and R is the density of heat production in the material configuration. The second law of thermodynamics postulates the irreversibility of entropy production and is mathematically expressed in the material configuration by the inequality

$$\dot{s} + \text{Div}\left[\frac{\mathbf{Q}}{\theta}\right] - \frac{R}{\theta} \geq 0, \quad (2.68)$$

where θ is the temperature and \dot{s} is the rate of the specific entropy in the material configuration. Combining the first and second laws of thermodynamics leads to the inequality

$$\dot{s} + \text{Div}\left[\frac{\mathbf{Q}}{\theta}\right] - \frac{\dot{e}}{\theta} + \frac{\mathbf{P} : \dot{\mathbf{F}}}{\theta} - \frac{\text{Div}\mathbf{Q}}{\theta} \geq 0. \quad (2.69)$$

By introducing the Helmholtz free energy per unit mass in the material configuration, written as a function of the specific internal energy, the specific entropy, and the temperature,

$$\Psi = e - \theta s, \quad (2.70)$$

its derivative with respect to time can be calculated as

$$\dot{\Psi} = \dot{e} - \dot{\theta}s - \theta\dot{s}. \quad (2.71)$$

By rewriting Equation 2.71 as

$$\dot{s} - \frac{\dot{e}}{\theta} = -\frac{\dot{\theta}}{\theta}s - \frac{\dot{\Psi}}{\theta} \quad (2.72)$$

and using the properties of the divergence (product rule) and the derivative (quotient rule) in

$$\text{Div}\left[\frac{\mathbf{Q}}{\theta}\right] = \frac{1}{\theta}\text{Div}\mathbf{Q} - \frac{1}{\theta^2}\mathbf{Q} \cdot \text{Grad}\theta, \quad (2.73)$$

Equation 2.69 is reduced to

$$-(\dot{\theta}s + \dot{\Psi}) - \frac{1}{\theta}\mathbf{Q} \cdot \text{Grad}\theta + \mathbf{P} : \dot{\mathbf{F}} \geq 0. \quad (2.74)$$

When maintaining a constant temperature (i.e., restricting to the isothermal non-dissipative case) and assuming that the material is homogeneous, the reduced Clausius–Duhem or dissipation inequality in the material configuration is obtained

$$\mathcal{D} = \mathbf{P} : \dot{\mathbf{F}} - \dot{\Psi} \geq 0. \quad (2.75)$$

In the spatial configuration the first law of thermodynamics is

$$\dot{e}_s = \mathcal{P}_{\text{int}}(t) + r - \text{div}\mathbf{q} = \boldsymbol{\sigma} : \mathbf{d} + r - \text{div}\mathbf{q}, \quad (2.76)$$

where \mathbf{q} is the vector field corresponding to the heat flux, \dot{e}_s is the rate of specific internal energy, and r is the density of heat production in the spatial configuration. The second law of thermodynamics in the spatial configuration is

$$\dot{s}_s + \operatorname{div}[\frac{\mathbf{q}}{\theta_s}] - \frac{r}{\theta_s} \geq 0, \quad (2.77)$$

where θ_s is the temperature and \dot{s}_s is the rate of the specific entropy in the spatial configuration. Combining the first and second laws of thermodynamics in the spatial configuration leads to the inequality

$$\dot{s}_s + \operatorname{div}[\frac{\mathbf{q}}{\theta_s}] - \frac{\dot{e}_s}{\theta_s} + \frac{\boldsymbol{\sigma} : \mathbf{d}}{\theta_s} - \frac{\operatorname{div}\mathbf{q}}{\theta_s} \geq 0. \quad (2.78)$$

By introducing the Helmholtz free energy per unit mass in the spatial configuration, written as a function of the specific internal energy, the specific entropy, and the temperature,

$$\psi = e_s - \theta s_s, \quad (2.79)$$

its derivative with respect to time can be calculated as

$$\dot{\psi} = \dot{e}_s - \dot{\theta}_s s_s - \theta_s \dot{s}_s. \quad (2.80)$$

By rewriting Equation 2.80 as

$$\dot{s}_s - \frac{\dot{e}_s}{\theta_s} = -\frac{\dot{\theta}_s}{\theta_s} s_s - \frac{\dot{\psi}}{\theta_s} \quad (2.81)$$

and using the properties of the divergence (product rule) and the derivative (quotient rule) in

$$\operatorname{div}[\frac{\mathbf{q}}{\theta_s}] = \frac{1}{\theta_s} \operatorname{div}\mathbf{q} - \frac{1}{\theta_s^2} \mathbf{q} \cdot \operatorname{grad}\theta_s, \quad (2.82)$$

Equation 2.78 is reduced to

$$-\left(\dot{\theta}_s s_s + \dot{\psi}\right) - \frac{1}{\theta_s} \mathbf{q} \cdot \operatorname{grad}\theta_s + \boldsymbol{\sigma} : \mathbf{d} \geq 0. \quad (2.83)$$

When maintaining a constant temperature (i.e., restricting to the isothermal non-dissipative case) and assuming that the material is homogeneous, the reduced Clausius–Duhem or dissipation inequality in the spatial configuration is obtained

$$\mathcal{D}_s = \boldsymbol{\sigma} : \mathbf{d} - \dot{\psi} \geq 0. \quad (2.84)$$

CHAPTER 3

The macroscopic constitutive model in logarithmic strain space

This chapter deals with a macroscopic constitutive model in elastoplasticity with large strains, in its formulation in logarithmic strain space. The macroscopic structural response of a material can be modelled either through a micromechanical or a phenomenological approach. A micromechanical approach is based on the polycrystalline response. After modelling the polycrystalline microstructure a crystal plasticity model is used to model the crystalline behaviour. The effective material behaviour is next computed with homogenisation techniques by taking the microstructural response of a Representative Volume Element (RVE). A particular challenge in this approach is the determination of the material parameters at the microscopic level and the boundary conditions between the grains. In macroscopic phenomenological modelling, the laws of thermodynamics describe the macroscopic behaviour of the material at the macroscopic level as a continuum. Parameter identification techniques give the material parameters needed in a phenomenological approach, see for example Kleuter et al. [30] and Mahnken et al. [31, 32, 33, 34, 35, 38]. A microstructural material model is compared with a macroscopical phenomenological model based on logarithmic strains in Lehmann et al. [76, 77]. This chapter is structured as follows: A macroscopic phenomenological model is presented following the standard literature on material modelling, see for example de Souza Neto et al. [16], Holzapfel [17], Ogden [18], or Bonet et al. [19]. A logarithmic strain space formulation with a structure adopted from the geometrically linear theory is used, following closely the methods developed by Miehe et al. in [20, 21] and by Apel in [22]. An additive Lagrangian formulation in the logarithmic strain space is first presented. The formulation of the yield criterion and the yield surface is given after presenting the description of the energy storage and the elastic response. The plastic flow rule and hardening law are defined for anisotropic elastoplasticity. The elastoplastic constitutive initial value problem is solved by a return mapping algorithm (or plastic corrector step) following the one presented in Simo and al. [29] for J₂ plasticity and in de Souza Neto et al. [16]. It is extended here to the case of anisotropic elastoplastic materials in logarithmic strain space. A particular attention is given to the modelling of problems in metal plasticity. Thermal effects are ignored and the material is assumed to be homogeneous, i.e., to be uniform on the continuum scale. Parts of this chapter have been published by Germain et al. in [13, 14, 15, 57, 68] and by Lehmann et al. in [76, 77].

3.1 The additive Lagrangian formulation in elastoplasticity

An additive decomposition of the logarithmic strain, usually deployed in small strain problems, is assumed

$$\mathbf{E} = \frac{1}{2} \ln \mathbf{C} = \mathbf{E}^e + \mathbf{E}^p, \quad (3.1)$$

where \mathbf{E}^e is the second-order elastic strain tensor, \mathbf{E}^p is the second-order plastic strain tensor, and \mathbf{C} is the right Cauchy–Green tensor. A spectral decomposition of the right Cauchy–Green strain tensor \mathbf{C} is applied

$$\mathbf{C} = \mathbf{F}^T \cdot \mathbf{F} = \sum_{i=1}^3 \lambda_i \mathbf{M}_i, \quad (3.2)$$

where $\{\lambda_i \in \mathbb{R}; i = 1, 2, 3\}$ are the real eigenvalues of \mathbf{C} and $\{\mathbf{M}_i \in \mathcal{M}_3(\mathbb{R}); i = 1, 2, 3\}$ are the associated eigenbases (Miehe [78]). The spectral representation allows an easier computation of the logarithmic strain

$$\mathbf{E} = \frac{1}{2} \sum_{i=1}^3 \ln \lambda_i \mathbf{M}_i. \quad (3.3)$$

The first and second derivatives of the logarithmic strain with respect to the right Cauchy–Green strain are defined by

$$\mathbb{P} = 2 \frac{\partial \mathbf{E}}{\partial \mathbf{C}} \quad \text{and} \quad \mathbb{L} = 2 \frac{\partial \mathbb{P}}{\partial \mathbf{C}} = 4 \frac{\partial^2 \mathbf{E}}{\partial \mathbf{C} \partial \mathbf{C}}. \quad (3.4)$$

The numerical implementation of these derivatives are introduced by Miehe et al. in [79]. The strain rate expressed as a function of the rate of deformation is defined by

$$\dot{\mathbf{E}} = \mathbb{P}_{\mathbf{F}} : \dot{\mathbf{F}}, \quad (3.5)$$

with

$$\mathbb{P}_{\mathbf{F}} = \frac{\partial \mathbf{E}}{\partial \mathbf{F}}. \quad (3.6)$$

The rate of deformation might be redefined as

$$\dot{\mathbf{F}} = \mathbb{P}_{\mathbf{F}}^{-1} : \dot{\mathbf{E}}. \quad (3.7)$$

Injecting Equation 3.7 in Equation 2.62 the stress power can be specified by

$$\begin{aligned} \mathcal{P}_{\text{int}}(t) &= \mathbf{P}(t) : \mathbb{P}_{\mathbf{F}}^{-1} : \dot{\mathbf{E}}(t) \\ &= [\mathbf{P}(t) : \mathbb{P}_{\mathbf{F}}^{-1}] : \dot{\mathbf{E}}(t) \\ &= \mathbf{T}(t) : \dot{\mathbf{E}}(t), \end{aligned} \quad (3.8)$$

with

$$\mathbf{T} = \mathbf{P} : \mathbb{P}_{\mathbf{F}}^{-1}. \quad (3.9)$$

$\dot{\mathbf{T}}$ is defined as the Lagrangian stress tensor work-conjugate to the logarithmic strain measure \mathbf{E} . The rate of the stress, a function of the rate of the logarithmic strain and the fourth-order elastoplastic tangent modulus, is defined by

$$\dot{\mathbf{T}} = \mathbb{E}^{ep} : \dot{\mathbf{E}}. \quad (3.10)$$

According to Equation 3.9, the first Piola–Kirchhoff stress tensor might be computed by

$$\mathbf{P} = \mathbf{T} : \mathbb{P}_F. \quad (3.11)$$

The second Piola–Kirchhoff stress \mathbf{S} is then defined by

$$\mathbf{S} = \mathbf{F}^{-1} \cdot \mathbf{P}. \quad (3.12)$$

By replacing \mathbf{P} in Equation 3.12 by Equation 3.11 and reformulating Equation 3.6 as a function of the right Cauchy–Green tensor \mathbf{C} , the second Piola–Kirchhoff stress can be written

$$\mathbf{S} = \mathbf{T} : \mathbb{P}. \quad (3.13)$$

The associated elastoplastic modulus \mathbb{C}^{ep} is defined by setting the rate of the Piola–Kirchhoff tensor as a function of the Lagrangian rate $\dot{\mathbf{C}}/2$ of deformation in the form

$$\dot{\mathbf{S}} = \mathbb{C}^{ep} : \frac{1}{2} \dot{\mathbf{C}}, \quad (3.14)$$

with

$$\mathbb{C}^{ep} = \mathbb{P}^T : \mathbb{E}^{ep} : \mathbb{P} + \mathbf{T} : \mathbb{L}. \quad (3.15)$$

In Equation 3.15 the transposition symbol $[\cdot]^T$ refers to an exchange of the first and last pairs of indices.

Remark: In Equation 3.15, \mathbb{E}^{ep} reduces to the fourth-order elasticity tensor \mathbb{E}^e for hyperelastic material behaviour.

3.2 Energy storage and elastic stress response

With the definition of the stress power in Equation 2.62, the reduced Clausius–Duhem inequality (Eq. 2.75) becomes

$$\mathcal{D} = \mathbf{T} : \dot{\mathbf{E}} - \dot{\Psi} \geq 0. \quad (3.16)$$

A more suitable or less general formulation of the total free energy density per volume in the material configuration in a logarithmic strain formulation as in Miehe et al. [20] might be the function

$$\Psi = \Psi(\mathbf{E}, \mathbf{E}^p, \alpha) = \Psi(\mathbf{E} - \mathbf{E}^p, \alpha) \quad (3.17)$$

of the set of internal variables $\mathcal{IV} = \{\mathbf{E}^p, \alpha\}$, where \mathbf{E}^p is the plastic strain tensor defined in Equation 3.1 and α is a scalar variable that models isotropic hardening. A decomposition of the total free energy density into an elastic and a plastic part, as usual for metals with large

strains, is also assumed. The plastic part is modelled by nonlinear isotropic hardening. With the previous restrictions, the free energy density is

$$\Psi(\mathbf{E}, \mathbf{E}^p, \alpha) = \Psi^e(\mathbf{E} - \mathbf{E}^p) + \Psi^p(\alpha) \quad (3.18)$$

$$= \Psi^e(\mathbf{E}^e) + \Psi^p(\alpha) \quad (3.19)$$

$$= \frac{1}{2} \mathbf{E}^e : \mathbb{E}^e : \mathbf{E}^e + \frac{1}{2} h \alpha^2 + [\sigma_\infty - \sigma_0] \left[\alpha + \frac{e^{-w\alpha}}{w} \right], \quad (3.20)$$

where $\{\mathbb{E}^e, h, \sigma_0, \sigma_\infty, w\}$ are material parameters, i.e., the fourth-order elasticity tensor, the isotropic hardening parameter, the initial yield stress, the infinite yield stress, and the saturation parameter, which defines the nonlinearity of the hardening. A consequence of the additive decomposition of the total strain in Equation 3.1 is that

$$\mathbf{T}^p = -\frac{\partial \Psi}{\partial \mathbf{E}^p} = \frac{\partial \Psi}{\partial \mathbf{E}} = \frac{\partial \Psi}{\partial \mathbf{E}^e} = \mathbf{T} = \mathbb{E}^e : \mathbf{E}^e. \quad (3.21)$$

Using the decomposition of the logarithmic strain (Eq. 3.1) and the dependence of the total free energy density on \mathbf{E}^e and α (Eq. 3.20), the dissipation inequality can be written (Itskov [80]) as

$$\mathcal{D} = (\mathbf{T} - \frac{\partial \Psi}{\partial \mathbf{E}^e}) : \dot{\mathbf{E}}^e + \mathbf{T} : \dot{\mathbf{E}}^p - \frac{\partial \Psi}{\partial \alpha} \dot{\alpha} \geq 0. \quad (3.22)$$

With the definition of the tensor \mathbf{T} in Equation 3.21, the Clausius–Duhem inequality is reduced to

$$\mathcal{D} = \mathbf{T} : \dot{\mathbf{E}}^p - \frac{\partial \Psi}{\partial \alpha} \dot{\alpha} \geq 0. \quad (3.23)$$

Subsequently, the variable \mathcal{A} defines

$$\mathcal{A} = \frac{\partial \Psi}{\partial \alpha} \quad (3.24)$$

and represents the hardening thermodynamical force.

3.3 The anisotropic yield criterion and the yield surface

The phenomenological behaviour of materials, such as metals, are described in three steps (de Souza Neto et al. [16]). The material is considered first as purely (hyper)elastic in the elastic domain

$$\mathcal{E} = \{ \mathbf{T} \mid \Phi(\mathbf{T}, \mathcal{A}) - \sqrt{\frac{2}{3}} \sigma_0 < 0 \}, \quad (3.25)$$

which is delimited by the yield stress and in which plastic yielding is not permitted. If the material is further loaded past the yield stress, then plastic yield (plastic flow) occurs on the yield surface. Hardening, i.e., the evolution of the yield stress, is next associated to the evolution of the plastic strain. The yield surface, which is a hypersurface, is defined by

$$\mathcal{Y} = \{ \mathbf{T} \mid \Phi(\mathbf{T}, \mathcal{A}) - \sqrt{\frac{2}{3}} \sigma_0 = 0 \}, \quad (3.26)$$

where Φ is a quadratic yield function (Hill-type criterion) defined by

$$\begin{aligned}\Phi(\mathbf{T}, \mathcal{A}) &= \|\mathbf{T}\|_{\mathbb{H}} - \sqrt{\frac{2}{3}}\mathcal{A} \\ &= \|\mathbf{T}\|_{\mathbb{H}} - \sqrt{\frac{2}{3}} [h\alpha + (\sigma_{\infty} - \sigma_0)(1 - e^{-w\alpha})],\end{aligned}\quad (3.27)$$

where

$$\|\mathbf{T}\|_{\mathbb{H}} = \sqrt{\mathbf{T} : \mathbb{H} : \mathbf{T}}. \quad (3.28)$$

\mathbb{H} is the fourth-order Hill-type tensor with the deviatoric property

$$\mathbb{H} : \mathbf{I} = \mathbf{0}. \quad (3.29)$$

For

$$\mathbb{H} = \mathbb{I}_{\text{dev}}^{\text{sym}} = \mathbb{I}^{\text{sym}} - \frac{1}{3}\mathbf{I} \otimes \mathbf{I} \quad (3.30)$$

Equation 3.27 degenerates to the classical von Mises function, where \mathbb{I}^{sym} is the symmetric fourth-order identity tensor and \mathbf{I} is the second-order identity tensor. For an orthotropic response, the tensor \mathbb{H} defined in Voigt notation (Miehe et al. [20]) is governed by nine parameters. In a Cartesian coordinate system aligned with the axes of orthotropy, the tensor has the simple coordinate representation

$$\mathbb{H} = \begin{bmatrix} \alpha_1 & \alpha_4 & \alpha_6 & 0 & 0 & 0 \\ \alpha_4 & \alpha_2 & \alpha_5 & 0 & 0 & 0 \\ \alpha_6 & \alpha_5 & \alpha_3 & 0 & 0 & 0 \\ 0 & 0 & 0 & \alpha_7 & 0 & 0 \\ 0 & 0 & 0 & 0 & \alpha_8 & 0 \\ 0 & 0 & 0 & 0 & 0 & \alpha_9 \end{bmatrix}. \quad (3.31)$$

Equation 3.29 is satisfied for the three dependencies

$$\alpha_4 = \frac{1}{2}(\alpha_3 - \alpha_1 - \alpha_2), \quad \alpha_5 = \frac{1}{2}(\alpha_1 - \alpha_2 - \alpha_3), \quad \alpha_6 = \frac{1}{2}(\alpha_2 - \alpha_1 - \alpha_3). \quad (3.32)$$

Orthotropic plastic yielding for an incompressible plastic flow is governed by six material parameters related to the initial yield stresses with respect to the principal axes of orthotropy

$$\begin{aligned}\alpha_1 &= \frac{2}{3} \frac{\sigma_0^2}{y_{11}^2}, \quad \alpha_2 = \frac{2}{3} \frac{\sigma_0^2}{y_{22}^2}, \quad \alpha_3 = \frac{2}{3} \frac{\sigma_0^2}{y_{33}^2}, \\ \alpha_7 &= \frac{1}{3} \frac{\sigma_0^2}{y_{12}^2}, \quad \alpha_8 = \frac{1}{3} \frac{\sigma_0^2}{y_{23}^2}, \quad \alpha_9 = \frac{1}{3} \frac{\sigma_0^2}{y_{31}^2}.\end{aligned}\quad (3.33)$$

Setting $y_{11} = y_{22} = y_{33} = \sigma_0$ and $y_{12} = y_{23} = y_{31} = \sigma_0/\sqrt{3}$ in Equation 3.33 and then in \mathbb{H} leads to isotropic plastic yielding (Eq. 3.30). For the case of multi-surface elastoplasticity, the decomposition of \mathbb{H} into Kelvin modes might be an alternative (Apel [22]).

3.4 Anisotropic plastic flow rule and the hardening law

The associative plasticity model requires the definition of evolution laws for the internal variables $\{\mathbf{E}^p, \alpha\}$, which are determined by the well-known principle of maximum plastic dissipation, see for example Hill [81] or Lubliner [82, 83]. The following anisotropic plastic flow rule and hardening law are defined in terms of the gradients of the yield criterion function.

$$\dot{\mathbf{E}}^p = \dot{\gamma} \mathbf{N} \quad (3.34)$$

and

$$\dot{\alpha} = \dot{\gamma} \mathbf{H}. \quad (3.35)$$

Here,

$$\mathbf{N} = \frac{\partial \Phi}{\partial \mathbf{T}} = \frac{\mathbb{H} : \mathbf{T}}{\|\mathbf{T}\|_{\mathbb{H}}} \quad (3.36)$$

is the flow vector and

$$\mathbf{H} = -\frac{\partial \Phi}{\partial \mathcal{A}} = \sqrt{\frac{2}{3}} \quad (3.37)$$

is the generalised hardening modulus defining the evolution of the hardening variables. In the rate independent case, the plastic multiplier $\dot{\gamma}$ is determined by the Karush–Kuhn–Tucker-type loading/unloading conditions (Luenberger [52])

$$\Phi(\mathbf{T}, \mathcal{A}) - \sqrt{\frac{2}{3}}\sigma_0 \leq 0, \quad \dot{\gamma} \geq 0, \quad \left[\Phi(\mathbf{T}, \mathcal{A}) - \sqrt{\frac{2}{3}}\sigma_0 \right] \dot{\gamma} = 0, \quad (3.38)$$

where \mathcal{A} is defined in Equation 3.24.

3.5 The return mapping algorithm

Writing the additive decomposition of the total strain, the hardening law, and the Karush–Kuhn–Tucker inequalities at time t , the elastoplastic constitutive initial value problem is obtained.

$$\begin{aligned} \dot{\mathbf{E}}(t) &= \dot{\mathbf{E}}^e(t) + \dot{\mathbf{E}}^p(t) \\ \dot{\alpha}(t) &= \dot{\gamma}(t) \mathbf{H}(t) \\ \dot{\gamma}(t) &\geq 0, \quad \Upsilon(t) \leq 0, \quad \Upsilon(t)\dot{\gamma}(t) = 0. \end{aligned} \quad (3.39)$$

Here,

$$\Upsilon(t) = \Phi(t) - \sqrt{\frac{2}{3}}\sigma_0. \quad (3.40)$$

By employing the flow rule from Equation 3.34, the elastoplastic constitutive initial value problem becomes

$$\begin{aligned} \dot{\mathbf{E}}^e(t) &= \dot{\mathbf{E}}(t) - \dot{\gamma}(t) \mathbf{N}(t) \\ \dot{\alpha}(t) &= \dot{\gamma}(t) \mathbf{H}(t) \\ \dot{\gamma}(t) &\geq 0, \quad \Upsilon(t) \leq 0, \quad \Upsilon(t)\dot{\gamma}(t) = 0. \end{aligned} \quad (3.41)$$

In order to solve the elastoplastic problem iteratively, the equations are discretised using the backwards Euler first-order scheme at time $t \in [t_n, t_{n+1}]$

$$\begin{aligned}\mathbf{E}_{n+1}^e &= \mathbf{E}_n^e + \Delta\mathbf{E} - \Delta\gamma \mathbf{N}_{n+1} \\ \alpha_{n+1} &= \alpha_n + \Delta\gamma \mathbf{H}_{n+1} \\ \Delta\gamma &\geq 0, \quad \Upsilon_{n+1} \leq 0, \quad \Upsilon_{n+1}\Delta\gamma = 0,\end{aligned}\tag{3.42}$$

where \mathbf{E}_{n+1}^e , α_{n+1} and $\Delta\gamma$ are the unknowns subjected to the Karush–Kuhn–Tucker constraints. At time $t \in [t_n, t_{n+1}]$, $\Delta\mathbf{E}$, \mathbf{E}_n^e and α_n are known from the previous step. $\Delta\gamma$ is called the incremental plastic multiplier. In the above, the following notation is adopted

$$\Delta(\cdot) = (\cdot)_{n+1} - (\cdot)_n.\tag{3.43}$$

The incremental problem in Equation 3.42 has two distinct solutions. The first possibility is when $\Delta\gamma = 0$, which means that there is no plastic flow evolution in the interval $[t_n, t_{n+1}]$, i.e., the problem is purely (hyper)elastic. It follows, automatically, that

$$\begin{aligned}\mathbf{E}_{n+1}^e &= \mathbf{E}_n^e + \Delta\mathbf{E} \\ \alpha_{n+1} &= \alpha_n \\ \Upsilon_{n+1} &\leq 0.\end{aligned}\tag{3.44}$$

The second solution takes place when the plastic multiplier is positive, i.e., $\Delta\gamma > 0$. In this case the system of equations in Equation 3.42 holds with the constraint

$$\Upsilon_{n+1} = 0.\tag{3.45}$$

The incremental problem is then solved between $[t_n, t_{n+1}]$ by the return mapping algorithm, following Simo et al. in [29] Chapter 3.3 and de Souza Neto et al. in [16] Chapter 7.2.4. The extension to anisotropic elastoplasticity in the logarithmic strain space is presented by a pseudo-algorithm in Algorithm 3.1. A schematic view of the return mapping algorithm (or plastic corrector step) is illustrated in Figure 3.1. The algorithms needed to find the unknown $\Delta\gamma$ and α_{n+1} and the fourth-order elastoplastic tangent modulus \mathbb{E}^{ep} are presented in the subsequent sections.

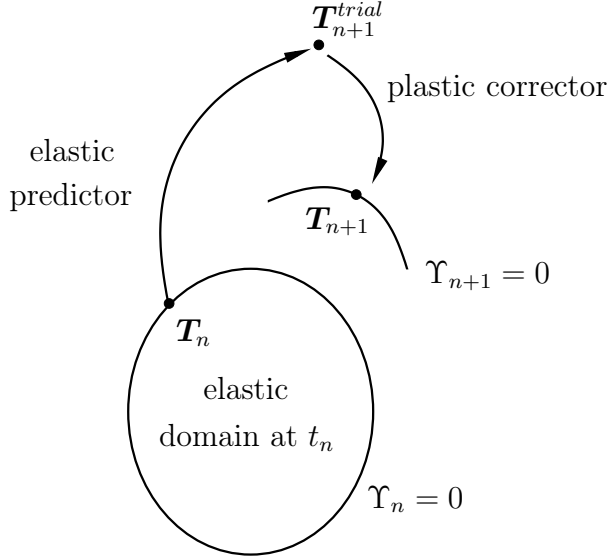


Figure 3.1: Schematic view of the return mapping, as in [16].

Algorithm 3.1: Return mapping algorithm for nonlinear anisotropic hardening

1. Compute trial elastic Lagrangian stress tensor;

$$\mathbf{E}_{n+1}^{e,trial} = \mathbf{E}_{n+1} - \mathbf{E}_n^p;$$

$$\mathbf{T}_{n+1}^{trial} = \mathbb{E}^e : \mathbf{E}_{n+1}^{e,trial};$$

$$\boldsymbol{\xi}_{n+1}^{trial} = \mathbb{H} : \mathbf{T}_{n+1}^{trial};$$

$$\|\boldsymbol{\xi}_{n+1}^{trial}\| = \|\mathbf{T}_{n+1}^{trial}\|_{\mathbb{H}};$$

2. Check yield condition;

$$\Delta\gamma = 0;$$

$$y(\alpha_n) = \sigma_0 + (\sigma_\infty - \sigma_0)(1 - e^{-w\alpha_n}) + h\alpha_n;$$

$$\Upsilon_{n+1}^{trial} = \|\boldsymbol{\xi}_{n+1}^{trial}\| - \sqrt{\frac{2}{3}}y(\alpha_n);$$

if $\Upsilon_{n+1}^{trial} > 0$ then

%plasticity takes place;

Compute $\Delta\gamma$ and α_{n+1} with Algorithm 3.2;

end

if $\Delta\gamma > 0$ then

%plasticity takes place;

Compute \mathbb{E}^{ep} with Section 3.5.2;

else

%elasticity takes place;

$\mathbb{E}^{ep} = \mathbb{E}^e$;

end

3. Update plastic strain ;

$$\mathbf{E}_{n+1}^p = \mathbf{E}_n^p + \Delta\gamma \mathbf{N}_{n+1};$$

4. Update Lagrangian stress tensor ;

$$\mathbf{T}_{n+1} = \mathbf{T}_n - \Delta\gamma \mathbb{E}^e : \mathbf{N}_{n+1};$$

5. return $\mathbf{E}_{n+1}^p, \mathbf{T}_{n+1}, \alpha_{n+1}$ and \mathbb{E}^{ep} ;

At the end of the return mapping, the plastic strain and the Lagrangian stress tensor have to be updated for the next increment. The update of the plastic strain follows from the additive decomposition of the total strains at time t_{n+1} by

$$\mathbf{E}_{n+1} = \mathbf{E}_{n+1}^e + \mathbf{E}_{n+1}^p. \quad (3.46)$$

By substituting \mathbf{E}_{n+1}^e from Equation 3.42 into the previous equation, it follows that

$$\mathbf{E}_{n+1} = \mathbf{E}_n^e + \Delta\mathbf{E} - \Delta\gamma\mathbf{N}_{n+1} + \mathbf{E}_{n+1}^p \quad (3.47)$$

and thus

$$\mathbf{E}_{n+1}^p = \mathbf{E}_{n+1} - \mathbf{E}_n^e - \Delta\mathbf{E} + \Delta\gamma\mathbf{N}_{n+1}. \quad (3.48)$$

Employing the definition of the operator Δ in Equation 3.43, the plastic strain becomes

$$\begin{aligned} \mathbf{E}_{n+1}^p &= \mathbf{E}_{n+1} - \mathbf{E}_n^e - \mathbf{E}_{n+1} + \mathbf{E}_n + \Delta\gamma\mathbf{N}_{n+1} \\ &= \mathbf{E}_n - \mathbf{E}_n^e + \Delta\gamma\mathbf{N}_{n+1}. \end{aligned} \quad (3.49)$$

With the decomposition of the total strain at time t_n by

$$\mathbf{E}_n = \mathbf{E}_n^e + \mathbf{E}_n^p, \quad (3.50)$$

the plastic strain at t_{n+1} is given by

$$\mathbf{E}_{n+1}^p = \mathbf{E}_n^p + \Delta\gamma\mathbf{N}_{n+1}. \quad (3.51)$$

The update of the Lagrangian stress tensor is

$$\mathbf{T}_{n+1} = \mathbb{E}^e : \mathbf{E}_{n+1}^e. \quad (3.52)$$

By employing Equation 3.42, it follows immediately that

$$\mathbf{T}_{n+1} = \mathbf{T}_n - \Delta\gamma\mathbb{E}^e : \mathbf{N}_{n+1}. \quad (3.53)$$

3.5.1 The incremental plastic multiplier

In the previous section, it was demonstrated that when plasticity takes place, the incremental plastic multiplier is positive and the constraint

$$\Upsilon_{n+1} = 0 \quad (3.54)$$

holds. This constraint permits the use of Newton's method in order to find the incremental plastic multiplier, i.e.,

$$\Delta\gamma^{(k+1)} = \Delta\gamma^{(k)} - \frac{\Upsilon_{n+1}}{\frac{d\Upsilon_{n+1}}{d\Delta\gamma}}, \quad (3.55)$$

where k denotes the increment. The challenge is then to find $d\Upsilon_{n+1}/d\Delta\gamma$ when dealing with anisotropic yielding. Subsequently, the mathematical process will be presented and, for the sake of legibility, the superscript increment is omitted. By considering Equation 3.40,

$$\Upsilon_{n+1} = \|\mathbf{T}_{n+1}\|_{\mathbb{H}} - \sqrt{\frac{2}{3}}y(\alpha_{n+1}), \quad (3.56)$$

where

$$y(\alpha_{n+1}) = \sigma_0 + [\sigma_\infty - \sigma_0] [1 - e^{-w\alpha_{n+1}}] + h\alpha_{n+1}. \quad (3.57)$$

This implies that

$$\begin{aligned} \frac{d\Upsilon_{n+1}}{d\Delta\gamma} &= \frac{\partial||\mathbf{T}_{n+1}||_{\mathbb{H}}}{\partial\Delta\gamma} - \sqrt{\frac{2}{3}} \frac{\partial y(\alpha_{n+1})}{\partial\Delta\gamma} \\ &= \frac{\partial||\mathbf{T}_{n+1}||_{\mathbb{H}}}{\partial\mathbf{T}_{n+1}} : \frac{\partial\mathbf{T}_{n+1}}{\partial\Delta\gamma} - \sqrt{\frac{2}{3}} \frac{\partial y(\alpha_{n+1})}{\partial\Delta\gamma}. \end{aligned} \quad (3.58)$$

Employing the definition of the hardening law in Equation 3.36,

$$\frac{d\Upsilon_{n+1}}{d\Delta\gamma} = \mathbf{N}_{n+1} : \frac{\partial\mathbf{T}_{n+1}}{\partial\Delta\gamma} - \sqrt{\frac{2}{3}} \frac{\partial y(\alpha_{n+1})}{\partial\Delta\gamma}. \quad (3.59)$$

Using Equation 3.53, it follows that

$$\frac{\partial\mathbf{T}_{n+1}}{\partial\Delta\gamma} = -\mathbb{E}^e : \mathbf{N}_{n+1} - \Delta\gamma\mathbb{E}^e : \frac{\partial\mathbf{N}_{n+1}}{\partial\mathbf{T}_{n+1}} : \frac{\partial\mathbf{T}_{n+1}}{\partial\Delta\gamma}. \quad (3.60)$$

Putting the terms in the Lagrangian stress together, the above equation becomes

$$\left(\mathbb{I}^{\text{sym}} + \Delta\gamma\mathbb{E}^e : \frac{\partial\mathbf{N}_{n+1}}{\partial\mathbf{T}_{n+1}} \right) : \frac{\partial\mathbf{T}_{n+1}}{\partial\Delta\gamma} = -\mathbb{E}^e : \mathbf{N}_{n+1} \quad (3.61)$$

and thus

$$\begin{aligned} \frac{\partial\mathbf{T}_{n+1}}{\partial\Delta\gamma} &= -\left(\mathbb{I}^{\text{sym}} + \Delta\gamma\mathbb{E}^e : \frac{\partial\mathbf{N}_{n+1}}{\partial\mathbf{T}_{n+1}} \right)^{-1} : \mathbb{E}^e : \mathbf{N}_{n+1} \\ &= -\left(\mathbb{C}^e + \Delta\gamma\frac{\partial\mathbf{N}_{n+1}}{\partial\mathbf{T}_{n+1}} \right)^{-1} : \mathbf{N}_{n+1} \\ &= -(\mathbb{C}^e + \mathbb{N})^{-1} : \mathbf{N}_{n+1}, \end{aligned} \quad (3.62)$$

where $\mathbb{C}^e = (\mathbb{E}^e)^{-1}$ is the fourth-order compliance tensor and

$$\mathbb{N} = \Delta\gamma \frac{\partial\mathbf{N}_{n+1}}{\partial\mathbf{T}_{n+1}}. \quad (3.63)$$

It follows that

$$\begin{aligned} \Rightarrow \frac{d\Upsilon_{n+1}}{d\Delta\gamma} &= -\mathbf{N}_{n+1} : (\mathbb{C}^e + \mathbb{N})^{-1} : \mathbf{N}_{n+1} - \sqrt{\frac{2}{3}} \frac{\partial y(\alpha_{n+1})}{\partial\Delta\gamma} \\ &= -\mathbf{N}_{n+1} : \mathbb{E}^* : \mathbf{N}_{n+1} - \sqrt{\frac{2}{3}} \frac{\partial y(\alpha_{n+1})}{\partial\Delta\gamma} \end{aligned} \quad (3.64)$$

with

$$\mathbb{E}^* = (\mathbb{C}^e + \mathbb{N})^{-1}. \quad (3.65)$$

Furthermore the definition of the internal variable at t_{n+1} , i.e.,

$$\alpha_{n+1} = \alpha_n + \sqrt{\frac{2}{3}}\Delta\gamma, \quad (3.66)$$

and the definition of y at t_{n+1} , i.e.,

$$y(\alpha_{n+1}) = \sigma_0 + [\sigma_\infty - \sigma_0] \left[1 - e^{-w(\alpha_n + \sqrt{\frac{2}{3}}\Delta\gamma)} \right] + h \left[\alpha_n + \sqrt{\frac{2}{3}}\Delta\gamma \right] \quad (3.67)$$

allow finding the second term of Equation 3.64

$$\frac{\partial y(\alpha_{n+1})}{\partial \Delta\gamma} = \sqrt{\frac{2}{3}} [h + w(\sigma_\infty - \sigma_0)e^{-w\alpha_{n+1}}]. \quad (3.68)$$

By substituting this term into Equation 3.64, it follows immediately that

$$\frac{d\Upsilon_{n+1}}{d\Delta\gamma} = -\mathbf{N}_{n+1} : \mathbb{E}^* : \mathbf{N}_{n+1} - \sqrt{\frac{2}{3}} [h + w(\sigma_\infty - \sigma_0)e^{-w\alpha_{n+1}}]. \quad (3.69)$$

There is now a second challenge, in the computation of Υ_{n+1}^{trial} in order to check the convergence of Newton's algorithm. The mathematical development starts with the definition of the Lagrangian stress by

$$\mathbf{T}_{n+1} = \mathbf{T}_{n+1}^{trial} - \Delta\gamma \mathbb{E}^e : \mathbf{N}_{n+1}. \quad (3.70)$$

Employing the property of the hardening law

$$\mathbb{H} : \mathbf{T}_{n+1} = ||\mathbf{T}_{n+1}||_{\mathbb{H}} \mathbf{N}_{n+1} \quad (3.71)$$

and

$$\mathbf{N}_{n+1} = \frac{\mathbb{H} : \mathbf{T}_{n+1}^{trial}}{||\mathbf{T}_{n+1}^{trial}||_{\mathbb{H}}} \Rightarrow ||\mathbf{T}_{n+1}^{trial}||_{\mathbb{H}} : \mathbf{N}_{n+1} = \mathbb{H} : \mathbf{T}_{n+1}^{trial}, \quad (3.72)$$

and applying the tensor product of Equation 3.70 with \mathbf{N}_{n+1} , it follows that

$$\mathbf{T}_{n+1} : \mathbf{N}_{n+1} = \mathbf{T}_{n+1}^{trial} : \mathbf{N}_{n+1} - \Delta\gamma \mathbb{E}^e : \mathbf{N}_{n+1} : \mathbf{N}_{n+1}. \quad (3.73)$$

The above equation is then multiplied by Hill's tensor \mathbb{H} from Equation 3.31

$$\mathbb{H} : \mathbf{T}_{n+1} : \mathbf{N}_{n+1} = \mathbb{H} : \mathbf{T}_{n+1}^{trial} : \mathbf{N}_{n+1} - \Delta\gamma \mathbb{H} : \mathbb{E}^e : \mathbf{N}_{n+1} : \mathbf{N}_{n+1}. \quad (3.74)$$

By incorporating Equation 3.72 in the above equation, it follows that

$$\mathbb{H} : \mathbf{T}_{n+1} : \mathbf{N}_{n+1} = ||\mathbf{T}_{n+1}^{trial}||_{\mathbb{H}} \mathbf{N}_{n+1} : \mathbf{N}_{n+1} - \Delta\gamma \mathbb{H} : \mathbb{E}^e : \mathbf{N}_{n+1} : \mathbf{N}_{n+1}. \quad (3.75)$$

Furthermore, by substituting, in the above equation, the expression for $\mathbb{H} : \mathbf{T}_{n+1}$ obtained from Equation 3.71, the previous equation becomes

$$||\mathbf{T}_{n+1}||_{\mathbb{H}} \mathbf{N}_{n+1} : \mathbf{N}_{n+1} = ||\mathbf{T}_{n+1}^{trial}||_{\mathbb{H}} \mathbf{N}_{n+1} : \mathbf{N}_{n+1} + 1 - \Delta\gamma \mathbb{H} : \mathbb{E}^e : \mathbf{N}_{n+1} : \mathbf{N}_{n+1}. \quad (3.76)$$

Since \mathbf{N} is a unit vector, $\mathbf{N}_{n+1} : \mathbf{N}_{n+1} = \mathbf{I}$, then

$$||\mathbf{T}_{n+1}||_{\mathbb{H}} = ||\mathbf{T}_{n+1}^{trial}||_{\mathbb{H}} - \Delta\gamma \mathbb{H} : \mathbb{E}^e : \mathbf{N}_{n+1} : \mathbf{N}_{n+1}. \quad (3.77)$$

Thus

$$\Upsilon_{n+1}^{trial} = ||\boldsymbol{\xi}_{n+1}^{trial}|| - \sqrt{\frac{2}{3}} y(\alpha_{n+1}) - \Delta\gamma \mathbf{N}_{n+1} : \mathbb{H} : \mathbb{E}^e : \mathbf{N}_{n+1}. \quad (3.78)$$

Algorithm 3.2 presents, in the form of a pseudo-algorithm, the computation of the internal variable and the incremental plastic multiplier using Newton's method.

Algorithm 3.2: Consistency condition. Determination of $\Delta\gamma$

Data: $\alpha_{n+1}^{(0)} = \alpha_n$, $\Delta\gamma^{(0)} = \alpha_n$, $k=0$ %iteration counter, convergence=false, $\varepsilon = 10^{-8}$,
 $\mathbf{N}_{n+1} = \frac{\boldsymbol{\xi}_{n+1}^{trial}}{\|\boldsymbol{\xi}_{n+1}^{trial}\|}$;

while $convergence==false$ **do**

$\mathbb{N} = \frac{\Delta\gamma^{(k)}}{\|\boldsymbol{\xi}_{n+1}^{trial}\|} [\mathbb{H} - \mathbf{N}_{n+1} \otimes \mathbf{N}_{n+1}]$;

$\mathbb{E}^* = [(\mathbb{E}^e)^{-1} + \mathbb{N}]^{-1}$;

$\frac{d\Upsilon_{n+1}}{d\Delta\gamma} = -\mathbf{N}_{n+1} : \mathbb{E}^* : \mathbf{N}_{n+1} - \frac{2}{3} [h + w(\sigma_\infty - \sigma_0)e^{-w\alpha_{n+1}^{(k)}}]$;

$\Delta\gamma^{(k+1)} = \Delta\gamma^{(k)} - \frac{\Upsilon_{n+1}}{\frac{d\Upsilon_{n+1}}{d\Delta\gamma}}$;

$\alpha_{n+1}^{(k+1)} = \alpha_{n+1}^{(k)} - \sqrt{\frac{2}{3}} \frac{\Upsilon_{n+1}}{\frac{d\Upsilon_{n+1}}{d\Delta\gamma}}$;

$y(\alpha_{n+1}^{(k+1)}) = \sigma_0 + [\sigma_\infty - \sigma_0] \left[1 - e^{-w\alpha_{n+1}^{(k+1)}} \right] + h\alpha_{n+1}^{(k+1)}$;

$\Upsilon_{n+1}^{trial} = \|\boldsymbol{\xi}_{n+1}^{trial}\| - \sqrt{\frac{2}{3}} y(\alpha_{n+1}^{(k+1)}) - \Delta\gamma^{(k+1)} \mathbf{N}_{n+1} : \mathbb{H} : \mathbb{E}^e : \mathbf{N}_{n+1}$;

if $|\Upsilon_{n+1}^{trial}| < \varepsilon$ **then**

| $convergence=true$;

else

| $k=k+1$;

end

end

return $\Delta\gamma$ and α_{n+1} ;

3.5.2 Elastoplastic tangent modulus

According to de Souza Neto et al. [16], the fourth-order elastoplastic tangent modulus \mathbb{E}^{ep} needed in Equation 3.15 is given by

$$\mathbb{E}^{ep} = \mathbb{E}^e - \mathbb{E}^e : \mathbb{N} : \mathbb{E}^e - \frac{(\mathbb{E}^e : \mathbf{N}_{n+1}) \otimes (\mathbf{N}_{n+1} : \mathbb{E}^e)}{\mathbf{N}_{n+1} : \mathbb{E}^e : \mathbf{N}_{n+1} + \frac{2}{3} [w(\sigma_\infty - \sigma_0)e^{-w\alpha_{n+1}} + h]} \quad (3.79)$$

where \mathbb{N} , \mathbf{N}_{n+1} , and α_{n+1} are given in Algorithm 3.2. For the case of isotropic elastoplasticity, the above equation reduces to (Simo et al. [29])

$$\mathbb{E}^{ep} = \kappa \mathbf{I} \otimes \mathbf{I} - 2\mu d_1 \mathbb{I}_{dev}^{sym} - 2\mu d_2 \mathbf{N}_{n+1} \otimes \mathbf{N}_{n+1}, \quad (3.80)$$

where

$$d_1 = 1 - \frac{2\mu\Delta\gamma}{\|\boldsymbol{\xi}_{n+1}^{trial}\|} \quad (3.81)$$

and

$$d_2 = \frac{1}{1 + \frac{h + w(\sigma_\infty - \sigma_0)e^{-w\alpha_{n+1}}}{3\mu}} - (1 - d_1). \quad (3.82)$$

Here, μ and κ are the shear and bulk moduli, respectively.

CHAPTER 4

Spectral decomposition and the Kelvin modes

In this chapter, the spectral decomposition of the fourth-order elasticity tensor \mathbb{E}^e is introduced for isotropic and anisotropic materials as a function of the typical Kelvin modes, following and summarising the papers from Mehrabadi et al. [23], Sutcliffe [24], Cowin et al. [25, 26], Chadwick et al. [27] and Mahnken [28]. This allows of creating and having a material library within the eight crystal systems, where the fourth-order elasticity tensor is defined by its material parameters and common projection tensors.

The present chapter is organised as follows: The spectral decomposition of the fourth-order elasticity tensor is first presented. The typical Kelvin modes are then exposed and an introduction is given to the spectral formulation for isotropic and anisotropic materials.

4.1 Spectral decomposition

The fourth-order elasticity tensor \mathbb{E}^e (Eq. 3.20) is assumed to have the following symmetries $\mathbb{E}_{ijkl}^e = \mathbb{E}_{jikl}^e = \mathbb{E}_{ijlk}^e = \mathbb{E}_{klij}^e$ for $i, j, k, l = 1 \dots 3$. In Voigt notation (Voigt [84]), the fourth-order elasticity tensor is defined by the following 6×6 matrix

$$\mathbb{E}^e = \begin{bmatrix} E_{1111} & E_{1122} & E_{1133} & E_{1112} & E_{1123} & E_{1131} \\ & E_{2222} & E_{2233} & E_{2212} & E_{2223} & E_{2231} \\ & & E_{3333} & E_{3312} & E_{3323} & E_{3331} \\ \text{SYM} & & E_{1212} & E_{1223} & E_{1231} & \\ & & & E_{2323} & E_{2331} & \\ & & & & E_{3131} & \end{bmatrix} = \begin{bmatrix} E_{11} & E_{12} & E_{13} & E_{14} & E_{15} & E_{16} \\ & E_{22} & E_{23} & E_{24} & E_{25} & E_{26} \\ & & E_{33} & E_{34} & E_{35} & E_{36} \\ \text{SYM} & & & E_{44} & E_{45} & E_{46} \\ & & & & E_{55} & E_{56} \\ & & & & & E_{66} \end{bmatrix}, \quad (4.1)$$

which is symmetric and has 21 material parameters. The eigenvalue problem

$$\mathbb{E}^e : \mathbf{N}_i = \lambda_i \mathbf{N}_i \quad \text{with} \quad \mathbf{N}_i : \mathbf{N}_j = \delta_{ij} \quad \text{for } i, j = 1 \dots 6 \quad (4.2)$$

allows a spectral representation of the fourth-order elasticity tensor as

$$\mathbb{E}^e = \sum_{k=1}^{n_{mode}} \bar{\lambda}_k \mathbb{P}_k, \quad (4.3)$$

where $\bar{\lambda}_k$ are the distinct eigenvalues of \mathbb{E}^e in the Voigt notation and $n_{mode} \in \{1 \dots 6\}$ represents the number of distinct eigenvalues, or, the number of modes. The maximal number of eigenvalues and eigentensors is six. When restricted to the space of symmetric tensors, as is the case for

the fourth-order elasticity tensor, the fourth-order elasticity tensor is positive definite, so the eigenvalues are real and positive. Recall that an $n \times n$ real matrix \mathbf{A} is said to be positive definite if $\mathbf{b}^T \cdot \mathbf{A} \cdot \mathbf{b} > 0$ for all non-zero vectors \mathbf{b} with real entries ($\mathbf{b} \in \mathbb{R}^n$), where \mathbf{b}^T denotes the transpose of \mathbf{b} . The multiplicity of the eigenvalues is defined to be

$$\mathbf{M}_k = \dim \mathbb{M}_k \quad \text{and} \quad \sum_{k=1}^{n_{mode}} \mathbf{M}_k = 6 \quad (4.4)$$

with

$$\mathbb{M}_k = \{i, \dots | \lambda_i \equiv \bar{\lambda}_k\} \quad \text{and} \quad \bar{\lambda}_k \neq \bar{\lambda}_l \quad \text{for } k, l = 1 \dots n_{mode}. \quad (4.5)$$

The projection operators (projection tensors or modal tensors), which are fourth-order tensors, in Equation 4.3 are defined, as functions of the eigentensors, by

$$\mathbb{P}_k = \sum_{i \in \mathbb{M}_k} \mathbf{N}_i \otimes \mathbf{N}_i \quad (4.6)$$

with the following properties

$$\sum_{k=1}^{n_{mode}} \mathbb{P}_k = \mathbb{I}^{sym} \quad \text{and} \quad \mathbb{P}_k : \mathbb{P}_l = \delta_{kl} \mathbb{P}_k \quad \text{for } k, l = 1 \dots n_{mode}. \quad (4.7)$$

The eigentensors are also referred to as the Kelvin modes (Mehrabadi et al. [23], Arramon et al. [85]), and were first introduced and determined by Lord Kelvin for many elastic crystal systems, in Kelvin [86]. Subsequently the eigentensors will also be referred to as the Kelvin modes. When the eigenvalues are all distinct, the projection tensors can be computed as in Walpole [87]

$$\mathbb{P}_k = \frac{\prod_{l=1/k}^{n_{mode}} (\mathbb{E}^e - \bar{\lambda}_l \mathbb{I}^{sym})}{\prod_{l=1/k}^{n_{mode}} (\bar{\lambda}_k - \bar{\lambda}_l)} \quad \text{for } k = 1 \dots n_{mode}. \quad (4.8)$$

Furthermore if \mathbf{N}_i in Equation 4.6 is the eigentensor corresponding to an isolated eigenvalue λ_i , then

$$V(\lambda_i) = \{\mathbf{N}_i \in \mathbb{R}^6 | (\mathbb{E}^e - \lambda_i \mathbb{I}) \mathbf{N}_i = \mathbf{0}\} = \ker(\mathbb{E}^e - \lambda_i \mathbb{I}) \quad (4.9)$$

is a one-dimensional vector space spanned by \mathbf{N}_i . If $\mathbf{N}_{j1}, \dots, \mathbf{N}_{jr}$ are mutually orthogonal eigentensors corresponding to a repeated eigenvalue of multiplicity r , then $V(\lambda_i)$ is an r -dimensional vector space spanned by $\mathbf{N}_{j1}, \dots, \mathbf{N}_{jr}$. Any non-zero linear combination of eigentensors that share the same eigenvalue λ_i , is itself an eigentensor of λ_i . Since \mathbb{E}^e is symmetric, the eigenspaces are orthogonal (Sutcliffe [24]).

Remark: The spectral decomposition of the fourth-order elasticity tensor allows an easier computation of the compliance tensor \mathbb{C}^e (Eq. 3.62), which is the tensor inverse to the elastic tensor \mathbb{E}^e . Indeed, only the eigenvalues are inverted

$$\mathbb{C}^e = (\mathbb{E}^e)^{-1} = \sum_{k=1}^{n_{mode}} (\bar{\lambda}_k)^{-1} \mathbb{P}_k. \quad (4.10)$$

4.2 Typical Kelvin modes

According to Mehrabadi et al. [23], the typical Kelvin modes can be divided into four categories: dilatation mode, isochoric extension mode, isochoric pure shear mode, and isochoric simple shear mode. The eigentensors corresponding to the isochoric and shear modes are different along the three directions in a Cartesian coordinate system (Fig. 4.1). For each mode, a graphical representation follows in the subsequent tensor representation of the different modes. In the

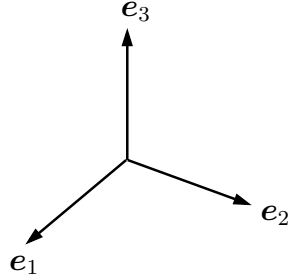


Figure 4.1: Coordinate system.

three-dimensional Cartesian coordinate system, the unit vectors codirectional with the e_1 , e_2 , and e_3 axes in Figure 4.1 are defined by

$$\mathbf{a}_1 = \begin{bmatrix} 1 \\ 0 \\ 0 \end{bmatrix}, \quad \mathbf{a}_2 = \begin{bmatrix} 0 \\ 1 \\ 0 \end{bmatrix} \quad \text{and} \quad \mathbf{a}_3 = \begin{bmatrix} 0 \\ 0 \\ 1 \end{bmatrix}. \quad (4.11)$$

The dilatation mode is defined by the tensor \mathbf{N}^d in Equation 4.12, with a graphical illustration in Figure 4.2.

$$\begin{aligned} \mathbf{N}^d &= \frac{1}{\sqrt{3}} (\mathbf{a}_1 \otimes \mathbf{a}_1 + \mathbf{a}_2 \otimes \mathbf{a}_2 + \mathbf{a}_3 \otimes \mathbf{a}_3) \\ &= \frac{1}{\sqrt{3}} \begin{bmatrix} 1 & 0 & 0 \\ 0 & 1 & 0 \\ 0 & 0 & 1 \end{bmatrix}. \end{aligned} \quad (4.12)$$

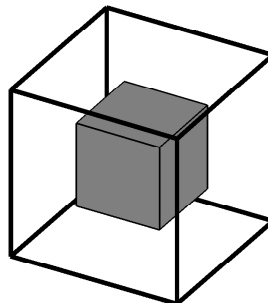


Figure 4.2: Dilatation mode.

The three isochoric extension modes along \mathbf{e}_1 , \mathbf{e}_2 , and \mathbf{e}_3 are defined by the tensors \mathbf{N}_1^e , \mathbf{N}_2^e , and \mathbf{N}_3^e , in Equation 4.13, Equation 4.14, and Equation 4.15, respectively. A graphical illustration is shown in Figure 4.3 for each direction.

$$\begin{aligned}\mathbf{N}_1^e &= \frac{1}{\sqrt{6}} (2\mathbf{a}_1 \otimes \mathbf{a}_1 - \mathbf{a}_2 \otimes \mathbf{a}_2 - \mathbf{a}_3 \otimes \mathbf{a}_3) \\ &= \frac{1}{\sqrt{6}} \begin{bmatrix} 2 & 0 & 0 \\ 0 & -1 & 0 \\ 0 & 0 & -1 \end{bmatrix}.\end{aligned}\quad (4.13)$$

$$\begin{aligned}\mathbf{N}_2^e &= \frac{1}{\sqrt{6}} (2\mathbf{a}_2 \otimes \mathbf{a}_2 - \mathbf{a}_1 \otimes \mathbf{a}_1 - \mathbf{a}_3 \otimes \mathbf{a}_3) \\ &= \frac{1}{\sqrt{6}} \begin{bmatrix} -1 & 0 & 0 \\ 0 & 2 & 0 \\ 0 & 0 & -1 \end{bmatrix}.\end{aligned}\quad (4.14)$$

$$\begin{aligned}\mathbf{N}_3^e &= \frac{1}{\sqrt{6}} (2\mathbf{a}_3 \otimes \mathbf{a}_3 - \mathbf{a}_1 \otimes \mathbf{a}_1 - \mathbf{a}_2 \otimes \mathbf{a}_2) \\ &= \frac{1}{\sqrt{6}} \begin{bmatrix} -1 & 0 & 0 \\ 0 & -1 & 0 \\ 0 & 0 & 2 \end{bmatrix}.\end{aligned}\quad (4.15)$$

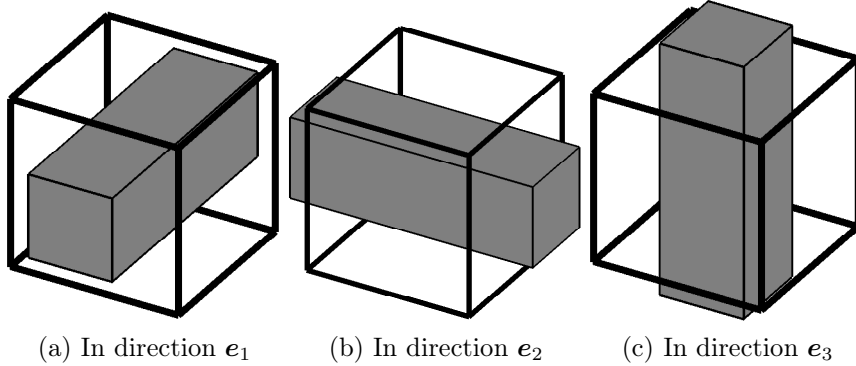


Figure 4.3: Isochoric extension mode.

The three isochoric pure shear modes along \mathbf{e}_1 , \mathbf{e}_2 , and \mathbf{e}_3 are defined by the tensors \mathbf{N}_1^p , \mathbf{N}_2^p , and \mathbf{N}_3^p , in Equation 4.16, Equation 4.17, and Equation 4.18, respectively. A graphical illustration is shown in Figure 4.4 for each direction.

$$\begin{aligned}\mathbf{N}_1^p &= \frac{1}{\sqrt{2}} (\mathbf{a}_2 \otimes \mathbf{a}_2 - \mathbf{a}_3 \otimes \mathbf{a}_3) \\ &= \frac{1}{\sqrt{2}} \begin{bmatrix} 0 & 0 & 0 \\ 0 & 1 & 0 \\ 0 & 0 & -1 \end{bmatrix}.\end{aligned}\quad (4.16)$$

$$\begin{aligned}\mathbf{N}_2^p &= \frac{1}{\sqrt{2}} (\mathbf{a}_3 \otimes \mathbf{a}_3 - \mathbf{a}_1 \otimes \mathbf{a}_1) \\ &= \frac{1}{\sqrt{2}} \begin{bmatrix} -1 & 0 & 0 \\ 0 & 0 & 0 \\ 0 & 0 & 1 \end{bmatrix}.\end{aligned}\quad (4.17)$$

$$\begin{aligned}\mathbf{N}_3^p &= \frac{1}{\sqrt{2}} (\mathbf{a}_1 \otimes \mathbf{a}_1 - \mathbf{a}_2 \otimes \mathbf{a}_2) \\ &= \frac{1}{\sqrt{2}} \begin{bmatrix} 1 & 0 & 0 \\ 0 & -1 & 0 \\ 0 & 0 & 0 \end{bmatrix}.\end{aligned}\quad (4.18)$$

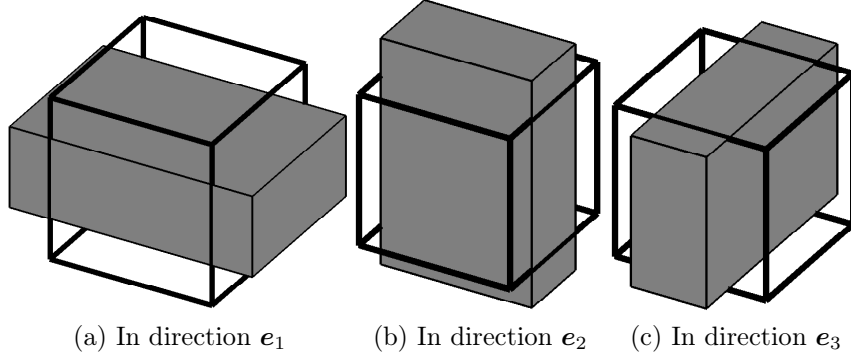


Figure 4.4: Isochoric pure shear mode.

The three isochoric simple shear modes along \mathbf{e}_1 , \mathbf{e}_2 , and \mathbf{e}_3 are defined by the tensors \mathbf{N}_1^s , \mathbf{N}_2^s , and \mathbf{N}_3^s , in Equation 4.19, Equation 4.20, and Equation 4.21, respectively. A graphical illustration is shown in Figure 4.5 for each direction.

$$\begin{aligned}\mathbf{N}_1^s &= \frac{1}{\sqrt{2}} (\mathbf{a}_2 \otimes \mathbf{a}_3 + \mathbf{a}_3 \otimes \mathbf{a}_2) \\ &= \frac{1}{\sqrt{2}} \begin{bmatrix} 0 & 0 & 0 \\ 0 & 0 & 1 \\ 0 & 1 & 0 \end{bmatrix}.\end{aligned}\quad (4.19)$$

$$\begin{aligned}\mathbf{N}_2^s &= \frac{1}{\sqrt{2}} (\mathbf{a}_3 \otimes \mathbf{a}_1 + \mathbf{a}_1 \otimes \mathbf{a}_3) \\ &= \frac{1}{\sqrt{2}} \begin{bmatrix} 0 & 0 & 1 \\ 0 & 0 & 0 \\ 1 & 0 & 0 \end{bmatrix}.\end{aligned}\quad (4.20)$$

$$\begin{aligned}\mathbf{N}_3^s &= \frac{1}{\sqrt{2}} (\mathbf{a}_1 \otimes \mathbf{a}_2 + \mathbf{a}_2 \otimes \mathbf{a}_1) \\ &= \frac{1}{\sqrt{2}} \begin{bmatrix} 0 & 1 & 0 \\ 1 & 0 & 0 \\ 0 & 0 & 0 \end{bmatrix}.\end{aligned}\quad (4.21)$$

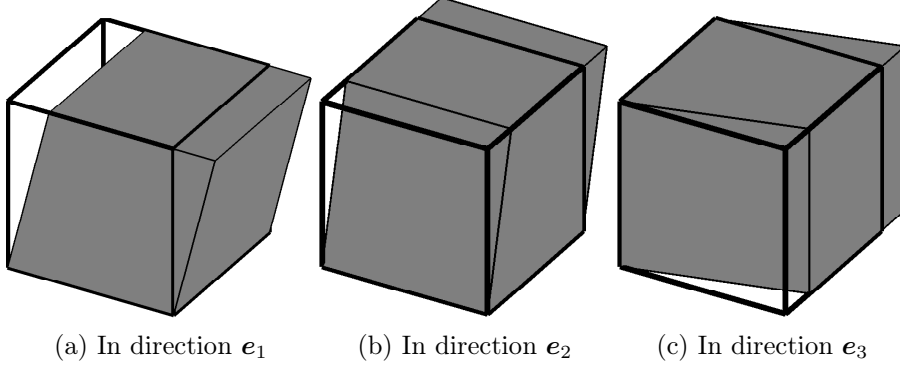


Figure 4.5: Isochoric simple shear mode.

From the definition of the isochoric extension and pure shear modes it can be seen that they are linearly dependent

$$\mathbf{N}_1^e + \mathbf{N}_2^e + \mathbf{N}_3^e = \mathbf{0} \quad (4.22)$$

$$\mathbf{N}_1^p + \mathbf{N}_2^p + \mathbf{N}_3^p = \mathbf{0}, \quad (4.23)$$

$$\mathbf{N}_i^p - \mathbf{N}_j^p + \sqrt{3}\mathbf{N}_k^e = \mathbf{0} \quad (4.24)$$

$$\mathbf{N}_i^e - \mathbf{N}_j^e - \sqrt{3}\mathbf{N}_k^p = \mathbf{0}. \quad (4.25)$$

Moreover the isochoric simple shear modes are linearly independent

$$\mathbf{N}_1^s + \mathbf{N}_2^s + \mathbf{N}_3^s \neq \mathbf{0}. \quad (4.26)$$

:	\mathbf{N}^d	\mathbf{N}_1^e	\mathbf{N}_2^e	\mathbf{N}_3^e	\mathbf{N}_1^p	\mathbf{N}_2^p	\mathbf{N}_3^p	\mathbf{N}_j^s
\mathbf{N}^d	1	0	0	0	0	0	0	0
\mathbf{N}_1^e	0	1	-1/2	-1/2	0	-\sqrt{3}/2	\sqrt{3}/2	0
\mathbf{N}_2^e	0	-1/2	1	-1/2	\sqrt{3}/2	0	-\sqrt{3}/2	0
\mathbf{N}_3^e	0	-1/2	-1/2	1	-\sqrt{3}/2	\sqrt{3}/2	0	0
\mathbf{N}_1^p	0	0	\sqrt{3}/2	-\sqrt{3}/2	1	-1/2	-1/2	0
\mathbf{N}_2^p	0	-\sqrt{3}/2	0	\sqrt{3}/2	-1/2	1	-1/2	0
\mathbf{N}_3^p	0	\sqrt{3}/2	-\sqrt{3}/2	0	-1/2	-1/2	1	0
\mathbf{N}_i^s	0	0	0	0	0	0	0	δ_{ij}

Table 4.1: Orthonormality of eigentensors

According to Sutcliffe [24], the eigentensors of an eigenspace are orthogonal to every tensor in any other eigenspace. The orthonormality of the eigentensors is presented in Table 4.1. Thereby an eigenbasis for symmetric second order tensors is

$$\mathbf{N}^d \oplus \mathbf{N}_i^e \oplus \mathbf{N}_i^p \oplus \mathbf{N}_1^s \oplus \mathbf{N}_2^s \oplus \mathbf{N}_3^s. \quad (4.27)$$

In Equation 4.27, the variable i is equal to 1, 2 or 3, i.e., no summation as in Einstein notation. The operator \oplus represents the direct sum of matrices or matrix addition of two matrices with the same dimension.

4.3 The Kelvin mode formulation for isotropic material

The material response for an isotropic material is uniform in all directions. In Voigt notation, the isotropic elasticity tensor is defined by

$$\mathbb{E}^e = \mathbb{E}_{\text{isotropic}}^e = \begin{bmatrix} E_{11} & E_{12} & E_{12} & 0 & 0 & 0 \\ & E_{11} & E_{12} & 0 & 0 & 0 \\ & & E_{11} & 0 & 0 & 0 \\ \text{SYM} & & & \frac{1}{2}(E_{11} - E_{12}) & 0 & 0 \\ & & & & \frac{1}{2}(E_{11} - E_{12}) & 0 \\ & & & & & \frac{1}{2}(E_{11} - E_{12}) \end{bmatrix} \quad (4.28)$$

and has two independent material constants, E_{11} and E_{12} . The number of eigenvalues is two so that the number of modes is equal to two. The first eigenvalue

$$\bar{\lambda}_1(M_1 = 1) = E_{11} + 2E_{12} = 3\kappa \quad (4.29)$$

has multiplicity one, where κ is the bulk modulus. The second eigenvalue has multiplicity five, and is proportional to the shear modulus (or the second Lamé parameter)

$$\bar{\lambda}_2(M_2 = 5) = E_{11} - E_{12} = 2\mu. \quad (4.30)$$

The bulk modulus κ and the shear modulus μ are related to the Young modulus E and the Poisson ratio ν by the following expressions

$$\kappa = \frac{E}{3(1 - 2\nu)} \quad (4.31)$$

and

$$\mu = \frac{E}{2(1 + \nu)}. \quad (4.32)$$

Note that the bulk modulus can also be expressed as functions of the first Lamé parameter

$$\lambda = \frac{E\nu}{(1 + \nu)(1 - 2\nu)} \quad (4.33)$$

by

$$\kappa = \lambda + \frac{2}{3}\mu. \quad (4.34)$$

The first projection tensor correlated to the first eigenvalue is associated with the dilatation mode and is actually the volumetric part of the unit tensor

$$\mathbb{P}_1 = \mathbf{N}^d \otimes \mathbf{N}^d = \mathbb{I}_{\text{vol}}. \quad (4.35)$$

The second projection tensor associated with the second eigenvalue is the sum of the tensor products of the isochoric extension, pure shear, and simple shear modes with themselves, which is actually the deviatoric part of the symmetric unit tensor

$$\mathbb{P}_2 = \mathbf{N}_i^e \otimes \mathbf{N}_i^e + \mathbf{N}_i^p \otimes \mathbf{N}_i^p + \mathbf{N}_1^s \otimes \mathbf{N}_1^s + \mathbf{N}_2^s \otimes \mathbf{N}_2^s + \mathbf{N}_3^s \otimes \mathbf{N}_3^s = \mathbb{I}_{dev}^{sym} \quad (4.36)$$

for $i = 1, 2$ or 3 . The spectral decomposition for an isotropic material amounts to a one-dimensional eigenspace spanned by the volumetric part of the unit tensor and a five-dimensional eigenspace

$$\mathbb{E}^e = \bar{\lambda}_1 \mathbb{P}_1 + \bar{\lambda}_2 \mathbb{P}_2 = 3\kappa \mathbb{I}_{vol} + 2\mu \mathbb{I}_{dev}^{sym}. \quad (4.37)$$

4.4 The Kelvin mode formulation for anisotropic materials

For anisotropy, the material response depends on the preferred directions. For example, a sheet of metal which is manufactured by a rolling process has a dependency on the direction of rolling. Furthermore, anisotropic materials are differentiated according to their belonging to one of the seven crystal systems (Chadwick et al. [27]): monoclinic, triclinic, orthorhombic (orthotropic), trigonal, tetragonal, hexagonal (transversely isotropic), and cubic.

4.4.1 The cubic crystal system

Materials which have a cubic crystal system include, for example, iron, copper, aluminum, nickel, gold and lead. In Voigt notation, the cubic tensor

$$\mathbb{E}^e = \mathbb{E}_{cubic}^e = \begin{bmatrix} E_{11} & E_{12} & E_{12} & 0 & 0 & 0 \\ & E_{11} & E_{12} & 0 & 0 & 0 \\ & & E_{11} & 0 & 0 & 0 \\ SYM & & & E_{55} & 0 & 0 \\ & & & & E_{55} & 0 \\ & & & & & E_{55} \end{bmatrix} \quad (4.38)$$

has three independent material constants E_{11} , E_{12} and E_{55} . The number of modes is equal to three, so that the tensor has three eigenvalues. The first eigenvalue

$$\bar{\lambda}_1(M_1 = 1) = E_{11} + 2E_{12} = 3\kappa \quad (4.39)$$

has multiplicity one, and is proportional to the bulk modulus. The second eigenvalue

$$\bar{\lambda}_2(M_2 = 2) = E_{11} - E_{12} = 2\mu \quad (4.40)$$

has multiplicity two, and is associated with the shear modulus. The third eigenvalue

$$\bar{\lambda}_3(M_3 = 3) = 2E_{55} \quad (4.41)$$

has multiplicity three. The first projection tensor associated with the first eigenvalue depends on the dilatation mode as for the isotropic tensor

$$\mathbb{P}_1 = \mathbf{N}^d \otimes \mathbf{N}^d = \mathbb{I}_{vol}. \quad (4.42)$$

The second projection tensor associated with the second eigenvalue is the sum of the tensor product of the isochoric extension and pure shear modes with themselves

$$\mathbb{P}_2 = \mathbf{N}_i^e \otimes \mathbf{N}_i^e + \mathbf{N}_i^p \otimes \mathbf{N}_i^p \quad (4.43)$$

for $i = 1, 2$ or 3 . The third projection tensor associated with the third eigenvalue is the sum of the tensor product of the three simple shear modes with themselves

$$\mathbb{P}_3 = \mathbf{N}_1^s \otimes \mathbf{N}_1^s + \mathbf{N}_2^s \otimes \mathbf{N}_2^s + \mathbf{N}_3^s \otimes \mathbf{N}_3^s. \quad (4.44)$$

The fourth-order material tensor can be rewritten as

$$\mathbb{E}^e = \bar{\lambda}_1 \mathbb{P}_1 + \bar{\lambda}_2 \mathbb{P}_2 + \bar{\lambda}_3 \mathbb{P}_3. \quad (4.45)$$

Thus the spectral decomposition of the cubic tensor consists of a dilatation, a two-dimensional and a three-dimensional eigenspace.

4.4.2 The orthorhombic (orthotropic) crystal system

Materials which have an orthorhombic crystal system include, for example, topaz and gallium. In Voigt notation, the orthorhombic tensor

$$\mathbb{E}^e = \mathbb{E}_{\text{orthorhombic}}^e = \begin{bmatrix} E_{11} & E_{12} & E_{13} & 0 & 0 & 0 \\ E_{21} & E_{22} & E_{23} & 0 & 0 & 0 \\ E_{31} & E_{32} & E_{33} & 0 & 0 & 0 \\ \text{SYM} & & & E_{44} & 0 & 0 \\ & & & & E_{55} & 0 \\ & & & & & E_{66} \end{bmatrix} \quad (4.46)$$

has nine independent material constants. The eigenvalues and eigenvectors are all distinct, i.e., the multiplicity for each eigenvalue is equal to one and the number of modes is six. The first three eigenvalues are computed by calculating the eigenvalues of the 3×3 matrix

$$\mathbf{B} = \begin{bmatrix} E_{11} & E_{12} & E_{13} \\ E_{12} & E_{22} & E_{23} \\ E_{13} & E_{23} & E_{33} \end{bmatrix}. \quad (4.47)$$

Thus the eigenvalues are

$$\begin{aligned} \bar{\lambda}_1(M_1 = 1) &= \bar{\lambda}_1(\mathbf{B}) \\ \bar{\lambda}_2(M_2 = 1) &= \bar{\lambda}_2(\mathbf{B}) \\ \bar{\lambda}_3(M_3 = 1) &= \bar{\lambda}_3(\mathbf{B}). \end{aligned} \quad (4.48)$$

The corresponding projection tensors are

$$\begin{aligned} \mathbb{P}_1 &\in \mathbf{N}^d \otimes \mathbf{N}^d \oplus \mathbf{N}_i^e \otimes \mathbf{N}_i^e \oplus \mathbf{N}_i^p \otimes \mathbf{N}_i^p \\ \mathbb{P}_2 &\in \mathbf{N}^d \otimes \mathbf{N}^d \oplus \mathbf{N}_i^e \otimes \mathbf{N}_i^e \oplus \mathbf{N}_i^p \otimes \mathbf{N}_i^p \\ \mathbb{P}_3 &\in \mathbf{N}^d \otimes \mathbf{N}^d \oplus \mathbf{N}_i^e \otimes \mathbf{N}_i^e \oplus \mathbf{N}_i^p \otimes \mathbf{N}_i^p \end{aligned} \quad (4.49)$$

with $i = 1, 2$ or 3 for any linear combination of these three tensors. According to Mehrabadi et al. [23], the projection tensor can be computed as follows

$$\begin{aligned}\mathbb{P}_1 &= \mathbf{N}_1^{orth} \otimes \mathbf{N}_1^{orth} \\ \mathbb{P}_2 &= \mathbf{N}_2^{orth} \otimes \mathbf{N}_2^{orth} \\ \mathbb{P}_3 &= \mathbf{N}_3^{orth} \otimes \mathbf{N}_3^{orth},\end{aligned}\quad (4.50)$$

where

$$\mathbf{N}_1^{orth} = Z(\bar{\lambda}_1, \bar{\lambda}_2, \bar{\lambda}_3) * \mathbf{D}(\bar{\lambda}_1) \quad (4.51)$$

$$\mathbf{N}_2^{orth} = Z(\bar{\lambda}_2, \bar{\lambda}_3, \bar{\lambda}_1) * \mathbf{D}(\bar{\lambda}_2) \quad (4.52)$$

$$\mathbf{N}_3^{orth} = Z(\bar{\lambda}_3, \bar{\lambda}_1, \bar{\lambda}_2) * \mathbf{D}(\bar{\lambda}_3) \quad (4.53)$$

with

$$\mathbf{D}(\lambda_k) = \begin{bmatrix} E_{12}E_{23} - E_{13}(E_{22} - \bar{\lambda}_k) & 0 & 0 \\ 0 & E_{12}E_{13} - E_{23}(E_{11} - \bar{\lambda}_k) & 0 \\ 0 & 0 & (E_{11} - \bar{\lambda}_k)(E_{22} - \bar{\lambda}_k) - E_{12}^2 \end{bmatrix} \quad (4.54)$$

and

$$\begin{aligned}Z(\bar{\lambda}_k, \bar{\lambda}_i, \bar{\lambda}_j) &= \frac{1}{(\bar{\lambda}_k - \bar{\lambda}_i)(\bar{\lambda}_k - \bar{\lambda}_j)[E_{12}(E_{13}^2 - E_{23}^2) - E_{13}E_{23}(E_{11} - E_{22})]} \\ &\times \{[E_{12}E_{13} - E_{23}(E_{11} - \bar{\lambda}_i)][(E_{11} - \bar{\lambda}_j) + E_{12} + E_{13}] \\ &- [E_{12}E_{23} - E_{13}(E_{22} - \bar{\lambda}_i)][E_{12} + (E_{22} - \bar{\lambda}_j) + E_{23}]\}\end{aligned}\quad (4.55)$$

Before carrying out the tensor product in Equation 4.50, \mathbf{N}_1^{orth} , \mathbf{N}_2^{orth} , and \mathbf{N}_3^{orth} should be normalised. The fourth, fifth and sixth eigenvalues for the orthorhombic system are defined as functions of the material constants by

$$\begin{aligned}\bar{\lambda}_4(M_4 = 1) &= 2E_{44} \\ \bar{\lambda}_5(M_5 = 1) &= 2E_{55} \\ \bar{\lambda}_6(M_6 = 1) &= 2E_{66}.\end{aligned}\quad (4.56)$$

The corresponding projection tensors are defined by the tensor product of the isochoric simple shear modes with themselves.

$$\begin{aligned}\mathbb{P}_4 &= \mathbf{N}_3^s \otimes \mathbf{N}_3^s \\ \mathbb{P}_5 &= \mathbf{N}_1^s \otimes \mathbf{N}_1^s \\ \mathbb{P}_6 &= \mathbf{N}_2^s \otimes \mathbf{N}_2^s\end{aligned}\quad (4.57)$$

Thus, the spectral decomposition of the orthorhombic tensor consists of six proper one-dimensional eigenspaces

$$\mathbb{E}^e = \bar{\lambda}_1\mathbb{P}_1 + \bar{\lambda}_2\mathbb{P}_2 + \bar{\lambda}_3\mathbb{P}_3 + \bar{\lambda}_4\mathbb{P}_4 + \bar{\lambda}_5\mathbb{P}_5 + \bar{\lambda}_6\mathbb{P}_6. \quad (4.58)$$

Since the eigenvalues are all distinct, the projection tensors can also be computed with Equation 4.8.

4.4.3 The trigonal crystal system

Materials which have a trigonal crystal system include α -quartz and tourmaline. In Voigt notation, the trigonal tensor with a 3-axis in the e_3 -direction (Fig. 4.1)

$$\mathbb{E}^e = \mathbb{E}_{\text{trigonal}, e_3}^e = \begin{bmatrix} E_{11} & E_{12} & E_{13} & 0 & 0 & E_{16} \\ & E_{11} & E_{13} & 0 & 0 & -E_{16} \\ & & E_{33} & 0 & 0 & 0 \\ \text{SYM} & & & \frac{1}{2}(E_{11} - E_{12}) & -E_{16} & 0 \\ & & & & E_{55} & 0 \\ & & & & & E_{55} \end{bmatrix} \quad (4.59)$$

has twelve independent material constants. The eigenvalues and eigenvectors are all distinct, i.e., they have multiplicity one, and the number of modes is six. The eigenvalues are calculated by splitting the previous tensor into two matrices

$$\mathbf{A} = \begin{bmatrix} E_{11} & E_{12} & E_{13} & E_{16} \\ E_{12} & E_{22} & E_{23} & -E_{16} \\ E_{13} & E_{23} & E_{33} & 0 \\ E_{16} & -E_{16} & 0 & E_{55} \end{bmatrix} \quad (4.60)$$

and

$$\mathbf{B} = \begin{bmatrix} \frac{1}{2}(E_{11} - E_{12}) & -E_{16} \\ -E_{16} & E_{55} \end{bmatrix}, \quad (4.61)$$

so that the eigenvalues are equal to

$$\begin{aligned} \bar{\lambda}_1(M_1 = 1) &= \bar{\lambda}_1(\mathbf{A}) \\ \bar{\lambda}_2(M_2 = 1) &= \bar{\lambda}_2(\mathbf{A}) \\ \bar{\lambda}_3(M_3 = 1) &= \bar{\lambda}_3(\mathbf{A}) \\ \bar{\lambda}_4(M_4 = 1) &= \bar{\lambda}_4(\mathbf{A}) \\ \bar{\lambda}_5(M_5 = 1) &= \bar{\lambda}_5(\mathbf{B}) \\ \bar{\lambda}_6(M_6 = 1) &= \bar{\lambda}_6(\mathbf{B}). \end{aligned} \quad (4.62)$$

The distinct projection tensors are computed for any linear combination of the four Kelvin mode tensors by

$$\begin{aligned} \mathbb{P}_1 &\in \mathbf{N}^d \otimes \mathbf{N}^d \oplus \mathbf{N}_i^e \otimes \mathbf{N}_i^e \oplus \mathbf{N}_i^p \otimes \mathbf{N}_i^p \oplus \mathbf{N}_3^s \otimes \mathbf{N}_3^s \\ \mathbb{P}_2 &\in \mathbf{N}^d \otimes \mathbf{N}^d \oplus \mathbf{N}_i^e \otimes \mathbf{N}_i^e \oplus \mathbf{N}_i^p \otimes \mathbf{N}_i^p \oplus \mathbf{N}_3^s \otimes \mathbf{N}_3^s \\ \mathbb{P}_3 &\in \mathbf{N}^d \otimes \mathbf{N}^d \oplus \mathbf{N}_i^e \otimes \mathbf{N}_i^e \oplus \mathbf{N}_i^p \otimes \mathbf{N}_i^p \oplus \mathbf{N}_3^s \otimes \mathbf{N}_3^s \\ \mathbb{P}_4 &\in \mathbf{N}^d \otimes \mathbf{N}^d \oplus \mathbf{N}_i^e \otimes \mathbf{N}_i^e \oplus \mathbf{N}_i^p \otimes \mathbf{N}_i^p \oplus \mathbf{N}_3^s \otimes \mathbf{N}_3^s \\ \mathbb{P}_5 &\in \mathbf{N}_s^1 \otimes \mathbf{N}_s^1 \oplus \mathbf{N}_2^s \otimes \mathbf{N}_2^s \\ \mathbb{P}_6 &\in \mathbf{N}_s^1 \otimes \mathbf{N}_s^1 \oplus \mathbf{N}_2^s \otimes \mathbf{N}_2^s. \end{aligned} \quad (4.63)$$

The projection operators $\mathbb{P}_{i=1\dots 6}$ can also be computed in this case with Equation 4.8. Thus the spectral decomposition of the trigonal tensor consists of the six proper one-dimensional eigenspaces

$$\mathbb{E}^e = \bar{\lambda}_1 \mathbb{P}_1 + \bar{\lambda}_2 \mathbb{P}_2 + \bar{\lambda}_3 \mathbb{P}_3 + \bar{\lambda}_4 \mathbb{P}_4 + \bar{\lambda}_5 \mathbb{P}_5 + \bar{\lambda}_6 \mathbb{P}_6. \quad (4.64)$$

4.4.4 Monoclinic crystal system

Materials which have a monoclinic crystal system include wolframite, gypsum, titanite, augite, and orthoclase. In Voigt notation, the monoclinic tensor in the e_1 -direction is defined by the tensor

$$\mathbb{E}^e = \mathbb{E}_{\text{monoclinic}, e_1}^e = \begin{bmatrix} E_{11} & E_{12} & E_{13} & 0 & E_{15} & 0 \\ & E_{22} & E_{23} & 0 & E_{25} & 0 \\ & & E_{33} & 0 & E_{35} & 0 \\ \text{SYM} & 0 & E_{44} & 0 & E_{46} & \\ & & & E_{55} & 0 & \\ & & & & E_{66} & \end{bmatrix} \quad (4.65)$$

which has 13 independent material constants. There are six modes and the eigenvalues, which are all distinct, i.e., multiplicity one, are calculated by splitting the previous tensor into two matrices

$$\mathbf{A} = \begin{bmatrix} E_{11} & E_{12} & E_{13} & E_{15} \\ E_{12} & E_{22} & E_{23} & E_{25} \\ E_{13} & E_{23} & E_{33} & E_{35} \\ E_{15} & E_{25} & E_{35} & E_{55} \end{bmatrix} \quad (4.66)$$

and

$$\mathbf{B} = \begin{bmatrix} E_{44} & E_{46} \\ E_{46} & E_{66} \end{bmatrix}, \quad (4.67)$$

so that the eigenvalues are equal to

$$\begin{aligned} \bar{\lambda}_1(M_1 = 1) &= \bar{\lambda}_1(\mathbf{A}) \\ \bar{\lambda}_2(M_2 = 1) &= \bar{\lambda}_2(\mathbf{A}) \\ \bar{\lambda}_3(M_3 = 1) &= \bar{\lambda}_3(\mathbf{A}) \\ \bar{\lambda}_4(M_4 = 1) &= \bar{\lambda}_4(\mathbf{A}) \\ \bar{\lambda}_5(M_5 = 1) &= \bar{\lambda}_5(\mathbf{B}) \\ \bar{\lambda}_6(M_6 = 1) &= \bar{\lambda}_6(\mathbf{B}). \end{aligned} \quad (4.68)$$

The distinct projection tensors are computed for any linear combination of the four Kelvin mode tensors by

$$\begin{aligned} \mathbb{P}_1 &\in \mathbf{N}^d \otimes \mathbf{N}^d \oplus \mathbf{N}_i^e \otimes \mathbf{N}_i^e \oplus \mathbf{N}_i^p \otimes \mathbf{N}_i^p \oplus \mathbf{N}_1^s \otimes \mathbf{N}_1^s \\ \mathbb{P}_2 &\in \mathbf{N}^d \otimes \mathbf{N}^d \oplus \mathbf{N}_i^e \otimes \mathbf{N}_i^e \oplus \mathbf{N}_i^p \otimes \mathbf{N}_i^p \oplus \mathbf{N}_1^s \otimes \mathbf{N}_1^s \\ \mathbb{P}_3 &\in \mathbf{N}^d \otimes \mathbf{N}^d \oplus \mathbf{N}_i^e \otimes \mathbf{N}_i^e \oplus \mathbf{N}_i^p \otimes \mathbf{N}_i^p \oplus \mathbf{N}_1^s \otimes \mathbf{N}_1^s \\ \mathbb{P}_4 &\in \mathbf{N}^d \otimes \mathbf{N}^d \oplus \mathbf{N}_i^e \otimes \mathbf{N}_i^e \oplus \mathbf{N}_i^p \otimes \mathbf{N}_i^p \oplus \mathbf{N}_1^s \otimes \mathbf{N}_1^s \\ \mathbb{P}_5 &\in \mathbf{N}_s^2 \otimes \mathbf{N}_s^2 \oplus \mathbf{N}_3^s \otimes \mathbf{N}_3^s \\ \mathbb{P}_6 &\in \mathbf{N}_s^2 \otimes \mathbf{N}_s^2 \oplus \mathbf{N}_3^s \otimes \mathbf{N}_3^s. \end{aligned} \quad (4.69)$$

They can also be computed with Equation 4.8.

In Voigt notation, the monoclinic tensor in the e_2 -direction is defined by the tensor

$$\mathbb{E}^e = \mathbb{E}_{\text{monoclinic}, e_2}^e = \begin{bmatrix} E_{11} & E_{12} & E_{13} & 0 & 0 & E_{16} \\ & E_{22} & E_{23} & 0 & 0 & E_{26} \\ & & E_{33} & 0 & 0 & E_{36} \\ \text{SYM} & & & E_{44} & E_{45} & 0 \\ & & & & E_{55} & 0 \\ & & & & & E_{66} \end{bmatrix} \quad (4.70)$$

which has 13 independent material constants. The number of modes is six and the eigenvalues, which are all distinct, i.e., they have multiplicity one, are calculated by splitting the previous tensor into two matrices

$$\mathbf{C} = \begin{bmatrix} E_{11} & E_{12} & E_{13} & E_{16} \\ E_{12} & E_{22} & E_{23} & E_{26} \\ E_{13} & E_{23} & E_{33} & E_{36} \\ E_{16} & E_{26} & E_{36} & E_{66} \end{bmatrix} \quad (4.71)$$

and

$$\mathbf{D} = \begin{bmatrix} E_{44} & E_{45} \\ E_{45} & E_{55} \end{bmatrix}, \quad (4.72)$$

so that the eigenvalues are equal to

$$\begin{aligned} \bar{\lambda}_1(M_1 = 1) &= \bar{\lambda}_1(\mathbf{C}) \\ \bar{\lambda}_2(M_2 = 1) &= \bar{\lambda}_2(\mathbf{C}) \\ \bar{\lambda}_3(M_3 = 1) &= \bar{\lambda}_3(\mathbf{C}) \\ \bar{\lambda}_4(M_4 = 1) &= \bar{\lambda}_3(\mathbf{C}) \\ \bar{\lambda}_5(M_5 = 1) &= \bar{\lambda}_5(\mathbf{D}) \\ \bar{\lambda}_6(M_6 = 1) &= \bar{\lambda}_6(\mathbf{D}). \end{aligned} \quad (4.73)$$

The distinct projection tensors are computed for any linear combination of the four Kelvin mode tensors by

$$\begin{aligned} \mathbb{P}_1 &\in \mathbf{N}^d \otimes \mathbf{N}^d \oplus \mathbf{N}_i^e \otimes \mathbf{N}_i^e \oplus \mathbf{N}_i^p \otimes \mathbf{N}_i^p \oplus \mathbf{N}_2^s \otimes \mathbf{N}_2^s \\ \mathbb{P}_2 &\in \mathbf{N}^d \otimes \mathbf{N}^d \oplus \mathbf{N}_i^e \otimes \mathbf{N}_i^e \oplus \mathbf{N}_i^p \otimes \mathbf{N}_i^p \oplus \mathbf{N}_2^s \otimes \mathbf{N}_2^s \\ \mathbb{P}_3 &\in \mathbf{N}^d \otimes \mathbf{N}^d \oplus \mathbf{N}_i^e \otimes \mathbf{N}_i^e \oplus \mathbf{N}_i^p \otimes \mathbf{N}_i^p \oplus \mathbf{N}_2^s \otimes \mathbf{N}_2^s \\ \mathbb{P}_4 &\in \mathbf{N}^d \otimes \mathbf{N}^d \oplus \mathbf{N}_i^e \otimes \mathbf{N}_i^e \oplus \mathbf{N}_i^p \otimes \mathbf{N}_i^p \oplus \mathbf{N}_2^s \otimes \mathbf{N}_2^s \\ \mathbb{P}_5 &\in \mathbf{N}_s^1 \otimes \mathbf{N}_s^1 \oplus \mathbf{N}_3^s \otimes \mathbf{N}_3^s \\ \mathbb{P}_6 &\in \mathbf{N}_s^1 \otimes \mathbf{N}_s^1 \oplus \mathbf{N}_3^s \otimes \mathbf{N}_3^s. \end{aligned} \quad (4.74)$$

They can also be computed with Equation 4.8.

In Voigt notation, the monoclinic tensor in the e_3 -direction is defined by

$$\mathbb{E}^e = \mathbb{E}_{\text{monoclinic}, e_3}^e = \begin{bmatrix} E_{11} & E_{12} & E_{13} & E_{14} & 0 & 0 \\ & E_{22} & E_{23} & E_{24} & 0 & 0 \\ & & E_{33} & E_{34} & 0 & 0 \\ \text{SYM} & & & E_{44} & 0 & 0 \\ & & & & E_{55} & E_{56} \\ & & & & & E_{66} \end{bmatrix} \quad (4.75)$$

which has 13 independent material constants. The eigenvalues are all distinct, i.e., multiplicity one, and the number of modes is six, and they are calculated by splitting the previous tensor into two matrices

$$\mathbf{G} = \begin{bmatrix} E_{11} & E_{12} & E_{13} & E_{14} \\ E_{12} & E_{22} & E_{23} & E_{24} \\ E_{13} & E_{23} & E_{33} & E_{34} \\ E_{14} & E_{24} & E_{34} & E_{44} \end{bmatrix} \quad (4.76)$$

and

$$\mathbf{H} = \begin{bmatrix} E_{55} & E_{56} \\ E_{56} & E_{66} \end{bmatrix}, \quad (4.77)$$

so that the eigenvalues are equal to

$$\begin{aligned} \bar{\lambda}_1(M_1 = 1) &= \bar{\lambda}_1(\mathbf{G}) \\ \bar{\lambda}_2(M_2 = 1) &= \bar{\lambda}_2(\mathbf{G}) \\ \bar{\lambda}_3(M_3 = 1) &= \bar{\lambda}_3(\mathbf{G}) \\ \bar{\lambda}_4(M_4 = 1) &= \bar{\lambda}_4(\mathbf{G}) \\ \bar{\lambda}_5(M_5 = 1) &= \bar{\lambda}_5(\mathbf{H}) \\ \bar{\lambda}_6(M_6 = 1) &= \bar{\lambda}_6(\mathbf{H}). \end{aligned} \quad (4.78)$$

The distinct projection tensors are computed for any linear combination of the four Kelvin mode tensors by

$$\begin{aligned} \mathbb{P}_1 &\in \mathbf{N}^d \otimes \mathbf{N}^d \oplus \mathbf{N}_i^e \otimes \mathbf{N}_i^e \oplus \mathbf{N}_i^p \otimes \mathbf{N}_i^p \oplus \mathbf{N}_3^s \otimes \mathbf{N}_3^s \\ \mathbb{P}_2 &\in \mathbf{N}^d \otimes \mathbf{N}^d \oplus \mathbf{N}_i^e \otimes \mathbf{N}_i^e \oplus \mathbf{N}_i^p \otimes \mathbf{N}_i^p \oplus \mathbf{N}_3^s \otimes \mathbf{N}_3^s \\ \mathbb{P}_3 &\in \mathbf{N}^d \otimes \mathbf{N}^d \oplus \mathbf{N}_i^e \otimes \mathbf{N}_i^e \oplus \mathbf{N}_i^p \otimes \mathbf{N}_i^p \oplus \mathbf{N}_3^s \otimes \mathbf{N}_3^s \\ \mathbb{P}_4 &\in \mathbf{N}^d \otimes \mathbf{N}^d \oplus \mathbf{N}_i^e \otimes \mathbf{N}_i^e \oplus \mathbf{N}_i^p \otimes \mathbf{N}_i^p \oplus \mathbf{N}_3^s \otimes \mathbf{N}_3^s \\ \mathbb{P}_5 &\in \mathbf{N}_s^1 \otimes \mathbf{N}_s^1 \oplus \mathbf{N}_2^s \otimes \mathbf{N}_2^s \\ \mathbb{P}_6 &\in \mathbf{N}_s^1 \otimes \mathbf{N}_s^1 \oplus \mathbf{N}_2^s \otimes \mathbf{N}_2^s. \end{aligned} \quad (4.79)$$

They can also be computed with Equation 4.8.

Thus the spectral decomposition of the monoclinic tensor consists of the six proper one-dimensional eigenspaces

$$\mathbb{E}^e = \bar{\lambda}_1 \mathbb{P}_1 + \bar{\lambda}_2 \mathbb{P}_2 + \bar{\lambda}_3 \mathbb{P}_3 + \bar{\lambda}_4 \mathbb{P}_4 + \bar{\lambda}_5 \mathbb{P}_5 + \bar{\lambda}_6 \mathbb{P}_6. \quad (4.80)$$

4.4.5 The triclinic crystal system

Materials having a triclinic crystal system include, for example, copper sulfate and some minerals such as plagioclase, microcline, rhodonite, turquoise, wollastonite, and amblygonite. The triclinic system has no restriction on the values of the fourth-order elasticity tensor \mathbb{E}^e , i.e., the 21 constants in Voigt notation are independent

$$\mathbb{E}^e = \mathbb{E}_{\text{triclinic}}^e = \begin{bmatrix} E_{11} & E_{12} & E_{13} & E_{14} & E_{15} & E_{16} \\ & E_{22} & E_{23} & E_{24} & E_{25} & E_{26} \\ & & E_{33} & E_{34} & E_{35} & E_{36} \\ & & & E_{44} & E_{45} & E_{46} \\ & & & & E_{55} & E_{56} \\ & & & & & E_{66} \end{bmatrix}_{\text{SYM}}. \quad (4.81)$$

The eigenvalues

$$\begin{aligned} \bar{\lambda}_1(M_1 = 1) &= \bar{\lambda}_1(\mathbb{E}^e) \\ \bar{\lambda}_2(M_2 = 1) &= \bar{\lambda}_2(\mathbb{E}^e) \\ \bar{\lambda}_3(M_3 = 1) &= \bar{\lambda}_3(\mathbb{E}^e) \\ \bar{\lambda}_4(M_4 = 1) &= \bar{\lambda}_4(\mathbb{E}^e) \\ \bar{\lambda}_5(M_5 = 1) &= \bar{\lambda}_5(\mathbb{E}^e) \\ \bar{\lambda}_6(M_6 = 1) &= \bar{\lambda}_6(\mathbb{E}^e) \end{aligned} \quad (4.82)$$

are all distinct, i.e., multiplicity one, and the number of modes is six. The distinct projection tensors are computed for any linear combination of the typical Kelvin mode tensors by

$$\begin{aligned}\mathbb{P}_1 &\in \mathbf{N}^d \otimes \mathbf{N}^d \oplus \mathbf{N}_i^e \otimes \mathbf{N}_i^e \oplus \mathbf{N}_i^p \otimes \mathbf{N}_i^p \oplus \mathbf{N}_s^1 \otimes \mathbf{N}_s^1 \oplus \mathbf{N}_2^s \otimes \mathbf{N}_2^s \oplus \mathbf{N}_3^s \otimes \mathbf{N}_3^s \\ \mathbb{P}_2 &\in \mathbf{N}^d \otimes \mathbf{N}^d \oplus \mathbf{N}_i^e \otimes \mathbf{N}_i^e \oplus \mathbf{N}_i^p \otimes \mathbf{N}_i^p \oplus \mathbf{N}_s^1 \otimes \mathbf{N}_s^1 \oplus \mathbf{N}_2^s \otimes \mathbf{N}_2^s \oplus \mathbf{N}_3^s \otimes \mathbf{N}_3^s \\ \mathbb{P}_3 &\in \mathbf{N}^d \otimes \mathbf{N}^d \oplus \mathbf{N}_i^e \otimes \mathbf{N}_i^e \oplus \mathbf{N}_i^p \otimes \mathbf{N}_i^p \oplus \mathbf{N}_s^1 \otimes \mathbf{N}_s^1 \oplus \mathbf{N}_2^s \otimes \mathbf{N}_2^s \oplus \mathbf{N}_3^s \otimes \mathbf{N}_3^s \\ \mathbb{P}_4 &\in \mathbf{N}^d \otimes \mathbf{N}^d \oplus \mathbf{N}_i^e \otimes \mathbf{N}_i^e \oplus \mathbf{N}_i^p \otimes \mathbf{N}_i^p \oplus \mathbf{N}_s^1 \otimes \mathbf{N}_s^1 \oplus \mathbf{N}_2^s \otimes \mathbf{N}_2^s \oplus \mathbf{N}_3^s \otimes \mathbf{N}_3^s \\ \mathbb{P}_5 &\in \mathbf{N}^d \otimes \mathbf{N}^d \oplus \mathbf{N}_i^e \otimes \mathbf{N}_i^e \oplus \mathbf{N}_i^p \otimes \mathbf{N}_i^p \oplus \mathbf{N}_s^1 \otimes \mathbf{N}_s^1 \oplus \mathbf{N}_2^s \otimes \mathbf{N}_2^s \oplus \mathbf{N}_3^s \otimes \mathbf{N}_3^s \\ \mathbb{P}_6 &\in \mathbf{N}^d \otimes \mathbf{N}^d \oplus \mathbf{N}_i^e \otimes \mathbf{N}_i^e \oplus \mathbf{N}_i^p \otimes \mathbf{N}_i^p \oplus \mathbf{N}_s^1 \otimes \mathbf{N}_s^1 \oplus \mathbf{N}_2^s \otimes \mathbf{N}_2^s \oplus \mathbf{N}_3^s \otimes \mathbf{N}_3^s.\end{aligned}\quad (4.83)$$

Since the eigenvalues are all distinct the projection tensors can also be computed with Equation 4.8.

Thus the spectral decomposition of the triclinic tensor consists of the six proper one-dimensional eigenspaces

$$\mathbb{E}^e = \bar{\lambda}_1 \mathbb{P}_1 + \bar{\lambda}_2 \mathbb{P}_2 + \bar{\lambda}_3 \mathbb{P}_3 + \bar{\lambda}_4 \mathbb{P}_4 + \bar{\lambda}_5 \mathbb{P}_5 + \bar{\lambda}_6 \mathbb{P}_6. \quad (4.84)$$

4.4.6 The tetragonal crystal system

Materials which have a tetragonal crystal system include, for example, rutile, zircon, pyrolusite and indium. In Voigt notation, the tetragonal tensor in the \mathbf{e}_1 -direction is defined by the tensor

$$\mathbb{E}^e = \mathbb{E}_{\text{tetragonal}, \mathbf{e}_1}^e = \begin{bmatrix} E_{11} & E_{13} & E_{13} & 0 & 0 & 0 \\ & E_{22} & E_{23} & 0 & 0 & 0 \\ & & E_{22} & 0 & 0 & 0 \\ \text{SYM} & & & E_{66} & 0 & 0 \\ & & & & E_{55} & 0 \\ & & & & & E_{66} \end{bmatrix} \quad (4.85)$$

which has six independent material constants. The number of eigenvalues is equal to five. Four eigenvalues have multiplicity one and one eigenvalue has multiplicity two. The number of modes is also equal to five. The five eigenvalues are

$$\begin{aligned}\bar{\lambda}_1(M_1 = 1) &= E_{11} + \sqrt{2}E_{13}(\tan \alpha + \sec \alpha) \\ \bar{\lambda}_2(M_2 = 1) &= E_{22} - E_{23} \\ \bar{\lambda}_3(M_3 = 1) &= E_{11} + \sqrt{2}E_{13}(\tan \alpha - \sec \alpha) \\ \bar{\lambda}_4(M_4 = 1) &= 2E_{55} \\ \bar{\lambda}_5(M_5 = 2) &= 2E_{66}\end{aligned}\quad (4.86)$$

with

$$\tan \alpha = \frac{\sqrt{2}}{4E_{13}}(E_{22} + E_{23} - E_{11}) \quad (4.87)$$

and

$$\sec \alpha = \sqrt{1 + \tan^2 \alpha}. \quad (4.88)$$

The five projection tensors are expressed as functions of the typical Kelvin modes and two dilatation modes by

$$\begin{aligned}\mathbb{P}_1 &= \mathbf{N}_1^{tetra} \otimes \mathbf{N}_1^{tetra} \\ \mathbb{P}_2 &= \mathbf{N}_1^p \otimes \mathbf{N}_1^p \\ \mathbb{P}_3 &= \mathbf{N}_2^{tetra} \otimes \mathbf{N}_2^{tetra} \\ \mathbb{P}_4 &= \mathbf{N}_1^s \otimes \mathbf{N}_1^s \\ \mathbb{P}_5 &= \mathbf{N}_2^s \otimes \mathbf{N}_2^s + \mathbf{N}_3^s \otimes \mathbf{N}_3^s.\end{aligned}\tag{4.89}$$

The two dilatation modes are computed by taking

$$\mathbf{N}_1^{tetra} = \begin{bmatrix} \frac{1}{2}(1 + \sin \alpha) + \frac{\sqrt{2}}{4} \cos \alpha & 0 & 0 \\ 0 & \frac{\sqrt{2}}{2} \cos \alpha + \frac{1}{2}(1 - \sin \alpha) & 0 \\ 0 & 0 & \frac{\sqrt{2}}{2} \cos \alpha + \frac{1}{2}(1 - \sin \alpha) \end{bmatrix}\tag{4.90}$$

and

$$\mathbf{N}_2^{tetra} = \begin{bmatrix} \frac{1}{2}(1 - \sin \alpha) - \frac{\sqrt{2}}{4} \cos \alpha & 0 & 0 \\ 0 & \frac{-\sqrt{2}}{2} \cos \alpha + \frac{1}{2}(1 + \sin \alpha) & 0 \\ 0 & 0 & \frac{-\sqrt{2}}{2} \cos \alpha + \frac{1}{2}(1 + \sin \alpha) \end{bmatrix}.\tag{4.91}$$

These tensors should be normalised before taking the tensor product in Equation 4.89.

In Voigt notation, the tetragonal tensor in the e_2 -direction is defined by the tensor

$$\mathbb{E}^e = \mathbb{E}_{\text{tetragonal}, e_2}^e = \begin{bmatrix} E_{11} & E_{12} & E_{13} & 0 & 0 & 0 \\ E_{22} & E_{12} & 0 & 0 & 0 & 0 \\ E_{11} & 0 & 0 & 0 & 0 & 0 \\ \text{SYM} & & E_{44} & 0 & 0 & 0 \\ & & & E_{44} & 0 & 0 \\ & & & & E_{66} & \end{bmatrix}\tag{4.92}$$

which has six independent material constants. The number of eigenvalues is equal to five. Four eigenvalues have multiplicity one and one eigenvalue has multiplicity two. The number of modes is also equal to five. The five eigenvalues are

$$\begin{aligned}\bar{\lambda}_1(M_1 = 1) &= E_{22} + \sqrt{2}E_{12}(\tan \alpha + \sec \alpha) \\ \bar{\lambda}_2(M_2 = 1) &= E_{11} - E_{13} \\ \bar{\lambda}_3(M_3 = 1) &= E_{22} + \sqrt{2}E_{12}(\tan \alpha - \sec \alpha) \\ \bar{\lambda}_4(M_4 = 1) &= 2E_{66} \\ \bar{\lambda}_5(M_5 = 2) &= 2E_{44}\end{aligned}\tag{4.93}$$

with

$$\tan \alpha = \frac{\sqrt{2}}{4E_{12}}(E_{11} + E_{13} - E_{22})\tag{4.94}$$

and $\sec \alpha$ from Equation 4.88. The five projection tensors are expressed as functions of the typical Kelvin modes and two dilatation modes by

$$\begin{aligned}\mathbb{P}_1 &= \mathbf{N}_1^{tetra} \otimes \mathbf{N}_1^{tetra} \\ \mathbb{P}_2 &= \mathbf{N}_2^p \otimes \mathbf{N}_2^p \\ \mathbb{P}_3 &= \mathbf{N}_2^{tetra} \otimes \mathbf{N}_2^{tetra} \\ \mathbb{P}_4 &= \mathbf{N}_2^s \otimes \mathbf{N}_2^s \\ \mathbb{P}_5 &= \mathbf{N}_1^s \otimes \mathbf{N}_1^s + \mathbf{N}_3^s \otimes \mathbf{N}_3^s.\end{aligned}\quad (4.95)$$

The two dilatation modes are computed by taking

$$\mathbf{N}_1^{tetra} = \begin{bmatrix} \frac{1}{2}(1 + \sin \alpha) + \frac{\sqrt{2}}{4} \cos \alpha & 0 & 0 \\ 0 & \frac{\sqrt{2}}{2} \cos \alpha + \frac{1}{2}(1 - \sin \alpha) & 0 \\ 0 & 0 & \frac{1}{2}(1 + \sin \alpha) + \frac{\sqrt{2}}{4} \cos \alpha \end{bmatrix} \quad (4.96)$$

and

$$\mathbf{N}_2^{tetra} = \begin{bmatrix} \frac{1}{2}(1 - \sin \alpha) - \frac{\sqrt{2}}{4} \cos \alpha & 0 & 0 \\ 0 & \frac{-\sqrt{2}}{2} \cos \alpha + \frac{1}{2}(1 + \sin \alpha) & 0 \\ 0 & 0 & \frac{1}{2}(1 - \sin \alpha) - \frac{\sqrt{2}}{4} \cos \alpha \end{bmatrix} \quad (4.97)$$

which should be normalised before taking the tensor product in Equation 4.95.

In Voigt notation, the tetragonal tensor in the e_3 -direction is defined by the tensor

$$\mathbb{E}^e = \mathbb{E}_{\text{tetragonal}, e_3}^e = \begin{bmatrix} E_{11} & E_{12} & E_{13} & 0 & 0 & 0 \\ & E_{11} & E_{13} & 0 & 0 & 0 \\ & & E_{33} & 0 & 0 & 0 \\ \text{SYM} & & & E_{44} & 0 & 0 \\ & & & & E_{55} & 0 \\ & & & & & E_{55} \end{bmatrix}. \quad (4.98)$$

The number of eigenvalues is equal to five. Four eigenvalues have multiplicity one and one eigenvalue have multiplicity two. The number of modes is also equal to five. The five eigenvalues are

$$\begin{aligned}\bar{\lambda}_1(M_1 = 1) &= E_{33} + \sqrt{2}E_{13}(\tan \alpha + \sec \alpha) \\ \bar{\lambda}_2(M_2 = 1) &= E_{11} - E_{12} \\ \bar{\lambda}_3(M_3 = 1) &= E_{33} + \sqrt{2}E_{13}(\tan \alpha - \sec \alpha) \\ \bar{\lambda}_4(M_4 = 1) &= 2E_{44} \\ \bar{\lambda}_5(M_5 = 2) &= 2E_{55}\end{aligned}\quad (4.99)$$

with

$$\tan \alpha = \frac{\sqrt{2}}{4E_{13}}(E_{11} + E_{12} - E_{33}) \quad (4.100)$$

and $\sec \alpha$ from Equation 4.88. The five projection tensors are expressed as functions of the typical Kelvin modes and two dilatation modes by

$$\begin{aligned}\mathbb{P}_1 &= \mathbf{N}_1^{tetra} \otimes \mathbf{N}_1^{tetra} \\ \mathbb{P}_2 &= \mathbf{N}_3^p \otimes \mathbf{N}_3^p \\ \mathbb{P}_3 &= \mathbf{N}_2^{tetra} \otimes \mathbf{N}_2^{tetra} \\ \mathbb{P}_4 &= \mathbf{N}_3^s \otimes \mathbf{N}_3^s \\ \mathbb{P}_5 &= \mathbf{N}_1^s \otimes \mathbf{N}_1^s + \mathbf{N}_2^s \otimes \mathbf{N}_2^s.\end{aligned}\tag{4.101}$$

The two dilatation modes are computed by taking

$$\mathbf{N}_1^{tetra} = \begin{bmatrix} \frac{1}{2}(1 + \sin \alpha) + \frac{\sqrt{2}}{4} \cos \alpha & 0 & 0 \\ 0 & \frac{1}{2}(1 + \sin \alpha) + \frac{\sqrt{2}}{4} \cos \alpha & 0 \\ 0 & 0 & \frac{\sqrt{2}}{2} \cos \alpha + \frac{1}{2}(1 - \sin \alpha) \end{bmatrix}\tag{4.102}$$

and

$$\mathbf{N}_2^{tetra} = \begin{bmatrix} \frac{1}{2}(1 - \sin \alpha) - \frac{\sqrt{2}}{4} \cos \alpha & 0 & 0 \\ 0 & \frac{1}{2}(1 - \sin \alpha) - \frac{\sqrt{2}}{4} \cos \alpha & 0 \\ 0 & 0 & \frac{-\sqrt{2}}{2} \cos \alpha + \frac{1}{2}(1 + \sin \alpha) \end{bmatrix}.\tag{4.103}$$

These tensors should be normalised before taking the tensor product in Equation 4.101.

The fourth-order elasticity tensor can be rewritten as

$$\mathbb{E}^e = \bar{\lambda}_1 \mathbb{P}_1 + \bar{\lambda}_2 \mathbb{P}_2 + \bar{\lambda}_3 \mathbb{P}_3 + \bar{\lambda}_4 \mathbb{P}_4 + \bar{\lambda}_5 \mathbb{P}_5.\tag{4.104}$$

4.4.7 The hexagonal crystal system (transverse isotropy)

Materials which have an hexagonal crystal system include, for example, beryll, magnesium, titanium, cobalt, zirconium and zinc. In Voigt notation, the hexagonal tensor in the e_1 -direction is defined by the tensor

$$\mathbb{E}^e = \mathbb{E}_{\text{transverse isotropy}, e_1}^e = \begin{bmatrix} E_{11} & E_{13} & E_{13} & 0 & 0 & 0 \\ & E_{22} & E_{23} & 0 & 0 & 0 \\ & & E_{22} & 0 & 0 & 0 \\ \text{SYM} & & & E_{66} & 0 & 0 \\ & & & & \frac{1}{2}(E_{22} - E_{23}) & 0 \\ & & & & & E_{66} \end{bmatrix}\tag{4.105}$$

which has five independent material constants. The number of modes is four. Two eigenvalues have multiplicity two. They have the same form as in Equation 4.86. The two last eigenvalues have multiplicity one. The four eigenvalues are thus defined by

$$\begin{aligned}\bar{\lambda}_1(M_1 = 1) &= E_{11} + \sqrt{2}E_{13}(\tan \alpha + \sec \alpha) \\ \bar{\lambda}_2(M_2 = 2) &= E_{22} - E_{23} \\ \bar{\lambda}_3(M_3 = 1) &= E_{11} + \sqrt{2}E_{13}(\tan \alpha - \sec \alpha) \\ \bar{\lambda}_4(M_4 = 2) &= 2E_{66}\end{aligned}\quad (4.106)$$

with

$$\tan \alpha = \frac{\sqrt{2}}{4E_{13}}(E_{22} + E_{23} - E_{11}) \quad (4.107)$$

and $\sec \alpha$ from Equation 4.88. The five projection tensors are expressed as functions of the typical Kelvin modes and two dilatation modes by

$$\begin{aligned}\mathbb{P}_1 &= \mathbf{N}_1^{hexa} \otimes \mathbf{N}_1^{hexa} \\ \mathbb{P}_2 &= \mathbf{N}_1^p \otimes \mathbf{N}_1^p + \mathbf{N}_1^s \otimes \mathbf{N}_1^s \\ \mathbb{P}_3 &= \mathbf{N}_2^{hexa} \otimes \mathbf{N}_2^{hexa} \\ \mathbb{P}_4 &= \mathbf{N}_2^s \otimes \mathbf{N}_2^s + \mathbf{N}_3^s \otimes \mathbf{N}_3^s.\end{aligned}\quad (4.108)$$

The two dilatation modes are computed by taking

$$\mathbf{N}_1^{hexa} = \begin{bmatrix} \frac{1}{2}(1 + \sin \alpha) + \frac{\sqrt{2}}{4} \cos \alpha & 0 & 0 \\ 0 & \frac{\sqrt{2}}{2} \cos \alpha + \frac{1}{2}(1 - \sin \alpha) & 0 \\ 0 & 0 & \frac{\sqrt{2}}{2} \cos \alpha + \frac{1}{2}(1 - \sin \alpha) \end{bmatrix} \quad (4.109)$$

and

$$\mathbf{N}_2^{hexa} = \begin{bmatrix} \frac{1}{2}(1 - \sin \alpha) - \frac{\sqrt{2}}{4} \cos \alpha & 0 & 0 \\ 0 & -\frac{\sqrt{2}}{2} \cos \alpha + \frac{1}{2}(1 + \sin \alpha) & 0 \\ 0 & 0 & -\frac{\sqrt{2}}{2} \cos \alpha + \frac{1}{2}(1 + \sin \alpha) \end{bmatrix}. \quad (4.110)$$

These tensors should be normalised before taking the tensor product in Equation 4.108.

In Voigt notation, the hexagonal tensor in the e_2 -direction is defined by the tensor

$$\mathbb{E}^e = \mathbb{E}_{\text{transverse isotropy}, e_2}^e = \begin{bmatrix} E_{11} & E_{12} & E_{13} & 0 & 0 & 0 \\ E_{22} & E_{22} & 0 & 0 & 0 & 0 \\ E_{11} & 0 & 0 & 0 & 0 & 0 \\ \text{SYM} & & E_{44} & 0 & 0 & 0 \\ & & & E_{44} & 0 & 0 \\ & & & & \frac{1}{2}(E_{11} - E_{13}) & \end{bmatrix} \quad (4.111)$$

with five independent material constants. The number of modes is four. Two eigenvalues have multiplicity two and two eigenvalues have multiplicity one. They have the same form as in Equation 4.93. The four eigenvalues are thus defined by

$$\begin{aligned}\bar{\lambda}_1(M_1 = 1) &= E_{22} + \sqrt{2}E_{12}(\tan \alpha + \sec \alpha) \\ \bar{\lambda}_2(M_2 = 2) &= E_{11} - E_{13} \\ \bar{\lambda}_3(M_3 = 1) &= E_{22} + \sqrt{2}E_{12}(\tan \alpha - \sec \alpha) \\ \bar{\lambda}_4(M_4 = 2) &= 2E_{12}\end{aligned}\quad (4.112)$$

with

$$\tan \alpha = \frac{\sqrt{2}}{4E_{12}}(E_{11} + E_{13} - E_{22}) \quad (4.113)$$

and $\sec \alpha$ from Equation 4.88. The projection tensor can be expressed as a function of the typical Kelvin modes and two dilatation modes by

$$\begin{aligned}\mathbb{P}_1 &= \mathbf{N}_1^{hexa} \otimes \mathbf{N}_1^{hexa} \\ \mathbb{P}_2 &= \mathbf{N}_2^p \otimes \mathbf{N}_2^p + \mathbf{N}_2^s \otimes \mathbf{N}_2^s \\ \mathbb{P}_3 &= \mathbf{N}_2^{hexa} \otimes \mathbf{N}_2^{hexa} \\ \mathbb{P}_4 &= \mathbf{N}_1^s \otimes \mathbf{N}_1^s + \mathbf{N}_3^s \otimes \mathbf{N}_3^s.\end{aligned}\quad (4.114)$$

The two dilatation modes are computed by taking

$$\mathbf{N}_1^{hexa} = \begin{bmatrix} \frac{1}{2}(1 + \sin \alpha) + \frac{\sqrt{2}}{4} \cos \alpha & 0 & 0 \\ 0 & \frac{\sqrt{2}}{2} \cos \alpha + \frac{1}{2}(1 - \sin \alpha) & 0 \\ 0 & 0 & \frac{1}{2}(1 + \sin \alpha) + \frac{\sqrt{2}}{4} \cos \alpha \end{bmatrix} \quad (4.115)$$

and

$$\mathbf{N}_2^{hexa} = \begin{bmatrix} \frac{1}{2}(1 - \sin \alpha) - \frac{\sqrt{2}}{4} \cos \alpha & 0 & 0 \\ 0 & -\frac{\sqrt{2}}{2} \cos \alpha + \frac{1}{2}(1 + \sin \alpha) & 0 \\ 0 & 0 & \frac{1}{2}(1 - \sin \alpha) - \frac{\sqrt{2}}{4} \cos \alpha \end{bmatrix}. \quad (4.116)$$

These tensors should be normalised before taking the tensor product in Equation 4.114.

In Voigt notation, the hexagonal tensor in the e_3 -direction is defined by the tensor

$$\mathbb{E}^e = \mathbb{E}_{\text{transverse isotropy}, e_3}^e = \begin{bmatrix} E_{11} & E_{12} & E_{13} & 0 & 0 & 0 \\ E_{11} & E_{13} & 0 & 0 & 0 & 0 \\ E_{33} & 0 & 0 & 0 & 0 & 0 \\ \text{SYM} & \frac{1}{2}(E_{11} - E_{12}) & 0 & 0 & 0 & 0 \\ & & E_{55} & 0 & 0 & 0 \\ & & & E_{55} & 0 & 0 \end{bmatrix} \quad (4.117)$$

with five independent material constants. The number of modes is four. Two eigenvalues have multiplicity two and two eigenvalues have multiplicity one. They have the same form as in Equation 4.99. The four eigenvalues are thus defined by

$$\begin{aligned}\bar{\lambda}_1(M_1 = 1) &= E_{33} + \sqrt{2}E_{13}(\tan \alpha + \sec \alpha) \\ \bar{\lambda}_2(M_2 = 2) &= E_{11} - E_{12} \\ \bar{\lambda}_3(M_3 = 1) &= E_{33} + \sqrt{2}E_{13}(\tan \alpha - \sec \alpha) \\ \bar{\lambda}_4(M_4 = 2) &= 2E_{55}\end{aligned}\quad (4.118)$$

with

$$\tan \alpha = \frac{\sqrt{2}}{4E_{13}}(E_{11} + E_{12} - E_{33}) \quad (4.119)$$

and $\sec \alpha$ from Equation 4.88. The projection tensor can be expressed as a function of the typical Kelvin modes and two dilatation modes by

$$\begin{aligned}\mathbb{P}_1 &= \mathbf{N}_1^{hexa} \otimes \mathbf{N}_1^{hexa} \\ \mathbb{P}_2 &= \mathbf{N}_3^p \otimes \mathbf{N}_3^p + \mathbf{N}_3^s \otimes \mathbf{N}_3^s \\ \mathbb{P}_3 &= \mathbf{N}_2^{hexa} \otimes \mathbf{N}_2^{hexa} \\ \mathbb{P}_4 &= \mathbf{N}_1^s \otimes \mathbf{N}_1^s + \mathbf{N}_2^s \otimes \mathbf{N}_2^s.\end{aligned}\quad (4.120)$$

The two dilatation modes are

$$\mathbf{N}_1^{hexa} = \begin{bmatrix} \frac{1}{2}(1 + \sin \alpha) + \frac{\sqrt{2}}{4} \cos \alpha & 0 & 0 \\ 0 & \frac{1}{2}(1 + \sin \alpha) + \frac{\sqrt{2}}{4} \cos \alpha & 0 \\ 0 & 0 & \frac{\sqrt{2}}{2} \cos \alpha + \frac{1}{2}(1 - \sin \alpha) \end{bmatrix} \quad (4.121)$$

and

$$\mathbf{N}_2^{hexa} = \begin{bmatrix} \frac{1}{2}(1 - \sin \alpha) - \frac{\sqrt{2}}{4} \cos \alpha & 0 & 0 \\ 0 & \frac{1}{2}(1 - \sin \alpha) - \frac{\sqrt{2}}{4} \cos \alpha & 0 \\ 0 & 0 & -\frac{\sqrt{2}}{2} \cos \alpha + \frac{1}{2}(1 + \sin \alpha) \end{bmatrix}. \quad (4.122)$$

These tensors should be normalised before taking the tensor product in Equation 4.120. The fourth-order elasticity tensor can be rewritten as

$$\mathbb{E}^e = \bar{\lambda}_1 \mathbb{P}_1 + \bar{\lambda}_2 \mathbb{P}_2 + \bar{\lambda}_3 \mathbb{P}_3 + \bar{\lambda}_4 \mathbb{P}_4. \quad (4.123)$$

Remark:

- It can be easily seen that there are similarities between the metals with cubic, hexagonal and tetragonal crystal systems.
- Table 4.2 summarises the decomposition of the elasticity tensor into Kelvin modes for isotropic materials and the seven crystal systems.

4.4.8 A numerical example

According to Sutcliffe [24], cobalt has the following material parameters in Voigt notation

$$\mathbb{E}^e = \begin{bmatrix} 30.7 & 16.5 & 10.27 & 0 & 0 & 0 \\ 16.5 & 30.7 & 10.27 & 0 & 0 & 0 \\ 10.27 & 10.27 & 35.81 & 0 & 0 & 0 \\ 0 & 0 & 0 & 7.1 & 0 & 0 \\ 0 & 0 & 0 & 0 & 7.55 & 0 \\ 0 & 0 & 0 & 0 & 0 & 7.55 \end{bmatrix}. \quad (4.124)$$

The cobalt matrix correspond to the hexagonal tensor in the \mathbf{e}_3 -direction. Thus the four eigenvalues are

$$\begin{aligned} \bar{\lambda}_1(M_1 = 1) &= E_{33} + \sqrt{2}E_{13}(\tan \alpha + \sec \alpha) \\ &= 35.81 + \sqrt{2} * 10.27 * (0.39211 + 1.07413) \\ &= 57.10563 \\ \bar{\lambda}_2(M_2 = 2) &= E_{11} - E_{12} = 30.7 - 16.5 = 14.2 \\ \bar{\lambda}_3(M_3 = 1) &= E_{33} + \sqrt{2}E_{13}(\tan \alpha - \sec \alpha) \\ &= 35.81 + \sqrt{2} * 10.27 * (0.39211 - 1.07413) \\ &= 25.90436 \\ \bar{\lambda}_4(M_4 = 2) &= 2E_{55} = 2 * 7.55 = 15.1 \end{aligned} \quad (4.125)$$

with

$$\tan \alpha = \frac{\sqrt{2}}{4E_{13}}(E_{11} + E_{12} - E_{33}) = \frac{\sqrt{2}}{4 * 10.27}(30.7 + 16.5 - 35.81) = 0.39211 \quad (4.126)$$

and

$$\sec \alpha = \sqrt{1 + \tan^2 \alpha} = 1.07413. \quad (4.127)$$

The corresponding eigentensors are

$$\begin{aligned} \mathbb{P}_1 &= \mathbf{N}_1^{hexa} \otimes \mathbf{N}_1^{hexa} \\ \mathbb{P}_2 &= \mathbf{N}_3^p \otimes \mathbf{N}_3^p + \mathbf{N}_3^s \otimes \mathbf{N}_3^s \\ \mathbb{P}_3 &= \mathbf{N}_2^{hexa} \otimes \mathbf{N}_2^{hexa} \\ \mathbb{P}_4 &= \mathbf{N}_1^s \otimes \mathbf{N}_1^s + \mathbf{N}_2^s \otimes \mathbf{N}_2^s. \end{aligned} \quad (4.128)$$

with \mathbf{N}_3^p , \mathbf{N}_1^s , \mathbf{N}_2^s , and \mathbf{N}_3^s from Equation 4.18, Equation 4.19, Equation 4.20, and Equation 4.21, respectively. The two dilatation modes \mathbf{N}_1^{hexa} and \mathbf{N}_2^{hexa} in Equation 4.128 are equal to

$$\mathbf{N}_1^{hexa} = \begin{bmatrix} 1.01168 & 0 & 0 \\ 0 & 1.01168 & 0 \\ 0 & 0 & 0.97578 \end{bmatrix} \quad (4.129)$$

and

$$\mathbf{N}_2^{hexa} = \begin{bmatrix} -0.01168 & 0 & 0 \\ 0 & -0.01168 & 0 \\ 0 & 0 & 0.02422 \end{bmatrix}, \quad (4.130)$$

where

$$\sin \alpha = \frac{\tan \alpha}{\sec \alpha} = \frac{0.39211}{1.07413} = 0.36505 \quad (4.131)$$

and

$$\cos \alpha = \frac{1}{\sec \alpha} = \frac{1}{1.07413} = 0.93099. \quad (4.132)$$

Before taking the tensor product in Equation 4.128, \mathbf{N}_1^{hexa} and \mathbf{N}_2^{hexa} should be normalised. Thus

$$\mathbf{N}_1^{hexa} = \begin{bmatrix} 0.58417 & 0 & 0 \\ 0 & 0.58417 & 0 \\ 0 & 0 & 0.56345 \end{bmatrix} \quad (4.133)$$

and

$$\mathbf{N}_2^{hexa} = \begin{bmatrix} -0.39841 & 0 & 0 \\ 0 & -0.39841 & 0 \\ 0 & 0 & 0.82616 \end{bmatrix}. \quad (4.134)$$

The eigenvalues and eigentensors which correspond to it can be found in Sutcliffe [24].

material	nb _{mode}	deg _{multiplicity}	Eigenvalues	Tensor bases
isotropic	2	1	$\lambda_1 = 3\kappa$	$\mathbb{P}_1 : \mathbf{N}^d$
		5	$\lambda_2 = 2\mu$	$\mathbb{P}_2 : \mathbf{N}_i^e, \mathbf{N}_i^p, \mathbf{N}_1^s, \mathbf{N}_2^s, \mathbf{N}_3^s$
cubic	3	1	$\lambda_1 = 3\kappa$	$\mathbb{P}_1 : \mathbf{N}^d$
		2	$\lambda_2 = 2\mu$	$\mathbb{P}_2 : \mathbf{N}_i^e, \mathbf{N}_i^p$
		3	$\lambda_3 = 2E_{55}$	$\mathbb{P}_3 : \mathbf{N}_1^s, \mathbf{N}_2^s, \mathbf{N}_3^s$
orthorhombic	6	1	$\bar{\lambda}_1(\mathbb{E}^e)$	$\mathbb{P}_1 : \mathbf{N}_1^{ortho}$
		1	$\bar{\lambda}_2(\mathbb{E}^e)$	$\mathbb{P}_2 : \mathbf{N}_2^{ortho}$
		1	$\bar{\lambda}_3(\mathbb{E}^e)$	$\mathbb{P}_3 : \mathbf{N}_3^{ortho}$
		1	$\bar{\lambda}_4 = 2E_{44}$	$\mathbb{P}_4 : \mathbf{N}_3^s$
		1	$\bar{\lambda}_5 = 2E_{55}$	$\mathbb{P}_5 : \mathbf{N}_1^s$
		1	$\bar{\lambda}_6 = 2E_{66}$	$\mathbb{P}_6 : \mathbf{N}_2^s$
trigonal(e_3)	6	1	$\bar{\lambda}_1(\mathbb{E}^e)$	$\mathbb{P}_1 : \mathbf{N}^d, \mathbf{N}_i^e, \mathbf{N}_i^p, \mathbf{N}_3^s$
		1	$\bar{\lambda}_2(\mathbb{E}^e)$	$\mathbb{P}_2 : \mathbf{N}^d, \mathbf{N}_i^e, \mathbf{N}_i^p, \mathbf{N}_3^s$
		1	$\bar{\lambda}_3(\mathbb{E}^e)$	$\mathbb{P}_3 : \mathbf{N}^d, \mathbf{N}_i^e, \mathbf{N}_i^p, \mathbf{N}_3^s$
		1	$\bar{\lambda}_4(\mathbb{E}^e)$	$\mathbb{P}_4 : \mathbf{N}^d, \mathbf{N}_i^e, \mathbf{N}_i^p, \mathbf{N}_3^s$
		1	$\bar{\lambda}_5(\mathbb{E}^e)$	$\mathbb{P}_5 : \mathbf{N}_1^s, \mathbf{N}_2^s$
		1	$\bar{\lambda}_6(\mathbb{E}^e)$	$\mathbb{P}_6 : \mathbf{N}_1^s, \mathbf{N}_2^s$
monoclinic(e_1)	6	1	$\bar{\lambda}_1(\mathbb{E}^e)$	$\mathbb{P}_1 : \mathbf{N}^d, \mathbf{N}_i^e, \mathbf{N}_i^p, \mathbf{N}_1^s$
		1	$\bar{\lambda}_2(\mathbb{E}^e)$	$\mathbb{P}_2 : \mathbf{N}^d, \mathbf{N}_i^e, \mathbf{N}_i^p, \mathbf{N}_1^s$
		1	$\bar{\lambda}_3(\mathbb{E}^e)$	$\mathbb{P}_3 : \mathbf{N}^d, \mathbf{N}_i^e, \mathbf{N}_i^p, \mathbf{N}_1^s$
		1	$\bar{\lambda}_4(\mathbb{E}^e)$	$\mathbb{P}_4 : \mathbf{N}^d, \mathbf{N}_i^e, \mathbf{N}_i^p, \mathbf{N}_1^s$
		1	$\bar{\lambda}_5(\mathbb{E}^e)$	$\mathbb{P}_5 : \mathbf{N}_2^s, \mathbf{N}_3^s$
		1	$\bar{\lambda}_6(\mathbb{E}^e)$	$\mathbb{P}_6 : \mathbf{N}_2^s, \mathbf{N}_3^s$
triclinic	6	1	$\bar{\lambda}_1(\mathbb{E}^e)$	$\mathbb{P}_1 : \mathbf{N}^d, \mathbf{N}_i^e, \mathbf{N}_i^p, \mathbf{N}_1^s, \mathbf{N}_2^s, \mathbf{N}_3^s$
		1	$\bar{\lambda}_2(\mathbb{E}^e)$	$\mathbb{P}_2 : \mathbf{N}^d, \mathbf{N}_i^e, \mathbf{N}_i^p, \mathbf{N}_1^s, \mathbf{N}_2^s, \mathbf{N}_3^s$
		1	$\bar{\lambda}_3(\mathbb{E}^e)$	$\mathbb{P}_3 : \mathbf{N}^d, \mathbf{N}_i^e, \mathbf{N}_i^p, \mathbf{N}_1^s, \mathbf{N}_2^s, \mathbf{N}_3^s$
		1	$\bar{\lambda}_4(\mathbb{E}^e)$	$\mathbb{P}_4 : \mathbf{N}^d, \mathbf{N}_i^e, \mathbf{N}_i^p, \mathbf{N}_1^s, \mathbf{N}_2^s, \mathbf{N}_3^s$
		1	$\bar{\lambda}_5(\mathbb{E}^e)$	$\mathbb{P}_5 : \mathbf{N}^d, \mathbf{N}_i^e, \mathbf{N}_i^p, \mathbf{N}_1^s, \mathbf{N}_2^s, \mathbf{N}_3^s$
		1	$\bar{\lambda}_6(\mathbb{E}^e)$	$\mathbb{P}_6 : \mathbf{N}^d, \mathbf{N}_i^e, \mathbf{N}_i^p, \mathbf{N}_1^s, \mathbf{N}_2^s, \mathbf{N}_3^s$
tetragonal(e_1)	5	1	$\bar{\lambda}_1 = E_{11} + \sqrt{2} E_{13}(\tan \alpha + \sec \alpha)$	$\mathbb{P}_1 : \mathbf{N}_1^{tetra}$
		1	$\bar{\lambda}_2 = E_{22} - E_{23}$	$\mathbb{P}_2 : \mathbf{N}_1^p$
		1	$\bar{\lambda}_3 = E_{11} + \sqrt{2} E_{13}(\tan \alpha - \sec \alpha)$	$\mathbb{P}_3 : \mathbf{N}_2^{tetra}$
		1	$\bar{\lambda}_4 = 2E_{55}$	$\mathbb{P}_4 : \mathbf{N}_1^s$
		2	$\bar{\lambda}_5 = 2E_{66}$	$\mathbb{P}_5 : \mathbf{N}_2^s, \mathbf{N}_3^s$
hexagonal(e_1)	4	1	$\bar{\lambda}_1 = E_{11} + \sqrt{2} E_{13}(\tan \alpha + \sec \alpha)$	$\mathbb{P}_1 : \mathbf{N}_1^{hexa}$
		2	$\bar{\lambda}_2 = E_{22} - E_{23}$	$\mathbb{P}_2 : \mathbf{N}_1^p, \mathbf{N}_1^s$
		1	$\bar{\lambda}_3 = E_{11} + \sqrt{2} E_{13}(\tan \alpha - \sec \alpha)$	$\mathbb{P}_3 : \mathbf{N}_2^{hexa}$
		2	$\bar{\lambda}_4 = 2E_{66}$	$\mathbb{P}_4 : \mathbf{N}_2^s, \mathbf{N}_3^s$

Table 4.2: Decomposition of the elasticity tensor into Kelvin modes.

Determining the deformed shape from equilibrium

This chapter deals with the determination of the deformed shape of a functional component from the equilibrium equation. Within this chapter, the Piola formulation for the equilibrium is first presented by using the definition of the boundary value problem in the material configuration. This allows finding the deformed configuration of a body when the surface traction and boundary values are given. This formulation is subsequently referred to as the direct mechanical problem. An analytical solution of this nonlinear boundary value problem is only possible for some trivial problems. Therefore the finite element method is used in order to achieve approximated solutions. A large amount of literature is available on the finite element method, see, for example, de Souza Neto et al. [16], Simo et al. [29], Wriggers [72], Hughes [89], and Zienkiewicz et al. [90]. The essentials in establishing finite element formulations are the linearisation of the weak form of the boundary value problem in the material configuration and the corresponding discretisation, as in Bonet et al. [19]. In this chapter, the Newton–Raphson method is used for solving the obtained nonlinear system of equations and is then presented following de Souza Neto et al. [16], Bonet et al. [19], and Wriggers [72]. From now on, the distributed body forces and inertia will be omitted, and the acceleration is assumed to vanish. Numerical examples for isotropic and anisotropic hyperelastic materials as well as for elastoplastic materials will illustrate the previous developments, where the macroscopic constitutive model in the logarithmic strain space presented in Chapter 3 will be used. The fourth-order elastic tensor is decomposed into Kelvin modes according to Chapter 4. Parts of this chapter have been published by Germain et al. in [13, 57, 68].

5.1 The direct mechanical problem

The nonlinear direct deformation map $\varphi = \varphi(\mathbf{X})$ in Equation 2.3 is determined for the given material coordinates \mathbf{X} by the requirement of equilibrium as embodied in the boundary value problem

$$\begin{aligned} \text{Div}(\mathbf{P}) &= \mathbf{0} \quad \text{in } \mathcal{B}_0 \quad (\text{Eq. 2.49}), \\ \mathbf{P} \cdot \mathbf{N} &= \overline{\mathbf{T}} \quad \text{on } \partial\mathcal{B}_0^{\overline{\mathbf{T}}} \quad (\text{Eq. 2.41}), \\ \varphi &= \overline{\varphi} \quad \text{on } \partial\mathcal{B}_0^{\overline{\varphi}}. \end{aligned} \tag{5.1}$$

In this boundary value problem, $\overline{\mathbf{T}}$ is a given traction per unit area in the material configuration (Neumann type boundary condition) and $\overline{\varphi}$ is a given boundary deformation (Dirichlet type boundary condition) (Fig. 2.1). Note that the first Piola–Kirchhoff tensor \mathbf{P} can also be

expressed as a function of the deformation gradient \mathbf{F} and the second Piola–Kirchhoff tensor \mathbf{S} by

$$\mathbf{P} = \mathbf{F} \cdot \mathbf{S}. \quad (5.2)$$

Furthermore note that the Neumann boundary conditions are identified physically with the surface traction. In order to impose the principle of virtual work in the material configuration, also denoted as the weak form, the equation of motion (Eq. 2.49) is multiplied with an arbitrary vector-valued function or test function or weighting function, $\boldsymbol{\eta} \in \mathcal{V} = \{\boldsymbol{\eta} \mid \boldsymbol{\eta} = \mathbf{0} \text{ on } \partial\mathcal{B}_0^{\overline{\varphi}}\}$. The weak form of the given boundary value problem, with the test function, is thus given by

$$\mathbf{G}(\boldsymbol{\varphi}, \boldsymbol{\eta}; \mathbf{X}) = \int_{\mathcal{B}_0} \boldsymbol{\eta} \cdot \operatorname{Div}(\mathbf{P}) \, dV = \mathbf{0} \quad \forall \boldsymbol{\eta} \in \mathcal{V}. \quad (5.3)$$

Using the product rule for the divergence, the weak form becomes

$$\mathbf{G}(\boldsymbol{\varphi}, \boldsymbol{\eta}; \mathbf{X}) = \int_{\mathcal{B}_0} \operatorname{Div}(\boldsymbol{\eta} \cdot \mathbf{P}) \, dV - \int_{\mathcal{B}_0} \operatorname{Grad}\boldsymbol{\eta} : \mathbf{P} \, dV = \mathbf{0}. \quad (5.4)$$

Applying the divergence theorem to the first term of the previous equation, it follows that

$$\mathbf{G}(\boldsymbol{\varphi}, \boldsymbol{\eta}; \mathbf{X}) = \int_{\partial\mathcal{B}_0^{\overline{\varphi}}} \boldsymbol{\eta} \cdot \mathbf{P} \cdot \mathbf{N} \, dA - \int_{\mathcal{B}_0} \operatorname{Grad}\boldsymbol{\eta} : \mathbf{P} \, dV = \mathbf{0}. \quad (5.5)$$

With the definition of the surface traction in the material configuration in Equation 2.41, the weak form is assumed to satisfy

$$\mathbf{G}(\boldsymbol{\varphi}, \boldsymbol{\eta}; \mathbf{X}) = \int_{\partial\mathcal{B}_0^{\overline{\varphi}}} \boldsymbol{\eta} \cdot \overline{\mathbf{T}} \, dA - \int_{\mathcal{B}_0} \operatorname{Grad}\boldsymbol{\eta} : \mathbf{P} \, dV = \mathbf{0}. \quad (5.6)$$

Regarding the test function as a virtual field $\delta\mathbf{x}$, since $\boldsymbol{\eta}$ is chosen arbitrarily, the weak form of the boundary value problem leads to the principle of virtual work

$$\delta W_{ext} - \delta W_{int} = \mathbf{0}, \quad (5.7)$$

where

$$\delta W_{ext} = \int_{\partial\mathcal{B}_0^{\overline{\varphi}}} \delta\mathbf{x} \cdot \overline{\mathbf{T}} \, dA = \int_{\partial\mathcal{B}_0^{\overline{\varphi}}} \boldsymbol{\eta} \cdot \overline{\mathbf{T}} \, dA \quad (5.8)$$

and

$$\delta W_{int} = \int_{\mathcal{B}_0} \operatorname{Grad}\delta\mathbf{x} : \mathbf{P} \, dV = \int_{\mathcal{B}_0} \operatorname{Grad}\boldsymbol{\eta} : \mathbf{P} \, dV. \quad (5.9)$$

Note that in Equation 5.6 the common virtual work statement has a parametrisation of all quantities in the given material coordinates \mathbf{X} .

5.2 Finite element analysis

The determination of the deformed configuration of a continuous body is carried out by a finite element analysis (FEA), i.e., the finite element method (FEM). A large amount of books on FEM have been published in the last decades, see for example de Souza Neto et al. [16], Wriggers [72], Hughes [89], and Zienkiewicz et al. [90]. The continuous body is first discretised, i.e.,

transformed into discrete parts, into n_{el} elements (Fig. 5.1 and Fig. 5.2). The weak form becomes thereby a nonlinear system of equations, which is solved by the Newton–Raphson method. A linearisation of the weak form (Eq. 5.6) gives the needed tangent stiffness matrix.

Remark: From now on, $[\cdot]^e$ refers to **element** and should not be confused with $[\cdot]^e$ in Chapter 3, which indicated **elastic** behaviour.

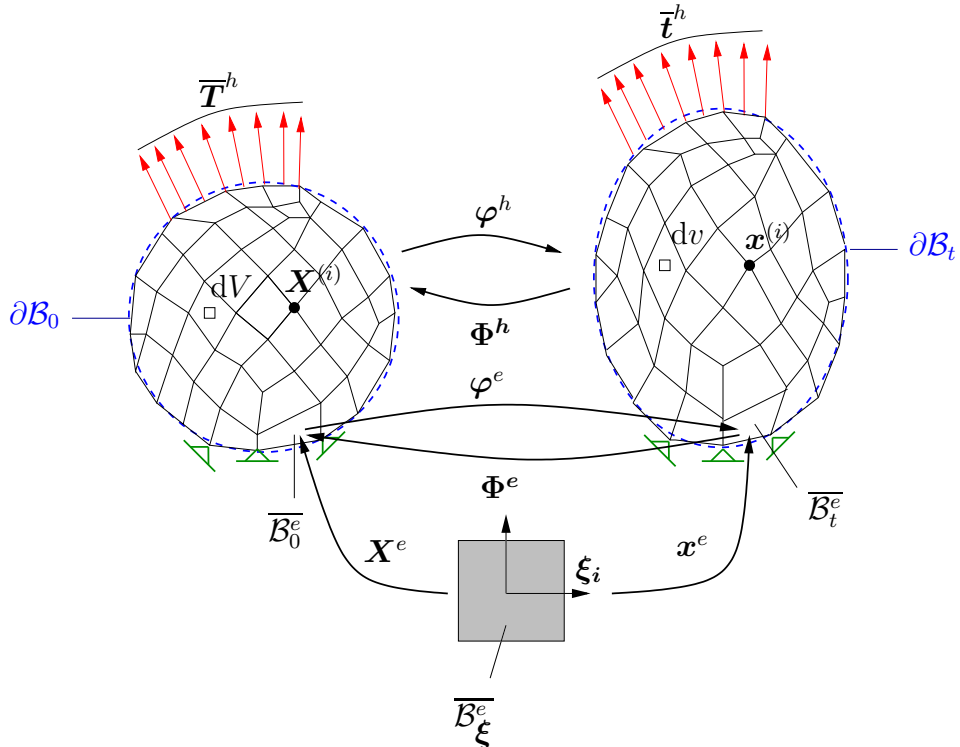


Figure 5.1: Discretisation of the material (right) and spatial (left) configurations.

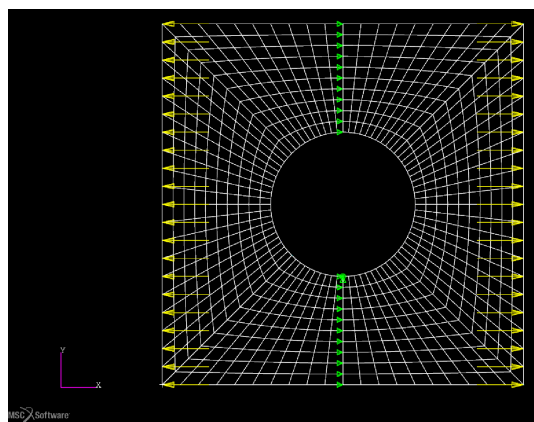


Figure 5.2: Discretisation of a body in the material configuration with MSC.Patran2010.2.

5.2.1 Discretisation

For the finite element solution of the boundary value problem (Eq. 5.1) the material and spatial domains \mathcal{B}_0 and \mathcal{B}_t are discretised into n_{el} elements as in Germain et al. [13], Scherer [66], and Wriggers [72], using

$$\mathcal{B}_0 \approx \mathcal{B}_0^h = \bigcup_{e=1}^{n_{el}} \mathcal{B}_0^e \quad \text{and} \quad \mathcal{B}_t \approx \mathcal{B}_t^h = \bigcup_{e=1}^{n_{el}} \mathcal{B}_t^e. \quad (5.10)$$

Following the standard isoparametric approach, both the geometry and the deformation maps are approximated on each element by the same shape functions

$$\begin{aligned} \mathbf{X}^e(\boldsymbol{\xi}) &= \sum_{i=1}^{n_{en}} \mathbf{X}^{(i)} N^{(i)}(\boldsymbol{\xi}), & \Phi^e(\boldsymbol{\xi}) &= \sum_{i=1}^{n_{en}} \Phi^{(i)} N^{(i)}(\boldsymbol{\xi}), \\ \mathbf{x}^e(\boldsymbol{\xi}) &= \sum_{i=1}^{n_{en}} \mathbf{x}^{(i)} N^{(i)}(\boldsymbol{\xi}), & \varphi^e(\boldsymbol{\xi}) &= \sum_{i=1}^{n_{en}} \varphi^{(i)} N^{(i)}(\boldsymbol{\xi}). \end{aligned} \quad (5.11)$$

Furthermore the shape functions $N^{(i)}$ are parametrised by isoparametric coordinates $\boldsymbol{\xi}$ defined on the isoparametric cube $\mathcal{B}\boldsymbol{\xi} = [-1, 1]^3$, where n_{en} is the total number of nodes per element, and $\mathbf{X}^{(i)} = \Phi^{(i)}$ and $\mathbf{x}^{(i)} = \varphi^{(i)}$ denote nodal values. Finally, using the Bubnov–Galerkin method, the test function is again approximated by the same shape functions $N^{(i)}$

$$\boldsymbol{\eta}^e(\boldsymbol{\xi}) = \sum_{i=1}^{n_{en}} \boldsymbol{\eta}^{(i)} N^{(i)}(\boldsymbol{\xi}). \quad (5.12)$$

The gradients of the test function in the material and spatial configurations become

$$\text{Grad}\boldsymbol{\eta}^e(\boldsymbol{\xi}) = \sum_{i=1}^{n_{en}} \boldsymbol{\eta}^{(i)} \otimes \text{Grad}N^{(i)}(\boldsymbol{\xi}) \quad (5.13)$$

and

$$\text{grad}\boldsymbol{\eta}^e(\boldsymbol{\xi}) = \sum_{i=1}^{n_{en}} \boldsymbol{\eta}^{(i)} \otimes \text{grad}N^{(i)}(\boldsymbol{\xi}). \quad (5.14)$$

Substituting the finite element approximations in the weak form (Eq. 5.6), the discrete equilibrium condition is obtained

$$\begin{aligned} \bigcup_{e=1}^{n_{el}} \mathbf{G}(\varphi^e, \boldsymbol{\eta}^e; \mathbf{X}^e) &= \bigcup_{e=1}^{n_{el}} \left[\int_{\partial\mathcal{B}_0^{\bar{T}, e}} \boldsymbol{\eta}^e \cdot \bar{\mathbf{T}} \, dA - \int_{\mathcal{B}_0^e} \text{Grad}\boldsymbol{\eta}^e : \mathbf{P} \, dV \right] = \mathbf{0} \\ &= \bigcup_{e=1}^{n_{el}} \left[\int_{\partial\mathcal{B}_0^{\bar{T}, e}} \sum_{i=1}^{n_{en}} \boldsymbol{\eta}^{(i)} N^{(i)} \cdot \bar{\mathbf{T}} \, dA - \int_{\mathcal{B}_0^e} \sum_{i=1}^{n_{en}} \boldsymbol{\eta}^{(i)} \otimes \text{Grad}N^{(i)} : \mathbf{P} \, dV \right]. \end{aligned} \quad (5.15)$$

According to tensor algebra (Gonzales et al. [71]),

$$(\mathbf{a} \otimes \mathbf{b}) : \mathbf{C} = \mathbf{a} \cdot \mathbf{C} \cdot \mathbf{b} = \mathbf{C} : (\mathbf{a} \otimes \mathbf{b}), \quad (5.16)$$

where \mathbf{a} and \mathbf{b} are vectors and \mathbf{C} a second-order tensor, and so

$$\begin{aligned} \bigcup_{e=1}^{n_{el}} \mathbf{G}(\boldsymbol{\varphi}^e, \boldsymbol{\eta}^e; \mathbf{X}^e) &= \bigcup_{e=1}^{n_{el}} \left[\int_{\partial B_0^{\bar{\mathbf{T}}, e}} \sum_{i=1}^{n_{en}} \boldsymbol{\eta}^{(i)} N^{(i)} \cdot \bar{\mathbf{T}} \, dA - \int_{B_0^e} \sum_{i=1}^{n_{en}} \boldsymbol{\eta}^{(i)} \cdot \mathbf{P} \cdot \text{Grad}N^{(i)} \, dV \right] \\ &= \bigcup_{e=1}^{n_{el}} \sum_{i=1}^{n_{en}} \boldsymbol{\eta}^{(i)} \left[\int_{\partial B_0^{\bar{\mathbf{T}}, e}} N^{(i)} \bar{\mathbf{T}} \, dA - \int_{B_0^e} \mathbf{P} \cdot \text{Grad}N^{(i)} \, dV \right] = \mathbf{0}. \end{aligned} \quad (5.17)$$

Since the test function was chosen arbitrarily

$$\int_{\partial B_0^{\bar{\mathbf{T}}, e}} N^{(i)} \bar{\mathbf{T}} \, dA - \int_{B_0^e} \mathbf{P} \cdot \text{Grad}N^{(i)} \, dV = \mathbf{0} \quad \forall \boldsymbol{\eta}^e. \quad (5.18)$$

Equation 5.18 can be seen as a residual that is expressed at each node point (i) by

$$\mathbf{r}^{(i)} = \mathbf{r}_{ext}^{(i)} - \mathbf{r}_{int}^{(i)} \quad \text{with} \quad i = 1 \dots n_{np}, \quad (5.19)$$

where n_{np} is the total number of nodes. The contributions to the internal and external nodal forces are then given by

$$\mathbf{r}_{int}^{(i)} = \bigcup_{e=1}^{n_{el}} \int_{B_0^e} \mathbf{P} \cdot \text{Grad}N^{(i)} \, dV, \quad (5.20)$$

and

$$\mathbf{r}_{ext}^{(i)} = \bigcup_{e=1}^{n_{el}} \int_{\partial B_0^{\bar{\mathbf{T}}, e}} N^{(i)} \bar{\mathbf{T}} \, dA, \quad (5.21)$$

where $\bigcup_{e=1}^{n_{el}}$ \mathbf{A} is an assembly operator with respect to the element number in an FE formulation. The nonlinear system of equations appearing in Equation 5.19 is then solved by the Newton–Raphson method.

5.2.2 The Newton–Raphson method

In the computation of the direct boundary value problem with the FEM, the aim is to iteratively find the position of the node \mathbf{x}_{n+1} at \mathfrak{F}_{n+1} starting with the position \mathbf{x}_n at \mathfrak{F}_n (Fig. 5.3), where

$$\mathbf{x}_n^{(k+1)} = \mathbf{x}_n^{(k)} + \Delta \mathbf{x}_n^{(k)} \quad (5.22)$$

or, in terms of the deformation map,

$$\boldsymbol{\varphi}_n^{(k+1)} = \boldsymbol{\varphi}_n^{(k)} + \Delta \boldsymbol{\varphi}_n^{(k)}. \quad (5.23)$$

The iteration counter is indicated by the superscript (k) in Equation 5.22 and Equation 5.23. Thus the next position \mathbf{x}_{n+1} is given by the last iteration of the Newton–Raphson algorithm. In order to find the main unknown $\Delta \mathbf{x}$ in Equation 5.22 or $\Delta \boldsymbol{\varphi}$ in Equation 5.23, respectively, the Newton–Raphson method starts with the development in a Taylor series of the weak form of the direct problem (Eq. 5.6)

$$\mathbf{G}(\mathbf{x} + \Delta \mathbf{x}, \mathfrak{F}) = \mathbf{G}(\mathbf{x}, \mathfrak{F}) + \mathcal{D}_{\boldsymbol{\varphi}} \mathbf{G}(\mathbf{x}, \mathfrak{F}) \Delta \mathbf{x} + \mathcal{O}(\mathbf{x}, \mathfrak{F}) = \mathbf{0}, \quad (5.24)$$

where $\mathcal{D}_\varphi \mathbf{G}(\mathbf{x}, \mathfrak{F})$ corresponds to the linearisation or directive derivative or Gâteaux derivative of the weak form \mathbf{G} in the direction $\Delta \mathbf{x}$ at \mathfrak{F} and $\mathcal{O}(\mathbf{x}, \mathfrak{F})$ is the rest of the function. The operator \mathcal{D} is called the Gâteaux operator. By setting to zero the rest of the Taylor series, it follows that

$$\mathbf{G}(\mathbf{x}, \mathfrak{F}) + \mathcal{D}_\varphi \mathbf{G}(\mathbf{x}, \mathfrak{F}) \Delta \mathbf{x} = \mathbf{0}. \quad (5.25)$$

In the notation of the discretised direct problem in Section 5.2.1, the previous equation becomes

$$\mathcal{D}_\varphi \mathbf{G} \cdot \Delta \mathbf{x} = -\mathbf{r}. \quad (5.26)$$

Thereby the sought unknown is given by

$$\Delta \mathbf{x} = -(\mathcal{D}_\varphi \mathbf{G})^{-1} \cdot \mathbf{r}. \quad (5.27)$$

The linearisation of the weak form followed by a discretisation, presented in the next section, allows finding a tangent matrix \mathbf{k} so that the equation remaining to be solved is

$$\Delta \mathbf{x} = -\mathbf{k}^{-1} \cdot \mathbf{r}. \quad (5.28)$$

The Newton–Raphson method is schematically illustrated in Figure 5.3 for three iterations. The residual \mathbf{r} is represented by the green colour, whereas the tangent matrix \mathbf{k} is plotted in blue. A pseudo-algorithm view of the Newton–Raphson method is also presented in Algorithm 5.1 for solving the direct mechanical problem. A disadvantage of the Newton–Raphson method is that the tangent matrix has to be solved for each iteration.

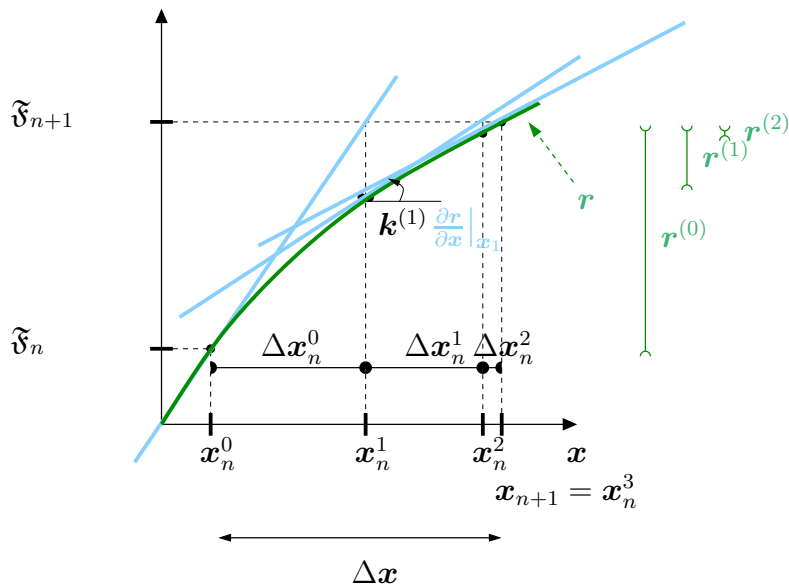


Figure 5.3: Graphical view of the Newton–Raphson method with three iterations.

5.2.3 Linearisation of the weak form

In order to find the tangent matrix \mathbf{k} needed in the Newton–Raphson method presented above, a linearisation of the weak form is required, as in Holzapfel [17] or Wriggers [72]. This is followed by a discretisation for the application of the FEM. The linearisation or directional derivative or

Algorithm 5.1: Pseudo-algorithm view of the Newton–Raphson method.

```

Data:  $\varepsilon = 10^{-6}$ , k=0, convergence=false;
Initialisation: Compute  $\mathbf{r}_{ext}^{(0)}$  and  $\mathbf{r}_{int}^{(0)}$  with Equation 5.21 and Equation 5.20;
Compute  $\mathbf{r}^{(0)}$  with Equation 5.19;
Compute  $\mathbf{k}^{(0)}$  with Equation 5.40;
if  $\|\mathbf{r}^{(0)}\| < \varepsilon$  then
  convergence=true;
  return  $\mathbf{x}_{n+1} = \mathbf{x}_n^{(0)}$ ;
else
  while convergence==false do
     $\Delta\mathbf{x}_n^{(k)} = -(\mathbf{k}^{(k)})^{-1} \cdot \mathbf{r}^{(k)}$ ;
     $\mathbf{x}_n^{(k+1)} = \mathbf{x}_n^{(k)} + \Delta\mathbf{x}_n^{(k)}$ ;
    Compute  $\mathbf{k}^{(k+1)}$  with Equation 5.40;
    Compute  $\mathbf{r}_{ext}^{(k+1)}$  and  $\mathbf{r}_{int}^{(k+1)}$  with Equation 5.21 and Equation 5.20;
    Compute  $\mathbf{r}^{(k+1)}$  with Equation 5.19;
    if  $\|\mathbf{r}^{(k+1)}\| < \varepsilon$  then
      convergence=true;
      return  $\mathbf{x}_{n+1} = \mathbf{x}_n^{(k+1)}$ ;
    else
      k=k+1;
    end
  end
end

```

Gâteaux derivative of the weak form \mathbf{G} in the direction $\Delta\boldsymbol{\varphi}$ at fixed material coordinates \mathbf{X} is given by

$$\bigcup_{e=1}^{n_{el}} \mathcal{D}_{\boldsymbol{\varphi}} \mathbf{G} = \bigcup_{e=1}^{n_{el}} \frac{d}{d\epsilon} \mathbf{G}(\boldsymbol{\varphi} + \epsilon \Delta\boldsymbol{\varphi}, \boldsymbol{\eta}; \mathbf{X})|_{\epsilon=0}, \quad (5.29)$$

where \mathcal{D} is the Gâteaux operator and ϵ is a scalar. By using Equation 5.6 the derivative of the weak form becomes

$$\bigcup_{e=1}^{n_{el}} \mathcal{D}_{\boldsymbol{\varphi}} \mathbf{G} = \bigcup_{e=1}^{n_{el}} \left[\int_{\mathcal{B}_0^e} \text{Grad} \boldsymbol{\eta} : \frac{\partial \mathbf{P}}{\partial \mathbf{F}} : \frac{d}{d\epsilon} \mathbf{F}(\boldsymbol{\varphi} + \epsilon \Delta\boldsymbol{\varphi}, \boldsymbol{\eta}; \mathbf{X})|_{\epsilon=0} dV \right]. \quad (5.30)$$

With the definition of \mathbf{F} in Equation 2.4, it follows that

$$\begin{aligned} \bigcup_{e=1}^{n_{el}} \mathcal{D}_{\boldsymbol{\varphi}} \mathbf{G} &= \bigcup_{e=1}^{n_{el}} \int_{\mathcal{B}_0^e} \text{Grad} \boldsymbol{\eta} : \frac{\partial \mathbf{P}}{\partial \mathbf{F}} : \text{Grad} \Delta\boldsymbol{\varphi} dV, \\ &= \bigcup_{e=1}^{n_{el}} \int_{\mathcal{B}_0^e} \text{Grad} \boldsymbol{\eta} : \mathbf{A} : \text{Grad} \Delta\boldsymbol{\varphi} dV. \end{aligned} \quad (5.31)$$

The fourth-order tangent operator \mathbb{A} decomposes into the material tangent operator \mathbb{C}^{ep} (Eq. 3.15) and a geometric contribution

$$\mathbb{A} := \frac{\partial \mathbf{P}}{\partial \mathbf{F}} = [\mathbf{F} \overline{\otimes} \mathbf{I}] : \mathbb{C}^{ep} : [\mathbf{F}^t \overline{\otimes} \mathbf{I}] + \mathbf{I} \overline{\otimes} \mathbf{S}. \quad (5.32)$$

In the above expression, \mathbf{I} denotes the unit tensor with coefficients δ_{ij} (Kroneker delta), $\overline{\otimes}$ denotes a non-standard dyadic product with $[\mathbf{A} \overline{\otimes} \mathbf{B}]_{ijkl} = A_{ik}B_{jl}$. A proof of Equation 5.32 is given in Appendix A. The fourth-order modulus \mathbb{C}^{ep} is defined in Equation 3.15, where the fourth-order elastoplastic tangent moduli \mathbb{E}^{ep} is computed with the return mapping algorithm presented in Chapter 3 in Algorithm 3.1.

The discretisation of the linearised weak form follows from Section 5.2.1. Setting

$$\Delta\varphi^e(\boldsymbol{\xi}) = \sum_{j=1}^{n_{en}} \Delta\varphi^{(j)} N^{(j)}(\boldsymbol{\xi}) \quad (5.33)$$

and

$$\text{Grad}\Delta\varphi^e(\boldsymbol{\xi}) = \sum_{j=1}^{n_{en}} \Delta\varphi^{(j)} \otimes \text{Grad}N^{(j)}(\boldsymbol{\xi}) \quad (5.34)$$

in Equation 5.31 with $i, j = 1 \dots n_{np}$, it follows that

$$\bigcup_{e=1}^{n_{el}} \mathcal{D}_\varphi \mathbf{G} = \bigcup_{e=1}^{n_{el}} \left[\int_{\mathcal{B}_0^e} \sum_{i=1}^{n_{en}} \boldsymbol{\eta}^{(i)} \otimes \text{Grad}N^{(i)} : \mathbb{A} : \sum_{j=1}^{n_{en}} \Delta\varphi^{(j)} \otimes \text{Grad}N^{(j)}(\boldsymbol{\xi}) \, dV \right]. \quad (5.35)$$

According to Equation 5.16, the above equation is transformed into

$$\bigcup_{e=1}^{n_{el}} \mathcal{D}_\varphi \mathbf{G} = \bigcup_{e=1}^{n_{el}} \left[\int_{\mathcal{B}_0^e} \left(\sum_{i=1}^{n_{en}} \boldsymbol{\eta}^{(i)} \cdot \mathbb{A} \cdot \text{Grad}N^{(i)} \right) : \sum_{j=1}^{n_{en}} \Delta\varphi^{(j)} \otimes \text{Grad}N^{(j)}(\boldsymbol{\xi}) \, dV \right] \quad (5.36)$$

and then into

$$\bigcup_{e=1}^{n_{el}} \mathcal{D}_\varphi \mathbf{G} = \bigcup_{e=1}^{n_{el}} \left[\int_{\mathcal{B}_0^e} \sum_{i=1}^{n_{en}} \boldsymbol{\eta}^{(i)} \cdot \mathbb{A} \cdot \sum_{j=1}^{n_{en}} \Delta\varphi^{(j)} \text{Grad}N^{(i)} \text{Grad}N^{(j)} \, dV \right]. \quad (5.37)$$

The summation terms are then put outside of the integral by

$$\bigcup_{e=1}^{n_{el}} \mathcal{D}_\varphi \mathbf{G} = \bigcup_{e=1}^{n_{el}} \sum_{i=1}^{n_{en}} \boldsymbol{\eta}^{(i)} \left[\sum_{j=1}^{n_{en}} \int_{\mathcal{B}_0^e} \mathbb{A} \cdot \text{Grad}N^{(i)} \cdot \text{Grad}N^{(j)} \, dV \Delta\varphi^{(j)} \right] \quad (5.38)$$

and it follows that

$$\bigcup_{e=1}^{n_{el}} \mathcal{D}_\varphi \mathbf{G} = \bigcup_{e=1}^{n_{el}} \sum_{i=1}^{n_{en}} \boldsymbol{\eta}^{(i)} \left[\sum_{j=1}^{n_{en}} \mathbf{k}^{(ij)} \Delta\varphi^{(j)} \right], \quad (5.39)$$

where the tangent stiffness matrix, i.e., the Jacobian matrix of the residual with respect to the spatial coordinates, is given by

$$\mathbf{k}^{(ij)} := \frac{\partial \mathbf{r}^{(i)}}{\partial \mathbf{x}^{(j)}} = \sum_{e=1}^{n_{el}} \int_{\mathcal{B}_0^e} \text{Grad}N^{(i)} \cdot \mathbb{A} \cdot \text{Grad}N^{(j)} \, dV. \quad (5.40)$$

In the above equation, \cdot denotes the contraction with the second index of the corresponding tangent operator.

5.3 Numerical examples

In this section, four numerical examples are presented to determine the deformed configuration of a functional component using the equilibrium equation. The examples are for isotropic and anisotropic hyperelastic materials as well as for isotropic and anisotropic elastoplastic materials.

5.3.1 Isotropic hyperelastic material

The first example deals with the determination of the deformed configuration of a bar in 3D. The undeformed configuration of the bar is plotted in Figure 5.4. The bar has a 10 mm square base and is 20 mm high. The bar is discretised by hexahedral element (HEX8) with MSC.Patran2010.2. The obtained number of elements is equal to 16 and the number of nodes is equal to 45. The bar is assumed to be clamped, i.e., fixed in the three directions, on its base (blue squares in Figure 5.4). Forces are applied on the top of the bar, which are illustrated in Figure 5.4 by red arrows. The applied force is equal to $18 \cdot 10^5$ units of force. The bar has isotropic hyperelastic behaviour. The material parameters used in the simulation are summarised in Table 5.1.

	elastic parameters	
E	211000	MPa
ν	0.3	-
\mathbb{E}^e	$3\kappa\mathbb{I}_{\text{vol}} + 2\mu\mathbb{I}_{\text{dev}}^{\text{sym}}$ (Eq. 4.37)	MPa

Table 5.1: Numerical example: Material parameters for an isotropic hyperelastic material.

The obtained deformed bar in the spatial configuration \mathcal{B}_t is plotted in Figure 5.5 with equivalent von Mises stress (MPa). The equivalent von Mises stress is obtained by computing the following formula

$$\sigma_{\text{eq}}^{\text{vm}} = \sqrt{\sigma_{11}^2 + \sigma_{22}^2 + \sigma_{33}^2 - \sigma_{11}\sigma_{22} - \sigma_{11}\sigma_{33} - \sigma_{22}\sigma_{33} + 3\sigma_{12}^2 + 3\sigma_{23}^2 + 3\sigma_{31}^2}. \quad (5.41)$$

5.3.2 Anisotropic hyperelastic material

The second example deals with the determination of the deformed configuration of a plate with a hole in 3D. The undeformed configuration of the plate is illustrated in Figure 5.6 and in Figure 5.7 in the $[X_1, X_2]$ plane. The plate has a 50 mm square base and is 10 mm thick. The diameter of the hole is equal to 2 mm. The plate is discretised by hexahedral element (HEX8) with MSC.Patran2010.2. The obtained number of elements is equal to 400 and the number of nodes is equal to 720. The left side of the plate is fixed in the three directions (blue squares in Figure 5.6 and Figure 5.7). Forces are applied on the right side of the plate, which are illustrated in Figure 5.6 and Figure 5.7 by red arrows. The applied force is equal to $5 \cdot 10^5$ units of force. The plate is assumed to have anisotropic hyperelastic behaviour. The material parameters used in the simulation are summarised in Table 5.2 and Table 5.3 for a cubic and a hexagonal hyperelastic material, respectively.

In order to see the difference in the deformed plate obtained when considering different crystal systems, the computation is done first with an isotropic hyperelastic material with the Kelvin

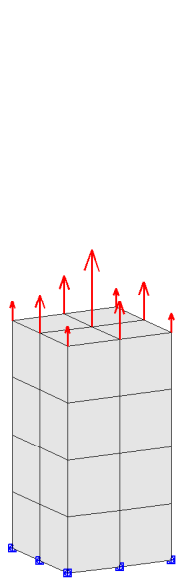


Figure 5.4: Undeformed configuration of a bar in the material configuration \mathcal{B}_0 .

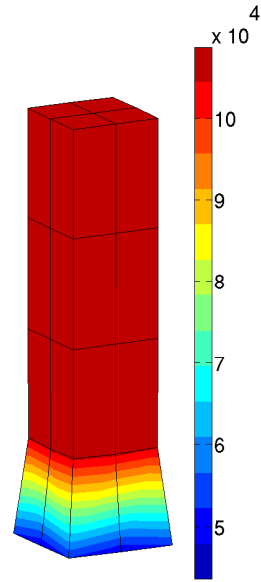


Figure 5.5: Deformed bar in the spatial configuration \mathcal{B}_t with equivalent von Mises stress $\sigma_{\text{eq}}^{\text{vm}}$ (MPa) with isotropic hyperelastic behaviour.

elastic parameters		
E	211000	MPa
ν	0.3	-
\mathbb{E}^e	$3\kappa\mathbb{P}_1 + 2\mu\mathbb{P}_2 + 2E_{55}\mathbb{P}_3$ (Eq. 4.45) $E_{55}=20000$	MPa MPa

Table 5.2: Numerical example: Material parameters for an anisotropic (cubic) hyperelastic material.

elastic parameters		
\mathbb{E}^e	$\lambda_1\mathbb{P}_1 + \lambda_2\mathbb{P}_2 + \lambda_3\mathbb{P}_3 + \lambda_4\mathbb{P}_4$ (Eq. 4.106 and Eq. 4.108)	MPa
	$E_{11}=100000$	MPa
	$E_{22}=300000$	MPa
	$E_{66}=20000$	MPa
	$E_{13}=120000$	MPa
	$E_{23}=240000$	MPa

Table 5.3: Numerical example: Material parameters for an anisotropic (hexagonal- e_1) hyperelastic material.

mode decomposition from Equation 4.37. The deformed plate obtained is shown in Figure 5.8 with the computation of the equivalent von Mises stress from Equation 5.41 in MPa in the $[x_1, x_2]$ plane. The deformed plate computed with the cubic parameters from Table 5.2 is illustrated in Figure 5.9 in the $[x_1, x_2]$ plane again with the equivalent von Mises stress (MPa). The deformed configuration of the plate with the hexagonal parameters from Table 5.3 is illustrated

in Figure 5.10 in the $[x_1, x_2]$ plane also with the equivalent von Mises stress (MPa). It can be seen that for the same force and boundary conditions, the different crystal systems give different deformed configurations. The hexagonal crystal system gives the most deformed configuration before the cubic crystal system. Furthermore, whereas the hole in the isotropic computation remains an ellipse, the hole in the cubic and hexagonal computations is more related to the form of an airplane wing.

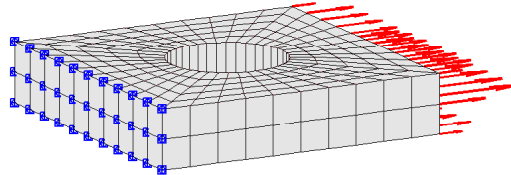


Figure 5.6: Undeformed plate with a hole in the material configuration \mathcal{B}_0 .

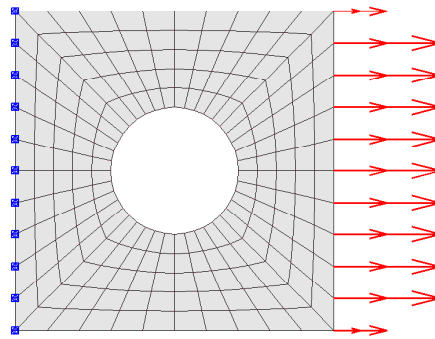


Figure 5.7: Undeformed configuration of a plate with a hole in \mathcal{B}_0 in the $[X_1, X_2]$ plane.

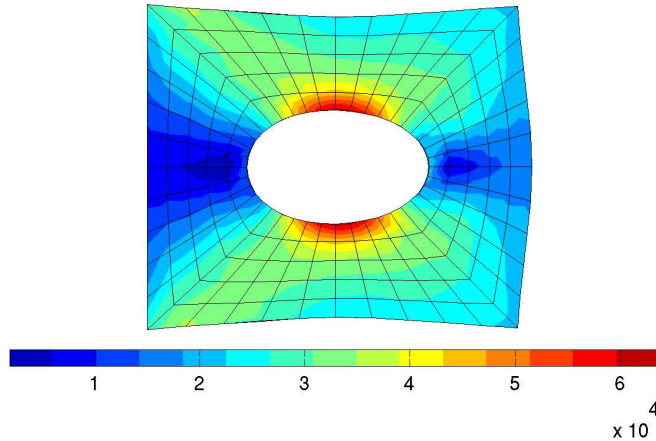


Figure 5.8: Deformed configuration of a plate with a hole in \mathcal{B}_t in the $[x_1, x_2]$ plane with equivalent von Mises stress $\sigma_{\text{eq}}^{\text{vm}}$ (MPa) with isotropic hyperelastic behaviour.

5.3.3 Isotropic elastoplastic material

The third example deals with the determination of the deformed configuration of a plate with four holes in 3D, as in Scherer [66]. The undeformed configuration of the plate is plotted in

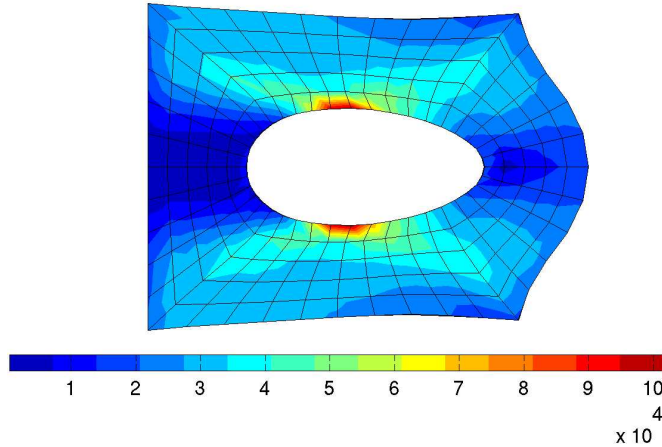


Figure 5.9: Deformed configuration of a plate with a hole in \mathcal{B}_t in the $[x_1, x_2]$ plane with equivalent von Mises stress $\sigma_{\text{eq}}^{\text{vm}}$ (MPa) with cubic hyperelastic behaviour.

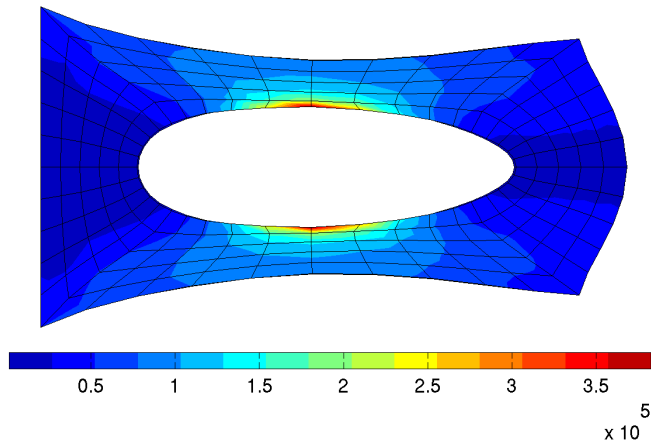


Figure 5.10: Deformed configuration of a plate with a hole in \mathcal{B}_t in the $[x_1, x_2]$ plane with equivalent von Mises stress $\sigma_{\text{eq}}^{\text{vm}}$ (MPa) with hexagonal hyperelastic behaviour.

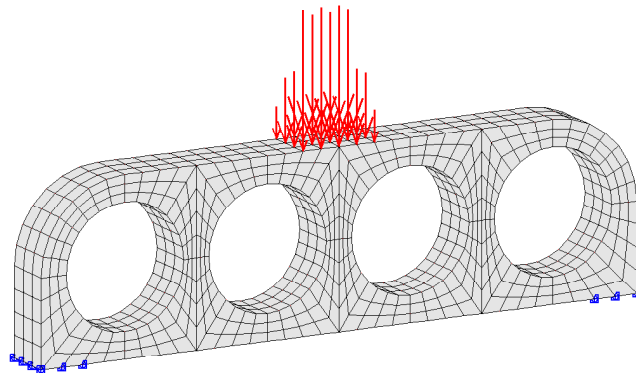
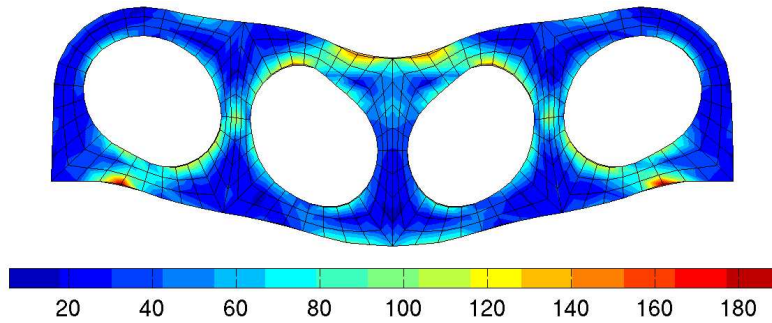
Figure 5.11. The plate is 70 mm long, 20 mm high and 6 mm thick. The diameter of the holes is equal to 14 mm. The plate is discretised by hexahedral element (HEX8) with MSC.Patran2010.2. The obtained number of elements is equal to 1134 and the number of nodes is equal to 1908. A square (3×4 nodes) on the left and right sides of the plate is fixed in the three directions (blue squares in Figure 5.11). Forces are applied on the top in the middle of the plate (red arrows). The applied force is equal to 1350 units of force in 10 increments (Eq. 5.22). The plate is assumed to have isotropic elastoplastic behaviour. The material parameters used in the simulation are summarised in Table 5.4 for an isotropic elastoplastic material with isotropic nonlinear hardening.

The deformed plate obtained is illustrated in Figure 5.12 in the $[x_1, x_3]$ plane with equivalent von Mises stress (Eq. 5.41). Figure 5.13 shows in the $[x_1, x_3]$ plane the distribution of the equivalent plastic strain computed using the equation

$$\mathbf{E}_{\text{eq}}^p = \sqrt{\frac{2}{3} \left[(\mathbf{E}_{11}^p)^2 + (\mathbf{E}_{22}^p)^2 + (\mathbf{E}_{33}^p)^2 + 2(\mathbf{E}_{12}^p)^2 + 2(\mathbf{E}_{23}^p)^2 + 2(\mathbf{E}_{31}^p)^2 \right]}. \quad (5.42)$$

	elastic parameters	
E	70000	MPa
ν	0.33	-
\mathbb{E}^e	$3\kappa\mathbb{I}_{\text{vol}} + 2\mu\mathbb{I}_{\text{dev}}^{\text{sym}}$	MPa
	plastic parameters	
h	100	MPa
σ_0	450	MPa
σ_∞	715	MPa
w	15	-
H	$\mathbb{I}_{\text{dev}}^{\text{sym}}$	-

Table 5.4: Numerical example: Material parameters for an isotropic elastoplastic material.

Figure 5.11: Undeformed configuration of a plate with four holes in \mathcal{B}_0 .Figure 5.12: Deformed plate with four holes in the spatial configuration \mathcal{B}_t ($[x_1, x_3]$ plane) with equivalent von Mises stress $\sigma_{\text{eq}}^{\text{vm}}$ (MPa) with isotropic elastoplastic behaviour.

5.3.4 Anisotropic elastoplastic material

The fourth example deals with the determination of the deformed configuration of a round plate in 3D as in Apel [22]. The undeformed configuration of the plate is plotted in Figure 5.14. The outer diameter of the plate is equal to 800 mm, whereas the inner diameter is equal to 400 mm. The round plate is 10 mm thick. The plate is discretised by hexahedral element (HEX8) with MSC.Patran2010.2. The obtained number of elements is equal to 320 and the number of nodes is equal to 720. The upper and lower surfaces of the round plate are assumed to be fixed in the x_3 direction (blue squares in Figure 5.14) so that no bulking takes place. Forces are applied

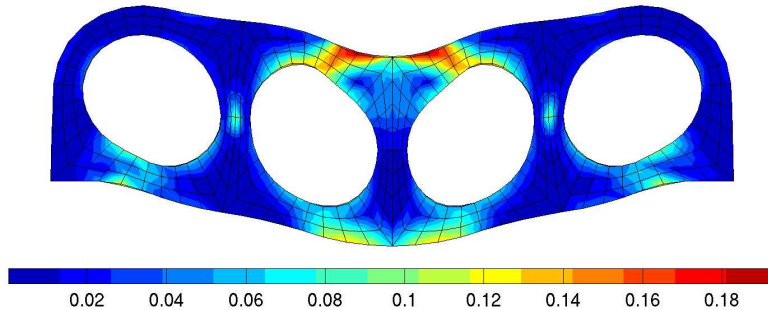


Figure 5.13: Deformed plate with four holes in the spatial configuration \mathcal{B}_t ($[x_1, x_3]$ plane) with equivalent plastic strain E_{eq}^p (-) with isotropic elastoplastic behaviour.

circularly on the interior of the plate (red arrows). The applied force is equal to $14 \cdot 10^4$ units of force in 10 increments (Eq. 5.22). The plate is assumed to have anisotropic elastoplastic behaviour. The material parameters used in the simulation are summarised in Table 5.5 for an anisotropic elastoplastic material following Equation 3.33. The material is assumed to have isotropic elastic and anisotropic (cubic) plastic response.

	elastic parameters	
E	70000	MPa
ν	0.33	-
E^e	$3\kappa\mathbb{I}_{\text{vol}} + 2\mu\mathbb{I}_{\text{dev}}^{\text{sym}}$	MPa
	plastic parameters	
h	100	MPa
σ_0	450	MPa
σ_∞	715	MPa
w	16.5	-
H	$y_{11}=400$ $y_{22}=400$ $y_{33}=400$ $y_{12}=400/\sqrt{3}$ $y_{23}=400/\sqrt{3}$ $y_{31}=400/\sqrt{3}$	
	MPa	

Table 5.5: Numerical example: Material parameters for an anisotropic (cubic) elastoplastic material.

Figure 5.15 shows the deformed configuration of the round plate in the $[x_1, x_2]$ plane with the equivalent von Mises stress calculated with Equation 5.41. Figure 5.16 illustrates in the $[x_1, x_2]$ plane the distribution of the equivalent plastic strain calculated with Equation 5.42. The effect of the anisotropic (cubic) yielding is shown by the fact that the inner hole does not remain perfectly circular as for an isotropic elastoplastic material. The maximum plastic strain is concentrated on $k\pi/4$ with $k=1,3,5,7$ as expected for cubic yielding. The same geometry, boundary conditions, and material parameters are used in a second computation but this time the forces are directed to the centre of the inner hole (Fig. 5.17). The applied force is equal to $2 \cdot 10^5$ units of force. Figure 5.18 shows the deformed configuration of the round plate in the $[x_1, x_2]$ plane

with the equivalent von Mises stress calculated with Equation 5.41. The effect of the anisotropic yielding is also here well illustrated. The deformed configuration looks like a flower. Figure 5.19 illustrates in the $[x_1, x_2]$ plane the distribution of the equivalent plastic strain calculated with Equation 5.42. As in the previous example, the maximum plastic strain is concentrated on $k\pi/4$ with $k=1,3,5,7$.

Remark:

- In FEM it is usual to make the convention that nodes with four neighbours have a force equal to 1, i.e., 1 unit of force, nodes with two neighbours have a force equal to 0.5, i.e., one-half a unit of force, and nodes on the border have a force equal to 0.25, i.e., one-quarter of a unit of force. This convention is well illustrated in Figure 5.5 in which the different lengths of the arrows are represented.
- All the computations were carried out with MatlabR2012a after obtaining the discretisation of the functional component with MSC.Patran2010.2. The assembly matrix is written in C [91] for the sake of computational costs.
- In the computation of elastoplastic problems, the set of internal variables \mathcal{IV} over the nodes has to be replaced at the beginning of the next increment by the set of internal variables \mathcal{IV} computed in the previous increment (the return mapping Algorithm 3.1).

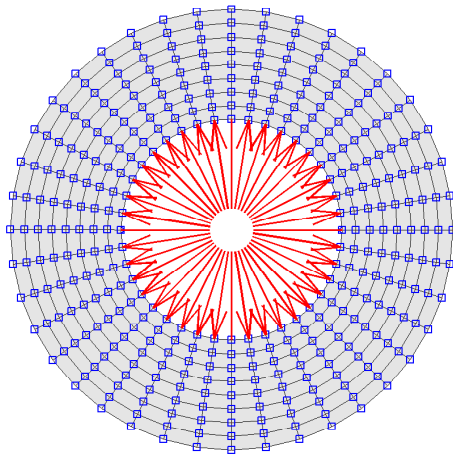


Figure 5.14: Undeformed round plate in the material configuration \mathcal{B}_0 in the $[X_1, X_2]$ plane.

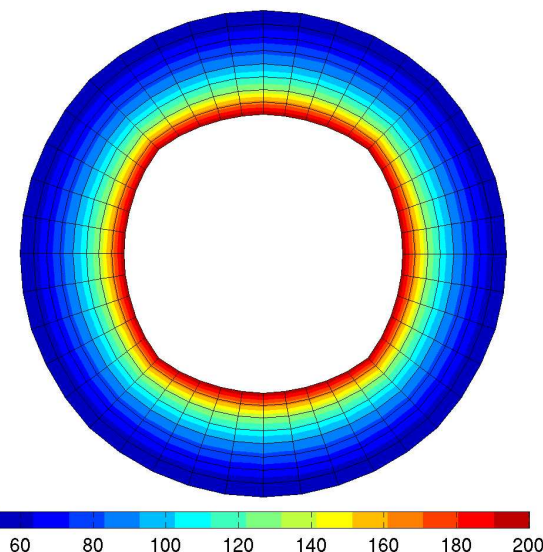


Figure 5.15: Deformed round plate in the spatial configuration \mathcal{B}_t ($[x_1, x_2]$ plane) with equivalent von Mises stress $\sigma_{\text{eq}}^{\text{vm}}$ (MPa) with anisotropic elastoplastic behaviour.

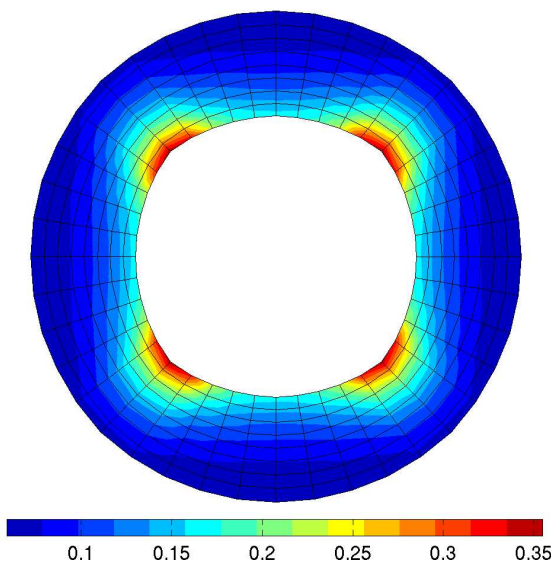


Figure 5.16: Deformed round plate in the spatial configuration \mathcal{B}_t ($[x_1, x_2]$ plane) with equivalent plastic strain E_{eq}^p (-) with anisotropic elastoplastic behaviour.

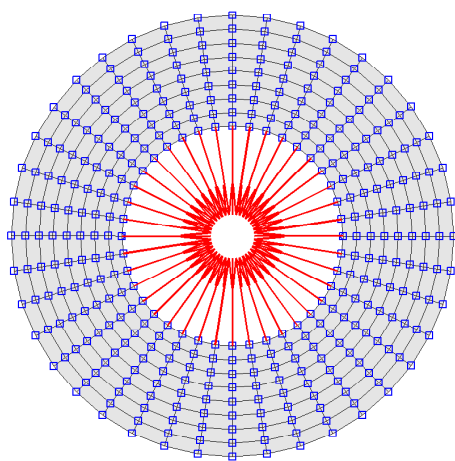


Figure 5.17: Undeformed plate in the material configuration \mathcal{B}_0 in the $[X_1, X_2]$ plane.

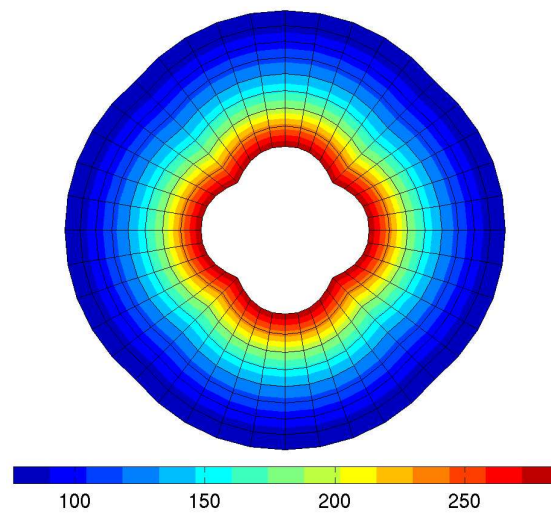


Figure 5.18: Deformed round plate in the spatial configuration \mathcal{B}_t ($[x_1, x_2]$ plane) with equivalent von Mises stress $\sigma_{\text{eq}}^{\text{vm}}$ (MPa) with anisotropic elastoplastic behaviour.

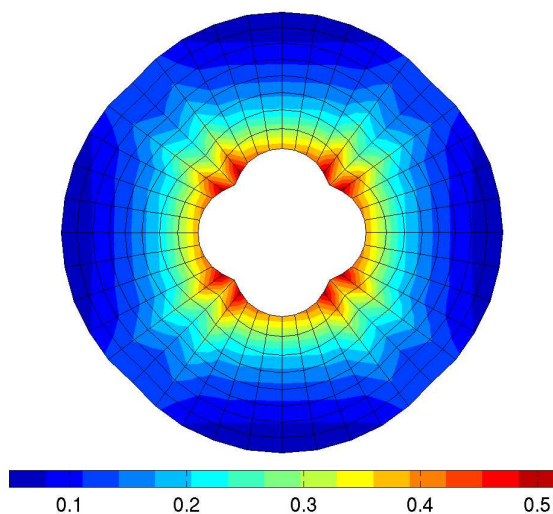


Figure 5.19: Deformed round plate in the spatial configuration \mathcal{B}_t ($[x_1, x_2]$ plane) with equivalent plastic strain E_{eq}^p (-) with anisotropic elastoplastic behaviour.

CHAPTER 6

Determining the undeformed shape from equilibrium

This chapter deals with the determination of the undeformed shape of a functional component from the equilibrium equation. A challenge in the design of functional parts is the determination of that initial, undeformed shape that, under a given load, will obtain the desired deformed shape. This is the inverse form finding problem and it is posed as follows: the deformed shape and the mechanical loading are given, whereas the inverse deformation map that determines the material configuration, i.e., the undeformed shape, is sought. This problem is inverse to the standard direct kinematic analysis in which the undeformed shape is known and the deformed shape is unknown, as presented in Chapter 5. A numerical procedure for the determination of the undeformed shape of a continuous body has been proposed in Govindjee et al. [1, 2]. Their work is restricted to materials that are either incompressible or isotropic compressible neo-Hookean. One result of their work is that the weak form of the inverse motion problem based on the Cauchy stress is more efficient and straightforward than the weak form based on the Eshelby stress (energy momentum tensor). The governing equation underlying the numerical analysis of the inverse form finding problem is therefore the common weak form of the momentum balance formulated in terms of the Cauchy stress tensor. However, the unconventional issue is that all quantities are parametrised in spatial coordinates. Later on, Fachinotti et al. [8] extended this method to the case of anisotropic hyperelasticity for a St. Venant type material, i.e., a material characterised by a quadratic free energy density in terms of the Green–Lagrange strain. The method originally proposed in Govindjee et al. [1] was extended to anisotropic hyperelasticity and elastoplasticity that is based on logarithmic (Hencky) strains in Germain et al. [13, 14, 15, 57, 69]. The governing equation for the resulting finite element analysis is the weak form of the momentum balance formulated in terms of the deformed configuration using the Cauchy stress tensor.

This chapter is structured as follows: In the first section, a Cauchy formulation is presented for determining the undeformed configuration of a continuous body for a given deformed configuration and associated boundary conditions, so that the equilibrium requirement (Eq. 2.37) is satisfied for the spatial configuration. The inverse problem is solved using the FEM in the same way as for solving the direct problem presented in Chapter 5. From now on, the distributed body forces and inertia will be omitted and the acceleration will be assumed to vanish. Numerical examples for isotropic and anisotropic hyperelastic materials as well as for elastoplastic materials will be presented to illustrate these developments, where the macroscopic constitutive model in the logarithmic strain space presented in Chapter 3 will be used. The fourth-order elasticity tensor will be decomposed into Kelvin modes as in Chapter 4. It will be demonstrated that the inverse formulation can be used for elastoplastic behaviour when a desired hardening state is given. Parts of this chapter have been published by Germain et al. in [13, 14, 15, 57, 67, 69, 70].

6.1 The inverse mechanical problem

The nonlinear inverse deformation map $\Phi = \Phi(\mathbf{x})$ in Equation 2.9 is determined for the given spatial coordinates \mathbf{x} by the following equilibrium statement in terms of spatial description quantities

$$\begin{aligned}\operatorname{div}(\boldsymbol{\sigma}) &= \mathbf{0} && \text{in } \mathcal{B}_t && (\text{Eq. 2.37}), \\ \boldsymbol{\sigma} \cdot \mathbf{n} &= \bar{\mathbf{t}} && \text{on } \partial\mathcal{B}_t^{\bar{\Phi}} && (\text{Eq. 2.32}), \\ \Phi &= \bar{\Phi} && \text{on } \partial\mathcal{B}_t^{\bar{\Phi}}.\end{aligned}\quad (6.1)$$

In the above boundary value problem, $\bar{\mathbf{t}}$ is a given traction, however now per unit area in the spatial configuration (Neumann data), and $\bar{\Phi}$ is a given boundary deformation (Dirichlet data) (Fig. 2.1). Note that the Dirichlet data in the material and spatial configurations on $\mathcal{B}_0^{\bar{\Phi}}$ and $\mathcal{B}_t^{\bar{\Phi}}$ are assumed to be identical. The symmetric Cauchy stress $\boldsymbol{\sigma}$ is obtained from the Piola–Kirchhoff stress by a push-forward using

$$J\boldsymbol{\sigma} = \mathbf{F} \cdot \mathbf{S} \cdot \mathbf{F}^T. \quad (6.2)$$

In order to satisfy the principle of virtual work in the spatial configuration, also referred to as the weak form as in Section 5.1, the equation of motion (Eq. 6.1) is multiplied by an arbitrary weighting function $\boldsymbol{\eta} \in \mathcal{V} = \{\boldsymbol{\eta} \mid \boldsymbol{\eta} = \mathbf{0} \text{ on } \partial\mathcal{B}_t^{\bar{\Phi}}\}$. The weak form of the given boundary value problem, with this weighting function, is thus given by

$$\mathbf{g}(\Phi, \boldsymbol{\eta}; \mathbf{x}) = \int_{\mathcal{B}_t} \boldsymbol{\eta} \cdot \operatorname{div}(\boldsymbol{\sigma}) \, dv = \mathbf{0} \quad \forall \boldsymbol{\eta} \in \mathcal{V}. \quad (6.3)$$

Using the product rule for the divergence, the weak form becomes

$$\mathbf{g}(\Phi, \boldsymbol{\eta}; \mathbf{x}) = \int_{\mathcal{B}_t} \operatorname{div}(\boldsymbol{\eta} \cdot \boldsymbol{\sigma}) \, dv - \int_{\mathcal{B}_t} \operatorname{grad}\boldsymbol{\eta} : \boldsymbol{\sigma} \, dv = \mathbf{0}. \quad (6.4)$$

Applying the divergence theorem to the first term of the previous equation, relating the volume integral over \mathcal{B}_t to the surface integral over $\partial\mathcal{B}_t^{\bar{\Phi}}$ in Equation 2.34, it follows that

$$\mathbf{g}(\Phi, \boldsymbol{\eta}; \mathbf{x}) = \int_{\partial\mathcal{B}_t^{\bar{\Phi}}} \boldsymbol{\eta} \cdot \boldsymbol{\sigma} \cdot \mathbf{n} \, da - \int_{\mathcal{B}_t} \operatorname{grad}\boldsymbol{\eta} : \boldsymbol{\sigma} \, dv = \mathbf{0}. \quad (6.5)$$

With the definition of the surface traction in the spatial configuration in Equation 2.32, the weak form is assumed to satisfy

$$\mathbf{g}(\Phi, \boldsymbol{\eta}; \mathbf{x}) = \int_{\partial\mathcal{B}_t^{\bar{\Phi}}} \boldsymbol{\eta} \cdot \bar{\mathbf{t}} \, da - \int_{\mathcal{B}_t} \operatorname{grad}\boldsymbol{\eta} : \boldsymbol{\sigma} \, dv = \mathbf{0}. \quad (6.6)$$

Regarding the weighting function as a virtual field $\delta \mathbf{X}$ since $\boldsymbol{\eta}$ is chosen arbitrarily, the weak form of the boundary value problem leads to the principle of virtual work

$$\delta W_{ext} - \delta W_{int} = \mathbf{0}, \quad (6.7)$$

where

$$\delta W_{ext} = \int_{\partial\mathcal{B}_t^{\bar{\mathbf{t}}}} \delta \mathbf{X} \cdot \bar{\mathbf{t}} \, da = \int_{\partial\mathcal{B}_t^{\bar{\mathbf{t}}}} \boldsymbol{\eta} \cdot \bar{\mathbf{t}} \, da \quad (6.8)$$

and

$$\delta W_{int} = \int_{\mathcal{B}_t} \text{grad} \delta \mathbf{X} : \boldsymbol{\sigma} \, dv = \int_{\mathcal{B}_t} \text{grad} \boldsymbol{\eta} : \boldsymbol{\sigma} \, dv \quad (6.9)$$

Clearly, Equation 6.6 is the same virtual work statement as in Equation 5.6, however all integrals extend now over the spatial configuration, which is here assumed given, and all quantities are parametrised in the given spatial coordinates \mathbf{x} .

6.2 Finite element analysis

The determination of the undeformed configuration of a continuous body for given applied forces and boundary conditions is performed by the FEM. The continuous body in the spatial configuration is first discretised into n_{el} elements following Section 5.2. The weak form becomes thereby a nonlinear system of equations, which is solved again by the Newton–Raphson method. A linearisation of the weak form (Eq. 6.6) gives the needed tangent stiffness matrix for an application of the inverse problem.

Remark: From now on, $[\cdot]^e$ refers again to **element** and should not be confused with $[\cdot]^e$ in Chapter 3 which refers to **elastic** behaviour.

6.2.1 Discretisation

For the finite element solution of the boundary value problem (Eq. 6.1), the discretisation of the domains is equivalent to the discretisation introduced in Section 5.2.1. The standard isoparametric approach is again used and the weighting function is moreover parametrised by the same shape function following the Bubnov–Galerkin method. Substituting the finite element approximations in the weak form (Eq. 6.6), the discrete equilibrium condition is obtained

$$\begin{aligned} \bigcup_{e=1}^{n_{el}} \mathbf{g}(\Phi^e, \boldsymbol{\eta}^e; \mathbf{x}^e) &= \bigcup_{e=1}^{n_{el}} \int_{\partial\mathcal{B}_t^{\bar{\mathbf{t}},e}} \boldsymbol{\eta}^e \cdot \bar{\mathbf{t}} \, da - \int_{\mathcal{B}_t^e} \text{grad} \boldsymbol{\eta}^e : \boldsymbol{\sigma} \, dv = \mathbf{0} \\ &= \bigcup_{e=1}^{n_{el}} \int_{\partial\mathcal{B}_t^{\bar{\mathbf{t}},e}} \sum_{i=1}^{n_{en}} \boldsymbol{\eta}^{(i)} N^{(i)} \cdot \bar{\mathbf{t}} \, da - \int_{\mathcal{B}_t^e} \sum_{i=1}^{n_{en}} \boldsymbol{\eta}^{(i)} \otimes \text{grad} N^{(i)} : \boldsymbol{\sigma} \, dv. \end{aligned} \quad (6.10)$$

According to Equation 5.16, the above equation leads to

$$\begin{aligned} \bigcup_{e=1}^{n_{el}} \mathbf{g}(\Phi^e, \boldsymbol{\eta}^e; \mathbf{x}^e) &= \bigcup_{e=1}^{n_{el}} \int_{\partial\mathcal{B}_t^{\bar{\mathbf{t}},e}} \sum_{i=1}^{n_{en}} \boldsymbol{\eta}^{(i)} N^{(i)} \cdot \bar{\mathbf{t}} \, da - \int_{\mathcal{B}_t^e} \sum_{i=1}^{n_{en}} \boldsymbol{\eta}^{(i)} \cdot \boldsymbol{\sigma} \cdot \text{grad} N^{(i)} \, dv \\ &= \bigcup_{e=1}^{n_{el}} \sum_{i=1}^{n_{en}} \boldsymbol{\eta}^{(i)} \left[\int_{\partial\mathcal{B}_t^{\bar{\mathbf{t}},e}} N^{(i)} \bar{\mathbf{t}} \, da - \int_{\mathcal{B}_t^e} \boldsymbol{\sigma} \cdot \text{grad} N^{(i)} \, dv \right] = \mathbf{0}. \end{aligned} \quad (6.11)$$

Since the test function was chosen arbitrarily

$$\int_{\partial\mathcal{B}_t^{\bar{\mathbf{t}},e}} N^{(i)} \bar{\mathbf{t}} \, da - \int_{\mathcal{B}_t^e} \boldsymbol{\sigma} \cdot \text{grad} N^{(i)} \, dv = \mathbf{0} \quad \forall \boldsymbol{\eta}^e. \quad (6.12)$$

As in the direct problem formulation, Equation 6.12 can be seen as a residual that is expressed at each node point (i) by

$$\mathbf{r}^{(i)} = \mathbf{r}_{ext}^{(i)} - \mathbf{r}_{int}^{(i)} \quad \text{with} \quad i = 1 \dots n_{np}, \quad (6.13)$$

where n_{np} is the total number of nodes. The contributions to the internal and external nodal forces are then given by

$$\mathbf{r}_{int}^{(i)} = \sum_{e=1}^{n_{el}} \int_{\mathcal{B}_t^e} \boldsymbol{\sigma} \cdot \text{grad}N^{(i)} dv \quad (6.14)$$

and

$$\mathbf{r}_{ext}^{(i)} = \sum_{e=1}^{n_{el}} \int_{\partial \mathcal{B}_t^e} N^{(i)} \bar{\mathbf{t}} da. \quad (6.15)$$

As in the formulation of the direct problem, the nonlinear system of equations appearing in Equation 6.13 is solved by the Newton–Raphson method.

Remark: Both contributions to internal and external nodal forces in the material and spatial configurations are related by a push-forward

$$\mathbf{r}_{int}^{(i)} = \sum_{e=1}^{n_{el}} \int_{\mathcal{B}_0^e} \mathbf{P} \cdot \text{Grad}N^{(i)} dV = \sum_{e=1}^{n_{el}} \int_{\mathcal{B}_t^e} \boldsymbol{\sigma} \cdot \text{grad}N^{(i)} dv \quad (6.16)$$

and

$$\mathbf{r}_{ext}^{(i)} = \sum_{e=1}^{n_{el}} \int_{\partial \mathcal{B}_0^e} N^{(i)} \bar{\mathbf{T}} dA = \sum_{e=1}^{n_{el}} \int_{\partial \mathcal{B}_t^e} N^{(i)} \bar{\mathbf{t}} da. \quad (6.17)$$

6.2.2 The Newton–Raphson method

In the solution of the inverse boundary value problem using the FEM, the aim is now to find iteratively the position of the node \mathbf{X}_{n+1} at \mathfrak{F}_{n+1} starting with the position \mathbf{X}_n at \mathfrak{F}_n (Fig. 5.3), where

$$\mathbf{X}_n^{(k+1)} = \mathbf{X}_n^{(k)} + \Delta \mathbf{X}_n^{(k)} \quad (6.18)$$

or, in term of the inverse deformation map,

$$\Phi_n^{(k+1)} = \Phi_n^{(k)} + \Delta \Phi_n^{(k)}. \quad (6.19)$$

The next position \mathbf{X}_{n+1} is again given by the last iteration of the Newton–Raphson algorithm. In order to find the main unknown $\Delta \mathbf{X}$ in Equation 6.18 or $\Delta \Phi$ in Equation 6.19, the Newton–Raphson method starts with the development in a Taylor series of the weak form of the inverse problem (Eq. 6.6)

$$\mathbf{g}(\mathbf{X} + \Delta \mathbf{X}, \mathfrak{F}) = \mathbf{g}(\mathbf{X}, \mathfrak{F}) + \mathcal{D}_{\Phi} \mathbf{g}(\mathbf{X}, \mathfrak{F}) \Delta \mathbf{X} + \mathcal{O}(\mathbf{X}, \mathfrak{F}) = \mathbf{0}, \quad (6.20)$$

where $\mathcal{D}_{\Phi} \mathbf{g}(\mathbf{X}, \mathfrak{F})$ corresponds to the linearisation of \mathbf{g} in the direction $\Delta \mathbf{X}$ at \mathfrak{F} and $\mathcal{O}(\mathbf{X}, \mathfrak{F})$ is the rest of the function. The operator \mathcal{D} is again the Gâteaux operator. By setting to zero the rest of the Taylor series, it follows that

$$\mathbf{g}(\mathbf{X}, \mathfrak{F}) + \mathcal{D}_{\Phi} \mathbf{g}(\mathbf{X}, \mathfrak{F}) \Delta \mathbf{X} = \mathbf{0}. \quad (6.21)$$

In the notation of the discretised inverse problem in Section 6.2.1, the previous equation becomes

$$\mathcal{D}_{\Phi} \mathbf{g} \cdot \Delta \mathbf{X} = -\mathbf{r}. \quad (6.22)$$

Thereby the sought unknown is given by

$$\Delta \mathbf{X} = -(\mathcal{D}_{\Phi} \mathbf{g})^{-1} \cdot \mathbf{r}. \quad (6.23)$$

The linearisation of the weak form followed by a discretisation, which are presented in the next section, allow finding a tangent matrix \mathbf{K} so that the equation, which has to be solved, becomes

$$\Delta \mathbf{X} = -\mathbf{K}^{-1} \cdot \mathbf{r}. \quad (6.24)$$

The Newton–Raphson method applied to the inverse problem is schematically illustrated in Figure 6.1 for three iterations. The residual \mathbf{r} is represented by the green colour, whereas the tangent matrix \mathbf{K} is plotted with blue colour. A pseudo-algorithm view of the Newton–Raphson method for an application to the inverse problem is also presented in Algorithm 6.1.

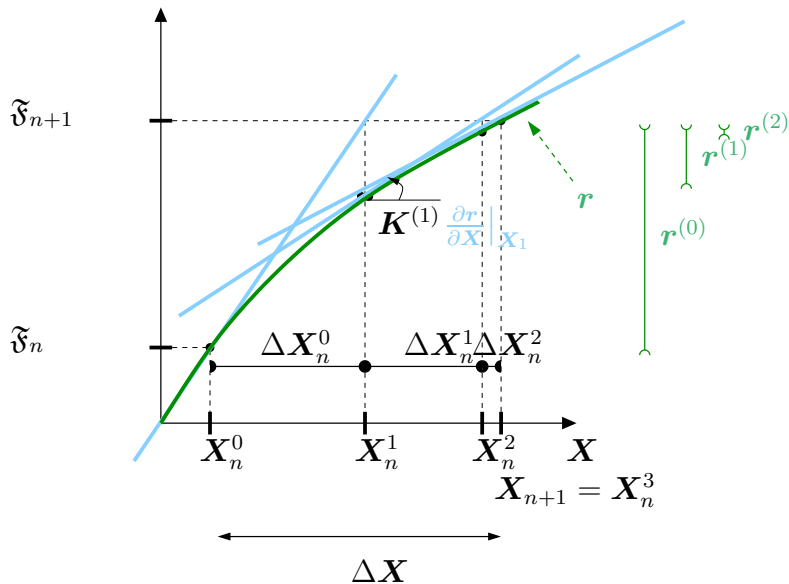


Figure 6.1: Graphical view of the Newton–Raphson method for the inverse problem with three iterations.

6.2.3 Linearisation of the weak form

In order to find the tangent matrix \mathbf{K} needed in the Newton–Raphson method presented above, a linearisation of the weak form \mathbf{g} is again required. This is then followed by a discretisation for an application of the FEM. The Gâteaux derivative of the weak form \mathbf{g} in the direction $\Delta \Phi$ at fixed spatial coordinates \mathbf{x} is given by

$$\bigcup_{e=1}^{n_{el}} \mathcal{D}_{\Phi} \mathbf{g} = \bigcup_{e=1}^{n_{el}} \frac{d}{d\epsilon} \mathbf{g}(\Phi + \epsilon \Delta \Phi, \boldsymbol{\eta}; \mathbf{x})|_{\epsilon=0}, \quad (6.25)$$

Algorithm 6.1: Pseudo-algorithm view of the Newton–Raphson method for an application to the inverse problem.

```

Data:  $\varepsilon = 10^{-6}$ , k=0, convergence=false;
initialisation: Compute  $\mathbf{r}_{ext}^{(0)}$  and  $\mathbf{r}_{int}^{(0)}$  with Equation 6.15 and Equation 6.14;
Compute  $\mathbf{r}^{(0)}$  with Equation 6.13;
Compute  $\mathbf{K}^{(0)}$  with Equation 6.36;
if  $\|\mathbf{r}^{(0)}\| < \varepsilon$  then
| convergence=true;
| return  $\mathbf{X}_{n+1} = \mathbf{X}_n^{(0)}$ ;
else
| while convergence==false do
| |  $\Delta\mathbf{X}_n^{(k)} = -(\mathbf{K}^{(k)})^{-1} \cdot \mathbf{r}^{(k)}$ ;
| |  $\mathbf{X}_n^{(k+1)} = \mathbf{X}_n^{(k)} + \Delta\mathbf{X}_n^{(k)}$ ;
| | Compute  $\mathbf{K}^{(k+1)}$  with Equation 6.36;
| | Compute  $\mathbf{r}_{ext}^{(k+1)}$  and  $\mathbf{r}_{int}^{(k+1)}$  with Equation 6.15 and Equation 6.14;
| | Compute  $\mathbf{r}^{(k+1)}$  with Equation 6.13;
| | if  $\|\mathbf{r}^{(k+1)}\| < \varepsilon$  then
| | | convergence=true;
| | | return  $\mathbf{X}_{n+1} = \mathbf{X}_n^{(k+1)}$ ;
| | else
| | | k=k+1;
| | end
| end
end

```

where \mathcal{D} is the Gâteaux operator and ϵ is a scalar operator. By using Equation 6.6, the derivative of the weak form becomes

$$\bigcup_{e=1}^{n_{el}} \mathcal{D}_{\Phi} \mathbf{g} = \bigcup_{e=1}^{n_{el}} \int_{\mathcal{B}_t^e} \text{grad} \boldsymbol{\eta} : \frac{\partial \boldsymbol{\sigma}}{\partial \mathbf{f}} : \frac{d}{d\epsilon} \mathbf{f}(\Phi + \epsilon \Delta \Phi, \boldsymbol{\eta}; \mathbf{x})|_{\epsilon=0} dv. \quad (6.26)$$

Using the definition of \mathbf{f} in Equation 2.10, it follows that

$$\begin{aligned} \bigcup_{e=1}^{n_{el}} \mathcal{D}_{\Phi} \mathbf{g} &= \bigcup_{e=1}^{n_{el}} \int_{\mathcal{B}_t^e} \text{grad} \boldsymbol{\eta} : \frac{\partial \boldsymbol{\sigma}}{\partial \mathbf{f}} : \text{grad} \Delta \Phi dv, \\ &= \bigcup_{e=1}^{n_{el}} \int_{\mathcal{B}_t^e} \text{grad} \boldsymbol{\eta} : \mathbf{a} : \text{grad} \Delta \Phi dv. \end{aligned} \quad (6.27)$$

The computation of the corresponding fourth-order tangent operator \mathbf{a} simplifies considerably if the following assumptions are made:

1. the surface tractions per unit area in $\partial \mathcal{B}_t^{\bar{t}}$ are given, i.e., they are independent of the inverse deformation map,

2. the material is homogeneous, i.e., $\boldsymbol{\sigma} = \boldsymbol{\sigma}(\mathbf{f}) \neq \boldsymbol{\sigma}(\mathbf{f}, \Phi)$.

With these assumptions, a follows in a straightforward manner from the relation between the Cauchy and the Piola–Kirchhoff stresses and application of the chain and product rules of differentiation

$$\mathbf{a} := \frac{\partial[j\mathbf{F} \cdot \mathbf{S} \cdot \mathbf{F}^T]}{\partial \mathbf{f}} = \boldsymbol{\sigma} \otimes \mathbf{F}^T - \mathbf{F} \overline{\otimes} \boldsymbol{\sigma} + j\mathbf{F} \cdot \left[\frac{1}{2} \mathbb{C}^{ep} : \frac{\partial \mathbf{C}}{\partial \mathbf{f}} \right] \cdot \mathbf{F}^T - \boldsymbol{\sigma} \underline{\otimes} \mathbf{F}. \quad (6.28)$$

In the above equation, $\underline{\otimes}$ denotes a non-standard dyadic product with $[\mathbf{A} \underline{\otimes} \mathbf{B}]_{ijkl} = A_{il}B_{jk}$. A proof of Equation 6.28 is given in Appendix B. The fourth-order elastoplastic modulus \mathbb{C}^{ep} is given by Equation 3.15.

The discretisation of the linearised weak form follows from Section 6.2.1. Setting

$$\Delta\Phi^e(\boldsymbol{\xi}) = \sum_{j=1}^{n_{en}} \Delta\Phi^{(j)} N^{(j)}(\boldsymbol{\xi}) \quad (6.29)$$

and

$$\text{grad}\Delta\Phi^e(\boldsymbol{\xi}) = \sum_{j=1}^{n_{en}} \Delta\Phi^{(j)} \otimes \text{grad}N^{(j)}(\boldsymbol{\xi}) \quad (6.30)$$

in Equation 6.27 with $i, j = 1 \dots n_{np}$, it follows that

$$\bigcup_{e=1}^{n_{el}} \mathcal{D}_\Phi \mathbf{g} = \bigcup_{e=1}^{n_{el}} \int_{\mathcal{B}_t^e} \sum_{i=1}^{n_{en}} \boldsymbol{\eta}^{(i)} \otimes \text{grad}N^{(i)} : \mathbf{a} : \sum_{j=1}^{n_{en}} \Delta\Phi^{(j)} \otimes \text{grad}N^{(j)}(\boldsymbol{\xi}) \, dv \quad (6.31)$$

According to Equation 5.16, the above equation is transformed into

$$\bigcup_{e=1}^{n_{el}} \mathcal{D}_\Phi \mathbf{g} = \bigcup_{e=1}^{n_{el}} \int_{\mathcal{B}_t^e} \left[\sum_{i=1}^{n_{en}} \boldsymbol{\eta}^{(i)} \cdot \mathbf{a} \cdot \text{grad}N^{(i)} \right] : \sum_{j=1}^{n_{en}} \Delta\Phi^{(j)} \otimes \text{grad}N^{(j)}(\boldsymbol{\xi}) \, dv \quad (6.32)$$

and then into

$$\bigcup_{e=1}^{n_{el}} \mathcal{D}_\Phi \mathbf{g} = \bigcup_{e=1}^{n_{el}} \int_{\mathcal{B}_t^e} \sum_{i=1}^{n_{en}} \boldsymbol{\eta}^{(i)} \cdot \mathbf{a} \cdot \sum_{j=1}^{n_{en}} \Delta\Phi^{(j)} \text{grad}N^{(i)} \text{grad}N^{(j)} \, dv. \quad (6.33)$$

The summation terms are then put outside of the integral by

$$\bigcup_{e=1}^{n_{el}} \mathcal{D}_\Phi \mathbf{g} = \bigcup_{e=1}^{n_{el}} \sum_{i=1}^{n_{en}} \boldsymbol{\eta}^{(i)} \sum_{j=1}^{n_{en}} \int_{\mathcal{B}_t^e} \mathbf{a} \cdot \text{grad}N^{(i)} \cdot \text{grad}N^{(j)} \, dv \Delta\Phi^{(j)} \quad (6.34)$$

and it follows that

$$\bigcup_{e=1}^{n_{el}} \mathcal{D}_\Phi \mathbf{g} = \bigcup_{e=1}^{n_{el}} \sum_{i=1}^{n_{en}} \boldsymbol{\eta}^{(i)} \left[\sum_{j=1}^{n_{en}} \mathbf{K}^{(ij)} \Delta\Phi^{(j)} \right], \quad (6.35)$$

where the tangent stiffness matrix, i.e., the Jacobian matrix of the residual with respect to the material coordinates, is given by

$$\mathbf{K}^{(ij)} := \frac{\partial \mathbf{r}^{(i)}}{\partial \mathbf{X}^{(j)}} = \bigcup_{e=1}^{n_{el}} \int_{\mathcal{B}_t^e} \text{grad}N^{(i)} \cdot \mathbf{a} \cdot \text{grad}N^{(j)} \, dv. \quad (6.36)$$

In the above equation, \cdot denotes again contraction with the second index of the corresponding tangent operator.

6.3 Numerical examples

In this section, four numerical examples are presented to determine the undeformed configuration of a functional component using the equilibrium equation. The examples are for isotropic and anisotropic hyperelastic materials as well as for isotropic elastoplastic materials. As validation, for each example, the undeformed shape obtained is used as input for the solution of the direct mechanical problem presented in Chapter 5. The difference between the given deformed shape used in the inverse problem and the one obtained with the direct problem are compared by

$$\varepsilon = \|\mathbf{x}^{\text{given to the inverse problem}} - \mathbf{x}(\mathbf{X}^{\text{obtained from the inverse problem}})\|^2 \text{ mm.} \quad (6.37)$$

A schematic view of the validation is given in Figure 6.2.

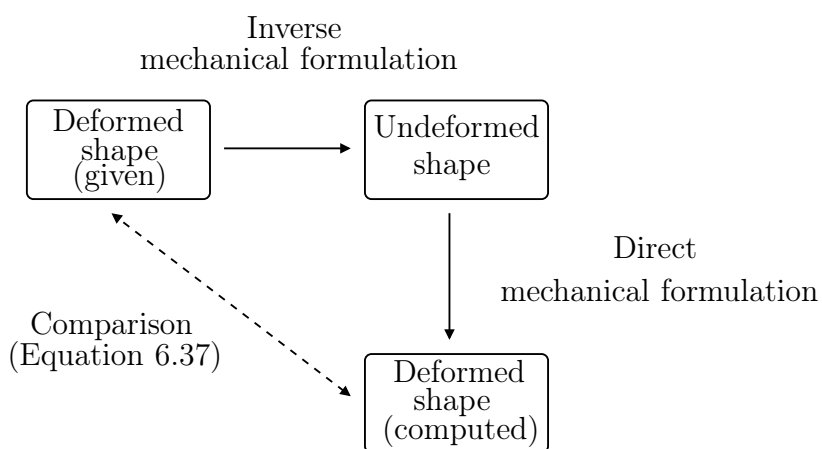


Figure 6.2: Schematic view for validating the inverse mechanical problem.

6.3.1 Isotropic hyperelastic material

The first example deals with the determination of the undeformed configuration of a thick cantilever under a distributed force, as in Germain et al. [13], Menzel et al. [92], or Miehe [93]. The known or given deformed configuration of the thick cantilever is plotted in Figure 6.3 in the $[\mathbf{x}_1, \mathbf{x}_3]$ plane and in Figure 6.4 in the $[\mathbf{x}_1, \mathbf{x}_2]$ plane. The cantilever is a three-dimensional extension of the classical two-dimensional Cook membrane. The left side of the shape is 48 mm high, whereas the right side is 12 mm high. The length of the shape is equal to 48 mm and the thickness is set to 8 mm. The shape is discretised by hexahedral element (HEX8) with MSC.Patran2010.2. The obtained number of elements is equal to 528 and the number of nodes is equal to 780. The shape is assumed to be clamped on the left side (blue squares in Fig. 6.3 and Fig. 6.4). Forces are applied on the right side of the shape in the vertical direction, which are illustrated in Figure 6.4 by red arrows. The applied force is equal to $5 \cdot 10^4$ units of force. The shape is assumed to have isotropic hyperelastic behaviour. The material parameters used in the simulation are summarised in Table 6.1.

The undeformed shape obtained is illustrated in Figure 6.5. As expected, the thick cantilever has the largest deformation in the \mathbf{X}_2 direction. For validation of this result, the undeformed shape illustrated in Figure 6.6 with boundary condition and load is taken as the input for the

	elastic parameters	
E	211000	MPa
ν	0.3	-
\mathbb{E}^e	$3\kappa\mathbb{I}_{\text{vol}} + 2\mu\mathbb{I}_{\text{dev}}^{\text{sym}}$ (Eq. 4.37)	MPa

Table 6.1: Numerical example: Material parameters for an isotropic hyperelastic material.

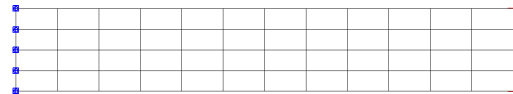


Figure 6.3: Deformed thick cantilever in the spatial configuration \mathcal{B}_t in the $[x_1, x_3]$ plane.

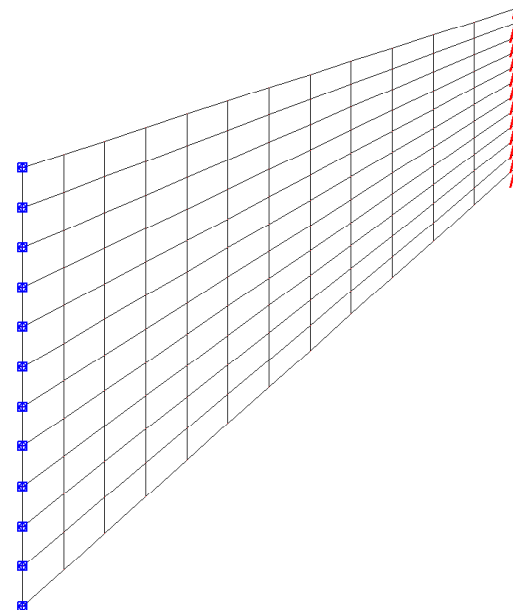


Figure 6.4: Deformed thick cantilever in the spatial configuration \mathcal{B}_t in the $[x_1, x_2]$ plane.

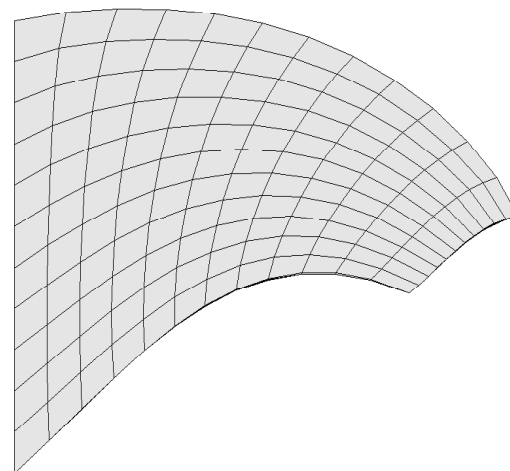


Figure 6.5: Undeformed thick cantilever in the material configuration \mathcal{B}_0 in the $[X_1, X_2]$ plane.

direct mechanical problem from Chapter 5. The computation gives the deformed configuration plotted in Figure 6.7 with equivalent von Mises stress (MPa) from Equation 5.41. ε calculated with Equation 6.37 is equal to $1.44 \cdot 10^{-17}$ mm.

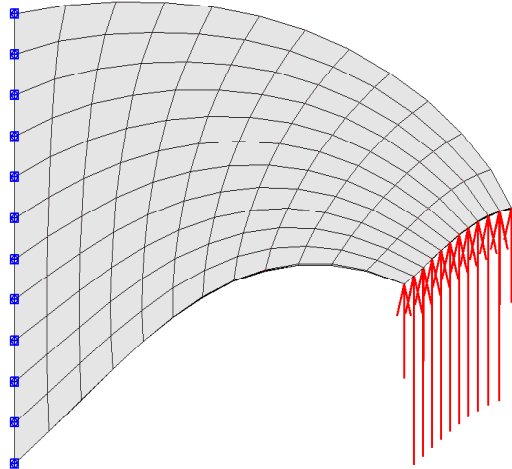


Figure 6.6: Undeformed thick cantilever in the material configuration \mathcal{B}_0 in the $[\mathbf{X}_1, \mathbf{X}_2]$ plane with loads and boundary conditions.

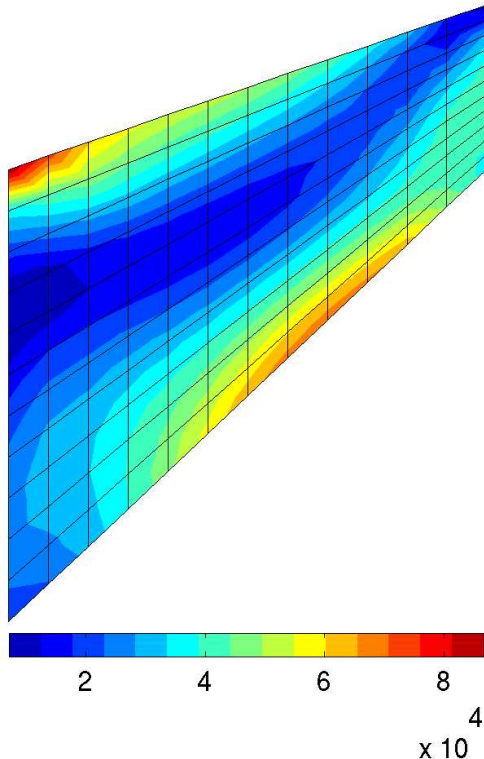


Figure 6.7: Deformed thick cantilever in the spatial configuration \mathcal{B}_t in the $[\mathbf{x}_1, \mathbf{x}_2]$ plane with equivalent von Mises stress $\sigma_{\text{eq}}^{\text{vnm}}$ (MPa) with isotropic hyperelastic behaviour.

6.3.2 Anisotropic hyperelastic material

The second example deals with the determination of the undeformed configuration of a plate (straight) with a square base in 3D. The known or given deformed configuration of the plate is plotted in Figure 6.8. The length of the plate is equal to 60 mm and the thickness is set to 3 mm. The shape is discretised by hexahedral element (HEX8) with MSC.Patran2010.2. The obtained number of elements is equal to 512 and the number of nodes is equal to 867. The border of the shape is clamped (blue squares in Figure 6.8). Forces are applied on the middle of the shape in the vertical direction, which are illustrated in Figure 6.8 by red arrows. The elements where the forces are applied are also restricted in their movements in the vertical direction. The applied force is equal to $25 \cdot 10^3$ units of force. The plate is assumed to have anisotropic hyperelastic behaviour. The material parameters used in the simulation are summarised in Table 6.2 and Table 6.3 for a cubic and a hexagonal hyperelastic material, respectively.

	elastic parameters	
E	202382	MPa
ν	0.328	-
E^e	$3\kappa\mathbb{P}_1 + 2\mu\mathbb{P}_2 + 2E_{55}\mathbb{P}_3$ (Eq. 4.45)	MPa
	$E_{55}=8000$	MPa

Table 6.2: Numerical example: Material parameters for an anisotropic (cubic) hyperelastic material.

	elastic parameters	
E^e	$\bar{\lambda}_1\mathbb{P}_1 + \bar{\lambda}_2\mathbb{P}_2 + \bar{\lambda}_3\mathbb{P}_3 + \bar{\lambda}_4\mathbb{P}_4$ (Eq. 4.106 and Eq. 4.108)	MPa
	$E_{11}=120000$	MPa
	$E_{22}=300000$	MPa
	$E_{66}=20000$	MPa
	$E_{13}=100000$	MPa
	$E_{23}=240000$	MPa

Table 6.3: Numerical example: Material parameters for an anisotropic (hexagonal- e_1) hyperelastic material.

In order to see the difference in the computed undeformed plate when considering different crystal systems, the computation is done first with an isotropic hyperelastic material with the Kelvin mode decomposition from Equation 4.37. The obtained undeformed plate is shown in Figure 6.9. The undeformed plated computed with the cubic parameters from Table 6.2 is illustrated in Figure 6.10. The undeformed configuration of the plate with the hexagonal parameters from Table 6.3 is illustrated in Figure 6.11. It can be seen that for the same force and boundary conditions, the different crystal systems give different undeformed configurations. Indeed the maximum deformation in the \mathbf{X}_3 direction attains 4.77 mm for the isotropic material, 9.57 mm for the cubic material, and 6.77 mm for the hexagonal material.

Again, for the validation of these results, the undeformed shapes obtained (Fig. 6.12, Fig. 6.14 and Fig. 6.16 with forces and boundary conditions) are used as input for the direct problem from Chapter 5 and the difference ε from Equation 6.37 is evaluated. For the isotropic case,

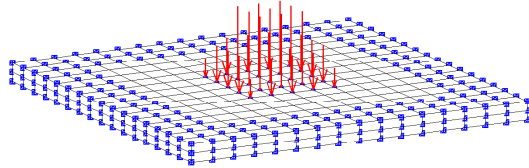


Figure 6.8: Deformed plate in the spatial configuration \mathcal{B}_t .

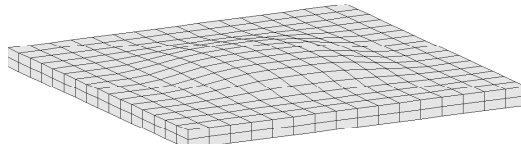


Figure 6.9: Undeformed plate in the material configuration \mathcal{B}_0 with isotropic hyperelastic behaviour.

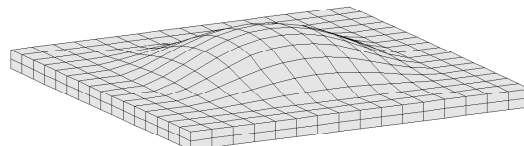


Figure 6.10: Undeformed plate in the material configuration \mathcal{B}_0 with cubic hyperelastic behaviour.

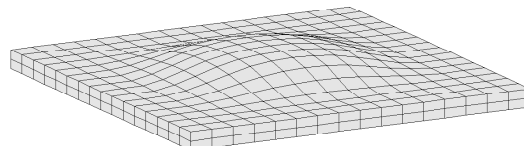


Figure 6.11: Undeformed plate in the material configuration \mathcal{B}_0 with hexagonal hyperelastic behaviour.

the computed deformed shape is illustrated in Figure 6.13 with equivalent von Mises stress (MPa) from Equation 5.41 and ε is equal to $1.68 \cdot 10^{-24}$ mm. For the cubic symmetry case, the computed deformed shape is illustrated in Figure 6.15 with equivalent von Mises stress (MPa) from Equation 5.41. ε is equal to $4.3 \cdot 10^{-14}$ mm. For the case of hexagonal behaviour, the computed deformed shape is illustrated in Figure 6.17 with equivalent von Mises stress (MPa) from Equation 5.41. ε is equal to $1.07 \cdot 10^{-21}$ mm. As expected, the different crystal systems give also different evolutions of the von Mises stress. Particularly for the hexagonal case, the predicted evolution is concentrated along \mathbf{x}_1 .

The third example deals with the determination of the undeformed configuration of a plate (straight and rectangular) with two layers in 3D under a distributed tension force, as in Germain et al. [13] and Apel [22]. The known or given deformed configuration of the two layers is plotted in Figure 6.18 in the $[\mathbf{x}_1, \mathbf{x}_2]$ plane. The length of the plate is equal to 100 mm, the width is set to 20 mm, and the thickness is equal to 6 mm. The shape is discretised by hexahedral element (HEX8) with MSC.Patran2010.2. The obtained number of elements is equal to 2000 and the

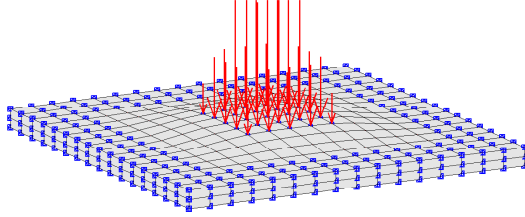


Figure 6.12: Undeformed plate in the material configuration \mathcal{B}_0 with forces and boundary conditions (isotropic material).

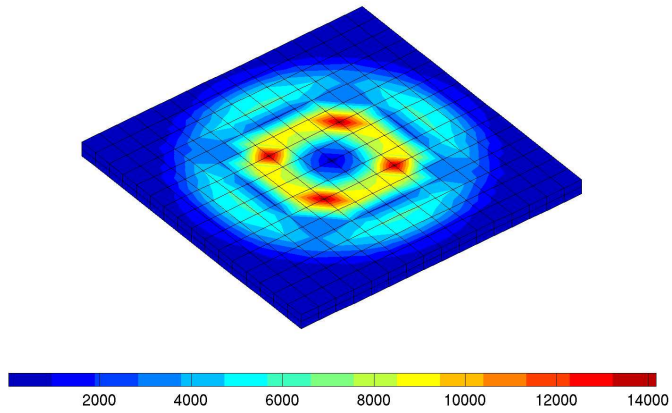


Figure 6.13: Deformed plate in the spatial configuration \mathcal{B}_t with equivalent von Mises stress $\sigma_{\text{eq}}^{\text{vm}}$ (MPa) (isotropic material).

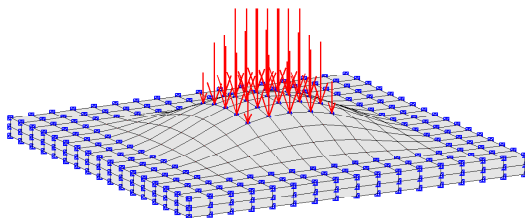


Figure 6.14: Undeformed plate in the material configuration \mathcal{B}_0 with forces and boundary conditions (cubic material).

number of nodes is equal to 2805. The left side of the shape is fixed in the three directions (blue squares in Fig. 6.18). Forces are applied on the right extremity of the shape in the x_1 direction, which are illustrated in Figure 6.18 by red arrows. The applied force is equal to 10^4 units of force. The plate is assumed to have orthotropic hyperelastic behaviour. The material parameters used in the simulation are summarised in Table 6.4.

The orthotropic axes of both layers make angles of α and β with the Cartesian basis, as in Germain et al. [13] and Apel [22] (Fig. 6.19). Thus the orthotropic tensor \mathbb{E}^e in Chapter 4 becomes

$$\mathbb{E}^e = \mathbf{R} \cdot \mathbb{E}_{\text{orthorhombic}}^e \cdot \mathbf{R}^T \quad (6.38)$$

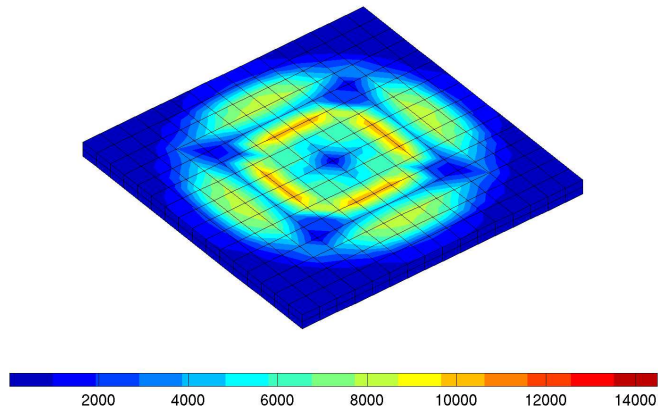


Figure 6.15: Deformed plate in the spatial configuration \mathcal{B}_t with equivalent von Mises stress $\sigma_{\text{eq}}^{\text{vm}}$ (MPa) (cubic material).

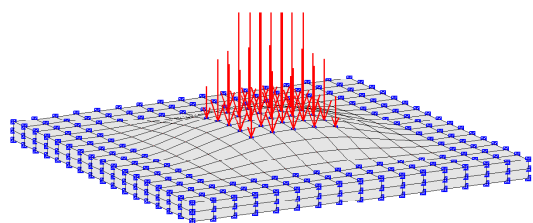


Figure 6.16: Undeformed plate in the material configuration \mathcal{B}_0 with forces and boundary conditions (hexagonal material).

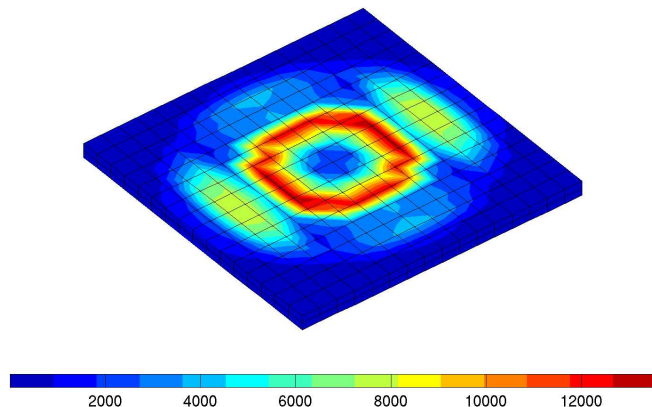


Figure 6.17: Deformed plate in the spatial configuration \mathcal{B}_t with equivalent von Mises stress $\sigma_{\text{eq}}^{\text{vm}}$ (MPa) (hexagonal material).

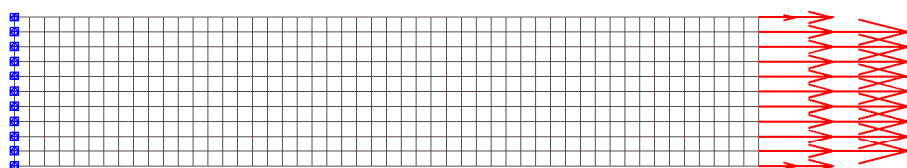


Figure 6.18: Deformed layer in the spatial configuration \mathcal{B}_t in the $[x_1, x_2]$ plane.

	elastic parameters	
	$E_{11} = 269511$	MPa
	$E_{22} = 281300$	MPa
	$E_{33} = 121288$	MPa
	$E_{44} = 90000$	MPa
	$E_{55} = 150000$	MPa
	$E_{66} = 70000$	MPa
	$E_{12} = 132270$	MPa
	$E_{13} = 95308$	MPa
	$E_{23} = 70423$	MPa

Table 6.4: Numerical example: Material parameters for an anisotropic (orthotropic) hyperelastic material.

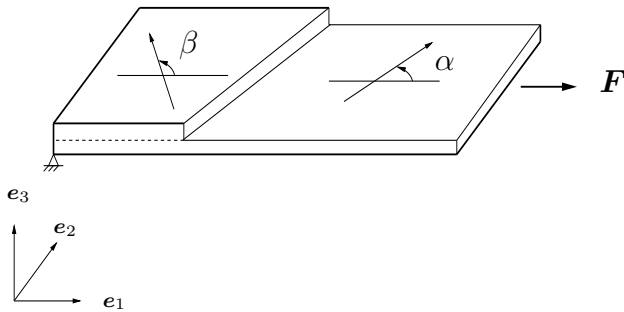


Figure 6.19: Deformed shape of straight, rectangular geometry in the spatial configuration \mathcal{B}_t .

with

$$\mathbf{R} = \begin{bmatrix} \cos^2(\Theta) & \sin^2(\Theta) & 0 & -2\cos(\Theta)\sin(\Theta) & 0 & 0 \\ \sin^2(\Theta) & \cos^2(\Theta) & 0 & 2\cos(\Theta)\sin(\Theta) & 0 & 0 \\ 0 & 0 & 1 & 0 & 0 & 0 \\ \cos(\Theta)\sin(\Theta) & -\cos(\Theta)\sin(\Theta) & 0 & \cos^2(\Theta) - \sin^2(\Theta) & 0 & 0 \\ 0 & 0 & 0 & 0 & \cos(\Theta) & \sin(\Theta) \\ 0 & 0 & 0 & 0 & -\sin(\Theta) & \cos(\Theta) \end{bmatrix}, \quad (6.39)$$

where $\Theta = \alpha$ or β .

In order to see the difference in the computed undeformed plate when considering different angles α and β , the computation is done first for $\alpha=0$ and $\beta=0$. The undeformed plate obtained is shown in Figure 6.20. The undeformed plate computed for $\alpha=\pi/6$ and $\beta=5\pi/6$ is illustrated in Figure 6.21. The undeformed configuration of the plate for $\alpha=5\pi/6$ and $\beta=\pi/6$ is illustrated in Figure 6.22. It can be seen that for the same force and boundary conditions, the different orthotropic angles considered give different undeformed configurations. As expected, Figure 6.22 rotates in the opposite direction from that of the undeformed layers in Figure 6.21. The length of the plate is reduced to 82.02 mm, 84.57 mm and 84.57 mm, respectively.

Again for the validation the obtained undeformed shapes (Fig. 6.23, Fig. 6.25 and Fig. 6.27 with forces and boundary conditions) are used as input for the solution of the direct problem from Chapter 5 and the difference ε from Equation 6.37 is evaluated. For $\alpha=0$ and $\beta=0$ the computed deformed shape is illustrated in Figure 6.24 with equivalent von Mises stress (MPa) from Equation 5.41. ε is equal to $3.12 \cdot 10^{-11}$ mm. For $\alpha=\pi/6$ and $\beta=5\pi/6$ the computed deformed

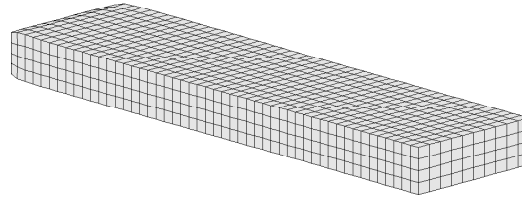


Figure 6.20: Undeformed layers in the material configuration \mathcal{B}_0 with $\alpha=0$ and $\beta=0$.

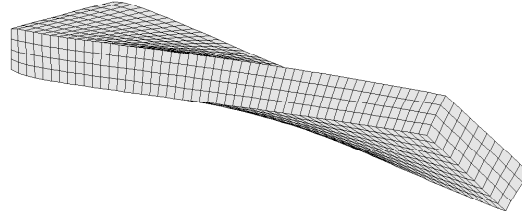


Figure 6.21: Undeformed layers in the material configuration \mathcal{B}_0 with $\alpha=\pi/6$ and $\beta=5\pi/6$.

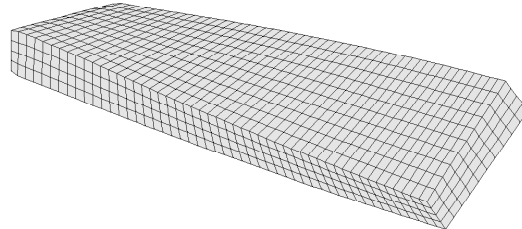


Figure 6.22: Undeformed layers in the material configuration \mathcal{B}_0 with $\alpha=5\pi/6$ and $\beta=\pi/6$.

shape is illustrated in Figure 6.26 with equivalent von Mises stress (MPa) from Equation 5.41. ε is equal to $6.98 \cdot 10^{-22}$ mm. For $\alpha=5\pi/6$ and $\beta=\pi/6$ the computed deformed shape is illustrated in Figure 6.28 with equivalent von Mises stress (MPa) from Equation 5.41. ε is equal to $6.87 \cdot 10^{-22}$ mm. As expected, the evolution of the von Mises stresses is symmetric for the case when $\alpha=0$ and $\beta=0$. It can also be seen that for the two last examples, the stresses are equal and that each evolution is symmetric when compared to the other. For example, the maximum stress is concentrated on the upper left side in Figure 6.26 and on the upper right side in Figure 6.28.

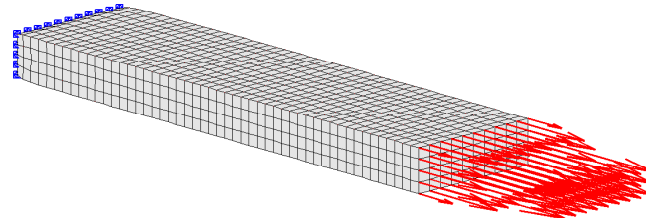


Figure 6.23: Undeformed layers in the material configuration \mathcal{B}_0 for $\alpha=0$ and $\beta=0$ with forces and boundary conditions.

It has been found that ε from Equation 6.37 is between $3.12 \cdot 10^{-11}$ mm and $1.68 \cdot 10^{-24}$ mm. It can be therefore be concluded that the inverse mechanical formulation succeeds in finding the appropriate undeformed configuration when dealing with hyperelastic behaviour.

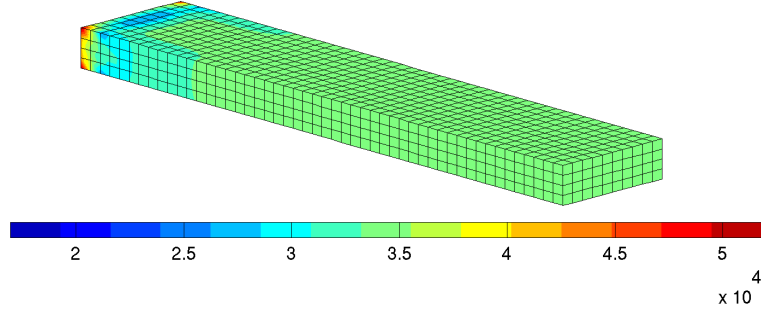


Figure 6.24: Deformed layers in the spatial configuration \mathcal{B}_t for $\alpha=0$ and $\beta=0$ with equivalent von Mises stress $\sigma_{\text{eq}}^{\text{vm}}$ (MPa).

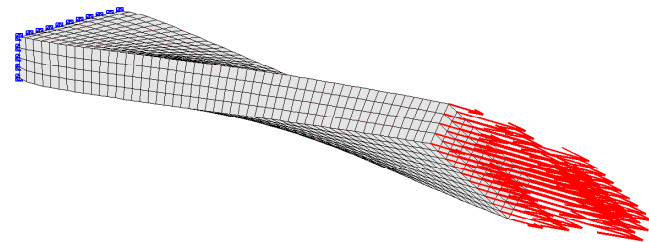


Figure 6.25: Undeformed layers in the material configuration \mathcal{B}_0 for $\alpha=\pi/6$ and $\beta=5\pi/6$ with forces and boundary conditions.

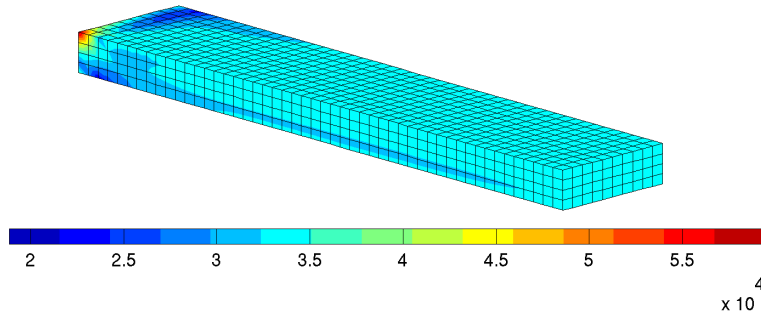


Figure 6.26: Deformed layers in the spatial configuration \mathcal{B}_t for $\alpha=\pi/6$ and $\beta=5\pi/6$ with equivalent von Mises stress $\sigma_{\text{eq}}^{\text{vm}}$ (MPa).

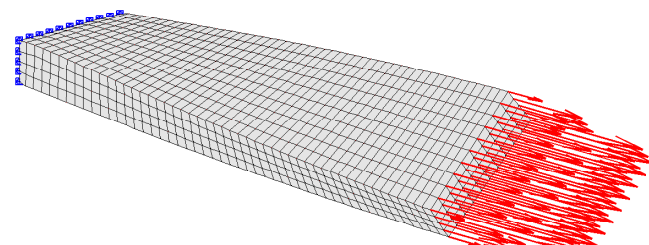


Figure 6.27: Undeformed layers in the material configuration \mathcal{B}_0 for $\alpha=5\pi/6$ and $\beta=\pi/6$ with forces and boundary conditions.

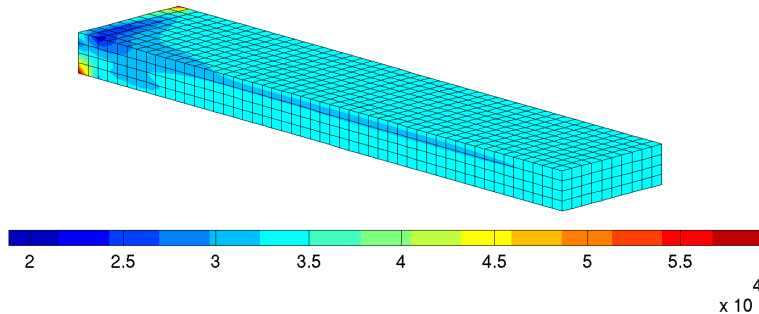


Figure 6.28: Deformed layers in the spatial configuration \mathcal{B}_t for $\alpha=5\pi/6$ and $\beta=\pi/6$ with equivalent von Mises stress σ_{eq}^{vm} (MPa).

6.3.3 Isotropic elastoplastic material

The next example deals with the determination of the undeformed configuration of a plate (straight and rectangular) in 3D. The known or given deformed configuration of the plate is plotted in Figure 6.29. The length of the plate is equal to 50 mm, the width is set to 25 mm, and the thickness is equal to 2 mm. The shape is discretised by hexahedral element (HEX8) with MSC.Patran2010.2. The obtained number of elements is equal to 338 and the number of nodes is equal to 756. The left side (one-half) of the shape is fixed in the three directions (blue squares in Fig. 6.29). Forces are applied on the other half in the vertical direction, which are illustrated in Figure 6.29 by red arrows. The applied force is equal to 40 units of force in 40 increments. The plate is assumed to have isotropic elastoplastic behaviour. The material parameters used in the simulation are summarised in Table 6.5. The undeformed plate obtained is shown in Figure 6.30.

	elastic parameters	
E	211000	MPa
ν	0.3	-
E^e	$3\kappa\mathbb{I}_{vol} + 2\mu\mathbb{I}_{dev}^{sym}$	MPa
	plastic parameters	
h	100	MPa
σ_0	415	MPa
σ_∞	750	MPa
w	15	-
H	\mathbb{I}_{dev}^{sym}	-

Table 6.5: Numerical example: Material parameters for an isotropic elastoplastic material.

Again, to validate the results, the undeformed shape obtained (Fig. 6.31 with forces and boundary conditions) is used as the input for the solution of the direct problem from Chapter 5 and the difference ε from Equation 6.37 is evaluated. The deformed shape obtained is illustrated in Figure 6.32 with equivalent von Mises stress (MPa) from Equation 5.41 and in Figure 6.33 with equivalent plastic strain (-) from Equation 5.42. ε is equal to $3.24 \cdot 10^3$ mm, i.e., the computation failed to restore the given deformed configuration. Thus Figure 6.31 is not the sought undeformed configuration of the given deformed configuration in Figure 6.29.

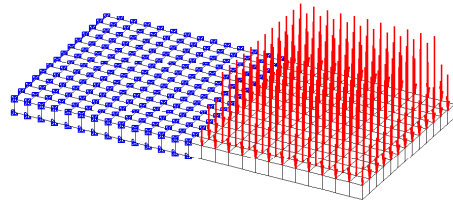


Figure 6.29: Deformed plate in the spatial configuration \mathcal{B}_t .

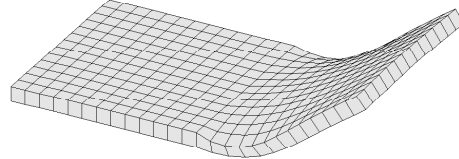


Figure 6.30: Undeformed plate in the material configuration \mathcal{B}_0 .

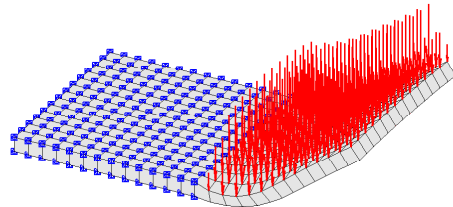


Figure 6.31: Undeformed plate in the material configuration \mathcal{B}_0 with load and boundary conditions.

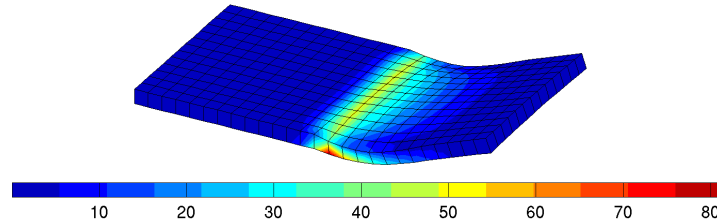


Figure 6.32: Deformed plate in the spatial configuration \mathcal{B}_t with equivalent von Mises stress $\sigma_{\text{eq}}^{\text{vm}}$ (MPa).

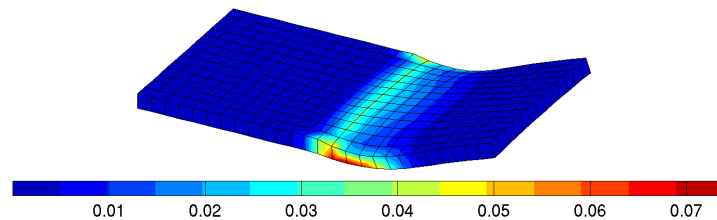


Figure 6.33: Deformed plate in the spatial configuration \mathcal{B}_t with equivalent plastic strain E_{eq}^p (-).

For the second example in isotropic elastoplasticity, the geometry, boundary conditions, forces, and material parameters from Section 5.3.3 are used. Here the straight shape is considered as the given deformed configuration of the component, i.e., Figure 5.11 is now the deformed

configuration and the undeformed configuration is sought. The undeformed plate obtained is shown in Figure 6.34 in the $[X_1, X_3]$ plane.

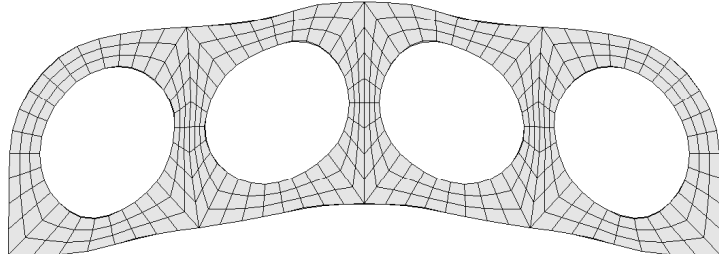


Figure 6.34: Undeformed plate with four holes in the material configuration \mathcal{B}_0 in the $[X_1, X_3]$ plane.

Again, for validation, the undeformed shape obtained (Fig. 6.35 with forces and boundary conditions) is used as the input for the solution of the direct problem from Chapter 5 and the difference ε from Equation 6.37 is evaluated. The deformed shape obtained is illustrated in Figure 6.36 with equivalent von Mises stress (MPa) from Equation 5.41 and in Figure 6.37 with equivalent plastic strain (-) from Equation 5.42 both in the $[x_1, x_3]$ plane. ε is equal to 21.73 mm, i.e., the computation failed again to restore the given deformed configuration. Thus Figure 6.35 is not the sought undeformed configuration of the given deformed configuration in Figure 5.11.

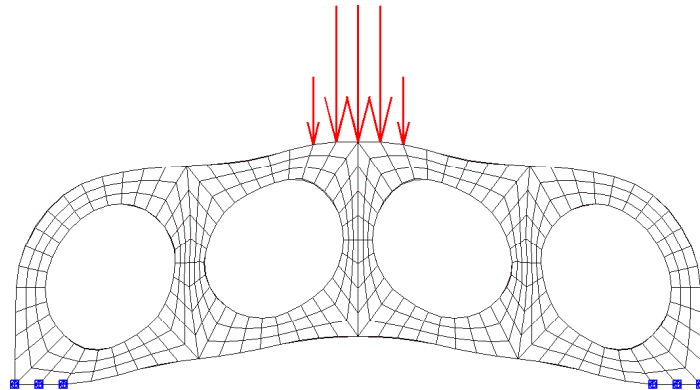


Figure 6.35: Undeformed plate with four holes in the material configuration \mathcal{B}_0 ($[X_1, X_3]$ plane) with load and boundary conditions.

It has been found that ε from Equation 6.37 is equal to 21.73 mm and $3.24 \cdot 10^3$ mm. It can be therefore be concluded that the inverse mechanical formulation does not succeed in finding the appropriate undeformed configuration when dealing with elastoplastic behaviour. The next section will discuss why, for elastoplastic behaviour, the inverse boundary value approach failed to find the undeformed configuration of a functional component when the deformed configuration, the load, and the boundary conditions were given.

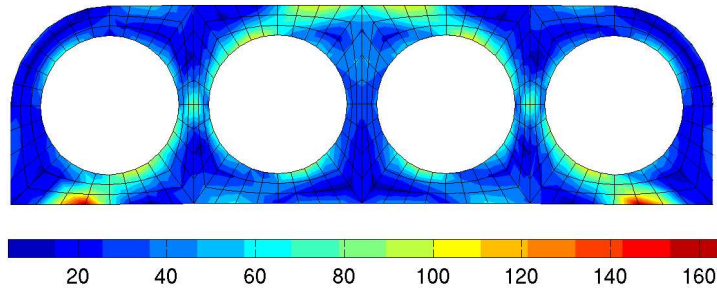


Figure 6.36: Deformed plate with four holes in the spatial configuration \mathcal{B}_t ($[x_1, x_3]$ plane) with equivalent von Mises stress $\sigma_{\text{eq}}^{\text{vm}}$ (MPa).

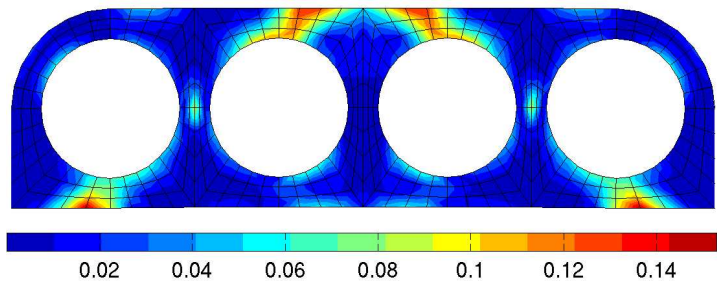


Figure 6.37: Deformed plate with four holes in the spatial configuration \mathcal{B}_t ($[x_1, x_3]$ plane) with equivalent plastic strain E_{eq}^p (-).

6.4 Discussion

It was shown in the previous section that the inverse formulation is not suitable for the determination of the undeformed configuration of a functional component in elastoplasticity when only the deformed configuration, the load, and the boundary conditions are given. For hyperelastic behaviour, on the contrary, the inverse problem gives appropriate results. This result arises from the fact that in hyperelasticity, the solution is unique whereas in elastoplasticity, the solution is multiple. These affirmations can be demonstrated by considering an uniaxial tension experiment as illustrated in Figure 6.38.

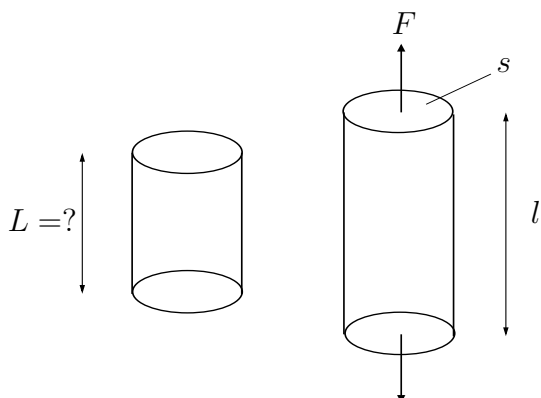


Figure 6.38: Uniaxial tension experiment with undeformed (left) and deformed (right) configurations.

The deformed configuration has a section s , a deformed length l , and is subjected to a force F . The undeformed length sought is denoted by L . The equilibrium equation of the uniaxial tension test gives

$$\sigma = \frac{F}{s} \quad (6.40)$$

and the kinematic theory enables expressing the deformation ε of the specimen as a function of its initial and final length by

$$\varepsilon = \frac{l}{L} - 1. \quad (6.41)$$

Figure 6.39 illustrates the stress-strain curve for the uniaxial tension experiment, which are related by the following equation

$$\sigma = E\varepsilon, \quad (6.42)$$

where E is the tangent of the curve (Young's modulus). The black arrow denotes the direct evolution and the red arrow the inverse evolution.

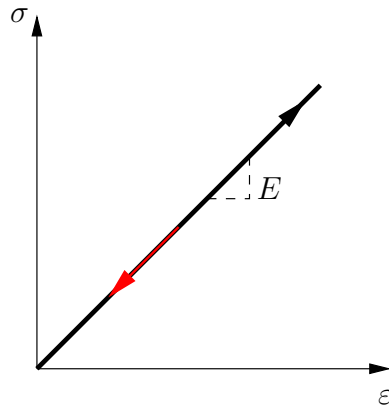


Figure 6.39: Uniaxial stress–strain curve in hyperelasticity.

By equating Equation 6.40 and Equation 6.42, it follows that

$$\frac{F}{s} = E\varepsilon. \quad (6.43)$$

By substituting the deformation ε in Equation 6.41, the previous equation becomes

$$\frac{F}{s} = E \left(\frac{l}{L} - 1 \right) \quad (6.44)$$

$$\frac{F}{sE} + 1 = \frac{l}{L} \quad (6.45)$$

$$L = \left(\frac{F}{sE} + 1 \right)^{-1} l. \quad (6.46)$$

Since the force F , the section s , the Young's modulus E , and the deformed length l are known, the undeformed length L is unique. No other condition is needed.

In elastoplasticity, the deformation depends on the elastic and plastic strains as follows

$$\varepsilon = \varepsilon^e + \varepsilon^p. \quad (6.47)$$

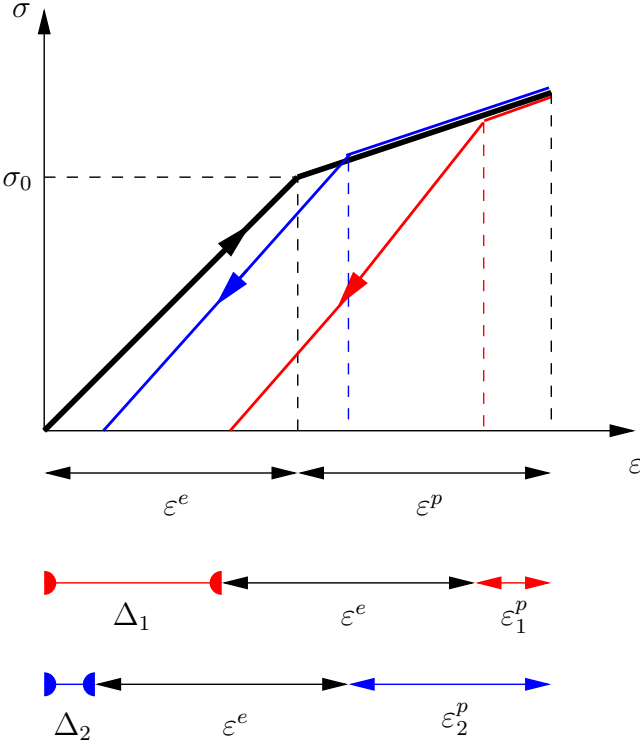


Figure 6.40: Uniaxial stress–strain curve in elastoplasticity.

Figure 6.40 illustrates the stress-strain curve for the uniaxial tension experiment in elastoplasticity. σ_0 denotes the elastic limit. The stress equation thus becomes

$$\begin{aligned}\sigma &= E\varepsilon^e \\ &= E(\varepsilon - \varepsilon^p) \\ &= E\left(\frac{l}{L} - 1 - \varepsilon^p\right).\end{aligned}\tag{6.48}$$

By employing Equation 6.40, it then follows that

$$\frac{F}{s} = E\left(\frac{l}{L} - 1 - \varepsilon^p\right)\tag{6.49}$$

and thus the undeformed length sought is

$$L = \left(\frac{F}{sE} + 1 + \varepsilon^p\right)^{-1} l.\tag{6.50}$$

The only remaining unknown is the plastic strain ε^p , which appears in the yield function

$$|\sigma| \leq \sigma_y = \sigma_o + h\varepsilon^p.\tag{6.51}$$

Therefore L and ε^p have to satisfy Equation 6.50 and Equation 6.51. Equation 6.50 is illustrated by the blue curve and the inequality in Equation 6.51 is represented by the yellow surface in Figure 6.41. The solution of this system of equations is thus the green curve in Figure 6.41, which is the intersection between the surface and the curve. So, if ε^p is unknown the undeformed length

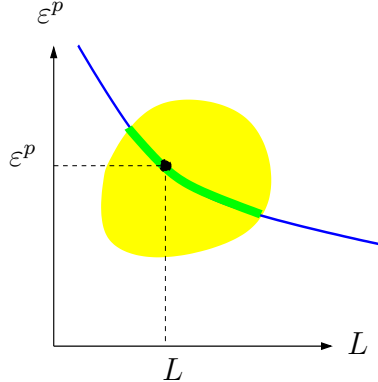


Figure 6.41: Schematic representation of Equation 6.50 and Equation 6.51.

L is not unique, all L on the green curve are possible solutions. On the other hand, if ε^p is known, then L is unique.

Furthermore, if the plastic strains are not previously known but are then given at the beginning of the inverse formulation, the computation is unable to find an appropriate path to the undeformed configuration sought. The computation might follow the red curve in Figure 6.40 and then calculate the wrong plastic deformation ε_1^p , and since the elastic deformation is unique, an error Δ_1 will appear, as illustrated in Figure 6.32 and Figure 6.33 or in Figure 6.36 and Figure 6.37. The computation might also follow the blue curve in Figure 6.40 and then again the wrong plastic deformation ε_2^p is calculated. This also leads to an error Δ_2 .

Following the macroscopic model presented in Chapter 3, the entire set of internal variables $\mathcal{IV} = \{\mathbf{E}^p, \alpha\}$ of the deformed functional component has then to be given at the beginning of the computation of the undeformed configuration. The greatest difficulty in applying this option arises from the lack of knowledge of their amount at each Gauss point on the mesh of the shape. Next, two examples will illustrate the previous discussion, in which the set of internal variables is given as input to the inverse formulation so that an appropriated undeformed configuration can be found. First the direct mechanical formulation presented in Chapter 5 is computed for a given undeformed configuration. The deformed configuration obtained and the set of internal variables are then used in the inverse mechanical formulation. The given and computed undeformed configurations are compared by calculating

$$\varepsilon = \|\mathbf{X}_{\text{given to the direct problem}} - \mathbf{X}_{\text{obtained from the inverse problem}}\|^2 \text{ mm.} \quad (6.52)$$

A schematic view is given in Figure 6.42.

Remark: In the solution of the inverse mechanical formulation, only one increment is required. Indeed, if the set of internal variables is given, the problem becomes elastic and path independent.

6.4.1 Example 1

For the first example, the same geometry, forces, and material parameters as in Section 6.3.3 are used. The undeformed configuration is here the straight plate as illustrated in Figure 6.43. The deformed configuration obtained with the direct mechanical formulation is shown in Figure 6.44 with the equivalent von Mises stress $\sigma_{\text{eq}}^{\text{vm}}$ (MPa) calculated with Equation 5.41 and in Figure 6.45

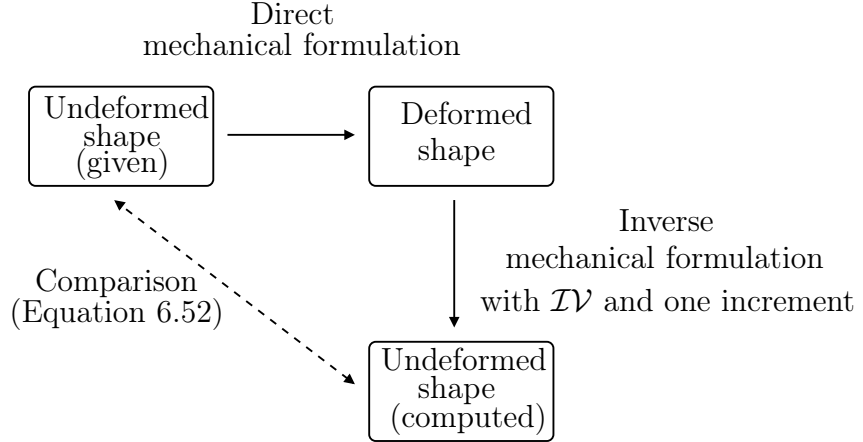


Figure 6.42: Schematic view of solving the inverse mechanical problem in elastoplasticity.

with the equivalent plastic strain E_{eq}^p (-) calculated with Equation 5.42. This deformed configuration and the corresponding set of internal variables are then taken as the input for the inverse mechanical problem as presented above. The computed undeformed configuration is illustrated in Figure 6.46. The calculation of ε in Equation 6.52 gives $3.64 \cdot 10^{-18}$ mm.

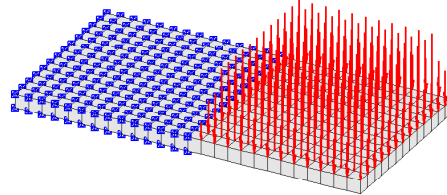


Figure 6.43: Undeformed plate in the material configuration \mathcal{B}_0 with boundary conditions and loads.

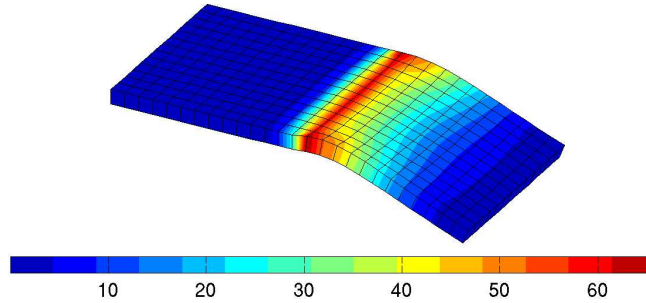


Figure 6.44: Deformed plate in the spatial configuration \mathcal{B}_t with equivalent von Mises stress $\sigma_{\text{eq}}^{\text{vm}}$ (MPa).

6.4.2 Example 2

For the second example, the same geometry, forces, and material parameters as in Section 5.3.3 and in Section 6.3.3 are used. The undeformed configuration is illustrated in Figure 5.11. The deformed configuration obtained is shown in Figure 5.12 with the equivalent von Mises stress

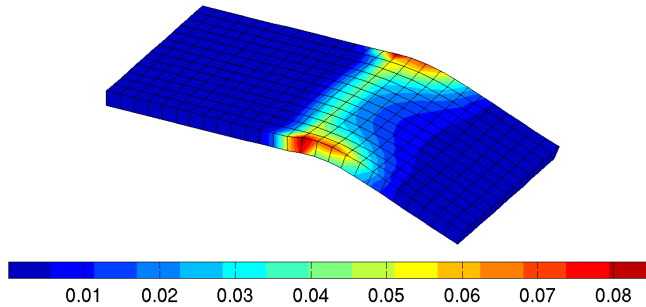


Figure 6.45: Deformed plate in the spatial configuration \mathcal{B}_t with equivalent plastic strain E_{eq}^p (-).

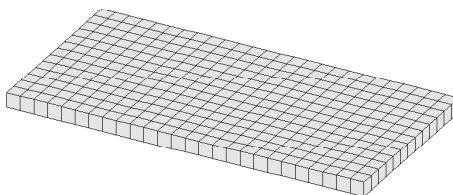


Figure 6.46: Undeformed plate in the material configuration \mathcal{B}_0 computed with the set of internal variables.

$\sigma_{\text{eq}}^{\text{vm}}$ (MPa) calculated with Equation 5.41 and in Figure 5.13 with the equivalent plastic strain E_{eq}^p (-) calculated with Equation 5.42. This deformed configuration and the corresponding set of internal variables are then taken as the input for the inverse mechanical problem as presented above. The computed undeformed configuration is illustrated in Figure 6.47. The calculation of ε in Equation 6.52 gives $9.68 \cdot 10^{-22}$ mm.

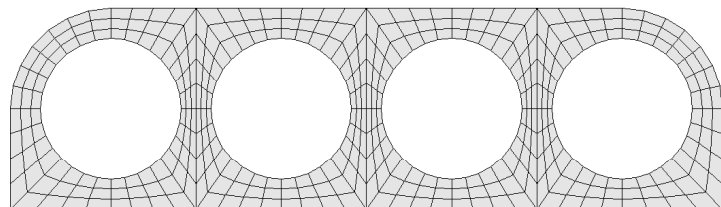


Figure 6.47: Undeformed thick cantilever in the material configuration \mathcal{B}_0 ($[X_1, X_3]$ plane) computed with the set of internal variables.

It has been found that ε from Equation 6.52 is equal to $9.68 \cdot 10^{-22}$ mm and $3.64 \cdot 10^{-18}$ mm. It can therefore be concluded that the inverse mechanical formulation succeeds in finding the appropriate undeformed configuration under elastoplastic behaviour when the set of internal variables is also given.

Since in general, the value of the set of internal variables is previously unknown at each Gauss point of the mesh, especially in forming processes, shape optimisation written as an inverse problem allows determining the undeformed configuration of a functional component in elastoplasticity, when only the deformed configuration, the force, and the boundary conditions are given. This particular case of shape optimisation is described in the next chapter.

Determining the undeformed shape from shape optimisation

As shown in the previous chapter, the determination of the undeformed shape of a functional component in elastoplasticity is achievable when the set of internal variables is also given. Since the set of internal variables is in general unknown, especially in forming processes, a challenging problem is to determine the undeformed shape for elastoplastic behaviour using shape optimisation. It is indeed possible to predict the original shape of a functional component in the sense of an inverse problem via successive iterations of the direct mechanical formulation.

This chapter is organised as follows: First, the definition of the optimisation problem for inverse form finding is presented. A brief review of the Limited Memory Broyden–Fletcher–Goldfarb–Shanno (L-BFGS) method is presented, following Nocedal et al. [53]. The L-BFGS was chosen for its efficiency (Nocedal et al. [53]) and will be used in the subsequent numerical examples. A discrete sensitivity analysis, which is necessary for the use of gradient-based optimisation algorithms, is next developed, following Schwarz [41], Luenberger [52], Nocedal et al. [53], Germain et al. [57, 67, 69], and Scherer [66]. The material coordinates or FE nodes \mathbf{X} are chosen as the design variables, i.e., node-based shape optimisation. The same discretisation is used for the material and spatial configurations of the functional component. An algorithm for avoiding mesh distortions, which might appear when taking the coordinates of the shape as design variables as in Scherer et al. [65], is also presented, following Germain et al. [67, 68]. Some numerical examples for isotropic and anisotropic hyperelastic materials as well as for elastoplastic material illustrate the previous developments. Parts of this chapter have been published by Germain et al. in [57, 67, 68, 69, 70].

7.1 Definition of the optimisation problem

The mathematical formulation of optimisation (minimisation or maximisation) problems is defined by the vector of design variables, the objective function, and constraint functions on the volume, the thickness, etc. If no constraints are imposed, the optimisation problem is said to be unconstrained. In this work, the inverse form finding problem is defined by the objective function f , which is a least squares minimisation of the difference between the target and the current deformed configuration of the workpiece,

$$\min_{\mathbf{X}} f(\mathbf{X}) = \frac{1}{2} \|\mathbf{x}^{\text{target}} - \mathbf{x}^{\text{current}}(\mathbf{X})\|^2, \quad (7.1)$$

where the material coordinates \mathbf{X} are the design variables, i.e., node-based shape optimisation. No constraint functions are defined, i.e., the inverse form finding problem is an unconstrained problem and the objective function f has to be minimised in order to find the sought undeformed

configuration of the workpiece. In Equation 7.1, the target deformed configuration $\mathbf{x}^{\text{target}}$ corresponds to the known and given deformed configuration. The current deformed configuration $\mathbf{x}^{\text{current}}$ is computed by the direct mechanical formulation presented in Chapter 5 from the undeformed configuration \mathbf{X} computed via an optimisation algorithm. Optimisation algorithms can be divided into three categories: Basic Descent Methods, Conjugate Gradient Methods, and Quasi-Newton Methods, see for example Luenberger [52], Nocedal et al. [53] and Schmidt [54]. In this work, the Limited Memory Broyden–Fletcher–Goldfarb–Shanno (L-BFGS) method, named after its discoverers, will be used. It is a gradient-based optimisation algorithm and belongs to the category of Limited Memory Quasi-Newton methods, which allows solving large problems. Gradient-based optimisation algorithms require the gradient of the objective function with respect to the design variables, i.e., a sensitivity analysis (presented subsequently). Furthermore the Hessian of the objective function is approximated in Limited Memory Quasi-Newton methods, and does not need to be exactly computed or entirely stored. Algorithm 7.1 presents briefly the shape optimisation process used for finding the undeformed configuration of a workpiece.

Remark: In this work the design variables are chosen as the entire nodes \mathbf{X} given by the discretisation but without the nodes which are subjected to displacement constraints, i.e., fixed in one or more directions. Scherer in [66] and Haslinger et al. in [94] add a third category, the controlled nodes, which are the nodes in the interior of the shape. Here mesh motion techniques for moving the interior nodes are used.

Algorithm 7.1: Pseudo-algorithm view of the shape optimisation concept applied to inverse form finding.

Data: material parameters, optimisation parameters, \mathfrak{F} , $\mathcal{B}_t^{\text{target}} = \mathcal{B}_t^{\text{current}} = \mathcal{B}_0^{\text{current}}$, $\varepsilon = 10^{-6}$;

Initialisation: Solve the direct boundary value problem in Chapter 5 with $\mathcal{B}_0^{\text{current}}$ and obtain $\mathcal{B}_t^{\text{current}}$;

Compute f by comparing $\mathcal{B}_t^{\text{current}}$ with $\mathcal{B}_t^{\text{target}}$;

while $f \geq \varepsilon$ **do**

Find a new \mathcal{B}_0 with a gradient-based optimisation algorithm, for example, Algorithm 7.2;

Solve the direct boundary value problem in Chapter 5 with \mathcal{B}_0 and obtain $\mathcal{B}_t^{\text{current}}$;

Compute f by comparing $\mathcal{B}_t^{\text{current}}$ with $\mathcal{B}_t^{\text{target}}$;

end

return \mathcal{B}_0 ;

7.2 The Limited Memory Broyden–Fletcher–Goldfarb–Shanno method

The L-BFGS is based on line search methods. At each iteration k , the line search gives

$$\mathbf{X}^{k+1} = \mathbf{X}^k + \alpha^k \mathbf{p}^k, \quad (7.2)$$

where α^k is the step length and \mathbf{p}^k is the search direction. The search direction \mathbf{p}^k is a function of the Hessian of the objective function and the gradient of the objective function

$$\mathbf{p}^k = -\mathcal{H}^k \cdot \frac{df(\mathbf{X}^k)}{d\mathbf{X}}. \quad (7.3)$$

The Hessian is updated at every iteration by calculating

$$\mathcal{H}^{k+1} = (\mathbf{V}^k)^T \cdot \mathcal{H}^k \cdot \mathbf{V}^k + \rho^k \mathbf{s}^k \cdot (\mathbf{s}^k)^T, \quad (7.4)$$

where

$$\rho^k = \frac{1}{(\mathbf{y}^k)^T \cdot \mathbf{s}^k}, \quad (7.5)$$

$$\mathbf{V}^k = \mathbf{I} - \rho^k \mathbf{y}^k \cdot (\mathbf{s}^k)^T, \quad (7.6)$$

$$\mathbf{s}^k = \mathbf{X}^{k+1} - \mathbf{X}^k \quad (7.7)$$

and

$$\mathbf{y}^k = \frac{df(\mathbf{X}^{k+1})}{d\mathbf{X}} - \frac{df(\mathbf{X}^k)}{d\mathbf{X}}. \quad (7.8)$$

The step length α^k is computed from a line search and has to satisfy the Wolfe conditions, i.e., the decrease condition set in Equation 7.9

$$f(\mathbf{X}^k + \alpha^k \mathbf{p}^k) \leq f(\mathbf{X}^k) + c_1 \alpha^k \left(\frac{df(\mathbf{X}^k)}{d\mathbf{X}} \right)^T \cdot \mathbf{p}^k \quad (7.9)$$

and the curvature condition given by Equation 7.10

$$\left(\frac{df(\mathbf{X}^k + \alpha^k \mathbf{p}^k)}{d\mathbf{X}} \right)^T \cdot \mathbf{p}^k \geq c_2 \left(\frac{df(\mathbf{X}^k)}{d\mathbf{X}} \right)^T \cdot \mathbf{p}^k, \quad (7.10)$$

where $c_1 \in (0, 1)$ and $c_2 \in (c_1, 1)$. If a backtracking approach is used, the curvature condition is no longer relevant: the decrease condition alone is sufficient. A pseudo-algorithmic view of the L-BFGS algorithm is given in Algorithm 7.2.

Remark:

- If \mathcal{H} in Equation 7.3 is replaced by the identity matrix, it becomes the Steepest Method.
- Equation 7.9 is also called the Armijo condition.
- In the subsequent numerical examples the open source program from Schmidt [54] is used.

7.3 Sensitivity analysis

In order to use gradient-based optimisation algorithms such as Algorithm 7.2, the gradient of the objective function has to be calculated, i.e., a sensitivity analysis has to be performed. Numerical and analytical gradients of the objective function for inverse form finding problems can be performed.

Algorithm 7.2: Pseudo-algorithm view of L-BFGS algorithm [53].

Initialisation: Choose a starting undeformed configuration \mathbf{X}^0 ;

Set $m=100$ [54], $k=0$ and $\varepsilon = 10^{-8}$;

Choose the initial Hessian approximation \mathcal{H}^0 ;

repeat

Compute $\mathbf{p}^k = -\mathcal{H}^k \cdot \frac{df(\mathbf{X}^k)}{d\mathbf{X}}$;

Compute $\mathbf{X}^{k+1} = \mathbf{X}^k + \alpha^k \mathbf{p}^k$;

Compute $\mathbf{s}^k = \mathbf{X}^{k+1} - \mathbf{X}^k$ and $\mathbf{y}^k = \frac{df(\mathbf{X}^{k+1})}{d\mathbf{X}} - \frac{df(\mathbf{X}^k)}{d\mathbf{X}}$;

Compute \mathcal{H}^{k+1} ;

Set $k = k + 1$;

until $\|\frac{df(\mathbf{X}^k)}{d\mathbf{X}}\| < \varepsilon$;

7.3.1 Numerical gradient

In gradient-based optimisation algorithms, numerical gradients can be found by the finite difference method. The finite difference method derives from the first order Taylor series, where

$$f(\mathbf{X} + h) = f(\mathbf{X}) + \frac{df(\mathbf{X})}{d\mathbf{X}}h + \mathcal{O}(h) \quad (7.11)$$

or

$$f(\mathbf{X} - h) = f(\mathbf{X}) - \frac{df(\mathbf{X})}{d\mathbf{X}}h - \mathcal{O}(h), \quad (7.12)$$

where h is the spacing. By equating the rest $\mathcal{O}(h)$ to zero, in Equation 7.11 and in Equation 7.12, the forward difference is given by

$$\frac{df(\mathbf{X})}{d\mathbf{X}} = \frac{f(\mathbf{X} + h) - f(\mathbf{X})}{h} \quad (7.13)$$

and the backward difference is provided by

$$\frac{df(\mathbf{X})}{d\mathbf{X}} = \frac{f(\mathbf{X}) - f(\mathbf{X} - h)}{h}. \quad (7.14)$$

The central difference is given by adding Equation 7.11 and Equation 7.12

$$\frac{df(\mathbf{X})}{d\mathbf{X}} = \frac{f(\mathbf{X} + h) - f(\mathbf{X} - h)}{2h}. \quad (7.15)$$

The programming of numerical gradients is straightforward but numerically very expensive. Indeed for every design variable, the direct mechanical problem has to be computed and thus the larger the number of design variables, the higher the computational costs. Furthermore when the spacing h in the finite difference is not properly chosen, it leads to relevant errors in the result of the shape optimisation (Schwarz [41]). To conclude, the use of numerical gradients in gradient-based optimisation algorithms is not suitable when dealing with shape optimisation problems, where the number of design variables, here the FE nodes, is large.

7.3.2 Analytical gradient

By applying the chain rule, the analytical gradient of the objective function with respect to the design variables \mathbf{X} is given by

$$\frac{df(\mathbf{X})}{d\mathbf{X}} = \frac{\partial f^{\text{explicit}}}{\partial \mathbf{X}} + \frac{\partial f}{\partial \mathbf{x}^{\text{current}}} \frac{d\mathbf{x}^{\text{current}}}{d\mathbf{X}}. \quad (7.16)$$

According to the implicit dependency of the objective function on the design variables \mathbf{X} in Equation 7.1, it follows that the first term in the analytical gradient vanishes, i.e.,

$$\frac{\partial f^{\text{explicit}}}{\partial \mathbf{X}} = \mathbf{0}. \quad (7.17)$$

The gradient restricts then to

$$\frac{df(\mathbf{X})}{d\mathbf{X}} = \frac{\partial f}{\partial \mathbf{x}^{\text{current}}} \frac{d\mathbf{x}^{\text{current}}}{d\mathbf{X}}. \quad (7.18)$$

The crucial step for the computation of the Jacobian matrix $d\mathbf{x}^{\text{current}} / d\mathbf{X}$ in Equation 7.18 is the mechanical equilibrium condition, as in Scherer [66]

$$\mathbf{r}^{\text{current}}(\mathbf{X}) = \mathbf{r}(\mathbf{x}^{\text{current}}(\mathbf{X}), \mathbf{X}) = \mathbf{r}_{\text{ext}} - \mathbf{r}_{\text{int}}(\mathbf{x}^{\text{current}}(\mathbf{X}), \mathbf{X}) = \mathbf{0}, \quad (7.19)$$

where \mathbf{r}_{ext} and \mathbf{r}_{int} are the internal and external nodal forces (Eq. 6.17 and Eq. 6.16). Taking the total differential of the above equation, it follows that

$$\frac{d\mathbf{r}^{\text{current}}}{d\mathbf{X}} = \frac{\partial \mathbf{r}^{\text{explicit}}}{\partial \mathbf{X}} + \frac{\partial \mathbf{r}}{\partial \mathbf{x}^{\text{current}}} \frac{d\mathbf{x}^{\text{current}}}{d\mathbf{X}} = \mathbf{0}. \quad (7.20)$$

After a rearrangement, the above equation becomes

$$\frac{d\mathbf{x}^{\text{current}}}{d\mathbf{X}} = - \left[\frac{\partial \mathbf{r}}{\partial \mathbf{x}^{\text{current}}} \right]^{-1} \frac{\partial \mathbf{r}^{\text{explicit}}}{\partial \mathbf{X}}. \quad (7.21)$$

Substituting now Equation 7.21 in Equation 7.18, the analytical gradient of the objective function with respect to the design variables is

$$\begin{aligned} \frac{df(\mathbf{X})}{d\mathbf{X}} &= - \frac{\partial f}{\partial \mathbf{x}^{\text{current}}} \left[\frac{\partial \mathbf{r}}{\partial \mathbf{x}^{\text{current}}} \right]^{-1} \frac{\partial \mathbf{r}^{\text{explicit}}}{\partial \mathbf{X}} \\ &= (\mathbf{x}^{\text{target}} - \mathbf{x}^{\text{current}}) \left[\frac{\partial \mathbf{r}}{\partial \mathbf{x}^{\text{current}}} \right]^{-1} \frac{\partial \mathbf{r}^{\text{explicit}}}{\partial \mathbf{X}}, \end{aligned} \quad (7.22)$$

where

$$\frac{\partial \mathbf{r}}{\partial \mathbf{x}^{\text{current}}} = \sum_{e=1}^{n_{el}} \int_{B_0^e} \text{Grad}N^2 \frac{\partial \mathbf{P}}{\partial \mathbf{F}} \cdot \text{Grad}N \, dV \quad (7.23)$$

and

$$\frac{\partial \mathbf{r}^{\text{explicit}}}{\partial \mathbf{X}} = \sum_{e=1}^{n_{el}} \int_{B_t^e} \text{grad}N^2 \frac{\partial \boldsymbol{\sigma}}{\partial \mathbf{f}} \cdot \text{grad}N \, dv. \quad (7.24)$$

Remark:

- Equation 7.23 and Equation 7.24 were previously defined in Chapter 5 by Equation 5.40 and in Chapter 6 by Equation 6.36.
- The objective function is assumed to depend implicitly only on \mathbf{X} .

7.4 A recursive algorithm for avoiding mesh distortion

A drawback of choosing the material coordinates as the design variables is the possible occurrence of mesh distortions. The optimisation algorithm is not able to find the appropriate minima, or else gets stuck after a few iterations. To illustrate the occurrence of possible mesh distortions, two numerical examples are computed with the optimisation algorithm L-BFGS presented in Section 7.2. Figure 7.1 and Figure 7.3 show the target deformed configuration of a functional component in the $[x_1, x_2]$ and $[x_1, x_3]$ planes which is the three-dimensional extension of the classical two-dimensional Cook's cantilever as presented in Section 6.3.1. Figure 7.2 and Figure 7.4 show the undeformed configuration in the $[X_1, X_2]$ and $[X_1, X_3]$ planes after two iterations of the L-BFGS optimisation algorithm, where some mesh distortions are well identified. Figure 7.5 shows the target deformed configuration of a plate with four holes in the $[x_1, x_3]$ plane as presented in Section 5.3.3 and in Section 6.3.3. Figure 7.6 shows the undeformed configuration in the $[X_1, X_3]$ plane after 14 iterations of the optimisation algorithm, where some mesh distortions are here again well identified. The same values for the forces and material parameters are used in both cases.

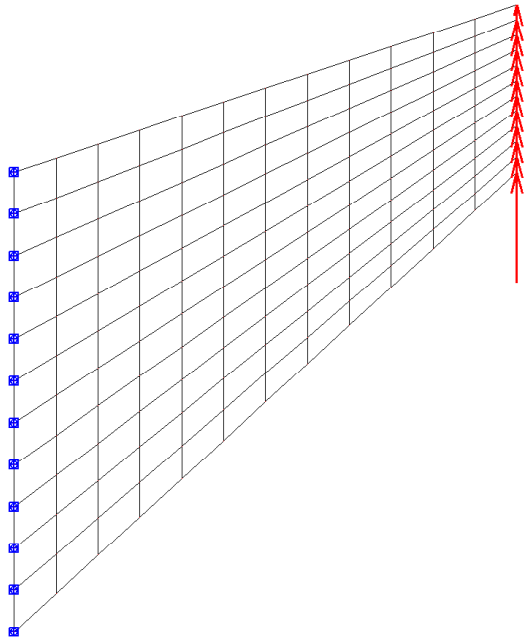


Figure 7.1: Deformed Cook's cantilever in $\mathcal{B}_t^{\text{target}}$ in the $[x_1, x_2]$ plane.

The idea of the strategy for avoiding mesh distortions is to perform successive optimisations by replacing the undeformed configuration needed in the next optimisation step by the previous optimised undeformed configuration:

- At the initialisation step, the material and optimisation parameters are given. The variable **TotalForce** = \mathfrak{F} , i.e., the known total force applied to the shape, is set. A variable **StepForce** representing the incremental force is defined by **StepForce** \ll **TotalForce**. Furthermore at the beginning as mentioned in Algorithm 7.1, $\boldsymbol{x}^{\text{target}} = \boldsymbol{x}^{\text{current}} = \boldsymbol{X}^{\text{current}}$. A direct mechanical problem is then computed with $\boldsymbol{X}^{\text{current}}$ and the initial force \mathfrak{F}^0 according to Chapter 5. The L-BFGS gradient-based optimisation algorithm, for example, is then computed with the analytical gradient presented in the above section for step 0.

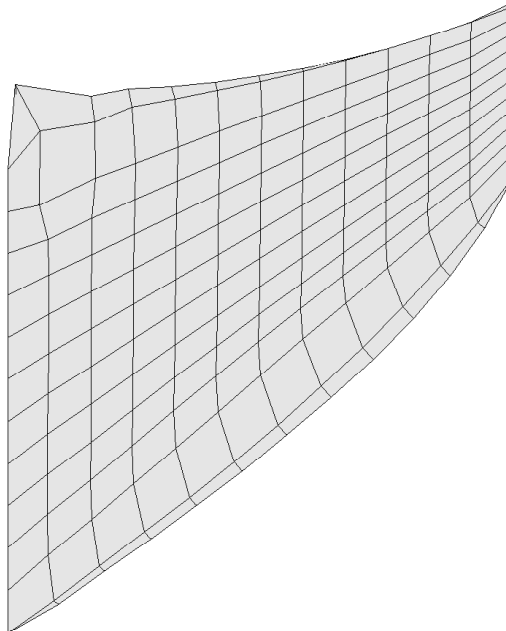


Figure 7.2: Undeformed Cook's cantilever in \mathcal{B}_0 in the $[\mathbf{X}_1, \mathbf{X}_2]$ plane after two iterations.

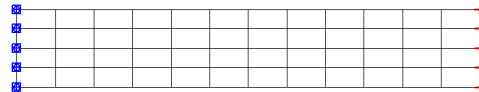


Figure 7.3: Deformed Cook's cantilever in \mathcal{B}_t in the $[\mathbf{x}_1, \mathbf{x}_3]$ plane.

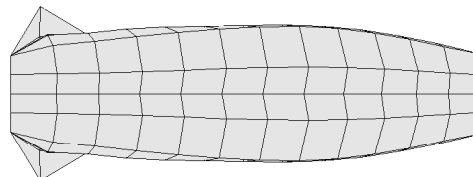


Figure 7.4: Undeformed Cook's cantilever in \mathcal{B}_0 in the $[\mathbf{X}_1, \mathbf{X}_3]$ plane after two iterations.

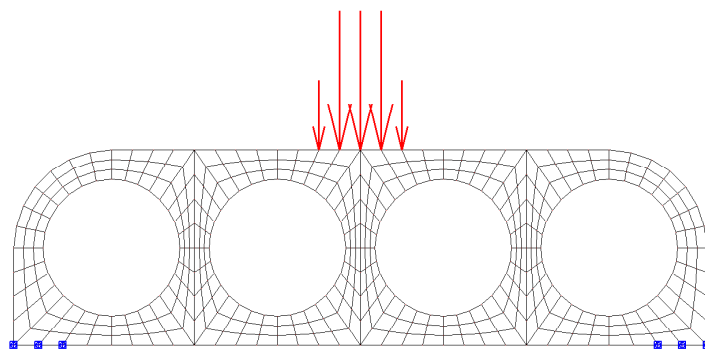


Figure 7.5: Deformed plate with four holes in $\mathcal{B}_t^{\text{target}}$ in the $[\mathbf{x}_1, \mathbf{x}_3]$ plane.

At the end of this initial optimisation step, the undeformed configuration \mathbf{X} for \mathfrak{F}^0 is obtained.

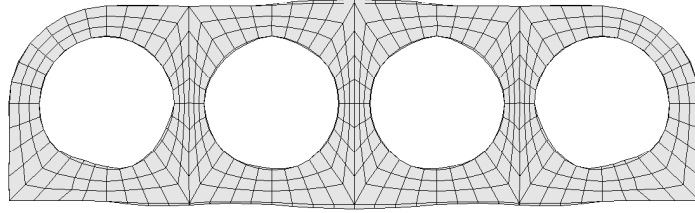


Figure 7.6: Undeformed plate with four holes in \mathcal{B}_0 in the $[X_1, X_3]$ plane after 14 iterations.

- For the next step, the new applied loading \mathfrak{F}^n is equal to the previous force \mathfrak{F}^{n-1} augmented by **StepForce**. Taking the previous computed undeformed configuration \mathbf{X}^{n-1} and the new loading \mathfrak{F}^n , the direct mechanical formulation is run according to Chapter 5 in order to obtain the current deformed configuration $\mathbf{x}^{\text{current},n}$ of the shape. The L-BFGS gradient-based optimisation algorithm, for example, can now be used and will give the undeformed configuration \mathbf{X}^n for \mathfrak{F}^n with the use of the analytical gradient performed as in the above section. This process is continued until **TotalForce** is reached.
- In case the **TotalForce** is reached, the undeformed configuration \mathbf{X} for the given total force is obtained.

A pseudo-algorithm view of this recursive process is described in Algorithm 7.3.

Algorithm 7.3: Pseudo-algorithm view of the strategy for avoiding mesh distortion in inverse form finding problems.

Data: material parameters, optimisation parameters, **TotalForce**, **StepForce**,
 $\mathcal{B}_t^{\text{target}} = \mathcal{B}_t^{\text{current}} = \mathcal{B}_0^{\text{current}}, \mathfrak{F}^0, n=1;$
Initialisation: Solve the direct boundary value problem in Chapter 5 with $\mathcal{B}_0^{\text{current}}$ and \mathfrak{F}^0 in order to obtain $\mathcal{B}_t^{\text{current}}(\mathfrak{F}^0)$;
Call the optimisation algorithm in order to find $\mathcal{B}_0^{\text{current}}(\mathfrak{F}^0)$;
while $|\mathfrak{F}^n| \leq |\text{TotalForce}|$ **do**
 $\mathfrak{F}^n = \mathfrak{F}^{n-1} + \text{StepForce};$
 Solve the direct boundary value problem as in Chapter 5 with $\mathcal{B}_0^{\text{current}}(\mathfrak{F}^{n-1})$ and \mathfrak{F}^n in
 order to obtain $\mathcal{B}_t^{\text{current}}(\mathfrak{F}^n)$;
 Call the optimisation algorithm in order to find $\mathcal{B}_0^{\text{current}}(\mathfrak{F}^n)$;
 $n=n+1;$
end
return $\mathcal{B}_0 = \mathcal{B}_0^{\text{current}}(\mathfrak{F}^n);$

7.5 Numerical examples

In this section are presented five numerical examples to determine the undeformed configuration of a functional component using shape optimisation. The examples are for isotropic and anisotropic hyperelastic materials as well as for isotropic and anisotropic elastoplastic materials. As validation, for each example, the undeformed shape obtained is again used as input for the computation of the direct mechanical problem as presented in Chapter 5. The difference is again calculated according to Equation 6.37.

7.5.1 Isotropic hyperelastic material

The first example deals with the determination of the undeformed configuration of a thick cantilever under a distributed force as in Section 6.3.1 and in Section 7.4 to prove the effectiveness of the recursive algorithm presented above. The given deformed configuration of the thick cantilever is plotted in Figure 7.1 and Figure 7.3. The geometry, the boundary conditions, and the material parameters are the same as in Section 6.3.1. The total applied force is again equal to $5 \cdot 10^4$ units of force, whereas **StepForce** needed in Algorithm 7.3 is equal to 500. The optimisation parameters are given in Table 7.1. The undeformed plate obtained is shown in Figure 7.7, Figure 7.8, and Figure 7.9 for the steps, where the forces are equal to, respectively, 10^4 , $3 \cdot 10^4$, and $5 \cdot 10^4$.

method	L-BFGS
HessianModify	1
LS	3
progTol	1e-14
optTol	1e-4

Table 7.1: Numerical example: Optimisation parameters for the isotropic elastoplastic example based on Schmidt [54].

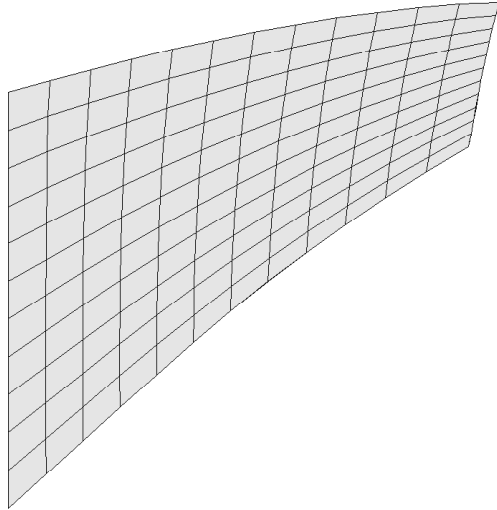


Figure 7.7: Undeformed thick cantilever in the material configuration \mathcal{B}_0 ($[\mathbf{X}_1, \mathbf{X}_2]$ plane) for $\mathfrak{F}=10^4$.

Again, to validate the results, the undeformed shape obtained (Fig. 7.10 with forces and boundary conditions) is used as the input for the computation of the direct problem from Chapter 5 and the difference ε from Equation 6.37 is evaluated. The deformed shape obtained is illustrated in Figure 7.11 with equivalent von Mises stress (MPa) from Equation 5.41. ε is equal to $9.77 \cdot 10^{-6}$ mm.

The second example deals with the determination of the undeformed configuration of a plate with four holes as in Section 5.3.3 and in Section 7.4 to prove the effectiveness of the recursive algorithm presented above. The given deformed configuration of the plate with four holes is

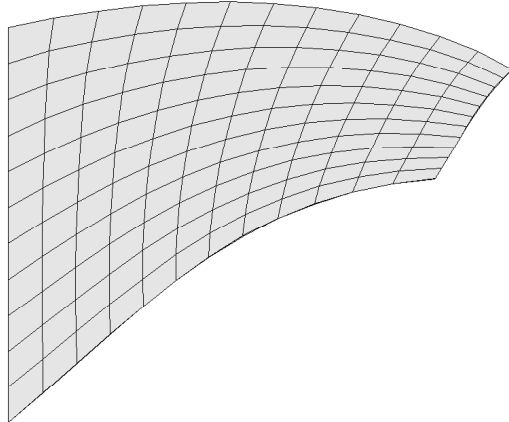


Figure 7.8: Undeformed thick cantilever in the material configuration \mathcal{B}_0 ($[\mathbf{X}_1, \mathbf{X}_2]$ plane) for $\mathfrak{F}=3\cdot10^4$.

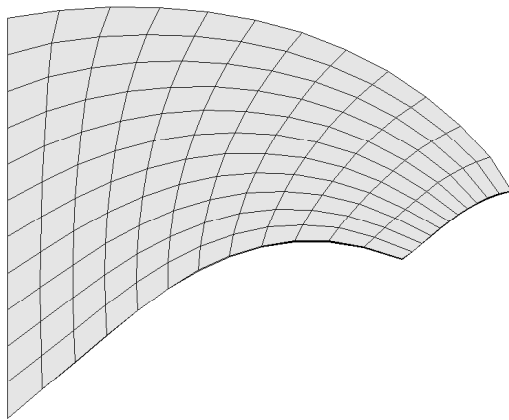


Figure 7.9: Undeformed thick cantilever in the material configuration \mathcal{B}_0 ($[\mathbf{X}_1, \mathbf{X}_2]$ plane) for $\mathfrak{F}=5\cdot10^4$.

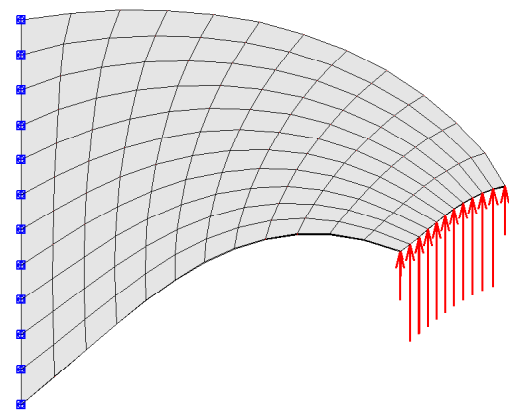


Figure 7.10: Undeformed thick cantilever in the material configuration \mathcal{B}_0 ($[\mathbf{X}_1, \mathbf{X}_2]$ plane) with load and boundary conditions.

plotted in Figure 7.5. The geometry, the boundary conditions, and the material parameters are the same as in Section 6.3.1. The total applied force is equal to $25\cdot10^3$ units of force (red arrows),

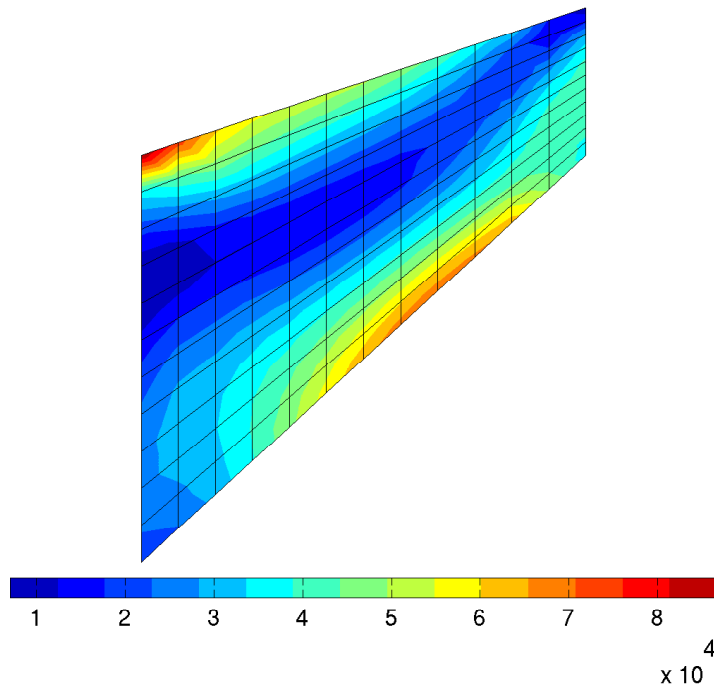


Figure 7.11: Deformed thick cantilever in the spatial configuration \mathcal{B}_t ($[\mathbf{x}_1, \mathbf{x}_2]$ plane) with equivalent von Mises stress $\sigma_{\text{eq}}^{\text{vm}}$ (MPa).

whereas **StepForce** needed in Algorithm 7.3 is equal to 500. The optimisation parameters are given in Table 7.1. The undeformed plate obtained is shown in Figure 7.12, Figure 7.13, and Figure 7.14 for the steps, where the forces are equal to $5 \cdot 10^3$, $15 \cdot 10^3$, and $25 \cdot 10^3$, respectively.

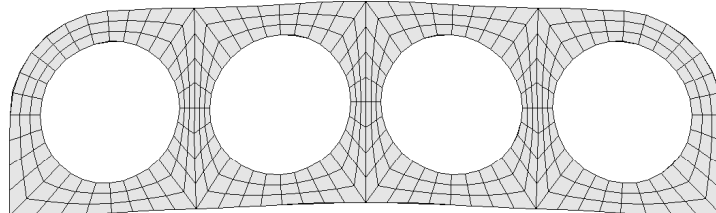


Figure 7.12: Undeformed plate with four holes in the material configuration \mathcal{B}_0 ($[\mathbf{X}_1, \mathbf{X}_3]$ plane) for $\mathfrak{F}=5 \cdot 10^3$.

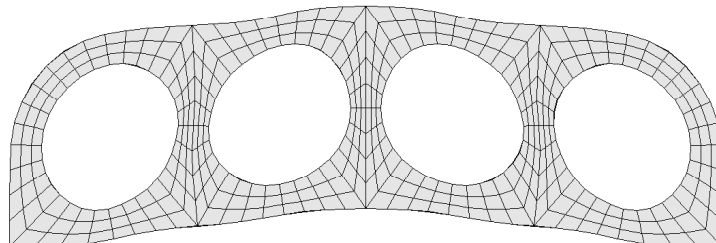


Figure 7.13: Undeformed plate with four holes in the material configuration \mathcal{B}_0 ($[\mathbf{X}_1, \mathbf{X}_3]$ plane) for $\mathfrak{F}=15 \cdot 10^3$.

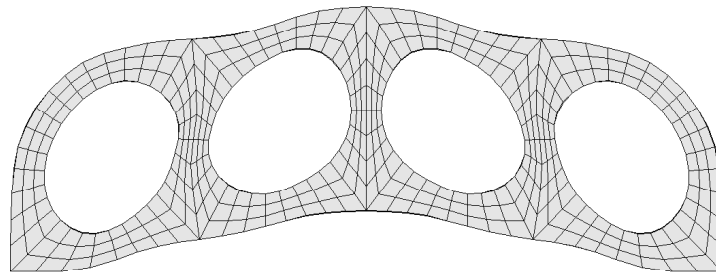


Figure 7.14: Undeformed plate with four holes in the material configuration \mathcal{B}_0 ($[X_1, X_3]$ plane) for $\mathfrak{F}=25 \cdot 10^3$.

Again, for validation, the undeformed shape obtained (Fig. 7.15 with forces and boundary conditions) is used as the input for the computation of the direct problem from Chapter 5 and the difference ε from Equation 6.37 is evaluated. The deformed shape obtained is illustrated in Figure 7.16 in the $[x_1, x_3]$ plane with equivalent von Mises stress (MPa) from Equation 5.41. ε is equal to $3.65 \cdot 10^{-8}$ mm.

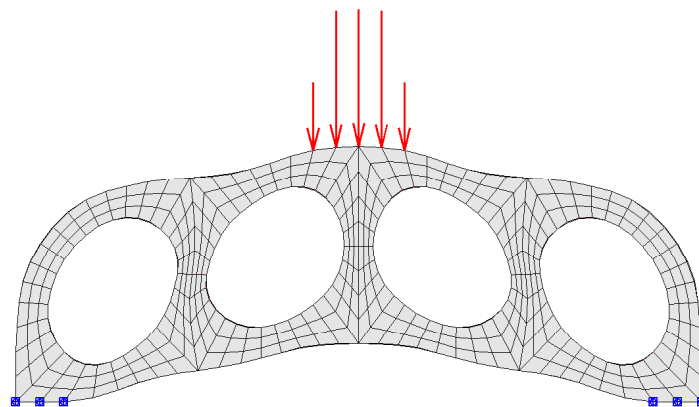


Figure 7.15: Undeformed plate with four holes in the material configuration \mathcal{B}_0 ($[X_1, X_3]$ plane) with load and boundary conditions.

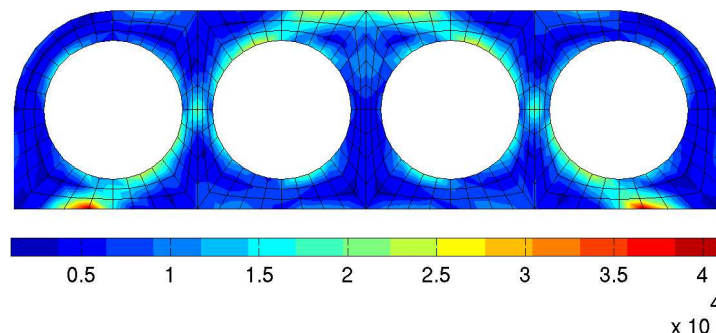


Figure 7.16: Deformed plate with four holes in the spatial configuration \mathcal{B}_t ($[x_1, x_3]$ plane) with equivalent von Mises stress $\sigma_{\text{eq}}^{\text{vm}}$ (MPa).

7.5.2 Anisotropic hyperelastic material

The third example deals with the determination of the undeformed configuration of a plate (here straight and rectangular) with a hole in 3D as in Section 5.3.3. The given deformed configuration of the plate with a hole is plotted in Figure 5.7. The geometry, the boundary conditions, and the material parameters are the same as in Section 5.3.3. The total applied force is equal to $5 \cdot 10^5$ units of force, whereas **StepForce** needed in Algorithm 7.3 is equal to 10^4 . The optimisation parameters are given in Table 7.1. The undeformed plate obtained is shown in Figure 7.17, Figure 7.18, and Figure 7.19 for the steps, where the forces are equal to 10^5 , $3 \cdot 10^5$, and $5 \cdot 10^5$, respectively.

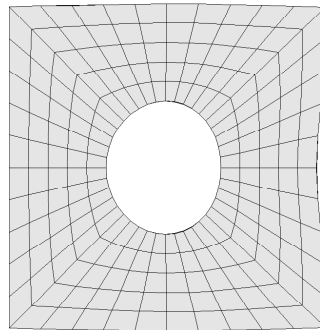


Figure 7.17: Undeformed plate with a hole in the material configuration \mathcal{B}_0 ($[\mathbf{X}_1, \mathbf{X}_2]$ plane) for $\mathfrak{F}=10^5$.

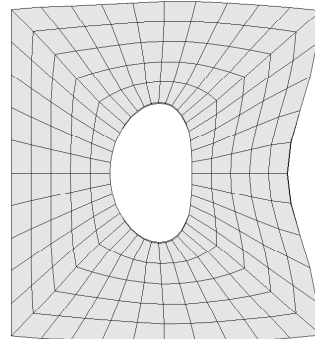


Figure 7.18: Undeformed plate with a hole in the material configuration \mathcal{B}_0 ($[\mathbf{X}_1, \mathbf{X}_2]$ plane) for $\mathfrak{F}=3 \cdot 10^5$.

Again, to validate the results, the undeformed shape obtained (Fig. 7.20 with forces and boundary conditions) is used as the input for the computation of the direct problem from Chapter 5 and the difference ε from Equation 6.37 is evaluated. The deformed shape obtained is illustrated in Figure 7.21 with equivalent von Mises stress (MPa) from Equation 5.41. ε is equal to $3.31 \cdot 10^{-9}$ mm.

It was found that ε from Equation 6.37 lies between $9.77 \cdot 10^{-6}$ mm and $3.31 \cdot 10^{-9}$ mm. It can be therefore be concluded that the shape optimisation formulation succeeds in finding the appropriate undeformed configuration when dealing with hyperelastic behaviour. The recursive algorithm has also proved its efficiency.

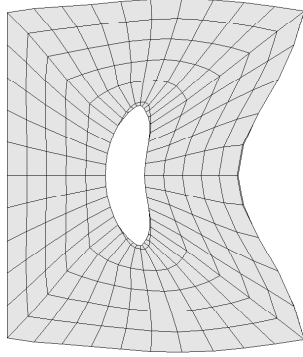


Figure 7.19: Undeformed plate with a hole in the material configuration \mathcal{B}_0 ($[\mathbf{X}_1, \mathbf{X}_2]$ plane) for $\mathfrak{F}=5\cdot10^5$.

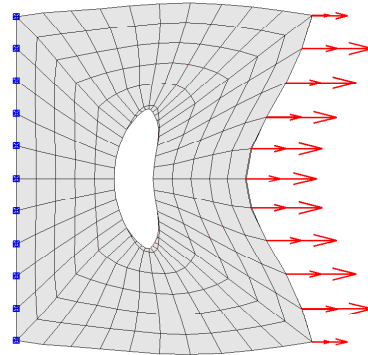


Figure 7.20: Undeformed plate with a hole in the material configuration \mathcal{B}_0 ($[\mathbf{X}_1, \mathbf{X}_2]$ plane) with load and boundary conditions.

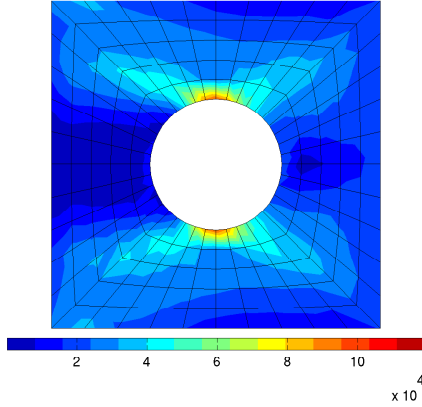


Figure 7.21: Deformed plate with a hole in the spatial configuration \mathcal{B}_t ($[\mathbf{x}_1, \mathbf{x}_2]$ plane) with equivalent von Mises stress $\sigma_{\text{eq}}^{\text{vms}}$ (MPa).

7.5.3 Isotropic elastoplastic material

The fourth example deals with the determination of the undeformed configuration of a plate (straight and circular) in 3D as in Germain et al. [67]. The undeformed configuration of the plate is plotted in Figure 7.22 in the $[\mathbf{x}_1, \mathbf{x}_2]$ plane and in Figure 7.23, which is a cut made in the middle of the plate in the $[\mathbf{x}_1, \mathbf{x}_3]$ plane. The radius of the plate is set to 25 mm and

the thickness is equal to 2 mm. The shape is discretised by hexahedral element (HEX8) with MSC.Patran2010.2. The number of elements obtained is equal to 180 and the number of nodes is equal to 402. The outer boundary of the shape is fixed in the three directions (blue squares in Figure 7.22 and Figure 7.23). The total applied force (red arrows) is equal to 1200 units of force in 10 increments in the vertical direction, whereas **StepForce** needed in Algorithm 7.3 is equal to 10. The plate is assumed to have isotropic elastoplastic behaviour. The material parameters used in the simulation are summarised in Table 7.2. The optimisation parameters are available in Table 7.1. The undeformed plate obtained is shown in Figure 7.24, Figure 7.25, and Figure 7.26 for the steps, where the forces are equal to 400, 800, and 1200, respectively.

	elastic parameters	
E	202382	MPa
ν	0.328	-
\mathbb{E}^e	$3\kappa\mathbb{I}_{vol} + 2\mu\mathbb{I}_{dev}^{sym}$	MPa
	plastic parameters	
h	308.5	MPa
σ_0	186.54	MPa
σ_∞	306.37	MPa
w	15.45	-
H	\mathbb{I}_{dev}^{sym}	-

Table 7.2: Numerical example: Material parameters for an isotropic elastoplastic material.

Again, to validate the results, the undeformed shape obtained (Fig. 7.27 with forces and boundary conditions) is used as the input for the computation of the direct problem from Chapter 5 and the difference ε from Equation 6.37 is evaluated. The deformed shape obtained is illustrated in Figure 7.28 with equivalent von Mises stress (MPa) from Equation 5.41 and in Figure 7.29 with equivalent plastic strain (-) from Equation 5.42. ε is equal to $3.07 \cdot 10^{-7}$ mm.

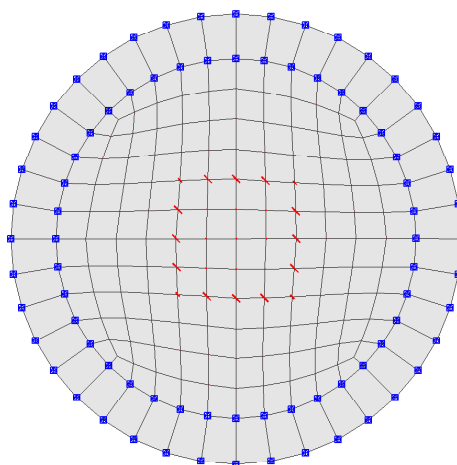


Figure 7.22: Deformed plate in the spatial configuration \mathcal{B}_t in the $[\mathbf{x}_1, \mathbf{x}_2]$ plane.

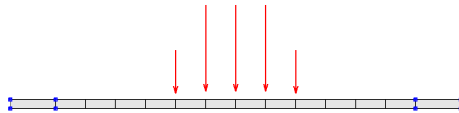


Figure 7.23: Cut of the deformed plate in the spatial configuration \mathcal{B}_t in the $[\mathbf{x}_1, \mathbf{x}_3]$ plane.



Figure 7.24: Cut of the undeformed plate in the material configuration \mathcal{B}_0 in the $[\mathbf{X}_1, \mathbf{X}_3]$ plane for $\mathfrak{F}=400$.



Figure 7.25: Cut of the undeformed plate in the material configuration \mathcal{B}_0 in the $[\mathbf{X}_1, \mathbf{X}_3]$ plane for $\mathfrak{F}=800$.



Figure 7.26: Cut of the undeformed plate in the material configuration \mathcal{B}_0 for in the $[\mathbf{X}_1, \mathbf{X}_3]$ plane $\mathfrak{F}=1200$.

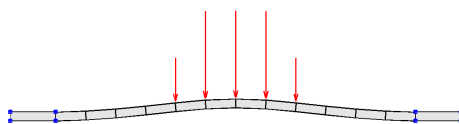


Figure 7.27: Cut of the undeformed plate in the material configuration \mathcal{B}_0 in the $[\mathbf{X}_1, \mathbf{X}_3]$ plane with load and boundary conditions.

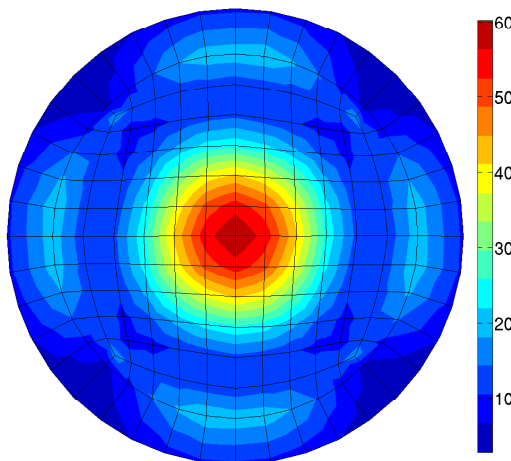


Figure 7.28: Deformed plate in the spatial configuration \mathcal{B}_t in the $[\mathbf{x}_1, \mathbf{x}_2]$ plane with equivalent von Mises stress $\sigma_{\text{eq}}^{\text{vm}}$ (MPa).

7.5.4 Anisotropic elastoplastic material

The fifth example deals with the determination of the undeformed configuration of a plate (straight and circular) with a hole in 3D as in Section 5.3.4 and in Germain et al. [68]. The deformed configuration is here the circular plate as illustrated in Figure 7.30 in the $[\mathbf{x}_1, \mathbf{x}_2]$ plane. The total applied force (red arrows) is equal to $15 \cdot 10^4$ units of force in 10 increments, whereas

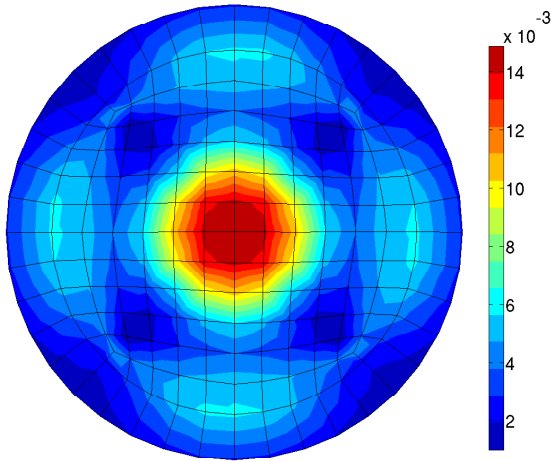


Figure 7.29: Deformed plate in the spatial configuration \mathcal{B}_t in the $[x_1, x_2]$ plane with equivalent plastic strain E_{eq}^p (-).

the variable **StepForce** in Algorithm 7.3 is set to 10^4 . The plate is assumed to have anisotropic elastoplastic behaviour. The material parameters used in the simulation are summarised in Table 5.5. The optimisation parameters are given in Table 7.1. The undeformed plate obtained is shown in Figure 7.31, Figure 7.32, and Figure 7.33 for the steps, where the forces are equal to $5 \cdot 10^4$, $10 \cdot 10^4$, and $15 \cdot 10^4$, respectively. Due to the anisotropy, the undeformed configuration of the plate is not circular, as would be expected for a material with isotropic elastoplastic behaviour.

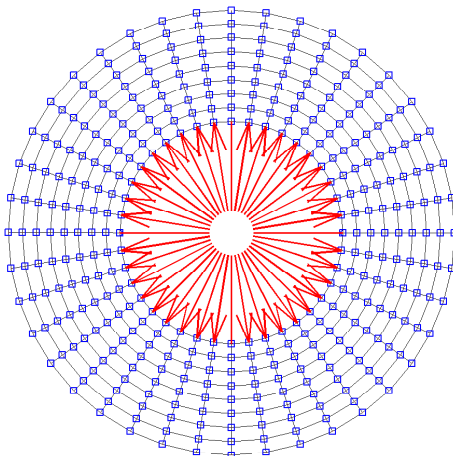


Figure 7.30: Deformed circular plate in the spatial configuration \mathcal{B}_t in the $[x_1, x_2]$ plane.

Again, for validation, the undeformed shape obtained (Fig. 7.34 with forces and boundary conditions) is used as the input for the computation of the direct problem from Chapter 5 and the difference ε from Equation 6.37 is evaluated. The deformed shape obtained is illustrated in Figure 7.35 with equivalent von Mises stress (MPa) from Equation 5.41 and in Figure 7.36 with equivalent plastic strain (-) from Equation 5.42. As expected, the maximal equivalent von Mises stress is concentrated at $k\pi/2$ with $k = 0, 1, 2, 3$. The maximal plastic deformations are concentrated at $k\pi/4$ with $k = 1, 3, 5, 7$. ε is equal to $1.83 \cdot 10^{-9}$ mm.

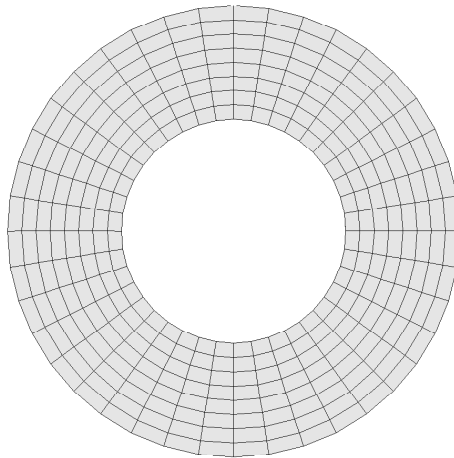


Figure 7.31: Undeformed plate in the material configuration \mathcal{B}_0 ($[X_1, X_2]$ plane) for $\mathfrak{F}=5\cdot10^4$.

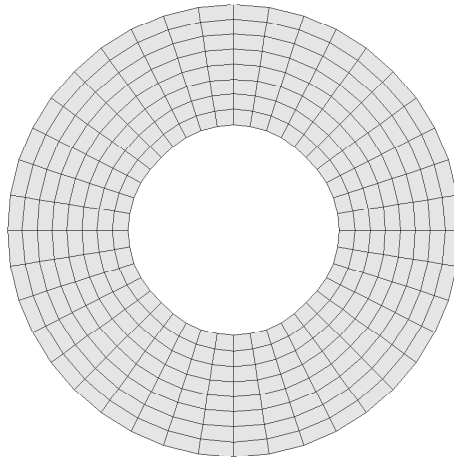


Figure 7.32: Undeformed plate in the material configuration \mathcal{B}_0 ($[X_1, X_2]$ plane) for $\mathfrak{F}=10\cdot10^4$.

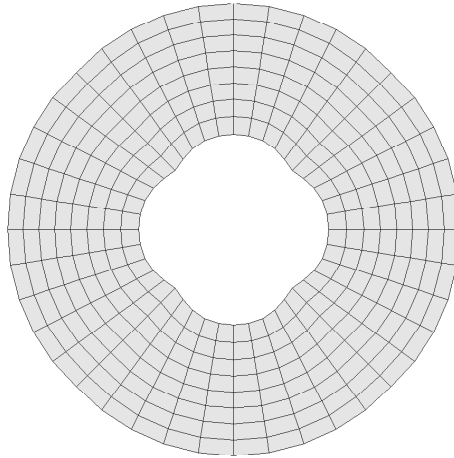


Figure 7.33: Undeformed plate in the material configuration \mathcal{B}_0 ($[X_1, X_2]$ plane) for $\mathfrak{F}=15\cdot10^4$.

It was found that ε from Equation 6.37 is in between $3.07\cdot10^{-7}$ mm and $1.83\cdot10^{-9}$ mm. It can therefore be concluded that the shape optimisation formulation succeeds in finding the appropriate undeformed configuration when dealing with elastoplastic behaviour.

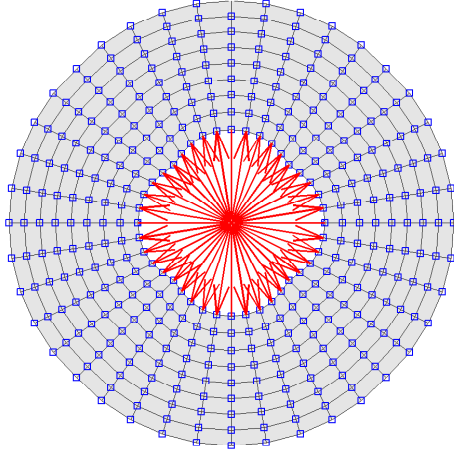


Figure 7.34: Undeformed plate in the material configuration \mathcal{B}_0 ($[X_1, X_2]$ plane) with load and boundary conditions.

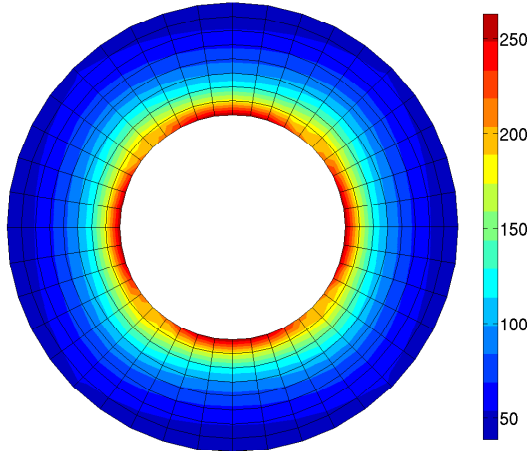


Figure 7.35: Deformed plate in the spatial configuration \mathcal{B}_t ($[x_1, x_2]$ plane) with equivalent von Mises stress $\sigma_{\text{eq}}^{\text{vm}}$ (MPa).

7.6 Discussion

When considering hyperelastic materials, the computation of the undeformed shape with the inverse mechanical formulation was faster than the computation with the shape optimisation as already published in Germain et al. [69, 70]. Indeed, for the computation of the thick cantilever in Section 6.3.1 and Section 7.5.1, the inverse mechanical formulation took 83.59 s whereas with the shape optimisation formulation, the computation finished after 187,993.04 s. Both methods were computed on an Intel Core2 Duo (2533 MHz). The difference in the computational costs is due to the recursive algorithm for avoiding mesh distortions, where for all increments the shape optimisation algorithm has to converge while for the inverse mechanical formulation only one increment is needed. Both computations gave also the same undeformed shape. Again, for the thick cantilever presented in Section 6.3.1 and Section 7.5.1 $\|\mathbf{X}^{\text{inverse mechanical formulation}} - \mathbf{X}^{\text{shape optimisation}}\|^2$ mm is equal to $8.3 \cdot 10^{-5}$ mm. So, when dealing

with hyperelasticity, the inverse mechanical formulation should be preferred.

When considering elastoplastic materials and when the set of internal variables is unknown for the deformed state, the shape optimisation formulation cannot be circumvented at this stage in order to find the undeformed shape of a functional component. To reduce the computational costs, adaptive mesh refinement might be another way to avoid mesh distortions.

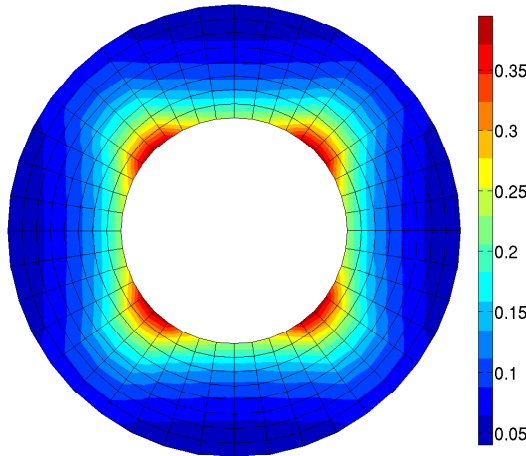


Figure 7.36: Deformed plate in the spatial configuration \mathcal{B}_t ($[x_1, x_2]$ plane) with equivalent plastic strain E_{eq}^p (-).

CHAPTER 8

Conclusion and outlook

The objective of the present work was the development of methods for the optimal determination of the initial shape of formed functional components, considering anisotropic hyperelastic and elastoplastic behaviours. The undeformed configuration of the functional component was sought when the desired deformed configuration, the mechanical loading, and the boundary conditions are given, i.e., an inverse form finding problem.

Chapter 1 includes an introduction to the underlying problem, a summary of related work, and an overview of the structure of the present work.

After having introduced the basics of continuum mechanics and the most important notation for the rest of the work in Chapter 2, a macroscopic phenomenological model was presented in Chapter 3 following the standard literature on material modelling. An additive decomposition of the logarithmic strain with a structure adopted from the geometrically linear theory was performed. The formulation of the yield criterion and the yield surface was given after presenting the description of the energy storage and the elastic response. The plastic flow rule and hardening law were defined for anisotropic elastoplasticity. The elastoplastic constitutive initial value problem was solved by a return mapping algorithm extended here to the case of anisotropic elastoplastic materials. Thermal effects were ignored and the material was assumed to be homogeneous.

In Chapter 4, the fourth-order elasticity tensor for the model built in Chapter 3 was decomposed into its spectral decomposition using the Kelvin modes. The anisotropy in the material was formulated according to the eight crystal systems: isotropic, monoclinic, triclinic, orthorhombic, trigonal, tetragonal, hexagonal and cubic.

In Chapter 5, a formulation for determining the deformed shape of a functional component from the equilibrium equation was first presented before providing the methods for solving the inverse form finding problem in the following two chapters. Within this part, the Piola formulation for the equilibrium was first deployed by using the definition of the boundary value problem in the material configuration. This allows finding the deformed configuration of a body when the surface traction and boundary values were given. This formulation was referred to as the direct mechanical problem. An analytical solution of this nonlinear boundary value problem is only possible for some trivial problems. Therefore the finite element method was used in order to find approximate solutions. The essential points in establishing the finite element formulations were the linearisation of the weak form of the boundary value problem in the material configuration and the corresponding discretisation. The Newton–Raphson method was used for solving the nonlinear systems of equations that were obtained. Distributed body forces and inertia were omitted and the acceleration was assumed to vanish. Numerical examples for isotropic and anisotropic hyperelastic materials as well as for elastoplastic materials illustrated the previously presented developments. The fourth-order elastic tensor used in the macroscopic constitutive model in the logarithmic strain space was decomposed into Kelvin modes.

In Chapter 6, for the first time a method was introduced to determine the undeformed configuration of a functional component. For the determination of the undeformed shape, the equilibrium equation was deployed. A Cauchy formulation was applied, so that the equilibrium requirement was satisfied for the spatial configuration, here named the inverse mechanical problem. All quantities were parametrised in spatial coordinates. The inverse mechanical problem was solved using the finite element method in the same way as for the direct problem. This formulation gave suitable results when dealing with hyperelastic materials: this was illustrated by three numerical examples. For elastoplastic behaviour, the provided deformed configuration, load, and boundary conditions were however no longer sufficient to reach the wanted undeformed configuration, as seen in two numerical examples for the case of isotropic elastoplasticity. It was demonstrated, by considering an uniaxial tension experiment in 1D, that if the set of internal variables corresponding to the deformed configuration is previously given, the target undeformed configuration can be reached for some elastoplastic examples. However, the inverse mechanical formulation remained inadequate for elastoplastic behaviour since in general the set of internal variables is unknown at the deformed state.

In Chapter 7, inverse form finding problems for elastoplastic behaviour were solved with gradient-based shape optimisation methods to overcome the limitation of the inverse mechanical formulation. Gradient-based shape optimisation methods were used in the sense of an inverse problem via successive iterations of the direct mechanical problem. This is justified, since the set of internal variables at the deformed state is usually unknown. The objective function of the optimisation problem was defined by a least squares minimisation of the difference between the target and the current deformed configuration of the workpiece. The design variables were defined by the discretised nodes of the functional component with the finite element method (node-based shape optimisation). This choice led, however, to mesh distortions in the undeformed shape, which were avoided by using a recursive algorithm. Between two iterations, the current optimised undeformed configuration was used in the computation of the next value of the objective function. The total applied force was then split over all entities. Five numerical examples illustrated the shape optimisation formulation with the recursive algorithm and demonstrated that the shape optimisation method is suitable for solving inverse form finding problems for elastoplastic behaviours of materials. Comparing the shape optimisation method and the inverse mechanical formulation in hyperelasticity, the difference between the computed undeformed configurations was negligible. However the inverse mechanical formulation incurred less computational costs.

In future research, the determination of the undeformed configuration of a functional component could be deployed for real world applications, e.g., in case the deformed configuration is obtained by a sheet-bulk metal forming process. To that end, the macroscopic model has to be extended to kinematic and combined hardening. The finite element formulation should be extended to solid-like shell elements, which are more appropriate for metal forming. A second particular challenge will be the modelling of the contact between the workpiece and the tool.

Appendices

Appendix A

Proof of Equation 5.32:

In index notation the fourth-order tensor \mathbb{A} becomes

$$A_{ijkl} = \frac{\partial P_{ij}}{\partial F_{kl}}. \quad (\text{A. 1})$$

According to Equation 5.2 the first Piola–Kirchhoff tensor \mathbf{P} reads

$$P_{ij} = F_{im}S_{mj}. \quad (\text{A. 2})$$

Thus incorporating Equation A. 2 into Equation A. 1 and using the product rule it leads to

$$\begin{aligned} A_{ijkl} &= \frac{\partial F_{im}S_{mj}}{\partial F_{kl}} \\ &= \frac{\partial F_{im}}{\partial F_{kl}}S_{mj} + F_{im}\frac{\partial S_{mj}}{\partial F_{kl}} \\ &= \delta_{ik}\delta_{ml}S_{mj} + F_{im}\frac{\partial S_{mj}}{\partial F_{kl}} \\ &= \delta_{ik}S_{lj} + F_{im}\frac{\partial S_{mj}}{\partial F_{kl}}. \end{aligned} \quad (\text{A. 3})$$

Since the second Piola–Kirchhoff tensor is symmetric

$$A_{ijkl} = \delta_{ik}S_{jl} + F_{im}\frac{\partial S_{mj}}{\partial F_{kl}} \quad (\text{A. 4})$$

Thus using the non-standard dyadic product $\overline{\otimes}$ it leads to

$$\mathbb{A} = \mathbf{I} \overline{\otimes} \mathbf{S} + \mathbb{B} \quad (\text{A. 5})$$

where

$$B_{ijkl} = F_{im}\frac{\partial S_{mj}}{\partial F_{kl}}. \quad (\text{A. 6})$$

In order to find \mathbb{B} the right Cauchy–Green tensor

$$\mathbf{C} = \mathbf{F}^t \cdot \mathbf{F} \Rightarrow C_{no} = F_{pn}F_{po} \quad (\text{A. 7})$$

is introduced in the second term of \mathbb{B} . It follows that

$$\begin{aligned} B_{ijkl} &= F_{im}\frac{\partial S_{mj}}{\partial F_{kl}} \\ &= F_{im}\frac{\partial S_{mj}}{\partial C_{no}}\frac{\partial C_{no}}{\partial F_{kl}} \\ &= F_{im}\frac{\partial S_{mj}}{\partial C_{no}}\left[\frac{\partial F_{pn}F_{po}}{\partial F_{kl}}\right]. \end{aligned} \quad (\text{A. 8})$$

With the definition of the product rule \mathbb{B} becomes

$$\begin{aligned}
 B_{ijkl} &= F_{im} \frac{\partial S_{mj}}{\partial C_{no}} \left[\frac{\partial F_{pn}}{\partial F_{kl}} F_{po} + F_{pn} \frac{\partial F_{po}}{\partial F_{kl}} \right] \\
 &= F_{im} \frac{\partial S_{mj}}{\partial C_{no}} [\delta_{pk} \delta_{nl} F_{po} + F_{pn} \delta_{pk} \delta_{ol}] \\
 &= F_{im} \frac{\partial S_{mj}}{\partial C_{no}} [F_{ko} \delta_{nl} + F_{kn} \delta_{ol}] \\
 &= F_{im} \left[\frac{\partial S_{mj}}{\partial C_{no}} F_{ko} \delta_{nl} + \frac{\partial S_{mj}}{\partial C_{no}} F_{kn} \delta_{ol} \right] \\
 &= F_{im} \left[\frac{\partial S_{mj}}{\partial C_{lo}} F_{ko} + \frac{\partial S_{mj}}{\partial C_{nl}} F_{kn} \right] \\
 &= F_{im} \left[\frac{\partial S_{mj}}{\partial C_{lo}} F_{ko} + \frac{\partial S_{mj}}{\partial C_{ol}} F_{ko} \right] \\
 &= F_{im} 2 \frac{\partial S_{mj}}{\partial C_{lo}} F_{ko} \\
 &= F_{im} C_{mjlo} F_{ko}.
 \end{aligned} \tag{A. 9}$$

In order to write the fourth-order tensor B into the tensor product of three fourth-order tensor as

$$B_{ijkl} = D_{ijmn} C_{mnop} G_{opkl}, \tag{A. 10}$$

Equation A. 9 is transformed into

$$\begin{aligned}
 F_{im} C_{mjlo} F_{ko} &= 2 F_{im} \frac{\partial S_{mn}}{\partial C_{lo}} \delta_{nj} F_{ko} \\
 &= 2 F_{im} \delta_{nj} \frac{\partial S_{mn}}{\partial C_{ol}} F_{ko} \\
 &= 2 F_{im} \delta_{nj} \frac{\partial S_{mn}}{\partial C_{op}} \delta_{pl} F_{ko} \\
 &= 2 F_{im} \delta_{nj} \frac{\partial S_{mn}}{\partial C_{op}} F_{ok}^t \delta_{pl}.
 \end{aligned} \tag{A. 11}$$

Thus as function of the non-standard dyadic product $\overline{\otimes}$

$$\mathbb{B} = [\mathbf{F} \overline{\otimes} \mathbf{I}] : \mathbb{C} : [\mathbf{F}^t \overline{\otimes} \mathbf{I}] \tag{A. 12}$$

Putting Equation A. 5 and Equation A. 12 together leads to

$$\mathbb{A} = \mathbf{I} \overline{\otimes} \mathbf{S} + [\mathbf{F} \overline{\otimes} \mathbf{I}] : \mathbb{C} : [\mathbf{F}^t \overline{\otimes} \mathbf{I}]. \tag{A. 13}$$

QED.

Appendix B

Proof of Equation 6.28:

Subsequently the following derivatives with respect to the inverse deformation gradient \mathbf{f} will be used [95, 96]

$$\frac{\partial j}{\partial \mathbf{f}} = j \mathbf{F}^t, \quad \frac{\partial \mathbf{F}}{\partial \mathbf{f}} = -\mathbf{F} \overline{\otimes} \mathbf{F}^t \quad \text{and} \quad \frac{\partial \mathbf{F}^t}{\partial \mathbf{f}} = -\mathbf{F}^t \underline{\otimes} \mathbf{F}. \quad (\text{B. 1})$$

According to Equation 6.2 the Cauchy stress tensor is given by

$$\boldsymbol{\sigma} = j \mathbf{F} \mathbf{S} \mathbf{F}^T. \quad (\text{B. 2})$$

In index notation it becomes

$$\sigma_{ij} = j F_{il} S_{lo} F_{oj}^T. \quad (\text{B. 3})$$

It follows then the following decomposition

$$a_{ijkp} = \frac{\partial \sigma_{ij}}{\partial f_{kp}} = \underbrace{\frac{\partial j}{\partial f_{kp}} F_{il} S_{lo} F_{oj}^T}_{\textcircled{1}} + j \underbrace{\frac{\partial F_{il}}{\partial f_{kp}} S_{lo} F_{oj}^T}_{\textcircled{2}} + j F_{il} \underbrace{\frac{\partial S_{lo}}{\partial f_{kp}} F_{oj}^T}_{\textcircled{3}} + j F_{il} S_{lo} \underbrace{\frac{\partial F_{oj}^T}{\partial f_{kp}}}_{\textcircled{4}} \quad (\text{B. 4})$$

where

$$\begin{aligned} \textcircled{1} \Rightarrow \frac{\partial j}{\partial f_{kp}} F_{il} S_{lo} F_{oj}^T &= \frac{\partial \det f}{\partial f_{kp}} F_{il} S_{lo} F_{oj}^T \\ &= \det f f_{kp}^{-T} F_{il} S_{lo} F_{oj}^T \\ &= j F_{il} S_{lo} F_{oj}^T f_{kp}^{-T} \\ &= \sigma_{ij} f_{kp}^{-T} \\ &= \sigma_{ij} F_{kp}^T \\ &= \boldsymbol{\sigma} \otimes \mathbf{F}^T, \end{aligned} \quad (\text{B. 5})$$

$$\begin{aligned} \textcircled{2} \Rightarrow j \frac{\partial F_{il}}{\partial f_{kp}} S_{lo} F_{oj}^T &= j \frac{\partial f_{il}^{-1}}{\partial f_{kp}} S_{lo} F_{oj}^T \\ &= -j f_{ik}^{-1} f_{lp}^{-T} S_{lo} F_{oj}^T \\ &= -j f_{ik}^{-1} F_{pl} S_{lo} F_{oj}^T \\ &= -F_{ik} \sigma_{kj} \\ &= -\mathbf{F} \overline{\otimes} \boldsymbol{\sigma}^T \\ &= -\mathbf{F} \overline{\otimes} \boldsymbol{\sigma}, \end{aligned} \quad (\text{B. 6})$$

and

$$\begin{aligned}
 \textcircled{3} \Rightarrow jF_{il} \frac{\partial S_{lo}}{\partial f_{kp}} F_{oj}^T &= jF_{il} \frac{\partial S_{lo}}{\partial C_{rv}} \frac{\partial C_{rv}}{\partial f_{kp}} F_{oj}^T \\
 &= jF_{il} \frac{1}{2} \frac{\partial 2S_{lo}}{\partial C_{rv}} \frac{\partial C_{rv}}{\partial f_{kp}} F_{oj}^T \\
 &= jF_{il} \frac{1}{2} \underbrace{\mathbb{C}_{lorv}}_{\textcircled{5}} \frac{\partial C_{rv}}{\partial f_{kp}} F_{oj}^T.
 \end{aligned} \tag{B. 7}$$

The right Cauchy–Green tensor is separately decomposed in order to find $\textcircled{5}$, i.e.,

$$C_{rv} = F_{rq}^T F_{qv} = f_{rq}^{-T} f_{qv}^{-1}. \tag{B. 8}$$

Thus

$$\begin{aligned}
 \textcircled{5} \Rightarrow \frac{\partial C_{rv}}{\partial f_{kp}} &= \frac{\partial f_{rq}^{-T}}{\partial f_{kp}} f_{qv}^{-1} + f_{rq}^{-T} \frac{\partial f_{qv}^{-1}}{\partial f_{kp}} \\
 &= -f_{rp}^{-T} f_{kq}^{-T} f_{qv}^{-1} - f_{rq}^{-T} f_{qp}^{-1} f_{kv}^{-T} \\
 &= -F_{rp}^T (F_{kq}^T F_{qv}) - (F_{rq}^T F_{qp}^T) F_{kv}^T \\
 &= -F_{rp}^T C_{kv} - C_{rp} F_{kv}^T \\
 &= -\underline{\mathbf{F}}^T \underline{\mathbf{C}} - \mathbf{C} \overline{\otimes} \mathbf{F}^T.
 \end{aligned} \tag{B. 9}$$

$\textcircled{3}$ is then rewritten by

$$\textcircled{3} \Rightarrow jF_{il} \frac{\partial S_{lo}}{\partial f_{kp}} F_{oj}^T = j\mathbf{F} \cdot \left[\frac{1}{2} \mathbb{C} : \frac{\partial \mathbf{C}}{\partial \mathbf{f}} \right] \cdot \mathbf{F}^T. \tag{B. 10}$$

The last term of the sought equation is given by

$$\begin{aligned}
 \textcircled{4} \Rightarrow jF_{il} S_{lo} \frac{\partial F_{oj}^T}{\partial f_{kp}} &= jF_{il} S_{lo} \frac{\partial f_{oj}^{-T}}{\partial f_{kp}} \\
 &= -jF_{il} S_{lo} f_{op}^{-T} f_{kj}^{-T} \\
 &= -j f_{kj}^{-T} F_{il} S_{lo} F_{op}^T \\
 &= -F_{kj}^T \sigma_{ip} \\
 &= -\sigma_{ip} F_{jk} \\
 &= -\underline{\boldsymbol{\sigma}} \underline{\otimes} \mathbf{F}.
 \end{aligned} \tag{B. 11}$$

Putting $\textcircled{1}$, $\textcircled{2}$, $\textcircled{3}$ and $\textcircled{4}$ together, the following expression is obtained

$$\Rightarrow \mathbf{a} = \boldsymbol{\sigma} \otimes \mathbf{F}^T - \mathbf{F} \overline{\otimes} \boldsymbol{\sigma} + j\mathbf{F} \cdot \left[\frac{1}{2} \mathbb{C} : \frac{\partial \mathbf{C}}{\partial \mathbf{f}} \right] \cdot \mathbf{F}^T - \underline{\boldsymbol{\sigma}} \underline{\otimes} \mathbf{F}, \tag{B. 12}$$

where

$$\frac{\partial \mathbf{C}}{\partial \mathbf{f}} = -\underline{\mathbf{F}}^T \underline{\mathbf{C}} - \mathbf{C} \overline{\otimes} \mathbf{F}^T. \tag{B. 13}$$

QED.

List of Symbols

\mathcal{B}_0	material or undeformed configuration	7
\mathcal{B}_t	spatial or deformed configuration	7
$\partial\mathcal{B}_0$	boundary of \mathcal{B}_0	8
$\partial\mathcal{B}_t$	boundary of \mathcal{B}_t	8
$\partial\mathcal{B}_0^T$	Neumann type boundary condition in the material configuration	8
$\partial\mathcal{B}_t^T$	Neumann type boundary condition in the spatial configuration	8
$\partial\mathcal{B}_0^\Phi$	Dirichlet type boundary condition in the material configuration	8
$\partial\mathcal{B}_t^\Phi$	Dirichlet type boundary condition in the spatial configuration	8
\mathcal{D}	dissipation	15
\mathcal{Y}	yield surface	20
\mathcal{E}	elastic domain	20
J	Jacobian determinant of the direct deformation gradient	8
j	Jacobian determinant of the inverse deformation gradient	9
Ψ	free energy density per volume in the undeformed configuration	19
Ψ^e	elastic free energy density per volume in the undeformed configuration ..	19
Ψ^p	plastic free energy density per volume in the undeformed configuration ..	19
ψ	Helmholtz free energy in the spatial configuration	16
h	isotropic hardening parameter	20
σ_0	initial yield stress	20
σ_∞	infinite yield stress	20
w	saturation parameter	20
m	mass	9
ρ_0	reference mass density	9
ρ	spatial mass density	9
e, e_s	specific internal energy in the material and spatial configurations	15
R, r	density of heat production in the material and spatial configurations ..	16
θ, θ_s	temperature in the material and spatial configurations	15
s, s_s	specific entropy in the material and spatial configurations	15
α	set of internal variables associated with the phenomenon of hardening ..	19
A	hardening thermodynamical force	20
y_{11}, y_{22}, y_{33}	normal yield stress	21
y_{12}, y_{23}, y_{31}	shear yield stress	21
δ_{ij}	Kronecker delta	31
$\lambda_i, \bar{\lambda}_i$	eigenvalue	31
f	objective function	99
λ	Lamé's first parameter	37
μ	Lamé's second parameter or shear modulus	37
κ	bulk modulus	37
E	Young's modulus	37
ν	Poisson's ratio	37

da	surface element of $\partial\mathcal{B}_t$	8
dA	surface element of $\partial\mathcal{B}_0$	8
dv	volume element of \mathcal{B}_t	8
dV	volume element of \mathcal{B}_0	8
Φ	quadratic yield function	21
\mathfrak{F}	net force	10
\mathbf{X}	material coordinates	7
\mathbf{x}	spatial coordinates	7
φ	direct deformation map	8
Φ	inverse deformation map	8
\mathbf{F}	direct deformation gradient	8
\mathbf{f}	inverse deformation gradient	8
\mathbf{E}	logarithmic (Hencky) total strain tensor	18
\mathbf{E}^e	elastic strain tensor	18
\mathbf{E}^p	plastic strain tensor	18
\mathbf{C}	right Cauchy-Green tensor	18
\mathbf{P}	first Piola-Kirchhoff tensor	12
\mathbf{S}	second Piola-Kirchhoff stress tensor	19
\mathbf{T}	Lagrangian stress tensor	19
\mathbf{I}	identity matrix	21
\mathbf{a}	acceleration	10
\mathbf{V}, \mathbf{v}	velocity field in the material and spatial configurations	10
\mathbf{b}	body force in the spatial configuration	11
\mathbf{B}	body force in the material configuration	12
$\bar{\mathbf{t}}$	Cauchy's traction	11
$\bar{\mathbf{T}}$	first Piola-Kirchhoff traction vector	12
\mathbf{n}	unit vector normal to a surface element da of $\partial\mathcal{B}_t$	8
\mathbf{N}	unit vector normal to a surface element dA of $\partial\mathcal{B}_0$	8
$\boldsymbol{\sigma}$	symmetric Cauchy stress tensor	11
\mathbf{H}	generalized hardening modulus	22
\mathbf{Q}, \mathbf{q}	heat flux in the material and spatial configurations	16
\mathbf{N}_i	eigentensor	32
$\mathbf{a}_1, \mathbf{a}_2, \mathbf{a}_3$	unit vectors	33
\mathbf{N}^d	dilatation mode	33
$\mathbf{N}_1^e, \mathbf{N}_2^e, \mathbf{N}_3^e$	isochoric extension modes	34
$\mathbf{N}_1^p, \mathbf{N}_2^p, \mathbf{N}_3^p$	isochoric pure shear modes	34
$\mathbf{N}_1^s, \mathbf{N}_2^s, \mathbf{N}_3^s$	isochoric simple shear modes	35
\mathbf{K}	tangent stiffness matrix	79
\mathbf{k}	tangent stiffness matrix	62
$\dot{\mathbf{E}}^p$	rate of plastic strain	20
$\dot{\alpha}$	rate of the set of internal variables	20
$\dot{\gamma}$	plastic multiplier	22
$\dot{\mathbf{E}}$	strain rate	18
$\dot{\mathbf{F}}$	rate of deformation	18
\mathcal{P}_{int}	stress power	13
\mathcal{P}_{ext}	external stress power	13

\mathcal{K}	kinetic energy	13
\mathbb{P}	first derivative of the logarithmic strain	18
\mathbb{L}	second derivative of the logarithmic strain	18
\mathbb{E}^e	elastic fourth-order stiffness tensor	20
\mathbb{H}	Hill tensor	21
\mathbb{I}^{sym}	fourth-order symmetric identity tensor	21
$\mathbb{I}_{\text{dev}}^{\text{sym}}$	deviatoric part of the fourth-order symmetric identity tensor	38
$\mathbb{I}_{\text{dev}}^{\text{sym}}$	volumetric part of the fourth-order symmetric identity tensor	37
\mathbb{C}^{ep}	elastic-plastic tangent modulus	19
\mathbb{P}_k	projection operator	32
\mathbf{A}	tangent operator	62
\mathbf{a}	tangent operator	79
\mathbf{A}^T	transpose of matrix \mathbf{A}	8
$\text{Grad}(\cdot)$	gradient operator with respect to the material coordinates	8
$\text{grad}(\cdot)$	gradient operator with respect to the spatial coordinates	9
$\text{div}(\cdot)$	spatial divergence operator with respect to spatial coordinates \mathbf{x}	11
$\text{Div}(\cdot)$	material divergence operator with respect to material coordinates \mathbf{X} ...	12
$\overline{\otimes}$	non-standard dyadic product	62
$\underline{\otimes}$	non-standard dyadic product	79
$\mathcal{D}_{\{\cdot\}}$	Gâteaux derivative	61
$\frac{\text{d}f(\mathbf{X})}{\text{d}\mathbf{X}}$	gradient of the objective function	103

List of Figures

1.1	Undeformed (left) circular and deformed (right) aluminium plates.	1
2.1	Material (right) and spatial (left) configurations.	7
3.1	Schematic view of the return mapping, as in [16].	24
4.1	Coordinate system.	33
4.2	Dilatation mode.	33
4.3	Isochoric extension mode.	34
4.4	Isochoric pure shear mode.	35
4.5	Isochoric simple shear mode.	36
5.1	Discretisation of the material (right) and spatial (left) configurations.	57
5.2	Discretisation of a body in the material configuration with MSC.Patran2010.2. .	57
5.3	Graphical view of the Newton–Raphson method with three iterations.	60
5.4	Undeformed configuration of a bar in the material configuration \mathcal{B}_0	64
5.5	Deformed bar in the spatial configuration \mathcal{B}_t with equivalent von Mises stress $\sigma_{\text{eq}}^{\text{vm}}$ (MPa) with isotropic hyperelastic behaviour.	64
5.6	Undeformed plate with a hole in the material configuration \mathcal{B}_0	65
5.7	Undeformed configuration of a plate with a hole in \mathcal{B}_0 in the $[\mathbf{X}_1, \mathbf{X}_2]$ plane. . .	65
5.8	Deformed configuration of a plate with a hole in \mathcal{B}_t in the $[\mathbf{x}_1, \mathbf{x}_2]$ plane with equivalent von Mises stress $\sigma_{\text{eq}}^{\text{vm}}$ (MPa) with isotropic hyperelastic behaviour. . .	65
5.9	Deformed configuration of a plate with a hole in \mathcal{B}_t in the $[\mathbf{x}_1, \mathbf{x}_2]$ plane with equivalent von Mises stress $\sigma_{\text{eq}}^{\text{vm}}$ (MPa) with cubic hyperelastic behaviour. . . .	66
5.10	Deformed configuration of a plate with a hole in \mathcal{B}_t in the $[\mathbf{x}_1, \mathbf{x}_2]$ plane with equivalent von Mises stress $\sigma_{\text{eq}}^{\text{vm}}$ (MPa) with hexagonal hyperelastic behaviour. .	66
5.11	Undeformed configuration of a plate with four holes in \mathcal{B}_0	67
5.12	Deformed plate with four holes in the spatial configuration \mathcal{B}_t ($[\mathbf{x}_1, \mathbf{x}_3]$ plane) with equivalent von Mises stress $\sigma_{\text{eq}}^{\text{vm}}$ (MPa) with isotropic elastoplastic behaviour. .	67
5.13	Deformed plate with four holes in the spatial configuration \mathcal{B}_t ($[\mathbf{x}_1, \mathbf{x}_3]$ plane) with equivalent plastic strain \mathbf{E}_{eq}^p (-) with isotropic elastoplastic behaviour. . . .	68
5.14	Undeformed round plate in the material configuration \mathcal{B}_0 in the $[\mathbf{X}_1, \mathbf{X}_2]$ plane. .	69
5.15	Deformed round plate in the spatial configuration \mathcal{B}_t ($[\mathbf{x}_1, \mathbf{x}_2]$ plane) with equivalent von Mises stress $\sigma_{\text{eq}}^{\text{vm}}$ (MPa) with anisotropic elastoplastic behaviour. . .	70
5.16	Deformed round plate in the spatial configuration \mathcal{B}_t ($[\mathbf{x}_1, \mathbf{x}_2]$ plane) with equivalent plastic strain \mathbf{E}_{eq}^p (-) with anisotropic elastoplastic behaviour.	70
5.17	Undeformed plate in the material configuration \mathcal{B}_0 in the $[\mathbf{X}_1, \mathbf{X}_2]$ plane.	71
5.18	Deformed round plate in the spatial configuration \mathcal{B}_t ($[\mathbf{x}_1, \mathbf{x}_2]$ plane) with equivalent von Mises stress $\sigma_{\text{eq}}^{\text{vm}}$ (MPa) with anisotropic elastoplastic behaviour. . .	71
5.19	Deformed round plate in the spatial configuration \mathcal{B}_t ($[\mathbf{x}_1, \mathbf{x}_2]$ plane) with equivalent plastic strain \mathbf{E}_{eq}^p (-) with anisotropic elastoplastic behaviour.	72

6.1	Graphical view of the Newton–Raphson method for the inverse problem with three iterations.	77
6.2	Schematic view for validating the inverse mechanical problem.	80
6.3	Deformed thick cantilever in the spatial configuration \mathcal{B}_t in the $[\mathbf{x}_1, \mathbf{x}_3]$ plane.	81
6.4	Deformed thick cantilever in the spatial configuration \mathcal{B}_t in the $[\mathbf{x}_1, \mathbf{x}_2]$ plane.	81
6.5	Undeformed thick cantilever in the material configuration \mathcal{B}_0 in the $[\mathbf{X}_1, \mathbf{X}_2]$ plane.	81
6.6	Undeformed thick cantilever in the material configuration \mathcal{B}_0 in the $[\mathbf{X}_1, \mathbf{X}_2]$ plane with loads and boundary conditions.	82
6.7	Deformed thick cantilever in the spatial configuration \mathcal{B}_t in the $[\mathbf{x}_1, \mathbf{x}_2]$ plane with equivalent von Mises stress $\sigma_{\text{eq}}^{\text{vm}}$ (MPa) with isotropic hyperelastic behaviour.	82
6.8	Deformed plate in the spatial configuration \mathcal{B}_t	84
6.9	Undeformed plate in the material configuration \mathcal{B}_0 with isotropic hyperelastic behaviour.	84
6.10	Undeformed plate in the material configuration \mathcal{B}_0 with cubic hyperelastic behaviour.	84
6.11	Undeformed plate in the material configuration \mathcal{B}_0 with hexagonal hyperelastic behaviour.	84
6.12	Undeformed plate in the material configuration \mathcal{B}_0 with forces and boundary conditions (isotropic material).	85
6.13	Deformed plate in the spatial configuration \mathcal{B}_t with equivalent von Mises stress $\sigma_{\text{eq}}^{\text{vm}}$ (MPa) (isotropic material).	85
6.14	Undeformed plate in the material configuration \mathcal{B}_0 with forces and boundary conditions (cubic material).	85
6.15	Deformed plate in the spatial configuration \mathcal{B}_t with equivalent von Mises stress $\sigma_{\text{eq}}^{\text{vm}}$ (MPa) (cubic material).	86
6.16	Undeformed plate in the material configuration \mathcal{B}_0 with forces and boundary conditions (hexagonal material).	86
6.17	Deformed plate in the spatial configuration \mathcal{B}_t with equivalent von Mises stress $\sigma_{\text{eq}}^{\text{vm}}$ (MPa) (hexagonal material).	86
6.18	Deformed layer in the spatial configuration \mathcal{B}_t in the $[\mathbf{x}_1, \mathbf{x}_2]$ plane.	86
6.19	Deformed shape of straight, rectangular geometry in the spatial configuration \mathcal{B}_t	87
6.20	Undeformed layers in the material configuration \mathcal{B}_0 with $\alpha=0$ and $\beta=0$	88
6.21	Undeformed layers in the material configuration \mathcal{B}_0 with $\alpha=\pi/6$ and $\beta=5\pi/6$	88
6.22	Undeformed layers in the material configuration \mathcal{B}_0 with $\alpha=5\pi/6$ and $\beta=\pi/6$	88
6.23	Undeformed layers in the material configuration \mathcal{B}_0 for $\alpha=0$ and $\beta=0$ with forces and boundary conditions.	88
6.24	Deformed layers in the spatial configuration \mathcal{B}_t for $\alpha=0$ and $\beta=0$ with equivalent von Mises stress $\sigma_{\text{eq}}^{\text{vm}}$ (MPa).	89
6.25	Undeformed layers in the material configuration \mathcal{B}_0 for $\alpha=\pi/6$ and $\beta=5\pi/6$ with forces and boundary conditions.	89
6.26	Deformed layers in the spatial configuration \mathcal{B}_t for $\alpha=\pi/6$ and $\beta=5\pi/6$ with equivalent von Mises stress $\sigma_{\text{eq}}^{\text{vm}}$ (MPa).	89
6.27	Undeformed layers in the material configuration \mathcal{B}_0 for $\alpha=5\pi/6$ and $\beta=\pi/6$ with forces and boundary conditions.	89
6.28	Deformed layers in the spatial configuration \mathcal{B}_t for $\alpha=5\pi/6$ and $\beta=\pi/6$ with equivalent von Mises stress $\sigma_{\text{eq}}^{\text{vm}}$ (MPa).	90

6.29 Deformed plate in the spatial configuration \mathcal{B}_t	91
6.30 Undeformed plate in the material configuration \mathcal{B}_0	91
6.31 Undeformed plate in the material configuration \mathcal{B}_0 with load and boundary conditions.	91
6.32 Deformed plate in the spatial configuration \mathcal{B}_t with equivalent von Mises stress $\sigma_{\text{eq}}^{\text{vm}}$ (MPa).	91
6.33 Deformed plate in the spatial configuration \mathcal{B}_t with equivalent plastic strain E_{eq}^p (-).	91
6.34 Undeformed plate with four holes in the material configuration \mathcal{B}_0 in the $[\mathbf{X}_1, \mathbf{X}_3]$ plane.	92
6.35 Undeformed plate with four holes in the material configuration \mathcal{B}_0 ($[\mathbf{X}_1, \mathbf{X}_3]$ plane) with load and boundary conditions.	92
6.36 Deformed plate with four holes in the spatial configuration \mathcal{B}_t ($[\mathbf{x}_1, \mathbf{x}_3]$ plane) with equivalent von Mises stress $\sigma_{\text{eq}}^{\text{vm}}$ (MPa).	93
6.37 Deformed plate with four holes in the spatial configuration \mathcal{B}_t ($[\mathbf{x}_1, \mathbf{x}_3]$ plane) with equivalent plastic strain E_{eq}^p (-).	93
6.38 Uniaxial tension experiment with undeformed (left) and deformed (right) configurations.	93
6.39 Uniaxial stress-strain curve in hyperelasticity.	94
6.40 Uniaxial stress-strain curve in elastoplasticity.	95
6.41 Schematic representation of Equation 6.50 and Equation 6.51.	96
6.42 Schematic view of solving the inverse mechanical problem in elastoplasticity.	97
6.43 Undeformed plate in the material configuration \mathcal{B}_0 with boundary conditions and loads.	97
6.44 Deformed plate in the spatial configuration \mathcal{B}_t with equivalent von Mises stress $\sigma_{\text{eq}}^{\text{vm}}$ (MPa).	97
6.45 Deformed plate in the spatial configuration \mathcal{B}_t with equivalent plastic strain E_{eq}^p (-).	98
6.46 Undeformed plate in the material configuration \mathcal{B}_0 computed with the set of internal variables.	98
6.47 Undeformed thick cantilever in the material configuration \mathcal{B}_0 ($[\mathbf{X}_1, \mathbf{X}_3]$ plane) computed with the set of internal variables.	98
7.1 Deformed Cook's cantilever in $\mathcal{B}_t^{\text{target}}$ in the $[\mathbf{x}_1, \mathbf{x}_2]$ plane.	104
7.2 Undeformed Cook's cantilever in \mathcal{B}_0 in the $[\mathbf{X}_1, \mathbf{X}_2]$ plane after two iterations.	105
7.3 Deformed Cook's cantilever in \mathcal{B}_t in the $[\mathbf{x}_1, \mathbf{x}_3]$ plane.	105
7.4 Undeformed Cook's cantilever in \mathcal{B}_0 in the $[\mathbf{X}_1, \mathbf{X}_3]$ plane after two iterations.	105
7.5 Deformed plate with four holes in $\mathcal{B}_t^{\text{target}}$ in the $[\mathbf{x}_1, \mathbf{x}_3]$ plane.	105
7.6 Undeformed plate with four holes in \mathcal{B}_0 in the $[\mathbf{X}_1, \mathbf{X}_3]$ plane after 14 iterations.	106
7.7 Undeformed thick cantilever in the material configuration \mathcal{B}_0 ($[\mathbf{X}_1, \mathbf{X}_2]$ plane) for $\mathfrak{F}=10^4$	107
7.8 Undeformed thick cantilever in the material configuration \mathcal{B}_0 ($[\mathbf{X}_1, \mathbf{X}_2]$ plane) for $\mathfrak{F}=3 \cdot 10^4$	108
7.9 Undeformed thick cantilever in the material configuration \mathcal{B}_0 ($[\mathbf{X}_1, \mathbf{X}_2]$ plane) for $\mathfrak{F}=5 \cdot 10^4$	108

7.10	Undeformed thick cantilever in the material configuration \mathcal{B}_0 ($[\mathbf{X}_1, \mathbf{X}_2]$ plane) with load and boundary conditions.	108
7.11	Deformed thick cantilever in the spatial configuration \mathcal{B}_t ($[\mathbf{x}_1, \mathbf{x}_2]$ plane) with equivalent von Mises stress $\sigma_{\text{eq}}^{\text{vm}}$ (MPa).	109
7.12	Undeformed plate with four holes in the material configuration \mathcal{B}_0 ($[\mathbf{X}_1, \mathbf{X}_3]$ plane) for $\mathfrak{F}=5 \cdot 10^3$	109
7.13	Undeformed plate with four holes in the material configuration \mathcal{B}_0 ($[\mathbf{X}_1, \mathbf{X}_3]$ plane) for $\mathfrak{F}=15 \cdot 10^3$	109
7.14	Undeformed plate with four holes in the material configuration \mathcal{B}_0 ($[\mathbf{X}_1, \mathbf{X}_3]$ plane) for $\mathfrak{F}=25 \cdot 10^3$	110
7.15	Undeformed plate with four holes in the material configuration \mathcal{B}_0 ($[\mathbf{X}_1, \mathbf{X}_3]$ plane) with load and boundary conditions.	110
7.16	Deformed plate with four holes in the spatial configuration \mathcal{B}_t ($[\mathbf{x}_1, \mathbf{x}_3]$ plane) with equivalent von Mises stress $\sigma_{\text{eq}}^{\text{vm}}$ (MPa).	110
7.17	Undeformed plate with a hole in the material configuration \mathcal{B}_0 ($[\mathbf{X}_1, \mathbf{X}_2]$ plane) for $\mathfrak{F}=10^5$	111
7.18	Undeformed plate with a hole in the material configuration \mathcal{B}_0 ($[\mathbf{X}_1, \mathbf{X}_2]$ plane) for $\mathfrak{F}=3 \cdot 10^5$	111
7.19	Undeformed plate with a hole in the material configuration \mathcal{B}_0 ($[\mathbf{X}_1, \mathbf{X}_2]$ plane) for $\mathfrak{F}=5 \cdot 10^5$	112
7.20	Undeformed plate with a hole in the material configuration \mathcal{B}_0 ($[\mathbf{X}_1, \mathbf{X}_2]$ plane) with load and boundary conditions.	112
7.21	Deformed plate with a hole in the spatial configuration \mathcal{B}_t ($[\mathbf{x}_1, \mathbf{x}_2]$ plane) with equivalent von Mises stress $\sigma_{\text{eq}}^{\text{vm}}$ (MPa).	112
7.22	Deformed plate in the spatial configuration \mathcal{B}_t in the $[\mathbf{x}_1, \mathbf{x}_2]$ plane.	113
7.23	Cut of the deformed plate in the spatial configuration \mathcal{B}_t in the $[\mathbf{x}_1, \mathbf{x}_3]$ plane.	114
7.24	Cut of the undeformed plate in the material configuration \mathcal{B}_0 in the $[\mathbf{X}_1, \mathbf{X}_3]$ plane for $\mathfrak{F}=400$	114
7.25	Cut of the undeformed plate in the material configuration \mathcal{B}_0 in the $[\mathbf{X}_1, \mathbf{X}_3]$ plane for $\mathfrak{F}=800$	114
7.26	Cut of the undeformed plate in the material configuration \mathcal{B}_0 for in the $[\mathbf{X}_1, \mathbf{X}_3]$ plane $\mathfrak{F}=1200$	114
7.27	Cut of the undeformed plate in the material configuration \mathcal{B}_0 in the $[\mathbf{X}_1, \mathbf{X}_3]$ plane with load and boundary conditions.	114
7.28	Deformed plate in the spatial configuration \mathcal{B}_t in the $[\mathbf{x}_1, \mathbf{x}_2]$ plane with equivalent von Mises stress $\sigma_{\text{eq}}^{\text{vm}}$ (MPa).	114
7.29	Deformed plate in the spatial configuration \mathcal{B}_t in the $[\mathbf{x}_1, \mathbf{x}_2]$ plane with equivalent plastic strain \mathbf{E}_{eq}^p (-).	115
7.30	Deformed circular plate in the spatial configuration \mathcal{B}_t in the $[\mathbf{x}_1, \mathbf{x}_2]$ plane.	115
7.31	Undeformed plate in the material configuration \mathcal{B}_0 ($[\mathbf{X}_1, \mathbf{X}_2]$ plane) for $\mathfrak{F}=5 \cdot 10^4$	116
7.32	Undeformed plate in the material configuration \mathcal{B}_0 ($[\mathbf{X}_1, \mathbf{X}_2]$ plane) for $\mathfrak{F}=10 \cdot 10^4$	116
7.33	Undeformed plate in the material configuration \mathcal{B}_0 ($[\mathbf{X}_1, \mathbf{X}_2]$ plane) for $\mathfrak{F}=15 \cdot 10^4$	116
7.34	Undeformed plate in the material configuration \mathcal{B}_0 ($[\mathbf{X}_1, \mathbf{X}_2]$ plane) with load and boundary conditions.	117
7.35	Deformed plate in the spatial configuration \mathcal{B}_t ($[\mathbf{x}_1, \mathbf{x}_2]$ plane) with equivalent von Mises stress $\sigma_{\text{eq}}^{\text{vm}}$ (MPa).	117

7.36 Deformed plate in the spatial configuration \mathcal{B}_t ($[\mathbf{x}_1, \mathbf{x}_2]$ plane) with equivalent plastic strain \mathbf{E}_{eq}^p (-).	118
---	-----

List of Tables

4.1	Orthonormality of eigentensors	36
4.2	Decomposition of the elasticity tensor into Kelvin modes.	54
5.1	Numerical example: Material parameters for an isotropic hyperelastic material . .	63
5.2	Numerical example: Material parameters for an anisotropic (cubic) hyperelastic material.	64
5.3	Numerical example: Material parameters for an anisotropic (hexagonal- e_1) hyperelastic material.	64
5.4	Numerical example: Material parameters for an isotropic elastoplastic material.	67
5.5	Numerical example: Material parameters for an anisotropic (cubic) elastoplastic material.	68
6.1	Numerical example: Material parameters for an isotropic hyperelastic material . .	81
6.2	Numerical example: Material parameters for an anisotropic (cubic) hyperelastic material.	83
6.3	Numerical example: Material parameters for an anisotropic (hexagonal- e_1) hyperelastic material.	83
6.4	Numerical example: Material parameters for an anisotropic (orthotropic) hyperelastic material.	87
6.5	Numerical example: Material parameters for an isotropic elastoplastic material.	90
7.1	Numerical example: Optimisation parameters for the isotropic elastoplastic example based on Schmidt [54].	107
7.2	Numerical example: Material parameters for an isotropic elastoplastic material.	113

Bibliography

- [1] S. Govindjee and P. A. Mihalic, “Computational methods for inverse finite elastostatics,” *Computer Methods in Applied Mechanics and Engineering*, vol. 136, no. 1-2, pp. 47–57, 1996.
- [2] ——, “Computational methods for inverse deformations in quasi-incompressible finite elasticity,” *International Journal for Numerical Methods in Engineering*, vol. 43, no. 5, pp. 821–838, 1998.
- [3] R. Shield, “Inverse deformation results in finite elasticity,” *Zeitschrift für angewandte Mathematik und Physik*, vol. 18, pp. 490–500, 1967.
- [4] S. Govindjee, “Finite deformation inverse design modeling with temperature changes, axis-symmetry and anisotropy,” *UCB/SEMM-1999/01, University of California at Berkley*, 1999.
- [5] M. Koishi and S. Govindjee, “Inverse design methodology of a tire,” *Tire Science and Technology*, vol. 29, pp. 155–170, 2001.
- [6] T. Yamada, “Finite element procedure of initial shape deformation for hyperelasticity,” *Structural Engineering and Mechanics*, vol. 6, pp. 173–183, 1998.
- [7] V. D. Fachinotti, A. Cardona, and P. Jetteur, “A finite element model for inverse design problems in large deformations anisotropic hyperelasticity,” *Mecánica Computacional*, vol. XXV, pp. 1269–1284, 2006.
- [8] ——, “Finite element modelling of inverse design problems in large deformations anisotropic hyperelasticity,” *International Journal for Numerical Methods in Engineering*, vol. 74, no. 6, pp. 894–910, 2008.
- [9] A. Albanesi, V. Fachinotti, and A. Cardona, “Inverse finite element method for large-displacement beams,” *International Journal for Numerical Methods in Engineering*, vol. 84, pp. 1166–1182, 2010.
- [10] A. Albanesi, V. Fachinotti, and M. Pucheta, “A review on design methods for compliant mechanisms,” *Mecánica Computacional*, vol. XXIX, pp. 59–72, 2010.
- [11] J. Lu, X. Zhou, and M. Raghavan, “Computational method of inverse elastostatics for anisotropic hyperelastic solids,” *International Journal for Numerical Methods in Engineering*, vol. 69, pp. 1239–1261, 2007.
- [12] X. Zhou and J. Lu, “Inverse formulation for geometrically exact stress resultant shells,” *International Journal for Numerical Methods in Engineering*, vol. 74, pp. 1278–1302, 2008.
- [13] S. Germain, M. Scherer, and P. Steinmann, “On inverse form finding for anisotropic hyperelasticity in logarithmic strain space,” *International Journal of Structural Changes in Solids – Mechanics and Applications*, vol. 2, no. 2, pp. 1–16, 2010.
- [14] ——, “On inverse form finding for anisotropic materials,” *Proceedings in Applied Mathematics and Mechanics*, vol. 10, no. 1, pp. 159–160, 2010.
- [15] S. Germain and P. Steinmann, “On inverse form finding for anisotropic elastoplastic materials,” *AIP Conference Proceedings*, vol. 1353, no. 1, pp. 1169–1174, 2011.

- [16] E. de Souza Neto, D. Peric, and D. Owen, *Computational Methods for Plasticity – Theory and Applications*. Wiley, 2008.
- [17] G. A. Holzapfel, *Nonlinear Solid Mechanics: A Continuum Approach for Engineering*. Wiley, 2000.
- [18] R. Ogden, *Non-Linear Elastic Deformations*. Dover Publications, 1997.
- [19] J. Bonet and R. D. Wood, *Nonlinear Continuum Mechanics for Finite Element Analysis*. Cambridge University Press, 1997.
- [20] C. Miehe, N. Apel, and M. Lambrecht, “Anisotropic additive plasticity in the logarithmic strain space: Modular kinematic formulation and implementation based on incremental minimization principles for standard materials,” *Computer Methods in Applied Mechanics and Engineering*, vol. 191, no. 47–48, pp. 5383–5425, 2002.
- [21] C. Miehe and N. Apel, “Anisotropic elastic-plastic analysis of shells at large strains. a comparison of multiplicative and additive approaches to enhanced finite element design and constitutive modelling,” *International Journal for Numerical Methods in Engineering*, vol. 61, no. 12, pp. 2067–2113, 2004.
- [22] N. Apel, “Approaches to the description of anisotropic material behaviour at finite elastic and plastic deformations, theory and numerics.” *Dissertationsschrift, Bericht Nr.: I-12 des Instituts für Mechanik (Bauwesen) Lehrstuhl I, Universität Stuttgart*, 2004.
- [23] M. Mehrabadi and S. Cowin, “Eigentensors of linear anisotropic elastic materials,” *Q.J. Mech. Appl. Math.*, vol. 43, no. 1, pp. 15–41, 1990.
- [24] S. Sutcliffe, “Spectral decomposition of the elasticity tensor,” *Journal of Applied Mechanics*, vol. 59, pp. 762–773, 1992.
- [25] S. Cowin and M. Mehrabadi, “On the identification of material symmetry for anisotropic elastic materials,” *Q.J. Mech. Appl. Math.*, vol. 40, no. 4, pp. 451–476, 1987.
- [26] ——, “The structure of the linear anisotropic elastic symmetries,” *J. Mech. Phys. Solids*, vol. 40, no. 7, pp. 1459–1471, 1992.
- [27] P. Chadwick, M. Vianello, and S. Cowin, “A new proof that the number of linear elastic symmetries is eight,” *J. Mech. Phys. Solids*, vol. 49, pp. 2471–2492, 2001.
- [28] R. Mahnken, “Anisotropy in geometrically non-linear elasticity with generalized Seth–Hill strain tensors projected to invariant subspaces,” *Commun. Numer. Meth. Engng*, vol. 21, pp. 405–418, 2005.
- [29] J. Simo and T. Hughes, *Computational Inelasticity*. Springer-Verlag, 1998.
- [30] B. Kleuter, A. Menzel, and P. Steinmann, “Generalized parameter identification for finite viscoelasticity,” *Computer Methods in Applied Mechanics and Engineering*, vol. 196, no. 35–36, pp. 3315–3334, 2007.
- [31] R. Mahnken and E. Stein, “A unified approach for parameter identification of inelastic material models in the frame of the finite element method,” *Computer Methods in Applied Mechanics and Engineering*, vol. 136, no. 3–4, pp. 225–258, 1996.
- [32] ——, “Parameter identification for finite deformation elasto-plasticity in principal directions,” *Computer Methods in Applied Mechanics and Engineering*, vol. 147, no. 1–2, pp. 17–39, 1997.

- [33] ——, “Parameter identification for viscoplastic models based on analytical derivatives of a least-squares functional and stability investigations,” *International Journal of Plasticity*, vol. 12, no. 4, pp. 451–479, 1996.
- [34] R. Mahnken, M. Johansson, and K. Runesson, “Parameter estimation for a viscoplastic damage model using a gradient-based optimization algorithm,” *Engineering Computations*, vol. 15, no. 7, pp. 925–955, 1998.
- [35] R. Mahnken, “A comprehensive study of a multiplicative elastoplasticity model coupled to damage including parameter identification,” *Computers & Structures*, vol. 74, no. 2, pp. 179–200, 2000.
- [36] ——, *Duale Methoden für nichtlineare Optimierungsprobleme in der Strukturmechanik*. Bericht Nr. F 92/3, Forschungs- und Seminarberichte aus dem Bereich der Mechanik der Universität Hannover, 1992.
- [37] ——, *Theoretische und numerische Aspekte zur Parameteridentifikation und Modellierung bei metallischen Werkstoffen*. Bericht Nr. F 98/2, Forschungs- und Seminarberichte aus dem Bereich der Mechanik der Universität Hannover, 1998.
- [38] R. Mahnken and E. Stein, “The identification of parameters for visco-plastic models via finite-element methods and gradient methods,” *Modelling Simul. Mater. Sci. Eng.*, vol. 2, pp. 597–616, 1994.
- [39] R. Haftka and R. Grandhi, “Structural shape optimization – A survey,” *Computer Methods in Applied Mechanics and Engineering*, vol. 57, pp. 91–106, 1986.
- [40] J. Samareh, “A survey of shape parameterization techniques,” *NASA CP-1999-20913657*, pp. 333–343, 1999.
- [41] S. Schwarz, “Sensitivitätsanalyse und Optimierung bei nicht linearem Strukturverhalten,” *Dissertationsschrift, Bericht Nr. 34 des Instituts für Baustatik, Universität Stuttgart*, 2001.
- [42] K.-U. Bletzinger, M. Firl, and F. Daoud, “Techniken der formoptimierung,” *Weirmarer Optimierungs- und Stochastiktage 2.0*, Dez. 2005.
- [43] K.-U. Bletzinger and E. Ramm, “Structural optimization and form finding of light weight structures,” *Computers and Structures*, vol. 79, pp. 2053–2062, 2001.
- [44] K.-U. Bletzinger, R. Wüchner, F. Daoud, and N. Camprubi, “Computational methods for form finding and optimization of shells and membranes,” *Computer Methods in Applied Mechanics and Engineering*, vol. 194, pp. 3438–3452, 2005.
- [45] L. Fourment and J. Chenot, “Optimal design for non-steady-state metal forming processes – Part I: Shape optimization method,” *International Journal for Numerical Methods in Engineering*, vol. 39, pp. 33–50, 1996.
- [46] ——, “Optimal design for non-steady-state metal forming processes – Part II: Application of shape optimization in forging,” *International Journal for Numerical Methods in Engineering*, vol. 39, pp. 51–65, 1996.
- [47] S. Badrinarayanan, A. Constantinescu, and N. Zabaras, “Preform design in metal forming,” *Numiform'95*, pp. 533–538, 1995.
- [48] A. Srikanth and N. Zabaras, “Shape optimization and preform design in metal forming processes,” *Computer Methods in Applied Mechanics and Engineering*, vol. 190, pp. 1859–1901, 2000.

- [49] J.-L. Chenot, E. Massoni, and L. Fourment, "Inverse problems in finite element simulation of metal forming processes," *Engineering Computations*, vol. 13, pp. 190–225, 1996.
- [50] K. Maute, S. Schwarz, and E. Ramm, "Adaptive topology optimization of elastoplastic structures," *Structural Optimization*, vol. 15, pp. 81–91, 1998.
- [51] S. Schwarz, K. Maute, and E. Ramm, "Topology and shape optimization for elastoplastic structural response," *Computer Methods in Applied Mechanics and Engineering*, vol. 190, pp. 2135–2155, 2001.
- [52] D. Luenberger, *Linear and Nonlinear Programming*. Addison-Wesley, 1984.
- [53] J. Nocedal and S. Wright, *Numerical Optimization*. Springer-Verlag, 2006.
- [54] M. Schmidt, <http://www.di.ens.fr/mschmidt/Software/minFunc.html>, 2005.
- [55] L. Sousa, C. Castro, C. António, and A. Santos, "Inverse methods in design of industrial forging processes," *Journal of Materials Processing Technology*, vol. 128, pp. 266–273, 2002.
- [56] J.-P. Ponthot and J.-P. Kleinermann, "A cascade optimization methodology for automatic parameter identification and shape/process optimization in metal forming simulation," *Computer Methods in Applied Mechanics and Engineering*, vol. 195, pp. 5472–5508, 2006.
- [57] S. Germain and P. Steinmann, "Shape optimization for anisotropic elastoplasticity in logarithmic strain space," *Computational Plasticity XI – Fundamentals and Applications*, pp. 1479–1490, 2011.
- [58] T. Yao and K. Choi, "3-d shape optimal design and automatic finite element regridding," *Int. J. Numer. Meth. Engng.*, vol. 28, pp. 369–384, 1989.
- [59] S. Ganapathysubramanian and N. Zabaras, "Computational design of deformation processes for materials with ductile damage," *Computer Methods in Applied Mechanics and Engineering*, vol. 192, pp. 147–183, 2003.
- [60] S. Archarjee and N. Zabaras, "The continuum sensitivity method for the computational design of three-dimensional deformation processes," *Computer Methods in Applied Mechanics and Engineering*, vol. 195, pp. 6822–6842, 2006.
- [61] F.-J. Barthold, "Theorie und numerik zur berechnung und optimierung von strukturen aus isotropen, hyperelastischen materialen," *Bericht Nr. F 93/2, Forschungs- und Seminarberichte aus dem Bereich der Mechanik der Universität Hannover*, 1993.
- [62] S. Schwarz and E. Ramm, "Sensitivity analysis and optimization for non-linear structural response," *Engineering Computations*, vol. 18, pp. 610–641, 2001.
- [63] R. Haftka and H. Adelman, "Recent developments in structural sensitivity analysis," *Structural Optimization*, vol. 1, pp. 137–151, 1989.
- [64] C. Burg, "Use of discrete sensitivity analysis to transform explicit simulation codes into design optimization codes," *Fourth Mississippi State Conference on Differential Equations and Computational Simulations, Electronic Journal of Differential Equations, Conference 03*, pp. 13–27, 1999.
- [65] M. Scherer, R. Denzer, and P. Steinmann, "A fictitious energy approach for shape optimization," *International Journal for Numerical Methods in Engineering*, vol. 82, pp. 269–302, 2010.
- [66] M. Scherer, "Regularizing constraints for mesh and shape optimization problems," *Dissertationsschrift, Band 5 des Lehrstuhls für Technische Mechanik, Universität Erlangen-Nürnberg*, 2011.

- [67] S. Germain and P. Steinmann, “Towards inverse form finding methods for a deep drawing steel DC04,” *Key Engineering Materials*, vol. 504–506, pp. 619–624, 2012.
- [68] ——, “On a recursive algorithm for avoiding mesh distortion in inverse form finding,” *Journal of the Serbian Society for Computational Mechanics*, vol. 6, no. 1, pp. 216–234, 2012.
- [69] ——, “A comparison between inverse form finding and shape optimization methods for anisotropic hyperelasticity in logarithmic strain space,” *Proceedings in Applied Mathematics and Mechanics*, vol. 11, no. 1, pp. 367–368, 2011.
- [70] ——, “On two different inverse form finding methods for hyperelastic and elastoplastic materials,” *Proceedings in Applied Mathematics and Mechanics*, vol. 12, pp. 263–264, 2012.
- [71] O. Gonzales and A. M. Stuart, *A First Course in Continuum Mechanics*. Cambridge University Press, 2008.
- [72] P. Wriggers, *Nichtlineare Finite-Element-Methoden*. Springer-Verlag, 2001.
- [73] I. Newton, *Mathematical Principles of Natural Philosophy*. Translated into English by Andrew Motte based on 3rd Latin edition from 1726, 1729, vol. 1.
- [74] T. J. Hughes and J. E. Marsden, “Some applications of geometry in continuum mechanics,” *Report on Mathematical Physics*, vol. 12, pp. 35–44, 1977.
- [75] P. Steinmann, M. Scherer, and R. Denzer, “Secret and joy of configurational mechanics: From foundations in continuum mechanics to applications in computational mechanics,” *Z. angew. Math. Mech.*, vol. 89, pp. 614–630, 2009.
- [76] E. Lehmann, S. Schmaltz, S. Germain, D. Fassmann, C. Weber, S. Löhner, M. Schaper, P. Steinmann, K. Willner, and P. Wriggers, “Material model identification for DC04 based on the numerical modelling of the polycrystalline microstructure and experimental data,” *Key Engineering Materials*, vol. 504–506, pp. 993–998, 2012.
- [77] E. Lehmann, S. Schmaltz, D. Fassmann, S. Germain, C. Weber, S. Löhner, M. Schaper, P. Steinmann, K. Willner, and P. Wriggers, “Identifikation eines Materialmodells für den DC04 basierend auf der numerischen Modellierung der polykristallinen Mikrostruktur und experimentellen Daten,” *Tagungsband zum 1. Workshop Blechmassivumformung 2011*, pp. 13–32, 2011.
- [78] C. Miehe, “Computation of isotropic tensor functions,” *Communications in Numerical Methods in Engineering*, vol. 9, no. 11, pp. 889–896, 1993.
- [79] C. Miehe and M. Lambrecht, “Algorithms for computation of stresses and elasticity moduli in terms of Seth–Hill’s family of generalized strain tensors,” *Communications in Numerical Methods in Engineering*, vol. 17, no. 5, pp. 337–353, 2001.
- [80] M. Itskov, “On the application of the additive decomposition of generalized strain measures in large strain plasticity,” *Mechanics Research Communications*, vol. 31, no. 5, pp. 507–517, 2004.
- [81] R. Hill, *The Mathematical Theory of Plasticity*. Oxford University Press, 1950.
- [82] J. Lubliner, *Plasticity Theory*. Dover Publications, 1990.
- [83] ——, “A maximum-dissipation principle in generalized plasticity,” *Acta Mechanica*, vol. 52, pp. 225–237, 1984.
- [84] W. Voigt, *Lehrbuch der Kristallphysik*. Teubner, 1910.

- [85] Y. Arramon, M. Mehrabadi, D. Martin, and S. Cowin, “A multidimensional anisotropic strength criterion based on Kelvin modes,” *International Journal of Solids and Structures*, vol. 37, pp. 2915–2935, 2000.
- [86] L. Kelvin, *Encyclopedia Britannica*. 9th ed., London and Edinburgh, 1878.
- [87] L. Walpole, “Fourth-rank tensors of the thirty-two crystal classes: Multiplication tables,” *Proceedings of the Royal Society of London. Series A., Mathematical and Physical Sciences*, vol. 391, no. 1800, pp. 149–179, 1984.
- [88] K. Meyberg and P. Vachenauer, *Höhere Mathematik 1*. Springer-Verlag, 1990.
- [89] T. J. Hughes, *The Finite Element Method*. Dover Publications, 2000.
- [90] O. Zienkiewicz and R. Taylor, *The Finite Element Method. Fifth edition*. Butterworth-Heinemann, 2000.
- [91] M. Galassi, J. Davies, J. Theiler, B. Gough, G. Jungman, P. Alken, M. Booth, and F. Rossi, *GNU Scientific Library*. Reference Manual, Edition 1.13, 2009.
- [92] A. Menzel and P. Steinmann, “On the comparison of two strategies to formulate orthotropic hyperelasticity,” *Journal of Elasticity*, vol. 62, pp. 171–201, 2001.
- [93] C. Miehe, “Aspects of the formulation and finite element implementation of large strain isotropic elasticity,” *International Journal for Numerical Methods in Engineering*, vol. 37, pp. 1981–2004, 1994.
- [94] J. Haslinger and P. Neittaanmäki, *Finite Element Approximation for Optimal Shape, Material and Topology Design*. Wiley, 1996.
- [95] M. Itskov, “On the theory of fourth-order tensors and their applications in computational mechanics,” *Comput. Methods Appl. Mech. Engrg.*, vol. 189, pp. 419–438, 2000.
- [96] O. Kintzel and Y. Başar, “Fourth-order tensors - tensor differentiation with applications to continuum mechanics. part i: Classical tensor analysis,” *Z. Angew. Math. Mech.*, vol. 86, pp. 291–311, 2006.

Index

- analytical gradient, 103
anisotropic material, 38
- balance of energy, 7
body force, 11
- Cauchy traction vector, 11
Cauchy's equation of equilibrium, 12
Cauchy's first equation of motion, 11
Cauchy's stress theorem, 11
Clausius–Duhem, 15, 16, 19, 20
crystal family, 38
cubic crystal system, 38
- deformed configuration, 7
density of heat production, 15, 16
design variable, 99
dilatation mode, 33
direct deformation gradient, 8
direct deformation map, 8
Dirichlet boundary condition, 55, 74
discretisation, 58, 75
dissipation inequality, 15, 16
divergence theorem, 11, 12, 74
- eigenvalue problem, 31
elastoplastic modulus, 19
entropy balance, 7
evolution laws, 22
external mechanical power, 13
- finite element method, 56, 75
first law of thermodynamics, 15
first Piola–Kirchhoff stress tensor, 12
first Piola–Kirchhoff traction vector, 12
free energy density, 19
- Gâteaux derivative, 61, 77
gradient-based algorithm, 99
- hardening, 19, 20, 22
hardening thermodynamical force, 20
heat flux, 15, 16
Helmholtz free energy, 15
hexagonal crystal system, 48
Hill tensor, 21
- infinite yield stress, 20
initial yield stress, 20
inverse deformation gradient, 8, 9
inverse deformation map, 8
inverse form finding, 73, 99
isochoric extension mode, 34
isochoric pure shear mode, 34
isochoric simple shear mode, 35
isotropic material, 37
- Jacobian determinant, 8, 9
- Karush–Kuhn–Tucker-type loading/unloading conditions, 22
Kelvin modes, 21, 31
kinematics of geometrically nonlinear continuum mechanics, 7
kinetic energy, 13
- Lagrangian stress tensor, 19
large strains, 19
least squares minimisation, 99
linearisation, 60, 77
logarithmic strain, 18, 20
- mass balance, 7
material configuration, 19

- mesh distortion, 104
momentum balance, 7
monoclinic crystal system, 42

Neumann boundary condition, 74
Neumann type boundary condition, 55
Newton's second law of motion, 10
Newton–Raphson method, 57, 59, 75, 76
node-based shape optimisation, 99
numerical gradient, 102

objective function, 99
orthorhombic crystal system, 39
orthotropy, 21

Piola formulation, 55
plastic flow rule, 22
plastic strain, 19
plastic yielding, 20
principle of virtual work, 56, 74
projection operator, 32

rate of deformation, 18
residual, 59, 76
right Cauchy–Green tensor, 18

saturation parameter, 20
second law of thermodynamics, 15
second Piola–Kirchhoff stress, 19
sensitivity analysis, 101
specific entropy, 15
specific internal energy, 15, 16
spectral decomposition, 31
spectral representation, 31
strain rate, 18
stress power, 13, 18
symmetric Cauchy stress, 74
symmetric Cauchy stress tensor, 11

tangent operator, 62, 78
tangent stiffness matrix, 62, 79
tetragonal crystal system, 45
triclinic crystal system, 44
trigonal crystal system, 41

undeformed configuration, 7

Voigt notation, 21
von Mises, 21

weak form, 56, 74

yield criterion, 22
yield function, 21
yield stress, 20
yield surface, 20

bereits veröffentlicht wurden:

1. Geisler, J.: Numerische und experimentelle Untersuchungen zum dynamischen Verhalten von Strukturen mit Fügestellen
2010, Band 1
2. Hossain, M.: Modelling and Computation of Polymer Curing
2010, Band 2
3. Görke, D.: Experimentelle und numerische Untersuchung des Normal- und Tangentialkontaktverhaltens rauer metallischer Oberflächen
2010, Band 3
4. Constantiniu, A.: A Hybrid Nodal-Element-Based Discretization Method
2010, Band 4
5. Scherer, M.: Regularizing Constraints for Mesh and Shape Optimization Problems
2011, Band 5
6. Fischer, P.: C^1 Continuous Methods in Computational Gradient Elasticity
2011, Band 6
7. Javili, A.: Thermomechanics of Solids Accounting for Surfaces and Interfaces
2012, Band 7
8. Germain, S.: On Inverse Form Finding for Anisotropic Materials in the Logarithmic Strain Space
2013, Band 8

